

**Proteins in Aqueous Nanodrops: Folding, Unfolding, and Gas-Phase Conformations  
Measured by Mass Spectrometry**

By

Daniel Mortensen

A dissertation submitted in partial satisfaction

of the requirements for the degree of

Doctor of Philosophy

in

Chemistry

in the

Graduate Division

of the

University of California, Berkeley

Committee in charge:

Professor Evan R. Williams, Chair  
Professor Kristie A. Boering  
Professor Robert M. Glaeser

Fall 2016

Proteins in Aqueous Nanodrops: Folding, Unfolding, and Gas-Phase Conformations Measured  
by Mass Spectrometry

©2016

by

Daniel Mortensen

# **Abstract**

Proteins in Aqueous Nanodrops: Folding, Unfolding, and Gas-Phase Conformations Measured by Mass Spectrometry

by

Daniel Mortensen

Doctor of Philosophy in Chemistry

University of California, Berkeley

Professor Evan R. Williams, Chair

Methods for measuring ultrafast ( $1 \mu\text{s}$ ) protein folding reactions, for forming highly charged protein ions, and for measuring the sizes and shapes of gas-phase protein ions are presented in this dissertation. Ultrafast protein folding is measured using rapid mixing from theta-glass emitters (double-barrel electrospray ionization emitters), in which reagent solutions are loaded into the different barrels of the emitters and rapid mixing occurs during electrospray ionization (ESI). Acidified aqueous solutions containing unfolded proteins are mixed with buffered aqueous solutions using the theta-glass emitters in order to increase the solution pH and induce protein folding during ESI. Reaction times in these experiments are obtained from the extent of folding that occurs and from folding time constants of model proteins. A  $1.0 \mu\text{s}$  reaction time is achieved in these experiments, whereas only reactions occurring in  $8 \mu\text{s}$  or greater could be monitored using rapid mixing techniques previously. A  $2.2 \mu\text{s}$  folding time constant for the formation of a  $\beta$ -hairpin in a 14 residue peptide and the  $1.5$  and  $<0.4 \mu\text{s}$  folding time constants for the formation of polyproline II helix structures in 21 and 16 residue peptides, respectively, are obtained. To the best of our knowledge, these are the fastest folding events that have been directly measured using a rapid mixing device. In the second method presented here, highly charged protein ions are formed by ESI simply by using emitters with submicron outer diameter tips rather than the micron or larger outer diameter tips typical used for ESI. Increased charging is obtained with the submicron outer diameter tips for proteins that are positively charged in solution as a result of Coulombic attraction between the positively charged protein molecules in solution and the negatively charged glass surfaces in the tips of the emitters, which results in protein unfolding occurring prior to ESI. Using submicron outer diameter tips is a simple way to obtain highly charged protein ions with ESI that does not require exposing the proteins to additional chemicals. The final method presented here is for relating the drift times of ions in travelling wave ion mobility spectrometry (TWIMS) with collisional cross sections using computational simulations. Collisional cross sections obtained using this method with gentle instrument conditions are very similar to those obtained using static drift ion mobility spectrometry (average difference =  $0.3\%$ ), demonstrating for the first time that collisional cross sections can be obtained from single TWIMS drift time measurements.

This work is lovingly dedicated to my wonderful wife,  
to our three children, and to my parents.

# Table of Contents

<b>Abstract.....</b>	1
<b>Table of Contents .....</b>	ii
<b>Acknowledgments .....</b>	v
<b>Chapter 1: Introduction .....</b>	1
1.1 Rapid Mixing and Protein Folding .....	1
1.2 Protein Folding and Mass Spectrometry Detection .....	2
1.3 Highly Charged Protein Ions .....	5
1.4 Protein Charging and ESI Emitter Tip Size.....	5
1.5 Ion Mobility Spectrometry.....	6
1.6 References.....	8
<b>Chapter 2: Theta-Glass Capillaries in Electrospray Ionization: Rapid Mixing and Short Droplet Lifetimes .....</b>	18
2.1 Introduction.....	18
2.2 Experimental .....	19
2.3 Results and Discussion .....	20
2.4 Conclusions.....	24
2.5 References.....	26
<b>Chapter 3: Investigating Protein Folding and Unfolding in Electrospray Nanodrops Upon Rapid Mixing Using Theta-Glass Emitters .....</b>	35
3.1 Introduction.....	35
3.2 Experimental Section .....	37
3.3 Results and Discussion .....	37
3.4 Conclusions.....	42
3.5 References.....	44
<b>Chapter 4: Ultrafast (1 <math>\mu</math>s) Mixing and Fast Protein Folding in Nanodrops Monitored by Mass Spectrometry .....</b>	51
4.1 Introduction.....	51
4.2 Experimental Section .....	52
4.3 Results and Discussion .....	53

4.4 Conclusions.....	60
4.5 References.....	61
<b>Chapter 5: Surface-Induced Protein Unfolding in Submicron Electrospray Emitters.....</b>	<b>69</b>
5.1 Introduction.....	69
5.2 Experimental Section .....	70
5.3 Results and Discussion .....	71
5.4 Conclusions.....	76
5.5 References.....	77
<b>Chapter 6: Electrothermal Supercharging of Proteins in Native MS: Effects of Protein Isoelectric Point, Buffer, and nanoESI-Emitter Tip Size.....</b>	<b>87</b>
6.1 Introduction.....	87
6.2 Experimental Section .....	88
6.3 Results and Discussion .....	89
6.4 Conclusions.....	94
6.5 References.....	95
<b>Chapter 7: Microsecond and Nanosecond Polyproline II Helix Formation in Aqueous Nanodrops Measured by Mass Spectrometry .....</b>	<b>104</b>
7.1 Introduction.....	104
7.2 Experimental .....	105
7.3 Results and Discussion .....	105
7.4 Conclusions.....	108
7.5 References.....	109
<b>Chapter 8: Collisional Cross Sections with T-Wave Ion Mobility Spectrometry without Experimental Calibration .....</b>	<b>115</b>
8.1 Introduction.....	115
8.2 Experimental .....	116
8.3 Calculations.....	117
8.4 Results and Discussion .....	120
8.5 Conclusions.....	123
8.6 References.....	124
<b>Appendix A: Schematic Diagram of the Experimental Setup and Relative Ionization Efficiency Measurements of Oxidized and Reduced DCIP.....</b>	<b>133</b>

<b>Appendix B: Electron Micrographs of the Tips of the Emitters, Mixing Efficiency Measurements, and TWIMS Drift Profiles .....</b>	<b>135</b>
<b>Appendix C: Mass spectra of hMb in 10, 100 and 500 mM aqueous ammonium acetate and ammonium bicarbonate solutions obtained with ~1465 and ~305 nm o.d. tips .....</b>	<b>139</b>
<b>Appendix D: Electron micrographs of the tips of the emitters and mass spectra of hMb, cyt <i>c</i>, and <math>\beta</math>-lac A in 100 mM aqueous ammonium acetate, formate, and bicarbonate solutions acquired under native MS conditions .....</b>	<b>141</b>
<b>Appendix E: A second-order polynomial relating TWIMS drift times with adjusted cross sections obtained using DTIMS cross sectional values is compared with that obtained using purely hypothetical adjusted cross sectional values .....</b>	<b>145</b>

## **Acknowledgments**

I would like to thank Professor Evan Williams for allowing me to join his research group and for providing me with the means and support I needed to obtain my doctorate degree in chemistry. I would also like to thank all the members of my research group at UC Berkeley, especially those who have directly contributed to my success, including Dr. Harry Sterling, Dr. Tawnya Flick, Dr. Catherine Cassou Going, and Anna Susa.

I would also like to thank those outside of the research lab who have helped me so much. My wife Lisa has been a constant support for me through hard times and good, and I could not have completed this work without her help. I would also like to thank my children who help motivate me with their loving smiles. And lastly I would like to thank my parents, Clint and Stacey Mortensen, who taught me at a young age the value of hard work.

# Chapter 1

## Introduction

### Part 1: Protein Folding

#### 1.1 Rapid Mixing and Protein Folding

Protein folding is a process in which proteins transition from elongated conformations to more compact globular conformations. The biological function of a protein depends on the conformation adopted by that protein after folding occurs. Protein folding pathways can include multiple folding steps,<sup>1,2</sup> and the formation of secondary structures, such as  $\alpha$ -helices,  $\beta$ -turns, and loops, often occur within the first tens of microseconds or less of folding.<sup>3,4</sup> However, the folding pathway and final folded conformation cannot yet be predicted from the amino acid sequence for all proteins, especially those containing more than ~100 amino acids.<sup>4,5</sup> Fast protein folding events can be investigated using numerous methods and techniques, including using mechanical force,<sup>1</sup> pressure jumps,<sup>6-8</sup> laser induced temperature jumps,<sup>9-13</sup> flash photolysis,<sup>14</sup> electron transfer,<sup>15</sup> and rapid mixing of two or more solutions.<sup>16-22</sup> Both laser induced temperature jump and flash photolysis techniques have been used to access extremely fast reaction times within the nanosecond time range,<sup>9-14</sup> and these techniques have had a dramatic impact on the current understanding of fast protein folding events.<sup>3</sup> However, few photolyzable triggers are available for use in investigating protein folding with flash photolysis,<sup>2</sup> and measuring folding events with laser induced temperature jumps sometimes results in protein folding time constants that are more than an order of magnitude faster than those obtained using rapid mixing techniques.<sup>2,23</sup> This is because the folding events induced by temperature jumps are in some cases different than those induced upon rapid mixing of a protein in a denaturing solution with a buffered aqueous solution.<sup>2,23</sup> Therefore, rapid mixing of two or more solutions remains one of the most common techniques for investigating fast protein folding.<sup>2,22</sup>

Rapid mixing devices commonly used to investigate protein folding reactions and other fast chemical reactions include laminar,<sup>20,21</sup> turbulent,<sup>17,19</sup> and chaotic<sup>16,18,22</sup> flow mixers. In these devices, reagent solutions are flowed into each other within micro-machined channels with diameters ranging in size from about 0.1 to 500  $\mu\text{m}$ , though the geometries of the mixing regions within these devices varies among the different types of mixers.<sup>2</sup> The reaction times obtained with these devices decreases with increasing solution flow rate,<sup>21,24</sup> and an 8  $\mu\text{s}$  reaction time was reported for a laminar flow mixer with a ~100 nL/s flow rate.<sup>25</sup> Protein folding events that occur too quickly to be directly measured with rapid mixing devices can be slowed by adding denaturants, such as guanidinium or urea, to the protein solution.<sup>26-28</sup> The folding time constant for a protein in a solution that does not contain denaturants is then obtained by plotting the protein folding time constants obtained at different denaturant concentrations and extrapolating to zero.<sup>26-28</sup> However, adding denaturants to protein solutions can alter the protein folding pathway, which can result in the protein folding time constants obtained using this method being

inaccurate.<sup>26,28</sup> Therefore, in order to accurately measure protein folding from highly unfolded states to compact globular states, rapid mixing devices capable of achieving faster reaction times are needed.

## 1.2 Protein Folding and Mass Spectrometry Detection

**1.2.1 Proteins in Electrospray Ionization Mass Spectrometry.** Electrospray ionization (ESI) mass spectrometry (MS) is a powerful tool for obtaining information about protein structure, including protein identification and analysis of posttranslational and other chemically induced modifications.<sup>29-32</sup> ESI can be used to form multiply charged gas-phase protein ions from solution, often without causing significant changes to the protein conformation. ESI MS is performed by applying a potential of between about 0.4 and 5 kV between the analyte solution and the inlet to the mass spectrometer, resulting in the formation of charged droplets from the analyte solution. ESI droplets are typically formed in atmosphere and undergo rapid desolvation, resulting in the charge density of the droplets increasing as solvent evaporation occurs. When the surface tension of a droplet can no longer support the amount of charge in the droplet, the droplet fissions, resulting in the loss of ~15% of the charge and ~2% of the mass of the droplet.<sup>33,34</sup> Protein ions are likely formed from ESI droplets by desolvation and droplet fission occurring until the droplet is the size of the protein and all of the charge remaining in the droplet is transferred to the protein,<sup>34-36</sup> though other possible mechanisms have been reported.<sup>37-39</sup>

Several factors are known to affect the charging of protein ions in ESI, including the pH<sup>40</sup> and surface tension<sup>36,41</sup> of the solvent, the solvent and protein basicities,<sup>42-44</sup> the protein isoelectric point (pI),<sup>45,46</sup> the size of the tips of the ESI emitters,<sup>47-50</sup> and instrument parameters.<sup>51,52</sup> One of the most important factors that affects protein charging, however, is the solution-phase conformation of the proteins prior to gaseous ion formation, with folded globular conformers typically resulting in lower charge states than unfolded conformers.<sup>53-57</sup> The relative abundance of different conformers in a solution can be obtained by modelling the charge state distributions in ESI mass spectra,<sup>53,54,57</sup> which has been done to measure protein conformation as a function of both temperature<sup>53,57</sup> and solution pH.<sup>54</sup>

**1.2.2 Rapid Mixing and Mass Spectrometry.** The use of ESI MS to monitor rapid mixing experiments provides several advantages, including high chemical specificity, high sensitivity, and rapid speed of analysis.<sup>58</sup> Several types of rapid mixers have been coupled with ESI MS, including laminar flow,<sup>25,59</sup> stopped flow,<sup>60</sup> and continuous flow<sup>61,62</sup> mixers in order to measure the kinetics of protein folding<sup>25,59,60</sup> and unfolding,<sup>62</sup> as well as to measure the reincorporation rates of non-covalent cofactors, such as heme groups, into the protein structure.<sup>61</sup> The fastest reaction time obtained with a conventional mixer coupled with MS is 200 µs, which was achieved using a laminar flow mixer with a flow rate of 10 µL/s.<sup>59</sup> This setup was used to investigate sub-ms folding steps of apo-myoglobin that occur after the 7 µs initial collapse or “burst phase” of the protein.<sup>63</sup>

Solutions have also been mixed during ESI prior to MS detection using a number of devices and techniques, including fused-droplet electrospray,<sup>64,65</sup> multiple channel electrospray,<sup>66,67</sup> extractive electrospray,<sup>68-70</sup> and dual-sprayer microchips.<sup>71-73</sup> Acids<sup>74,75</sup> and bases,<sup>76</sup> as well as other chemical reagents,<sup>75</sup> have been added to electrospray droplets by exposing the droplets to either acidic<sup>74</sup> or basic<sup>76</sup> vapors in an ESI interface or by flowing continuous streams of solution from hypodermic needles through ESI plumes.<sup>75</sup> Solution phase-

reactions monitored with MS have been carried out in charged microdroplets using ambient ion soft landing,<sup>77</sup> desorption electrospray ionization,<sup>78,79</sup> and microdroplet fusion.<sup>80</sup> Microdroplet fusion is accomplished by orthogonally colliding droplets, which are formed by the atomization of reagent solutions using a nebulizing gas, and has been used to measure protein unfolding, hydrogen deuterium exchange, and bimolecular reduction-oxidation in droplets at reaction times of >13  $\mu$ s.<sup>80</sup> Reaction times in microdroplet fusion are estimated from the velocity of the fused droplets and the distance between the droplet collision point and the inlet to the mass spectrometer.<sup>80</sup>

Solutions can also be mixed in ESI droplets using theta-glass emitters, which are double-barrel ESI emitters that resemble the Greek letter  $\theta$  “theta” when turned on end. Different reagent solutions are loaded into the different barrels of these emitters and are separated by a divider that extends to the tip of the emitter. When ESI is initiated, the solutions exit the emitter and mix in the ESI droplets. These devices were first used to form non-covalent complexes between the short peptide KAA and the glycopeptide vancomycin and to exchange hydrogen and deuterium with vancomycin during ESI.<sup>81</sup> Theta-glass emitters have also been used to unfold proteins in ESI droplets by mixing proteins in aqueous solutions with acidified aqueous solutions.<sup>82</sup>

In Chapter 2, rapid mixing from theta-glass emitters is used to carry out the bimolecular oxidation-reduction reaction between L-ascorbic acid and 2,6-dichloroindophenol during ESI. An apparent reaction time of ~274  $\mu$ s is obtained from the extent of product formation that occurs in the ESI droplets and from the rate constant of this reaction in bulk solution. However, the rates of bimolecular reactions in microdroplets can be up to three orders of magnitude greater than those in bulk solution.<sup>78,83</sup> This is because the rapid evaporation of a droplet increases both the concentrations of the reagents and the surface area to volume ratio within the droplet and can result in up to a 4 unit change in the droplet pH occurring.<sup>84,85</sup> Therefore, the true reaction time in these experiments is likely one to three orders of magnitude less than the 274  $\mu$ s apparent reaction time (i.e. less than 27  $\mu$ s). Results from this study demonstrate that bimolecular reactions are readily monitored with rapid mixing from theta-glass emitters and that ESI droplet lifetimes can be very short.

**1.2.3 Protein Folding in ESI Droplets.** Although many studies of protein *unfolding* during ESI have been reported, there are relatively few on protein *folding* during ESI. Acid-denatured proteins in ESI droplets have been exposed to basic vapors in an ESI interface, resulting in bimodal charge state distributions for some proteins that are consistent with protein folding occurring during ESI.<sup>86</sup> However, it is often difficult to find solution conditions that result in charge state distributions similar to those obtained when acidified droplets are exposed to gaseous bases,<sup>86</sup> possibly suggesting that the folded protein conformations resulting from these experiments are different than those adopted by the proteins in bulk solution. In a separate study by Sterling and Williams, it was reported that ESI of thermally denatured myoglobin resulted in low charge state ions consistent with a folded protein structure, suggesting that protein folding may have occurred in the ESI droplets as a result of evaporative cooling.<sup>56</sup>

In Chapter 3, protein folding is induced during ESI by rapidly mixing acid-denatured proteins with either water or buffered aqueous solutions using theta-glass emitters. Reaction times are obtained from the extent of folding that occurs in these experiments for proteins (cytochrome *c* and myoglobin) with known folding time constants (57 and 7  $\mu$ s, respectively). Similar reaction times of ~7 and ~9  $\mu$ s are obtained for these respective proteins in droplets comprised of buffered aqueous solutions even though the folding time constants of these proteins

differ by about an order of magnitude. These results indicate that protein folding events that occur on the ~10  $\mu$ s timescale can be readily investigated using rapid mixing from theta-glass emitters coupled with MS.

The extent to which solution-phase reactions can occur in ESI droplets formed from theta-glass emitters depends on the droplet lifetime, which depends on several factors, including the composition and initial diameter of the droplets.<sup>87</sup> Several models have been reported<sup>88-91</sup> for predicting the initial size of ESI droplets on the basis of the solution flow rate and other solution and instrument conditions. Dülcks and coworkers compared some of these models<sup>92</sup> and reported that they result in initial droplet sizes that vary by about three orders of magnitude from ~10<sup>-4</sup> to ~10<sup>-7</sup> m for the same water, methanol, acetic acid solution under identical conditions. Therefore, the exact relationship between the initial droplet diameter and the instrument and solution conditions is not fully known. However, the experimental results used to derive these models all clearly indicate that the initial droplet diameter depends on the solution flow rate,<sup>88-90,93</sup> which also depends on several factors, including the size of the tip of the ESI emitter and the backing pressure applied to the solutions during ESI.<sup>47,93</sup>

In order to probe different reaction times with the theta-glass emitters, the solution flow rate was varied (Chapter 4). This was done by changing the backing pressure applied to the solutions and by using emitters with different tip sizes, resulting in flow rates between about 48 and 2880 pL/s. The reaction times obtained in these experiments increase with increasing flow rate from 1.0  $\mu$ s at 48 pL/s to 22  $\mu$ s at 2880 pL/s. Nominally the same reaction times are obtained at the different flow rates for three different proteins (Trp-cage, myoglobin, and cytochrome *c*) that have folding time constants that differ by more than an order of magnitude (4.1, 7, and 57  $\mu$ s, respectively), indicating that the reaction times obtained in these experiments are highly reproducible. The ultrafast 1.0  $\mu$ s reaction time reported in Chapter 4 is about an order of magnitude less than the fastest 8  $\mu$ s reaction time obtained with a conventional mixer, and the flow rate used to obtain this 1.0  $\mu$ s reaction time (48 pLs) is about 2000 times less than the flow rate (~100 nL/s) used to obtain the 8  $\mu$ s reaction time with a conventional mixer.<sup>25</sup> These results show that faster reaction times are accessed with rapid mixing from theta-glass emitters coupled with MS than with any other rapid mixing technique currently available and that substantially less sample is used than in conventional mixing devices.

**1.2.4 Applications of Rapid Mixing from Theta-Glass Emitters.** In Chapter 4, rapid mixing from theta-glass emitters is used to measure the 2.2  $\mu$ s folding time constant for the formation of a  $\beta$ -hairpin in a 14 residue peptide, and in Chapter 7, to measure the 1.5 and <0.4  $\mu$ s folding time constants for the formation of polyproline II helix structures in 21 and 16 residue peptides, respectively. To the best of our knowledge, these are the fastest folding events that have been directly measured using a rapid mixing technique. The formation of the polyproline II helix structures reported in Chapter 7 occurs in droplets composed of buffered aqueous solutions. Formation kinetics for polyproline II helix structures in native-like buffered aqueous solutions have not been measured previously, despite the common occurrence of these structures in natively folded proteins.<sup>94-97</sup> Therefore, the folding time constants reported in Chapter 7 are the first of their kind and should prove useful in developing computational models of protein folding. Rapid mixing from theta-glass emitters should also prove useful in measuring the folding times and elucidating the mechanisms of numerous other fast folding events, as well as for studying bimolecular and more complex reactions.

## Part 2: Charging and Conformation of Protein Ions Formed with ESI

### 1.3 Highly Charged Protein Ions

High charge state ions are advantageous in MS because they can increase both resolution and sensitivity for charge detection instruments, such as orbitrap and ion cyclotron mass spectrometers.<sup>98,99</sup> High charge state ions also fragment more readily, often resulting in increased structural information in tandem MS.<sup>100-102</sup> High charge state ions typically have fewer cation adducts than low charge state ions,<sup>46,103</sup> and unresolved adducts broaden ion peaks in mass spectra, resulting in lower resolution and mass measuring accuracy.<sup>104</sup> It is often desirable to increase the extent to which protein ions charge in ESI without disrupting the solution-phase conformation of protein molecules prior to ESI. Increased charging can be obtained from both denaturing<sup>73,105-111</sup> and buffered aqueous<sup>111-118</sup> solutions by adding supercharging reagents, such as m-nitrobenzyl alcohol or propylene carbonate, to the solutions.<sup>110,117</sup> Supercharging reagents do not disrupt the conformation of protein molecules in bulk solution,<sup>41,113,117,119</sup> but in ESI droplets, solvent evaporation causes the concentration of the supercharging reagents to increase, resulting in protein denaturation occurring in the droplets and highly charged gas-phase ions being produced.<sup>41,56,113,117</sup> Exposing folded proteins in ESI droplets to acidic<sup>74</sup> or basic<sup>76</sup> vapors in the interface of mass spectrometers also results in unfolding and high charging. Increased charging can also be obtained by adding trivalent metal ions to protein solutions at concentrations that do not disrupt protein conformations. During ESI, these trivalent ions can adduct to a protein and provide more charge than is provided by a proton or other monovalent cations, such as sodium or potassium, that are commonly found in aqueous solutions.<sup>120</sup>

Highly charged protein ions can also be formed from solutions in which proteins have native-like conformations and activities by using electrothermal supercharging. In electrothermal supercharging, ions are formed from buffered aqueous solutions using high spray potentials, which result in collisional heating of the ESI droplets and unfolding of the proteins.<sup>121-123</sup> Thus, electrothermal supercharging can be used to generate high charge state ions from buffered aqueous solutions without adding additional chemicals to the solutions. Electrothermal supercharging results in charge states that are as high or higher than those obtained from denaturing solutions.<sup>122</sup> Electron capture dissociation of the 16+ charge state of cytochrome *c* formed from both denaturing solutions and from electrothermal supercharging results in the same extent of sequence coverage but with some differences in the cleavage sites.<sup>122</sup> Thus, a greater extent of sequence coverage is obtained by tandem MS of the high charge state ions formed from both electrothermal supercharging and from denaturing solutions than is obtained by tandem MS of the ions generated using only one of these methods.<sup>122</sup> The relative effectiveness of ammonium and sodium salts at inducing electrothermal supercharging is correlated with an increased propensity to induce protein aggregation in solution.<sup>123</sup> The effect of protein pI on the extent of charging resulting from electrothermal supercharging has also been investigated,<sup>122,123</sup> and electrothermal supercharging is generally slightly more effective for proteins that are positively charged in solution than for proteins that are negatively charged in solution.<sup>122</sup>

### 1.4 Protein Charging and ESI Emitter Tip Size

Increased charging for protein and peptide ions formed from denaturing solutions can also be obtained by using ESI emitters with smaller tip sizes. For example, the average charge of

angiotensin I ions formed from a denaturing solution increased from ~1.7 to ~2.8 when the tip outer diameter was decreased from ~5 to ~1  $\mu\text{m}$ .<sup>47</sup> Increased charging was also reported for cytochrome c and ubiquitin ions formed from denaturing solutions with <100 nm outer diameter tips compared to that obtained with 1  $\mu\text{m}$  outer diameter tips.<sup>50</sup> The increased charging with the smaller tip sizes reported in these studies was attributed to the formation of smaller droplets with higher charge densities.<sup>47,50</sup> Increased charging with decreasing tip size was also reported for protein and peptide ions formed from denaturing solutions with ESI emitters with adjustable orifice sizes.<sup>48,49</sup> In these devices, the orifice size is varied between 1 and >10  $\mu\text{m}$  by adjusting the position of silicon chips.

Increased charging with decreasing ESI emitter tip size has only been reported for proteins that are positively charged in solution,<sup>47-50</sup> suggesting that the increased charging obtained with decreasing tip size may depend on the charge of the protein molecules in solution. ESI emitters are typically prepared from borosilicate<sup>47,50</sup> or other forms of silicon<sup>48,49</sup> that contain silanol groups,<sup>124</sup> and in aqueous solutions, a fraction of the silanol groups is deprotonated, resulting in a net negative charge on glass surfaces.<sup>124</sup> Thus, the increased charging obtained with decreasing tip size for proteins that are positively charged in solution may result from Coulombic attraction to the negatively charged glass surfaces in the tips of the ESI emitters resulting in protein unfolding occurring prior to ESI. Interactions between positively charged protein molecules and negatively charged glass surfaces are known to occur in solution,<sup>125-128</sup> and interactions between proteins and surfaces often result in substantial changes in the conformations of proteins.<sup>129</sup>

In Chapters 5 and 6, the origins of the increased charging with decreasing tip size is investigated by comparing the extent of charging obtained for protein ions formed from aqueous solutions using ESI emitters with micron and submicron outer diameter tips. Increased charging is obtained with decreasing tip size for proteins that are positively charged in solution but not for proteins that are negatively charged in solution. The increased charging obtained for the proteins that are positively charged in solution is consistent with protein unfolding occurring with the submicron outer diameter tips. This increased charging only occurring for proteins that are positively charged in solution is also consistent with the unfolding occurring as a result of Coulombic attraction between the positively charged protein molecules in solution and the negatively charged glass surfaces in the tips of the ESI emitters. The results in Chapters 5 and 6 demonstrate a method for producing high charge states that does not require the addition of extra reagents either to the analyte solution or in the gas phase. In Chapter 6, it is demonstrated that the extent of charging obtained with the smaller tips for positively charged proteins in solution can be increased even further by using high spray potentials, which result in electrothermal supercharging of the proteins in the ESI droplets.

## 1.5 Ion Mobility Spectrometry

Information about the conformations of gas-phase ions can be obtained using ion mobility spectrometry (IMS), which separates ions based on collisional cross section. In IMS, ions are accelerated by an electric field through a drift region filled with a buffer gas. As ions traverse the drift region, collisions with the buffer gas occur, resulting in the velocity of the ions being damped. Ions with large cross sections undergo more collisions with the buffer gas than ions with small cross sections, resulting in the velocity of large ions being damped more than the velocity of small ions. IMS has been utilized in numerous applications, including the separation

of atomic ions,<sup>130,131</sup> small clusters,<sup>131-133</sup> and complex mixtures, such as those resulting from tryptic digests,<sup>134-136</sup> and the study of gas-phase conformations of proteins,<sup>137-139</sup> protein complexes,<sup>140-142</sup> and even viruses.<sup>143</sup> Various types of IMS devices have been coupled with MS detection, including static drift tube,<sup>144-146</sup> aspiration,<sup>147,148</sup> field-asymmetric,<sup>149-151</sup> and travelling-wave<sup>152,153</sup> IMS devices, which have different electric field geometries and operate in different pressure regimes.<sup>154,155</sup>

The first commercially available IMS device fully integrated with MS detection was the travelling wave ion mobility spectrometer (TWIMS), which was released in 2006. The drift region in a TWIMS device consists of a series of ring electrodes, in which ions are radially confined by applying RF potentials of opposite polarity to adjacent electrodes.<sup>156</sup> A potential wave is generated in the TWIMS device by applying a DC potential to a set of adjacent ring electrodes, and this wave is moved through the device with time. Some ions traverse the device at the velocity of the wave, and others are overtaken by the wave, resulting in ion separation.<sup>156,157</sup> Determining collisional cross sections of ions using TWIMS is typically done by calibrating the time required for ions to traverse the device with collisional cross sections of ions measured using static drift IMS,<sup>155,158-160</sup> and this calibration process can be time consuming.

A method for directly measuring the mobility of ions using a TWIMS device has been reported by others.<sup>161</sup> SIMION modelling was used to derive an equation relating the collisional cross section of an ion and the velocity of the potential wave with the minimum wave amplitude required for the ion to traverse the cell at the wave velocity. This minimum amplitude is obtained by incrementally increasing the wave amplitude until the ions traverses the device at the velocity of the wave. Cross sections obtained using this method are the same as those obtained using static drift IMS to within 5%.<sup>161</sup> However, no method is currently available for determining the collisional cross sections of ions from single TWIMS drift time measurements.<sup>140,155,157,162</sup>

In Chapter 8, a method for obtaining collisional cross sections from single TWIMS drift time measurements using commercially available TWIMS devices is presented. This method relies on computational simulations that are developed on the basis of SIMION modelling of the TWIMS potential wave and equations that describe the motion of ions in gases induced by electric fields. Collisional cross sections obtained using this method with gentle instrument settings are very similar to those obtained using static drift IMS devices (average difference = 0.3%), indicating for the first time that collisional cross sections can be obtained from single TWIMS drift time measurements. Therefore, the method presented in Chapter 8 eliminates the need to calibrate TWIMS devices with previously measured collisional cross sections and, thus, expedites the process of obtaining collisional cross sections with TWIMS.

## 1.6 References

- (1) Cecconi, C.; Shank, E. A.; Bustamante, C.; Marqusee, S. Direct observation of the three-state folding of a single protein molecule. *Science* **2005**, *309*, 2057-2060.
- (2) Kathuria, S. V.; Chan, A.; Graceffa, R.; Nobrega, R. P.; Matthews, C. R.; Irving, T. C.; Perot, B.; Bilsel, O. Advances in Turbulent Mixing Techniques to Study Microsecond Protein Folding Reactions. *Biopolymers* **2013**, *99*, 888-896.
- (3) Kubelka, J.; Hofrichter, J.; Eaton, W. A. The protein folding ‘speed limit’. *Curr. Opin. Struct. Biol.* **2004**, *14*, 76-88.
- (4) Lindorff-Larsen, K.; Piana, S.; Dror, R. O.; Shaw, D. E. How Fast-Folding Proteins Fold. *Science* **2011**, *334*, 517-520.
- (5) Lapidus, L. J. Exploring the top of the protein folding funnel by experiment. *Curr. Opin. Struct. Biol.* **2013**, *23*, 30-35.
- (6) Woenckhaus, J.; Kohling, R.; Thiagarajan, P.; Littrell, K. C.; Seifert, S.; Royer, C. A.; Winter, R. Pressure-jump small-angle x-ray scattering detected kinetics of staphylococcal nuclease folding. *Biophys. J.* **2001**, *80*, 1518-1523.
- (7) Torrent, J.; Font, J.; Herberhold, H.; Marchal, S.; Ribo, M.; Ruan, K. C.; Winter, R.; Vilanova, M.; Lange, R. The use of pressure-jump relaxation kinetics to study protein folding landscapes. *Biochim. Biophys. Acta, Proteins Proteomics* **2006**, *1764*, 489-496.
- (8) Prigozhin, M. B.; Liu, Y.; Wirth, A. J.; Kapoor, S.; Winter, R.; Schulten, K.; Gruebele, M. Misplaced helix slows down ultrafast pressure-jump protein folding. *Proc. Natl. Acad. Sci. U. S. A.* **2013**, *110*, 8087-8092.
- (9) Thompson, P.; Eaton, W.; Hofrichter, J. Laser temperature jump study of the helix reversible arrow coil kinetics of an alanine peptide interpreted with a 'kinetic zipper' model. *Biochemistry* **1997**, *36*, 9200-9210.
- (10) Gai, F.; Du, D.; Xu, Y. Infrared temperature-jump study of the folding dynamics of alpha-helices and beta-hairpins. *Methods Mol. Biol.* **2007**, *350*, 1-20.
- (11) Dyer, R. B.; Brauns, E. B. Laser-Induced Temperature Jump Infrared Measurements of RNA Folding. *Methods Enzymol.* **2009**, *469*, 353-372.
- (12) Chen, J.; Rempel, D. L.; Gau, B. C.; Gross, M. L. Fast Photochemical Oxidation of Proteins and Mass Spectrometry Follow Submillisecond Protein Folding at the Amino-Acid Level. *J. Am. Chem. Soc.* **2012**, *134*, 18724-18731.
- (13) Jones, K. C.; Peng, C. S.; Tokmakoff, A. Folding of a heterogeneous beta-hairpin peptide from temperature-jump 2D IR spectroscopy. *Proc. Natl. Acad. Sci. U. S. A.* **2013**, *110*, 2828-2833.
- (14) Jones, C. M.; Henry, E. R.; Hu, Y.; Chan, C. K.; Luck, S. D.; Bhuyan, A.; Roder, H.; Hofrichter, J.; Eaton, W. A. Fast Events in Protein-Folding Initiated by Nanosecond Laser Photolysis. *Proc. Natl. Acad. Sci. U. S. A.* **1993**, *90*, 11860-11864.
- (15) Pascher, T.; Chesick, J. P.; Winkler, J. R.; Gray, H. B. Protein folding triggered by electron transfer. *Science* **1996**, *271*, 1558-1560.
- (16) Bringer, M.; Gerdts, C.; Song, H.; Tice, J.; Ismagilov, R. Microfluidic systems for chemical kinetics that rely on chaotic mixing in droplets. *Philos. Trans. R. Soc. A* **2004**, *362*, 1087-1104.
- (17) Majumdar, Z. K.; Sutin, J. D. B.; Clegg, R. M. Microfabricated continuous-flow, turbulent, microsecond mixer. *Rev. Sci. Instrum.* **2005**, *76*, 125103.

- (18) Hassell, D.; Zimmerman, W. Investigation of the convective motion through a staggered herringbone micromixer at low Reynolds number flow. *Chem. Eng. Sci.* **2006**, *61*, 2977-2985.
- (19) Matsumoto, S.; Yane, A.; Nakashima, S.; Hashida, M.; Fujita, M.; Goto, Y.; Takahashi, S. A rapid flow mixer with 11- $\mu$ s mixing time microfabricated by a pulsed-laser ablation technique: Observation of a barrier-limited collapse in cytochrome c folding. *J. Am. Chem. Soc.* **2007**, *129*, 3840-3841.
- (20) Wang, C.; Hu, Y.; Hu, T. Biophysical Micromixer. *Sensors* **2009**, *9*, 5379-5389.
- (21) Gambin, Y.; Simonnet, C.; VanDelinder, V.; Deniz, A.; Groisman, A. Ultrafast microfluidic mixer with three-dimensional flow focusing for studies of biochemical kinetics. *Lab Chip* **2010**, *10*, 598-609.
- (22) Li, Y.; Zhang, D.; Feng, X.; Xu, Y.; Liu, B. A microsecond microfluidic mixer for characterizing fast biochemical reactions. *Talanta* **2012**, *88*, 175-180.
- (23) Narayanan, R.; Zhu, L.; Velmurugu, Y.; Roca, J.; Kuznetsov, S. V.; Prehna, G.; Lapidus, L. J.; Ansari, A. Exploring the Energy Landscape of Nucleic Acid Hairpins Using Laser Temperature-Jump and Microfluidic Mixing. *J. Am. Chem. Soc.* **2012**, *134*, 18952-18963.
- (24) Park, H.; Qiu, X.; Rhoades, E.; Korlach, J.; Kwok, L.; Zipfel, W.; Webb, W.; Pollack, L. Achieving uniform mixing in a microfluidic device: Hydrodynamic focusing prior to mixing. *Anal. Chem.* **2006**, *78*, 4465-4473.
- (25) Wu, L.; Lapidus, L. J. Combining Ultrarapid Mixing with Photochemical Oxidation to Probe Protein Folding. *Anal. Chem.* **2013**, *85*, 4920-4924.
- (26) Makhatadze, G. I. Thermodynamics of protein interactions with urea and guanidinium hydrochloride. *J. Phys. Chem. B* **1999**, *103*, 4781-4785.
- (27) Pace, C. N.; Shaw, K. L. Linear extrapolation method of analyzing solvent denaturation curves. *Proteins* **2000**, *4*, 1-7.
- (28) Maxwell, K.; Wildes, D.; Zarrine-Afsar, A.; de los Rios, M.; Brown, A.; Friel, C.; Hedberg, L.; Horng, J.; Bona, D.; Miller, E.; Vallee-Belisle, A.; Main, E.; Bemporad, F.; Qiu, L.; Teilum, K.; Vu, N.; Edwards, A.; Ruczinski, I.; Poulsen, F.; Kragelund, B.; Michnick, S.; Chiti, F.; Bai, Y.; Hagen, S.; Serrano, L.; Oliveberg, M.; Raleigh, D.; Wittung-Stafshede, P.; Radford, S.; Jackson, S.; Sosnick, T.; Marqusee, S.; Davidson, A.; Plaxco, K. Protein folding: Defining a "standard" set of experimental conditions and a preliminary kinetic data set of two-state proteins. *Protein Sci.* **2005**, *14*, 602-616.
- (29) Kruppa, G.; Schoeniger, J.; Young, M. A top down approach to protein structural studies using chemical cross-linking and Fourier transform mass spectrometry. *Rapid Commun. Mass Spectrom.* **2003**, *17*, 155-162.
- (30) Aebersold, R.; Mann, M. Mass spectrometry-based proteomics. *Nature* **2003**, *422*, 198-207.
- (31) Siuti, N.; Kelleher, N. L. Decoding protein modifications using top-down mass spectrometry. *Nat. Methods* **2007**, *4*, 817-821.
- (32) Pan, J.; Borchers, C. H. Top-down structural analysis of posttranslationally modified proteins by Fourier transform ion cyclotron resonance-MS with hydrogen/deuterium exchange and electron capture dissociation. *Proteomics* **2013**, *13*, 974-981.
- (33) Gomez, A.; Tang, K. Charge and fission of droplets in electrostatic sprays. *Phys. Fluids* **1994**, *6*, 404-414.
- (34) Fernandez de la Mora, J. Electrospray ionization of large multiply charged species proceeds via Dole's charged residue mechanism. *Anal. Chim. Acta* **2000**, *406*, 93-104.

- (35) Dole, M.; Mack, L. L.; Hines, R. L.; Mobley, R. C.; Ferguson, L. D.; Alice, M. B. Molecular Beams of Macroions. *J. Phys. Chem.* **1968**, *49*, 2240-2249.
- (36) Iavarone, A. T.; Williams, E. R. Mechanism of charging and supercharging molecules in electrospray ionization. *J. Am. Chem. Soc.* **2003**, *125*, 2319-2327.
- (37) Iribarne, J. V.; Thomson, B. A. On the evaporation of small ions from charged droplets. *J. Chem. Phys.* **1976**, *64*, 2287-2294.
- (38) Hogan Jr., C. J.; Carroll, J. A.; Rohrs, H. W.; Biswas, P.; Gross, M. L. Charge Carrier Field Emission Determines the Number of Charges on Native State Proteins in Electrospray Ionization. *J. Am. Chem. Soc.* **2008**, *130*, 6926-6927.
- (39) Hogan Jr., C. J.; Carroll, J. A.; Rohrs, H. W.; Biswas, P.; Gross, M. L. Combined Charged Residue-Field Emission Model of Macromolecular Electrospray Ionization. *Anal. Chem.* **2009**, *81*, 369-377.
- (40) Wang, G.; Cole, R. B. Disparity Between Solution-phase Equilibria and Charge State Distributions in Positive-ion Electrospray Mass Spectrometry. *Org. Mass Spectrom.* **1994**, *29*, 419-427.
- (41) Sterling, H. J.; Cassou, C. A.; Trnka, M. J.; Burlingame, A. L.; Krantz, B. A.; Williams, E. R. The role of conformational flexibility on protein supercharging in native electrospray ionization. *Phys. Chem. Chem. Phys.* **2011**, *13*, 18288-18296.
- (42) Loo, R. R. O.; Smith, R. D. Proton-Transfer Reactions of Multiply-Charged Peptide and Protein Cations and Anions. *J. Mass Spectrom.* **1995**, *30*, 339-347.
- (43) Williams, E. R. Proton Transfer Reactivity of Large Multiply Charged Ions. *J. Mass Spectrom.* **1996**, *31*, 831-842.
- (44) Iavarone, A. T.; Jurchen, J. C.; Williams, E. R. Effects of solvent on the maximum charge state and charge state distribution of protein ions produced by electrospray ionization. *J. Am. Soc. Mass Spectrom.* **2000**, *11*, 976-985.
- (45) Nielsen, M. L.; Savitski, M. M.; Kjeldsen, F.; Zubarev, R. A. Physicochemical properties determining the detection probability of tryptic peptides in Fourier transform mass spectrometry. A correlation study. *Anal. Chem.* **2004**, *76*, 5872-5877.
- (46) Pan, P.; Gunawardena, H. P.; Xia, Y.; McLuckey, S. A. Nanoelectrospray ionization of protein mixtures: Solution pH and protein pI. *Anal. Chem.* **2004**, *76*, 1165-1174.
- (47) Li, Y.; Cole, R. B. Shifts in peptide and protein charge state distributions with varying spray tip orifice diameter in nanoelectrospray Fourier transform ion cyclotron resonance mass spectrometry. *Anal. Chem.* **2003**, *75*, 5739-5746.
- (48) Ek, P.; Sjodahl, J.; Roeraade, J. Electrospray ionization from a gap with adjustable width. *Rapid Commun. Mass Spectrom.* **2006**, *20*, 3176-3182.
- (49) Ek, P.; Schonberg, T.; Sjodahl, J.; Jacksen, J.; Vieider, C.; Emmer, A.; Roeraade, J. Electrospray ionization from an adjustable gap between two silicon chips. *J. Mass Spectrom.* **2009**, *44*, 171-181.
- (50) Yuill, E. M.; Sa, N.; Ray, S. J.; Hieftje, G. M.; Baker, L. A. Electrospray Ionization from Nanopipette Emitters with Tip Diameters of Less than 100 nm. *Anal. Chem.* **2013**, *85*, 8498-8502.
- (51) Thomson, B. Declustering and fragmentation of protein ions from an electrospray ion source. *J. Am. Soc. Mass Spectrom.* **1997**, *8*, 1053-1058.
- (52) Page, J. S.; Kelly, R. T.; Tang, K.; Smith, R. D. Ionization and transmission efficiency in an electrospray ionization-mass spectrometry interface. *J. Am. Soc. Mass Spectrom.* **2007**, *18*, 1582-1590.

- (53) Mirza, U.; Cohen, S.; Chait, B. Heat-Induced Conformational-Changes in Proteins Studied by Electrospray Ionization Mass-Spectrometry. *Anal. Chem.* **1993**, *65*, 1-6.
- (54) Konermann, L.; Silva, E.; Sogbein, O. Electrochemically induced pH changes resulting in protein unfolding in the ion source of an electrospray mass spectrometer. *Anal. Chem.* **2001**, *73*, 4836-4844.
- (55) Kaltashov, I.; Eyles, S. Studies of biomolecular conformations and conformational dynamics by mass spectrometry. *Mass Spectrom. Rev.* **2002**, *21*, 37-71.
- (56) Sterling, H. J.; Williams, E. R. Origin of Supercharging in Electrospray Ionization of Noncovalent Complexes from Aqueous Solution. *J. Am. Soc. Mass Spectrom.* **2009**, *20*, 1933-1943.
- (57) Liu, J.; Konermann, L. Irreversible Thermal Denaturation of Cytochrome c Studied by Electrospray Mass Spectrometry. *J. Am. Soc. Mass Spectrom.* **2009**, *20*, 819-828.
- (58) Lee, E. D.; Muck, W.; Henion, J. D.; Covey, T. R. Real-Time Reaction Monitoring by Continuous-Introduction Ion-Spray Tandem Mass-Spectrometry. *J. Am. Chem. Soc.* **1989**, *111*, 4600-4604.
- (59) Vahidi, S.; Stocks, B. B.; Liaghati-Mobarhan, Y.; Konermann, L. Submillisecond Protein Folding Events Monitored by Rapid Mixing and Mass Spectrometry-Based Oxidative Labeling. *Anal. Chem.* **2013**, *85*, 8618-8625.
- (60) Kolakowski, B.; Konermann, L. From small-molecule reactions to protein folding: Studying biochemical kinetics by stopped-flow electrospray mass spectrometry. *Anal. Biochem.* **2001**, *292*, 107-114.
- (61) Simmons, D. A.; Konermann, L. Characterization of transient protein folding intermediates during myoglobin reconstitution by time-resolved electrospray mass spectrometry with on-line isotopic pulse labeling. *Biochemistry* **2002**, *41*, 1906-1914.
- (62) Zinck, N.; Stark, A.; Wilson, D. J.; Sharon, M. An Improved Rapid Mixing Device for Time-Resolved Electrospray Mass Spectrometry Measurements. *ChemistryOpen* **2014**, *3*, 109-114.
- (63) Ballew, R.; Sabelko, J.; Gruebele, M. Direct observation of fast protein folding: The initial collapse of apomyoglobin. *Proc. Natl. Acad. Sci. U. S. A.* **1996**, *93*, 5759-5764.
- (64) Chang, D.; Lee, C.; Shiea, J. Detecting Large Biomolecules from High-Salt Solutions by Fused-Droplet Electrospray Ionization Mass Spectrometry. *Anal. Chem.* **2002**, *74*, 2465-2469.
- (65) Shieh, I.; Lee, C.; Shiea, J. Eliminating the Interferences from TRIS Buffer and SDS in Protein Analysis by Fused-Droplet Electrospray Ionization Mass Spectrometry. *J. Proteome Res.* **2005**, *4*, 606-612.
- (66) Hong, C.; Tsai, F.; Shiea, J. A Multiple Channel Electrospray Source Used To Detect Highly Reactive Ketenes from a Flow Pyrolyzer. *Anal. Chem.* **2000**, *72*, 1175-1178.
- (67) Shiea, J.; Chang, D.; Lin, C.; Jiang, S. Generating Multiply Charged Protein Ions by Ultrasonic Nebulization/Multiple Channel-Electrospray Ionization Mass Spectrometry. *Anal. Chem.* **2001**, *73*, 4983-4987.
- (68) Chen, H.; Venter, A.; Cooks, R. G. Extractive electrospray ionization for direct analysis of undiluted urine, milk and other complex mixtures without sample preparation. *Chem. Commun.* **2006**, *19*, 2042-2044.
- (69) Law, W. S.; Wang, R.; Hu, B.; Berchtold, C.; Meier, L.; Chen, H.; Zenobi, R. On the Mechanism of Extractive Electrospray Ionization. *Anal. Chem.* **2010**, *82*, 4494-4500.

- (70) Tian, Y.; Chen, J.; Ouyang, Y.; Qu, G.; Liu, A.; Wang, X.; Liu, C.; Shi, J.; Chen, H.; Jiang, G. Reactive extractive electrospray ionization tandem mass spectrometry for sensitive detection of tetrabromobisphenol A derivatives. *Anal. Chim. Acta* **2014**, *814*, 49-54.
- (71) Prudent, M.; Rossier, J. S.; Lion, N.; Girault, H. H. Microfabricated dual sprayer for on-line mass tagging of phosphopeptides. *Anal. Chem.* **2008**, *80*, 2531-2538.
- (72) Prudent, M.; Mendez, M. A.; Jana, D. F.; Corminboeuf, C.; Girault, H. H. Formation and study of single metal ion-phospholipid complexes in biphasic electrospray ionization mass spectrometry. *Metalomics* **2010**, *2*, 400-406.
- (73) Miladinovic, S. M.; Fornelli, L.; Lu, Y.; Piech, K. M.; Girault, H. H.; Tsybin, Y. O. In-Spray Supercharging of Peptides and Proteins in Electrospray Ionization Mass Spectrometry. *Anal. Chem.* **2012**, *84*, 4647-4651.
- (74) Kharlamova, A.; Prentice, B. M.; Huang, T.; McLuckey, S. A. Electrospray Droplet Exposure to Gaseous Acids for the Manipulation of Protein Charge State Distributions. *Anal. Chem.* **2010**, *82*, 7422-7429.
- (75) Yang, S. H.; Wijeratne, A. B.; Li, L.; Edwards, B. L.; Schug, K. A. Manipulation of Protein Charge States through Continuous Flow-Extractive Desorption Electrospray Ionization: A New Ambient Ionization Technique. *Anal. Chem.* **2011**, *83*, 643-647.
- (76) Kharlamova, A.; McLuckey, S. A. Negative Electrospray Droplet Exposure to Gaseous Bases for the Manipulation of Protein Charge State Distributions. *Anal. Chem.* **2011**, *83*, 431-437.
- (77) Badu-Tawiah, A. K.; Campbell, D. I.; Cooks, R. G. Reactions of Microsolvated Organic Compounds at Ambient Surfaces: Droplet Velocity, Charge State, and Solvent Effects. *J. Am. Soc. Mass Spectrom.* **2012**, *23*, 1077-1094.
- (78) Girod, M.; Moyano, E.; Campbell, D. I.; Cooks, R. G. Accelerated bimolecular reactions in microdroplets studied by desorption electrospray ionization mass spectrometry. *Chem. Sci.* **2011**, *2*, 501-510.
- (79) Miao, Z.; Chen, H.; Liu, P.; Liu, Y. Development of Submillisecond Time-Resolved Mass Spectrometry Using Desorption Electrospray Ionization. *Anal. Chem.* **2011**, *83*, 3994-3997.
- (80) Lee, J. K.; Kim, S.; Nam, H. G.; Zare, R. N. Microdroplet fusion mass spectrometry for fast reaction kinetics. *Proc. Natl. Acad. Sci. U. S. A.* **2015**, *112*, 3898-3903.
- (81) Mark, L. P.; Gill, M. C.; Mahutte, M.; Derrick, P. J. Dual nano-electrospray for probing solution interactions and fast reactions of complex biomolecules. *Eur. J. Mass Spectrom.* **2012**, *18*, 439-446.
- (82) Fisher, C. M.; Kharlamova, A.; McLuckey, S. A. Affecting Protein Charge State Distributions in Nano-Electrospray Ionization via In-Spray Solution Mixing Using Theta Capillaries. *Anal. Chem.* **2014**, *86*, 4581-4588.
- (83) Badu-Tawiah, A. K.; Campbell, D. I.; Cooks, R. G. Accelerated C–N Bond Formation in Dropcast Thin Films on Ambient Surfaces. *J. Am. Soc. Mass Spectrom.* **2012**, *23*, 1461-1468.
- (84) Gatlin, C.; Tureček, F. Acidity Determination in Droplets Formed by Electrospraying Methanol-Water Solutions. *Anal. Chem.* **1994**, *66*, 712-718.
- (85) Girod, M.; Dagany, X.; Antoine, R.; Dugourd, P. Relation between charge state distributions of peptide anions and pH changes in the electrospray plume. A mass

- spectrometry and optical spectroscopy investigation. *Int. J. Mass Spectrom.* **2011**, *308*, 41-48.
- (86) Kharlamova, A.; DeMuth, J. C.; McLuckey, S. A. Vapor Treatment of Electrospray Droplets: Evidence for the Folding of Initially Denatured Proteins on the Sub-Millisecond Time-Scale. *J. Am. Soc. Mass Spectrom.* **2012**, *23*, 88-101.
- (87) Grimm, R. L.; Beauchamp, J. L. Evaporation and Discharge Dynamics of Highly Charged Droplets of Heptane, Octane, and *p*-Xylene Generated by Electrospray Ionization. *Anal. Chem.* **2002**, *74*, 6291-6297.
- (88) Pfeifer, R. J.; Hendricks, C. D. Parametric Studies of Electrohydrodynamic Spraying. *AIAA J.* **1968**, *6*, 496-502.
- (89) Wilm, M. S.; Mann, M. Electrospray and Taylor-Cone theory, Dole's beam of macromolecules at last? *Int. J. Mass Spectrom. Ion Processes* **1994**, *136*, 167-180.
- (90) Fernandez De La Mora J; Loscertales, I. G. The current emitted by highly conducting Taylor cones. *J. Fluid Mech.* **1994**, *260*, 155-184.
- (91) Gañán-Calvo, A. M.; Dávila, J.; Barrero, A. Current and Droplet Size in the Electrospraying of Liquids. Scaling Laws. *J. Aerosol Sci.* **1997**, *28*, 249-275.
- (92) Schmidt, A.; Karas, M.; Dülcks, T. Effect of Different Solution Flow Rates on Analyte Ion Signals in nano-ESI MS, or: When Does ESI Turn into nano-ESI? *J. Am. Soc. Mass Spectrom.* **2003**, *14*, 492-500.
- (93) Tang, K.; Gomez, A. Monodisperse Electrosprays of Low Electric Conductivity Liquids in the Cone-Jet Mode. *J. Colloid Interface Sci.* **1996**, *184*, 500-511.
- (94) Adzhubei, A. A.; Sternberg, M. J. E. Left-Handed Polyproline-II Helices Commonly Occur in Globular-Proteins. *J. Mol. Biol.* **1993**, *229*, 472-493.
- (95) Bochicchio, B.; Tamburro, A. M. Polyproline II structure in proteins: Identification by chiroptical spectroscopies, stability, and functions. *Chirality* **2002**, *14*, 782-792.
- (96) Cubellis, M. V.; Caillez, F.; Blundell, T. L.; Lovell, S. C. Properties of polyproline II, a secondary structure element implicated in protein-protein interactions. *Proteins Struct. Funct. Bioinf.* **2005**, *58*, 880-892.
- (97) Berisio, R.; Loguercio, S.; De Simone, A.; Zagari, A.; Vitagliano, L. Polyproline helices in protein structures: A statistical survey. *Protein Peptide Lett.* **2006**, *13*, 847-854.
- (98) Marshall, A. G.; Hendrickson, C. L.; Jackson, G. S. Fourier transform ion cyclotron resonance mass spectrometry: A primer. *Mass Spectrom. Rev.* **1998**, *17*, 1-35.
- (99) Zubarev, R. A.; Makarov, A. Orbitrap Mass Spectrometry. *Anal. Chem.* **2013**, *85*, 5288-5296.
- (100) Iavarone, A. T.; Williams, E. R. Collisionally activated dissociation of supercharged proteins formed by electrospray ionization. *Anal. Chem.* **2003**, *75*, 4525-4533.
- (101) Iavarone, A. T.; Paech, K.; Williams, E. R. Effects of charge state and cationizing agent on the electron capture dissociation of a peptide. *Anal. Chem.* **2004**, *76*, 2231-2238.
- (102) Madsen, J. A.; Brodbelt, J. S. Comparison of Infrared Multiphoton Dissociation and Collision-Induced Dissociation of Supercharged Peptides in Ion Traps. *J. Am. Soc. Mass Spectrom.* **2009**, *20*, 349-358.
- (103) Flick, T. G.; Cassou, C. A.; Chang, T. M.; Williams, E. R. Solution Additives that Desalt Protein Ions in Native Mass Spectrometry. *Anal. Chem.* **2012**, *84*, 7511-7517.
- (104) McKay, A. R.; Ruotolo, B. T.; Ilag, L. L.; Robinson, C. V. Mass measurements of increased accuracy resolve heterogeneous populations of intact ribosomes. *J. Am. Chem. Soc.* **2006**, *128*, 11433-11442.

- (105) Iavarone, A. T.; Jurchen, J. C.; Williams, E. R. Supercharged protein and peptide ions formed by electrospray ionization. *Anal. Chem.* **2001**, *73*, 1455-1460.
- (106) Iavarone, A. T.; Williams, E. R. Supercharging in electrospray ionization: effects on signal and charge. *Int. J. Mass Spectrom.* **2002**, *219*, 63-72.
- (107) Davies, N. W.; Wiese, M. D.; Browne, S. G. A. Characterisation of major peptides in 'jack jumper' ant venom by mass spectrometry. *Toxicon* **2004**, *43*, 173-183.
- (108) Kjeldsen, F.; Giessing, A. M. B.; Ingrell, C. R.; Jensen, O. N. Peptide sequencing and characterization of post-translational modifications by enhanced ion-charging and liquid chromatography electron-transfer dissociation tandem mass spectrometry. *Anal. Chem.* **2007**, *79*, 9243-9252.
- (109) Valeja, S. G.; Tipton, J. D.; Emmett, M. R.; Marshall, A. G. New Reagents for Enhanced Liquid Chromatographic Separation and Charging of Intact Protein Ions for Electrospray Ionization Mass Spectrometry. *Anal. Chem.* **2010**, *82*, 7515-7519.
- (110) Teo, C. A.; Donald, W. A. Solution Additives for Supercharging Proteins beyond the Theoretical Maximum Proton-Transfer Limit in Electrospray Ionization Mass Spectrometry. *Anal. Chem.* **2014**, *86*, 4455-4462.
- (111) Going, C. C.; Williams, E. R. Supercharging with m-Nitrobenzyl Alcohol and Propylene Carbonate: Forming Highly Charged Ions with Extended, Near-Linear Conformations. *Anal. Chem.* **2015**, *87*, 3973-3980.
- (112) Lomeli, S. H.; Yin, S.; Loo, R. R. O.; Loo, J. A. Increasing Charge While Preserving Noncovalent Protein Complexes for ESI-MS. *J. Am. Soc. Mass Spectrom.* **2009**, *20*, 593-596.
- (113) Sterling, H. J.; Williams, E. R. Real-Time Hydrogen/Deuterium Exchange Kinetics via Supercharged Electrospray Ionization Tandem Mass Spectrometry. *Anal. Chem.* **2010**, *82*, 9050-9057.
- (114) Regazzoni, L.; Bertoletti, L.; Vistoli, G.; Colombo, R.; Aldini, G.; Serra, M.; Carini, M.; Caccialanza, G.; De Lorenzi, E. A Combined High-Resolution Mass Spectrometric and in silico Approach for the Characterisation of Small Ligands of  $\beta_2$ -Microglobulin. *ChemMedChem* **2010**, *5*, 1015-1025.
- (115) Erba, E. B.; Ruotolo, B. T.; Barsky, D.; Robinson, C. V. Ion Mobility-Mass Spectrometry Reveals the Influence of Subunit Packing and Charge on the Dissociation of Multiprotein Complexes. *Anal. Chem.* **2010**, *82*, 9702-9710.
- (116) Yin, S.; Loo, J. A. Top-down mass spectrometry of supercharged native protein-ligand complexes. *Int. J. Mass Spectrom.* **2011**, *300*, 118-122.
- (117) Sterling, H. J.; Kintzer, A. F.; Feld, G. K.; Cassou, C. A.; Krantz, B. A.; Williams, E. R. Supercharging Protein Complexes from Aqueous Solution Disrupts their Native Conformations. *J. Am. Soc. Mass Spectrom.* **2012**, *23*, 191-200.
- (118) Metwally, H.; McAllister, R. G.; Popa, V.; Konermann, L. Mechanism of Protein Supercharging by Sulfolane and m-Nitrobenzyl Alcohol: Molecular Dynamics Simulations of the Electrospray Process. *Anal. Chem.* **2016**, *88*, 5345-5354.
- (119) Sterling, H. J.; Daly, M. P.; Feld, G. K.; Thoren, K. L.; Kintzer, A. F.; Krantz, B. A.; Williams, E. R. Effects of Supercharging Reagents on Noncovalent Complex Structure in Electrospray Ionization from Aqueous Solutions. *J. Am. Soc. Mass Spectrom.* **2010**, *21*, 1762-1774.
- (120) Flick, T. G.; Williams, E. R. Supercharging with Trivalent Metal Ions in Native Mass Spectrometry. *J. Am. Soc. Mass Spectrom.* **2012**, *23*, 1885-1895.

- (121) Sterling, H. J.; Cassou, C. A.; Susa, A. C.; Williams, E. R. Electrothermal Supercharging of Proteins in Native Electrospray Ionization. *Anal. Chem.* **2012**, *84*, 3795-3801.
- (122) Cassou, C. A.; Sterling, H. J.; Susa, A. C.; Williams, E. R. Electrothermal Supercharging in Mass Spectrometry and Tandem Mass Spectrometry of Native Proteins. *Anal. Chem.* **2013**, *85*, 138-146.
- (123) Cassou, C. A.; Williams, E. R. Anions in Electrothermal Supercharging of Proteins with Electrospray Ionization Follow a Reverse Hofmeister Series. *Anal. Chem.* **2014**, *86*, 1640-1647.
- (124) Behrens, S. H.; Grier, D. G. The charge of glass and silica surfaces. *J. Chem. Phys.* **2001**, *115*, 6716-6721.
- (125) Pennathur, S.; Santiago, J. Electrokinetic transport in nanochannels. 2. Experiments. *Anal. Chem.* **2005**, *77*, 6782-6789.
- (126) Freedman, K. J.; Jurgens, M.; Prabhu, A.; Ahn, C. W.; Jemth, P.; Edel, J. B.; Kim, M. J. Chemical, Thermal, and Electric Field Induced Unfolding of Single Protein Molecules Studied Using Nanopores. *Anal. Chem.* **2011**, *83*, 5137-5144.
- (127) Yusko, E. C.; Johnson, J. M.; Majd, S.; Prangkio, P.; Rollings, R. C.; Li, J.; Yang, J.; Mayer, M. Controlling protein translocation through nanopores with bio-inspired fluid walls. *Nat. Nanotechnol.* **2011**, *6*, 253-260.
- (128) Anderson, B. N.; Muthukumar, M.; Meller, A. pH Tuning of DNA Translocation Time through Organically Functionalized Nanopores. *ACS Nano* **2013**, *7*, 1408-1414.
- (129) Gray, J. J. The interaction of proteins with solid surfaces. *Curr. Opin. Struct. Biol.* **2004**, *14*, 110-115.
- (130) Cohen, M. J.; Karasek, F. W. Plasma Chromatography - a New Dimension for Gas Chromatography and Mass Spectrometry. *J. Chromatogr. Sci.* **1970**, *8*, 330-337.
- (131) Bowers, M. T.; Kemper, P. R.; Vonhelden, G.; Vankoppen, P. A. M. Gas-Phase Ion Chromatography - Transition-Metal State Selection and Carbon Cluster Formation. *Science* **1993**, *260*, 1446-1451.
- (132) St Louis, R. H.; Hill, H. H. J.; Eiceman, G. A. Ion Mobility Spectrometry in Analytical Chemistry. *Crit. Rev. Anal. Chem.* **1990**, *21*, 321-356.
- (133) Jarrold, M. F. Drift-Tube Studies of Atomic Clusters. *J. Phys. Chem.* **1995**, *99*, 11-21.
- (134) Kaur-Atwal, G.; Weston, D. J.; Green, P. S.; Crosland, S.; Bonner, P. L. R.; Creaser, C. S. Analysis of tryptic peptides using desorption electrospray ionisation combined with ion mobility spectrometry/mass spectrometry. *Rapid Commun. Mass Spectrom.* **2007**, *21*, 1131-1138.
- (135) Djidja, M. C.; Francese, S.; Loadman, P. M.; Sutton, C. W.; Scriven, P.; Claude, E.; Snel, M. F.; Franck, J.; Salzet, M.; Clench, M. R. Detergent addition to tryptic digests and ion mobility separation prior to MS/MS improves peptide yield and protein identification for in situ proteomic investigation of frozen and formalin-fixed paraffin-embedded adenocarcinoma tissue sections. *Proteomics* **2009**, *9*, 2750-2763.
- (136) Stauber, J.; MacAleese, L.; Franck, J.; Claude, E.; Snel, M.; Kaletas, B. K.; Wiel, I. M. V. D.; Wisztorski, M.; Fournier, I.; Heeren, R. M. A. On-Tissue Protein Identification and Imaging by MALDI-Ion Mobility Mass Spectrometry. *J. Am. Soc. Mass Spectrom.* **2010**, *21*, 338-347.
- (137) Shelimov, K. B.; Clemmer, D. E.; Hudgins, R. R.; Jarrold, M. F. Protein Structure *in Vacuo*: Gas-Phase Conformations of BPTI and Cytochrome c. *J. Am. Chem. Soc.* **1997**, *119*, 2240-2248.

- (138) Badman, E. R.; Hoaglund-Hyzer, C. S.; Clemmer, D. E. Monitoring structural changes of proteins in an ion trap over similar to 10-200 ms: Unfolding transitions in cytochrome *c* ions. *Anal. Chem.* **2001**, *73*, 6000-6007.
- (139) Myung, S.; Badman, E. R.; Lee, Y. J.; Clemmer, D. E. Structural transitions of electrosprayed ubiquitin ions stored in an ion trap over similar to 10 ms to 30 s. *J. Phys. Chem. A* **2002**, *106*, 9976-9982.
- (140) Ruotolo, B. T.; Giles, K.; Campuzano, I.; Sandercock, A. M.; Bateman, R. H.; Robinson, C. V. Evidence for macromolecular protein rings in the absence of bulk water. *Science* **2005**, *310*, 1658-1661.
- (141) Loo, J. A.; Berhane, B.; Kaddis, C. S.; Wooding, K. M.; Xie, Y. M.; Kaufman, S. L.; Chernushevich, I. V. Electrospray ionization mass spectrometry and ion mobility analysis of the 20S proteasome complex. *J. Am. Soc. Mass Spectrom.* **2005**, *16*, 998-1008.
- (142) Utrecht, C.; Versluis, C.; Watts, N. R.; Wingfield, P. T.; Steven, A. C.; Heck, A. J. R. Stability and shape of hepatitis B virus capsids in vacuo. *Angew. Chem. Int. Ed.* **2008**, *47*, 6247-6251.
- (143) Thomas, J. J.; Bothner, B.; Traina, J.; Benner, W. H.; Siuzdak, G. Electrospray ion mobility spectrometry of intact viruses. *Spectrosc. Int. J.* **2004**, *18*, 31-36.
- (144) McDaniel, E. W.; Barnes, W. S.; Martin, D. W. Drift Tube-Mass Spectrometer for Studies of Low-Energy Ion-Molecule Reactions. *Rev. Sci. Instrum.* **1962**, *33*, 2-6.
- (145) Hoaglund, C. S.; Valentine, S. J.; Sporleider, C. R.; Reilly, J. P.; Clemmer, D. E. Three-dimensional ion mobility/TOFMS analysis of electrosprayed biomolecules. *Anal. Chem.* **1998**, *70*, 2236-2242.
- (146) Tang, K. Q.; Li, F. M.; Shvartsburg, A. A.; Strittmatter, E. F.; Smith, R. D. Two-dimensional gas-phase separations coupled to mass Spectrometry for analysis of complex mixtures. *Anal. Chem.* **2005**, *77*, 6381-6388.
- (147) Räsänen, R.; Nousiainen, M.; Peräkorpi, K.; Sillanpää, M.; Polari, L.; Anttalainen, O.; Utriainen, M. Determination of gas phase triacetone triperoxide with aspiration ion mobility spectrometry and gas chromatography-mass spectrometry. *Analyt. Chim. Acta* **2008**, *623*, 59-65.
- (148) Arnanthigo, Y.; Anttalainen, O.; Safaei, Z.; Sillanpää, M. Sniff-testing for indoor air contaminants from new buildings environment detecting by aspiration-type ion mobility spectrometry. *Int. J. Ion Mobility Spectrom.* **2016**, *19*, 15-30.
- (149) Purves, R. W.; Guevremont, R. Electrospray ionization high-field asymmetric waveform ion mobility spectrometry-mass spectrometry. *Anal. Chem.* **1999**, *71*, 2346-2357.
- (150) Robinson, E. W.; Williams, E. R. Multidimensional separations of ubiquitin conformers in the gas phase: Relating ion cross sections to H/D exchange measurements. *J. Am. Soc. Mass Spectrom.* **2005**, *16*, 1427-1437.
- (151) Shvartsburg, A. A.; Li, F. M.; Tang, K. Q.; Smith, R. D. High-resolution field asymmetric waveform ion mobility spectrometry using new planar geometry analyzers. *Anal. Chem.* **2006**, *78*, 3706-3714.
- (152) Giles, K.; Williams, J. P.; Pringle, S. D.; Wildgoose, J. L.; Slade, S. E.; Thalassinos, K.; Bateman, R. H.; Bowers, M. T.; Scrivens, J. H. An investigation of the mobility separation of some peptide and protein ions using a new hybrid quadrupole/travelling wave IMS/oa-ToF instrument. *Int. J. Mass Spectrom.* **2007**, *261*, 1-12.
- (153) Giles, K.; Williams, J. P.; Campuzano, I. Enhancements in travelling wave ion mobility resolution. *Rapid Commun. Mass Spectrom.* **2011**, *25*, 1559-1566.

- (154) Kanu, A. B.; Dwivedi, P.; Tam, M.; Matz, L.; Hill, H. H., Jr. Ion mobility-mass spectrometry. *J. Mass Spectrom.* **2008**, *43*, 1-22.
- (155) Lanucara, F.; Holman, S. W.; Gray, C. J.; Eyers, C. E. The power of ion mobility-mass spectrometry for structural characterization and the study of conformational dynamics. *Nat. Chem.* **2014**, *6*, 281-294.
- (156) Giles, K.; Pringle, S. D.; Worthington, K. R.; Little, D.; Wildgoose, J. L.; Bateman, R. H. Applications of a travelling wave-based radio-frequency-only stacked ring ion guide. *Rapid Commun. Mass Spectrom.* **2004**, *18*, 2401-2414.
- (157) Shvartsburg, A. A.; Smith, R. D. Fundamentals of Traveling Wave Ion Mobility Spectrometry. *Anal. Chem.* **2008**, *80*, 9689-9699.
- (158) Ruotolo, B. T.; Benesch, J. L. P.; Sandercock, A. M.; Hyung, S.; Robinson, C. V. Ion mobility-mass spectrometry analysis of large protein complexes. *Nat. Protoc.* **2008**, *3*, 1139-1152.
- (159) Thalassinos, K.; Grabenauer, M.; Slade, S. E.; Hilton, G. R.; Bowers, M. T.; Scrivens, J. H. Characterization of Phosphorylated Peptides Using Traveling Wave-Based and Drift Cell Ion Mobility Mass Spectrometry. *Anal. Chem.* **2009**, *81*, 248-254.
- (160) Smith, D. P.; Knapman, T. W.; Campuzano, I.; Malham, R. W.; Berryman, J. T.; Radford, S. E.; Ashcroft, A. E. Deciphering drift time measurements from travelling wave ion mobility spectrometry-mass spectrometry studies. *Eur. J. Mass Spectrom.* **2009**, *15*, 113-130.
- (161) Giles, K.; Wildgoose, J. L.; Langridge, D. J.; Campuzano, I. A method for direct measurement of ion mobilities using a travelling wave ion guide. *Int. J. Mass Spectrom.* **2010**, *298*, 10-16.
- (162) Ruotolo, B. T.; Hyung, S.; Robinson, P. M.; Giles, K.; Bateman, R. H.; Robinson, C. V. Ion mobility-mass spectrometry reveals long-lived, unfolded intermediates in the dissociation of protein complexes. *Angew. Chem. Int. Ed.* **2007**, *46*, 8001-8004.

## Chapter 2

# Theta-Glass Capillaries in Electrospray Ionization: Rapid Mixing and Short Droplet Lifetimes

This Chapter is reproduced with permission from  
Mortensen, D.M.; Williams, E.R.

“Theta-Glass Capillaries in Electrospray Ionization:  
Rapid Mixing and Short Droplet Lifetimes”  
*Analytical Chemistry* **2014**, *86*, 9315–9321  
© 2014 American Chemical Society

### 2.1 Introduction

Rapid mixing of two or more solutions is often required to investigate the kinetics of fast chemical and biochemical reactions.<sup>1–3</sup> Mixers that are commonly used for this purpose include laminar,<sup>4,5</sup> turbulent,<sup>6,7</sup> and chaotic<sup>8–10</sup> flow mixers, where the dead time decreases with increasing flow rate.<sup>4,11</sup> The performance of these types of mixers has been extensively reviewed.<sup>12,13</sup> A dead time of 8  $\mu$ s has been achieved with a flow rate of  $\sim$ 100 nL/s using laminar flow mixers.<sup>14</sup> The use of mass spectrometry (MS) to monitor reactions in mixing experiments has the advantage of high chemical specificity. Several in-line mixers have been coupled to MS, including continuous,<sup>15,16</sup> stopped,<sup>17,18</sup> and laminar<sup>3</sup> flow mixers. The shortest dead time reported for mixers coupled to MS is 200  $\mu$ s.<sup>3</sup>

Numerous techniques have also been used to mix solutions during the electrospray process, including fused-droplet electrospray,<sup>19,20</sup> multiple channel electrospray,<sup>21,22</sup> extractive electrospray,<sup>23–25</sup> and dual-sprayer microchips.<sup>26–28</sup> Both desorption electrospray ionization<sup>2,29–31</sup> and ambient ion soft landing<sup>32</sup> techniques have been used to carry out solution-phase reactions in charged microdroplets. Similarly, mixing from theta-glass emitters (double-barrel wire-in-a-capillary emitters made from theta glass) has been used to form noncovalent complexes,<sup>33</sup> conduct hydrogen/deuterium exchange reactions,<sup>33</sup> unfold proteins,<sup>34</sup> and introduce supercharging reagents to protein solutions,<sup>34</sup> all during the electrospray process. Mixing in microdroplets has the potential advantage of minimizing sample volume,<sup>35–37</sup> but reported mixing times in microdroplets are greater than those in laminar flow mixers. For example, complete mixing of two 80  $\mu$ m diameter ballistic droplets takes  $\sim$ 10 ms to occur,<sup>38</sup> and complete mixing within a 25  $\mu$ m diameter droplet generated by flowing multiple streams of aqueous reagent solutions into an inert stream of water immiscible oil occurs in  $\sim$ 2 ms.<sup>37</sup>

Microdroplets formed in atmosphere can undergo desolvation, and the droplet lifetime depends on the evaporation rate. Evaporation rates of heptane, octane, and xylene electrospray droplets ranging in initial size from 3 to 60  $\mu$ m have been measured using phase Doppler anemometry,<sup>39</sup> and the evaporation rate depends on both the solvent and the square of the initial droplet diameter. The initial diameter of electrospray droplets generated using capillaries with outer diameters as small as 12.5  $\mu$ m<sup>40</sup> to as large as a centimeter<sup>41,42</sup> have been measured using various techniques, including optical microscopy,<sup>42,43</sup> flash shadowgraph techniques,<sup>44–46</sup> phase Doppler techniques,<sup>39,44,47–50</sup> scanning mobility particle sizers,<sup>51,52</sup> and white light particle counters.<sup>41</sup> Electrospray droplets have been observed from an electrospray capillary with an outer diameter (o.d.) as small as 12.5  $\mu$ m using a stereomicroscope,<sup>40</sup> but droplets from a

capillary with an o.d. of  $<1\text{ }\mu\text{m}$  were too small to be visualized.<sup>40</sup> The initial size of an electrospray droplet can depend on the tip diameter for a given solution, but heptane droplets generated from an electrospray capillary with an outer diameter of 0.45 mm can have initial diameters of  $\sim 200\text{ }\mu\text{m}$ ,<sup>46</sup> whereas ethylene glycol droplets generated from a 10 mm o.d. electrospray capillary can have initial diameters as small as  $\sim 1.5\text{ }\mu\text{m}$ .<sup>40</sup> Therefore, the exact relationship between the size of the electrospray capillary and the initial size of the droplet depends on many factors. There are several models<sup>42,53–55</sup> that have been reported for determining the size of droplets generated using electrospray based on the flow rate and various other solution and instrumental conditions. Schmidt et al.<sup>40</sup> compared several of these models and reported that they predicted droplet diameters differing by 4 orders of magnitude ( $7.7 \times 10^{-8}$  to  $1.4 \times 10^{-4}\text{ m}$ ) for the same water/methanol/acetic acid solution under otherwise identical conditions.

As droplets evaporate, the surface area to volume ratio and the concentration of reagents increase and up to a 4 unit change in the pH can occur.<sup>56,57</sup> These factors can increase the rate of product formation in droplets by 1–3 orders of magnitude over bulk solution rates.<sup>31,58–60</sup> The relative contribution of each of these factors to the increased rate of product formation is unknown.

In this study, theta-glass emitters were used to mix solutions during nanoelectrospray ionization (nano-ESI). The extent of mixing between solutions loaded into opposite barrels was measured by carrying out a fast complexation equilibrium reaction, and an apparent droplet lifetime was obtained by monitoring a fast redox reaction with a known forward rate constant. On the basis of increased rates of product formation in droplets compared to rates in bulk solution measured by others, the droplet lifetime is estimated to be less than  $\sim 27\text{ }\mu\text{s}$ .

## 2.2 Experimental

Mass spectra were acquired using a 9.4 T Fourier-transform ion cyclotron resonance mass spectrometer that is described in detail elsewhere.<sup>61</sup> Nanoelectrospray ionization was performed using premium theta glass (Warner Instruments, LLC, Hamden, CT) pulled into tips using a model p-87 Flaming/ Brown micropipette puller equipped with an FB330B square box filament (Sutter Instruments Co., Novato, CA). Theta glass is a borosilicate glass capillary divided into two separate barrels by a borosilicate glass wall. Platinum wires connected to the ground of the instrument were brought into contact with the solution in each barrel, and electrospray was initiated by applying a potential of  $\sim -700\text{ V}$  to the heated capillary of the nanoelectrospray interface. A backing pressure of  $\sim 10\text{ psi}$  ( $\text{CO}_2$ ) was applied to the solutions during electrospray using a pressure regulator. A schematic of this experimental setup is shown in Scheme A.1 in Appendix A. A Hitachi tabletop microscope TM-1000 scanning electron microscope (Hitachi High-Technologies Co., Tokyo, Japan) was used to image the tips. All reported uncertainties are one standard deviation from three replicate measurements. Diffusion coefficients used to model the diffusion of  $\text{K}^+$ ,  $\text{Na}^+$ , and 18C6 in water are 0.00196,<sup>62</sup> 0.00163,<sup>63</sup> and  $0.00060\text{ }\mu\text{m}^2/\mu\text{s}$ ,<sup>64</sup> respectively.

Leu-enkephalin acetate salt hydrate, met-enkephalin acetate salt hydrate, L-ascorbic acid, and 18-crown-6 were obtained from Sigma-Aldrich (St. Louis, MO), KCl was from Mallinckrodt Baker, Inc. (Phillipsburg, NJ), HCl 0.1 N was from EMD Millipore Chemicals (Darmstadt, Germany), and 2,6-dichloroindophenol Na salt and NaCl were from Fisher Scientific (Fair Lawn,

NJ). All chemicals were used without further purification, and all solutions were prepared in 18.2 MΩ water from a Milli-Q integral water purification system (Millipore, Billerica, MA).

## 2.3 Results and Discussion

### 2.3.1 Characterization of Theta-Glass ESI Emitters.

Theta-glass capillaries are divided into two separate barrels by a central divider, which after the pulling process extends to the end of the tip (Figure 2.1a; tip oriented so that the divider is perpendicular to the sample stand). Thus, solutions loaded into opposite barrels do not mix until flow is initiated by applying a potential to the capillary of the nanoelectrospray interface and a backing pressure is applied to the solutions. The tip o.d. is  $1.71 \pm 0.04 \mu\text{m}$  perpendicular to the divider (Figure 2.1a) and  $1.36 \pm 0.02 \mu\text{m}$  along the axis of the divider (Figure 2.1b). The thickness of the outer wall is uniform in both orientations ( $0.16 \pm 0.02 \mu\text{m}$ ) and is the same as the inner divider thickness ( $0.16 \pm 0.01 \mu\text{m}$ ). The length of the emitters is  $5.47 \pm 0.05 \text{ cm}$ .

### 2.3.2 Measuring Relative Flow Rates of Individual Barrels.

The overall flow rate from both barrels was obtained by measuring the change in volume and mass of an aqueous solution of 500 μM NaCl and 500 μM 18-crown-6 after spraying for ~10 min (density of 1.0 mg/mL for water containing less than 1% NaCl).<sup>65</sup> The flow rate is  $1.4 \pm 0.4 \text{ nL/s}$ , which is 2 orders of magnitude lower than the flow rates of common mixers in which high mixing efficiency is achieved on the order of tens of microseconds.<sup>13</sup> The flow rate remains relatively constant when the backing pressure is doubled and when the ionic strength of the solution differs by more than an order of magnitude (data not shown).

In order to obtain quantitative information from mixing experiments preformed using theta-glass emitters, the flow rate of each barrel must be measured individually. To determine the relative flow rate of each barrel, 10 μM solutions (pH = 2) of Leu-enkephalin (L-Enk) and Met-enkephalin (M-Enk) (polypeptides YGGFX, X = L and M, respectively) were prepared and loaded into the separate barrels. The protonated forms of the peptides were observed in the mass spectra at a ratio of  $1.8 \pm 0.1$  to 1, L-Enk to M-Enk (Figure 2.2a). To determine the relative ionization efficiencies of these peptides, an equimolar mixture of L-Enk and M-Enk was prepared (5 μM, pH = 2) and loaded into both barrels of the theta-glass emitters. On the basis of the relative abundances of the protonated forms of the peptides, the relative ionization efficiency of L-Enk to M-Enk is  $1.7 \pm 0.1$  (Figure 2.2b). Although these peptides differ by only a single amino acid, even minor differences in structure can lead to significant differences in ionization efficiencies.<sup>66</sup> The relative flow rates of the individual barrels were established using the relative abundances and ionization efficiencies of the internal standards, and in this experiment, the relative flow rate of the LEnk solution to the M-Enk solution was  $1.1 \pm 0.1$  to 1, suggesting that relative flow rates are nearly even and are highly reproducible between tips.

### 2.3.3 Mixing Efficiency.

In order to determine the extent of mixing that occurs in these experiments, a fast complexation equilibrium reaction was performed using the theta-glass emitters. If incomplete mixing occurs in these experiments, only a portion of the reagents loaded into the opposite barrels will interact during the electrospray process and the ratio of products to reactants in the mass spectra will be lower than that at equilibrium. Complexation of 18-crown-6 (18C6) with K<sup>+</sup> in water has a forward rate constant of  $2.45 \times 10^9 \text{ mol s}^{-1}$  and an equilibrium constant of 116.4 (values are averages of values measured by others).<sup>67</sup> Protonated 18C6 is not

observed in the mass spectra, so the product to reactant ratio cannot be measured directly. For this reason,  $^{18}\text{C6}$  is mixed with  $\text{Na}^+$  to form the complex  $[^{18}\text{C6} + \text{Na}]^+$ , which has an equilibrium constant of 7.0 (average of values measured by others).<sup>67</sup>

A solution (A) containing 100  $\mu\text{M}$   $^{18}\text{C6}$  and 500  $\mu\text{M}$  NaCl ( $\text{pH} = 2$ ) was mixed with solutions (B) containing between 50 and 1000  $\mu\text{M}$  KCl ( $\text{pH} = 2$ ). A calibration curve for the ratio  $[^{18}\text{C6} + \text{K}]^+ / [^{18}\text{C6} + \text{Na}]^+$  was generated as a function of the initial concentration of  $\text{K}^+$  over the initial concentration of  $\text{Na}^+$  in solution ( $[\text{K}]_o / [\text{Na}]_o$ ) (Figure 2.3a). A representative mass spectrum of a premixed solution of A and B, where the initial concentrations of  $\text{Na}^+$  and  $\text{K}^+$  are equal, is inset into Figure 2.3a. To determine how the relative abundances of the two complex ions reflect the corresponding abundances in solution, an equilibrium ratio is derived from the equilibrium constants of the two complexes. The equilibrium constants of these complexes are

$$K_M = \frac{[^{18}\text{C6} + M]_{\text{eq}}}{[^{18}\text{C6}]_{\text{eq}} [M]_{\text{eq}}} \quad (1)$$

where  $M = \text{Na}^+$  or  $\text{K}^+$ ,  $K_M$  is the equilibrium constant of the reaction involving  $M$ ,  $[^{18}\text{C6} + M]_{\text{eq}}$  and  $[^{18}\text{C6}]_{\text{eq}}$  are the equilibrium concentrations of the complexed and uncomplexed forms of  $^{18}\text{C6}$ , respectively, and  $[M]_{\text{eq}}$  is the equilibrium concentration of  $M$ . In all experiments, <1% of  $M$  is complexed with  $^{18}\text{C6}$ , so  $[M]_{\text{eq}}$  is approximated as the initial concentration of  $M$ ,  $[M]_o$ . Solving eq 1 for both  $\text{Na}^+$  and  $\text{K}^+$ , rearranging, and dividing  $[^{18}\text{C6} + \text{K}]_{\text{eq}}$  by  $[^{18}\text{C6} + \text{Na}]_{\text{eq}}$  gives eq 2:

$$\frac{[^{18}\text{C6} + \text{K}]_{\text{eq}}}{[^{18}\text{C6} + \text{Na}]_{\text{eq}}} = \frac{K_K}{K_{\text{Na}}} \frac{[\text{K}]_o}{[\text{Na}]_o} \quad (2)$$

The ratio  $[^{18}\text{C6} + \text{K}]_{\text{eq}} / [^{18}\text{C6} + \text{Na}]_{\text{eq}}$  as a function of the ratio  $[\text{K}]_o / [\text{Na}]_o$  is linear with a slope of 16.8 (Figure 2.3a), which is nearly the same as the expected value of  $K_K / K_{\text{Na}} = 16.6$ . This result indicates that the ratios of abundances of the two complex ions are approximately equal to their relative abundances in solution.

The extent of mixing between two solutions loaded into opposite barrels of the theta-glass emitters was determined by loading solution A into one barrel and solutions of B into the other barrel. L-Enk and M-Enk were used as internal standards in these respective solutions to determine the relative flow rates of the two barrels. The initial concentrations of  $\text{Na}^+$  and  $\text{K}^+$  in the droplets were determined from the initial concentrations of the ions in the respective solutions and from the respective flow rates. The ratio  $[^{18}\text{C6} + \text{K}]^+ / [^{18}\text{C6} + \text{Na}]^+$  in the mass spectra of the solutions mixed from the theta-glass emitters as a function of the same ratio determined from the linear fit to the calibration curve data results in a line with a slope of 0.99 and a correlation coefficient of 0.97 (Figure 2.3b). These results indicate that the complexation of  $^{18}\text{C6}$  with  $\text{K}^+$  reaches equilibrium during nano-ESI and that complete mixing occurs between solutions sprayed from opposite barrels of the theta-glass emitters.

**2.3.4 Estimates of the Mixing Time.** An estimate of the maximum time required for mixing to occur in the electrospray droplets was made by assuming that the mixing time is diffusion-limited. Concentration profiles in the droplet are modeled as a function of both the

distance from the center of the droplet,  $d$ , and time,  $t$ , using the classical solution to Fick's second law of diffusion for finite boundary conditions:

$$c(d,t) = \left( \frac{c_o}{2} \right) - \left( \frac{c_o}{2} \right) \operatorname{erf} \left( \frac{d}{2\sqrt{Dt}} \right) \quad (3)$$

where  $c(d,t)$  is the concentration as a function of  $d$  and  $t$ ,  $c_o$  is the concentration at  $t = 0$ ,  $c_o/2$  is the equilibrium concentration (assuming even flow from both barrels),  $\operatorname{erf}$  is the error function, and  $D$  is the diffusion coefficient. Only diffusion in the direction perpendicular to the solution interface is considered, and the outer boundaries correspond to the droplet radius. Because there is significant uncertainty in the initial droplet size in these experiments, mixing times are calculated for droplets with initial diameters of one-half and one-tenth the outer diameter of the tip of the electrospray capillary (o.d.). Because mixing should occur across the interface between the solutions in the absence of turbulent flow, the tip diameter of 1.71  $\mu\text{m}$ , measured perpendicular to the inner divider, is used as the o.d.

The concentration of  $\text{K}^+$ ,  $\text{Na}^+$ , and  $18\text{C}6$  as a function of the distance from the center of a 0.86  $\mu\text{m}$  droplet (one-half the o.d.) at 0, 23, and 732  $\mu\text{s}$  are shown in Figure 2.4a–c, respectively. The relative concentrations of  $[18\text{C}6 + \text{K}]^+$  and  $[18\text{C}6 + \text{Na}]^+$  were calculated as a function of the distance from the center of the droplet using the concentration profiles in Figure 2.4a–c and the equilibrium constants (eq 1). Relative concentrations of the complexes as a function of the distance from the center of a 0.86  $\mu\text{m}$  droplet at 0, 29, and 732  $\mu\text{s}$  are shown in Figure 2.4d–f, respectively. From these data, the ratio  $[18\text{C}6 + \text{K}]^+/[18\text{C}6 + \text{Na}]^+$  as a function of time can be determined. At 23 and 732  $\mu\text{s}$  for all initial concentrations of  $\text{K}^+$  in solution B, this ratio is  $\sim 42\%$  and  $\sim 90\%$  of the equilibrium ratio, respectively. On the basis of the standard deviations of the calibration curve data ( $\sim 10\%$  of the average values, Figure 2.3a), the ratio of the complexes at 732  $\mu\text{s}$  would be nominally the same within the uncertainty of the measurement as that from a premixed solution and mixing would appear complete. Similar extents of diffusion-limited mixing in a 0.17  $\mu\text{m}$  droplet (one-tenth the o.d.) would take 0.9 and 29  $\mu\text{s}$  to occur, respectively. These mixing times are upper limits because droplet evaporation reduces the droplet radius<sup>39</sup> and, therefore, the distance material must diffuse. Turbulence in the droplet will also significantly increase the rate of mixing over that of a diffusion-limited system.

The effect that turbulence might have on the mixing times in these experiments is estimated by comparing the calculated diffusion-limited mixing times to the measured mixing times of coalescing ballistic microdroplets, studied by Graceffa et al.<sup>38</sup> In that study, 80  $\mu\text{m}$  diameter ballistic droplets were generated using two synchronized drop-on-demand inkjet systems, and droplets containing aqueous cytochrome *c* were collided with droplets containing aqueous sodium acetate buffer. Stroboscopic synchrotron radiation microbeam small-angle X-ray scattering was used to image the redistribution of cytochrome *c* within the newly formed 100  $\mu\text{m}$  droplets, and cytochrome *c* was uniformly distributed after  $\sim 10$  ms. Diffusion of  $18\text{C}6$ ,  $\text{K}^+$ , and  $\text{Na}^+$  in a 100  $\mu\text{m}$  droplet would take  $\sim 10$  s to form the complexes  $[18\text{C}6 + \text{K}]^+$  and  $[18\text{C}6 + \text{Na}]^+$  at 90% of the equilibrium ratio, indicating that turbulence increased the mixing rate in the ballistic microdroplets by 3 orders of magnitude over the rate of diffusion-limited mixing. If turbulence contributes equally to mixing from the theta-glass emitters, complete mixing could occur in well under a microsecond.

To estimate the extent of mixing that occurs in the Taylor cone prior to droplet formation, the volume of solution in the Taylor cone is estimated as the volume of a cone with a height 4

times the o.d.<sup>68</sup> and with a radius equal to the o.d. At the measured flow rate of  $1.4 \pm 0.4$  nL/s, a reagent molecule spends less than 11  $\mu$ s in the Taylor cone prior to droplet formation. This suggests that a significant extent of mixing will occur prior to droplet formation if contributions from turbulent mixing are significant, but mixing will primarily occur in the droplet if mixing is diffusion-limited.

**2.3.5 Droplet Lifetimes.** An upper limit to the lifetime of a droplet can be obtained by measuring the extent to which a reaction with a known rate constant occurs during nano-ESI. The reduction of 2,6-dichloroindophenol (DCIP) by L-ascorbic acid (L-AA) (Scheme 2.1) has a forward rate constant of  $5.6 \times 10^4$  L mol<sup>-1</sup> s<sup>-1</sup> at pH = 3.<sup>69</sup> A solution (C) containing 10  $\mu$ M DCIP (pH = 3) was loaded into one barrel of the theta-glass emitters, and solutions (D) containing between 10 and 50 mM L-AA (pH = 3) were loaded into the other barrel. Figure 2.5a shows a representative mass spectrum resulting from mixing solutions C and D (50 mM L-AA) from the theta-glass emitters. Due to the large excess of L-AA in solution, L-AA carries away a substantial fraction of the available charge in the form of protonated L-AA (*m/z* 177.039, data not shown), resulting in a low signal-to-noise ratio for DCIP. The protonated oxidized and reduced forms of DCIP have overlapping isotope distributions, but these ions can be readily resolved (inset to Figure 2.5a, the third isotope peak of oxidized DCIP and the first isotope peak of reduced DCIP are shown). The fraction of DCIP that is reduced increases as a function of the concentration of L-AA in solution D (Figure 2.5b).

Because the initial concentration of L-AA is in large excess of the initial concentration of DCIP, this reaction can be modeled using pseudo-first-order reaction kinetics. The pseudo-first-order integrated rate law for this reaction is

$$[\text{L-AA}]_0 k_f t = \ln \left( \frac{[\text{oDCIP}]_0}{[\text{oDCIP}]_t} \right) \quad (4)$$

where  $[\text{L-AA}]_0$  is the initial concentration of L-AA,  $k_f$  is the forward reaction rate constant,  $t$  is the reaction time, and  $[\text{oDCIP}]_0$  and  $[\text{oDCIP}]_t$  are the concentrations of oxidized DCIP at times 0 and  $t$ , respectively. The initial concentration of oxidized DCIP in the droplet was determined using the initial concentration of oxidized DCIP in solution C and the relative abundances of the internal standards (L-Enk in solution C and M-Enk in solution D).  $[\text{oDCIP}]_t$  was calculated from the abundances of the oxidized and reduced forms of DCIP using the equation

$$[\text{oDCIP}]_t = [\text{oDCIP}]_0 \frac{A_{\text{oDCIP}}}{A_{\text{oDCIP}} + i_{\text{DCIP}} \cdot A_{\text{rDCIP}}} \quad (5)$$

where  $A_{\text{oDCIP}}$  and  $A_{\text{rDCIP}}$  are the abundances of the oxidized and reduced forms of DCIP, respectively, and  $i_{\text{DCIP}}$  is the relative ionization efficiency of the oxidized form of DCIP relative to the reduced form.  $i_{\text{DCIP}}$  was measured separately (Figure A.1, Appendix A) and is  $1.0 \pm 0.2$ , which is in good agreement with a previously published value<sup>2</sup> of  $1.09 \pm 0.08$ . Combining eq 4 with eq 5 gives eq 6:

$$[L-AA]_o k_f t = \ln \left( \frac{A_{0DCIP} + i_{DCIP} \cdot A_{tDCIP}}{A_{0DCIP}} \right) \quad (6)$$

which was used to determine the apparent reaction time. On the basis of the rate constant from bulk solution, the average apparent reaction time is  $274 \pm 60 \mu\text{s}$ . This value does not appear to change as a function of the concentration of L-AA in solution D (Figure 2.5c).

The average apparent reaction time is an upper limit to the droplet lifetime because the rates of chemical reactions in rapidly desolvating droplets are greater than in bulk solution.<sup>58</sup> The rapid desolvation of a droplet leads to increased reagent concentrations, a larger surface area to volume ratio, and a decrease in pH. Cumulatively, these factors can increase the rate of product formation within a rapidly desolvating droplet by between 1 and 3 orders of magnitude,<sup>58</sup> but the relative contributions of each of these factors are poorly characterized. The forward rate constant for the reduction of DCIP by L-AA increases by less than 3% from pH = 3 to pH = 1,<sup>69</sup> so pH changes likely have little impact on the rate of product formation in these experiments. However, increases in reagent concentrations and the surface area to volume ratio within the droplet occur, so the true average lifetime of a nano-ESI droplet may be between 10 and 1000 times less than the average apparent reaction time based on the bulk solution rate. Thus, mixing and reactions in these experiments likely occur between about 27  $\mu\text{s}$  and 270 ns. Some product formation will occur in the Taylor cone, which will contribute to a greater apparent droplet lifetime, so the actual droplet lifetime is likely less than 27  $\mu\text{s}$ . This same reaction was previously used to characterize a continuous flow mixing system combined with desorption electrospray (DESI) mass spectrometry of the subsequent liquid jet stream. A mixing time of 2.5 ms was reported, with an instrumental time resolution of 300  $\mu\text{s}$  at longer times obtained by increasing the distance between the mixer and the DESI source. The mixing time we report for this reaction is at least 2 orders of magnitude lower.

The mixing time in conventional mixers is typically controlled by varying either the solution flow rate or the geometry of the mixing region.<sup>13</sup> In nano-ESI, the droplet lifetime depends on the initial droplet diameter,<sup>39</sup> and thus on the diameter of the tip of the electrospray capillary<sup>40</sup> as well as the solution flow rate.<sup>42,53-55</sup> It should be possible to acquire kinetic data at multiple time points using theta-glass emitters by varying either the diameter of the tip of the emitters or the backing pressure to control the solution flow rate.

## 2.4 Conclusions

Theta-glass emitters were used to mix two different solutions during the electrospray process at a flow rate of  $1.4 \pm 0.4 \text{ nL/s}$ . This flow rate is 2 orders of magnitude less than typical flow rates for common mixers in which mixing is achieved in tens of microseconds.<sup>13</sup> On the basis of probable sizes of electrospray droplets, rates of diffusion, and mixing times of coalescing ballistic microdroplets, complete mixing from theta-glass emitters likely occurs within a few microseconds. Thus, mixing from theta-glass emitters is competitive with the fastest mixers reported in the literature<sup>14</sup> and 2 orders of magnitude faster than any mixer previously coupled to MS.<sup>3</sup>

The reduction of DCIP by L-AA performed using the theta-glass emitters was monitored with the mass spectrometer to obtain a lifetime of nano-ESI droplets. The resulting value of  $274 \pm 60 \mu\text{s}$  is an upper limit to the droplet lifetime because both the reagent concentrations and the surface area to volume ratio increase as the droplet evaporates and because some product

formation likely occurs in the Taylor cone prior to droplet formation. On the basis of previously reported results that show that reaction rates in droplets can be 10–1000-fold higher than rates in bulk solution, we estimate that the true droplet lifetime is between 27  $\mu$ s and 270 ns. The rapid mixing and short droplet lifetime achieved using these theta-glass emitters should make it possible to monitor fast reactions using MS. Because the initial droplet diameter, and therefore the droplet lifetime, depends on both the size of the tip of the electrospray capillary and the solution flow rate, the acquisition of reaction data at multiple time points should be possible by either using theta-glass emitters with variously sized tips or by changing solution flow rates.

## 2.5 References

- (1) Losey, M.; Schmidt, M.; Jensen, K. *Ind. Eng. Chem. Res.* **2001**, *40*, 2555-2562.
- (2) Miao, Z.; Chen, H.; Liu, P.; Liu, Y. *Anal. Chem.* **2011**, *83*, 3994-3997.
- (3) Vahidi, S.; Stocks, B. B.; Liaghati-Mobarhan, Y.; Konermann, L. *Anal. Chem.* **2013**, *85*, 8618-8625.
- (4) Gambin, Y.; Simonnet, C.; VanDelinder, V.; Deniz, A.; Groisman, A. *Lab Chip* **2010**, *10*, 598-609.
- (5) Wang, C.; Hu, Y.; Hu, T. *Sensors* **2009**, *9*, 5379-5389.
- (6) Matsumoto, S.; Yane, A.; Nakashima, S.; Hashida, M.; Fujita, M.; Goto, Y.; Takahashi, S. *J. Am. Chem. Soc.* **2007**, *129*, 3840-3841.
- (7) Majumdar, Z. K.; Sutin, J. D. B.; Clegg, R. M. *Rev. Sci. Instrum.* **2005**, *76*, 125103.
- (8) Bringer, M.; Gerdts, C.; Song, H.; Tice, J.; Ismagilov, R. *Philos. Trans. R. Soc. London, Ser. A* **2004**, *362*, 1087-1104.
- (9) Hassell, D.; Zimmerman, W. *Chem. Eng. Sci.* **2006**, *61*, 2977-2985.
- (10) Li, Y.; Zhang, D.; Feng, X.; Xu, Y.; Liu, B. *Talanta* **2012**, *88*, 175-180.
- (11) Park, H.; Qiu, X.; Rhoades, E.; Korlach, J.; Kwok, L.; Zipfel, W.; Webb, W.; Pollack, L. *Anal. Chem.* **2006**, *78*, 4465-4473.
- (12) Capretto, L.; Cheng, W.; Hill, M.; Zhang, X. *Top. Curr. Chem.* **2011**, *304*, 27-68.
- (13) Kathuria, S. V.; Chan, A.; Graceffa, R.; Nobrega, R. P.; Matthews, C. R.; Irving, T. C.; Perot, B.; Bilsel, O. *Biopolymers* **2013**, *99*, 888-896.
- (14) Wu, L.; Lapidus, L. *J. Anal. Chem.* **2013**, *85*, 4920-4924.
- (15) Wilson, D.; Konermann, L. *Anal. Chem.* **2003**, *75*, 6408-6414.
- (16) Lee, V.; Chen, Y.; Konermann, L. *Anal. Chem.* **1999**, *71*, 4154-4159.
- (17) Kolakowski, B.; Konermann, L. *Anal. Biochem.* **2001**, *292*, 107-114.
- (18) Orsnes, H.; Graf, T.; Degn, H. *Anal. Chem.* **1998**, *70*, 4751-4754.
- (19) Chang, D.; Lee, C.; Shiea, J. *Anal. Chem.* **2002**, *74*, 2465-2469.
- (20) Shieh, I.; Lee, C.; Shiea, J. *J. Proteome Res.* **2005**, *4*, 606-612.
- (21) Hong, C.; Tsai, F.; Shiea, J. *Anal. Chem.* **2000**, *72*, 1175-1178.
- (22) Shiea, J.; Chang, D.; Lin, C.; Jiang, S. *Anal. Chem.* **2001**, *73*, 4983-4987.
- (23) Chen, H.; Venter, A.; Cooks, R. G. *Chem. Commun.* **2006**, *19*, 2042-2044.
- (24) Law, W. S.; Wang, R.; Hu, B.; Berchtold, C.; Meier, L.; Chen, H.; Zenobi, R. *Anal. Chem.* **2010**, *82*, 4494-4500.
- (25) Tian, Y.; Chen, J.; Ouyang, Y.; Qu, G.; Liu, A.; Wang, X.; Liu, C.; Shi, J.; Chen, H.; Jiang, G. *Anal. Chim. Acta* **2014**, *814*, 49-54.
- (26) Prudent, M.; Rossier, J. S.; Lion, N.; Girault, H. H. *Anal. Chem.* **2008**, *80*, 2531-2538.
- (27) Prudent, M.; Mendez, M. A.; Jana, D. F.; Corminboeuf, C.; Girault, H. H. *Metalomics* **2010**, *2*, 400-406.
- (28) Miladinovic, S. M.; Fornelli, L.; Lu, Y.; Piech, K. M.; Girault, H. H.; Tsybin, Y. O. *Anal. Chem.* **2012**, *84*, 4647-4651.
- (29) Barbara, J. E.; Eyler, J. R.; Powell, D. H. *Rapid Commun. Mass Spectrom.* **2008**, *22*, 4121-4128.
- (30) Miao, Z.; Chen, H. *J. Am. Soc. Mass Spectrom.* **2009**, *20*, 10-19.
- (31) Girod, M.; Moyano, E.; Campbell, D. I.; Cooks, R. G. *Chem. Sci.* **2011**, *2*, 501-510.
- (32) Badu-Tawiah, A. K.; Campbell, D. I.; Cooks, R. G. *J. Am. Soc. Mass Spectrom.* **2012**, *23*, 1077-1094.

- (33) Mark, L. P.; Gill, M. C.; Mahut, M.; Derrick, P. J. *Eur. J. Mass Spectrom.* **2012**, *18*, 439-446.
- (34) Fisher, C. M.; Kharlamova, A.; McLuckey, S. A. *Anal. Chem.* **2014**, *86*, 4581-4588.
- (35) Akiyama, S.; Takahashi, S.; Kimura, T.; Ishimori, K.; Morishima, I.; Nishikawa, Y.; Fujisawa, T. *Proc. Natl. Acad. Sci. U. S. A.* **2002**, *99*, 1329-1334.
- (36) Acevedo-Malavé, A.; García-Sucre, M. *AIP Adv.* **2011**, *1*, 032118.
- (37) Song, H.; Chen, D. L.; Ismagilov, R. F. *Angew. Chem. Int. Ed.* **2006**, *45*, 7336-7356.
- (38) Graceffa, R.; Burghammer, M.; Davies, R. J.; Riekel, C. *Appl. Phys. Lett.* **2012**, *101*, 254101.
- (39) Grimm, R. L.; Beauchamp, J. L. *Anal. Chem.* **2002**, *74*, 6291-6297.
- (40) Schmidt, A.; Karas, M.; Dülcks, T. *J. Am. Soc. Mass Spectrom.* **2003**, *14*, 492-500.
- (41) Meesters, G. M. H.; Vercoulen, P. H. W.; Marijnissen, J. C. M.; Scarlett, B. *J. Aerosol Sci.* **1992**, *23*, 37-49.
- (42) Wilm, M. S.; Mann, M. *Int. J. Mass Spectrom. Ion Processes* **1994**, *136*, 167-180.
- (43) Chen, X.; Jia, L.; Yin, X.; Cheng, J.; Lu, J. *Phys. Fluids* **2005**, *17*, 032101.
- (44) Tang, K.; Gomez, A. *J. Aerosol Sci.* **1994**, *25*, 1237-1249.
- (45) Rosell-Llompart, J.; Fernandez De La Mora, J. *J. Aerosol Sci.* **1994**, *25*, 1093-1119.
- (46) Gomez, A.; Tang, K. *Phys. Fluids* **1994**, *6*, 404-414.
- (47) Sankar, S. V.; Weber, B. J.; Kamemoto, D. Y.; Bachalo, W. D. *Appl. Opt.* **1991**, *30*, 4914-4920.
- (48) Olumee, Z.; Callahan, J. H.; Vertes, A. *J. Phys. Chem. A* **1998**, *102*, 9154-9160.
- (49) Gemci, T.; Hitron, R.; Chigier, N. Proceedings of the 18th Annual Conference on Liquid Atomization & Spray Systems, Zaragoza, Spain, Sept 9–11, 2002; <http://www.ilasseurope.org/ICLASS/ilass2002/papers/114.pdf>.
- (50) Nemes, P.; Marginean, I.; Vertes, A. *Anal. Chem.* **2007**, *79*, 3105-3116.
- (51) Chen, D.; Pui, D. Y. H.; Kaufman, S. L. *J. Aerosol Sci.* **1995**, *26*, 963-977.
- (52) Chen, D.; Pui, D. Y. H. *Aerosol Sci. Technol.* **2009**, *27*, 367-380.
- (53) Gañán-Calvo, A. M.; Dávila, J.; Barrero, A. *J. Aerosol Sci.* **1997**, *28*, 249-275.
- (54) Pfeifer, R. J.; Hendricks, C. D. *AIAA J.* **1968**, *6*, 496-502.
- (55) Fernandez De La Mora J; Loscertales, I. G. *J. Fluid Mech.* **1994**, *260*, 155-184.
- (56) Gatlin, C.; Tureček, F. *Anal. Chem.* **1994**, *66*, 712-718.
- (57) Girod, M.; Dagany, X.; Antoine, R.; Dugourd, P. *Int. J. Mass Spectrom.* **2011**, *308*, 41-48.
- (58) Badu-Tawiah, A. K.; Campbell, D. I.; Cooks, R. G. *J. Am. Soc. Mass Spectrom.* **2012**, *23*, 1461-1468.
- (59) Badu-Tawiah, A. K.; Campbell, D. I.; Cooks, R. G. *J. Am. Soc. Mass Spectrom.* **2012**, *23*, 1077-1084.
- (60) Badu-Tawiah, A. K.; Li, A.; Jjunju, F. P. M.; Cooks, R. G. *Angew. Chem. Int. Edit.* **2012**, *51*, 9417-9421.
- (61) Jurchen, J. C.; Williams, E. R. *J. Am. Chem. Soc.* **2003**, *125*, 2817-2826.
- (62) Harned, H.; Nuttall, R. *J. Am. Chem. Soc.* **1947**, *69*, 736-740.
- (63) Fell, C. J. D.; Hutchison, H. P. *J. Chem. Eng. Data* **1971**, *16*, 427-429.
- (64) Leist, D. G. *J. Chem. Soc. Faraday Trans.* **1991**, *87*, 597-601.
- (65) *CRC Handbook of Chemistry and Physics*, 55th ed.; Weast, R. C., Ed.; CRC Press: Boca Raton, FL, 1974.
- (66) Oss, M.; Kruve, A.; Herodes, K.; Leito, I. *Anal. Chem.* **2010**, *82*, 2865-2872.

- (67) Izatt, R. M.; Bradshaw, J. S.; Nielsen, S. A.; Lamb, J. D.; Christensen, J. J.; Sen, D. *Chem. Rev.* **1985**, *85*, 271-339.
- (68) Wang, Y.; Tan, M. K.; Go, D. B.; Chang, H. *Europhys. Lett.* **2012**, *99*, 64003.
- (69) Karayannis, M. I. *Talanta* **1976**, *23*, 27-30.

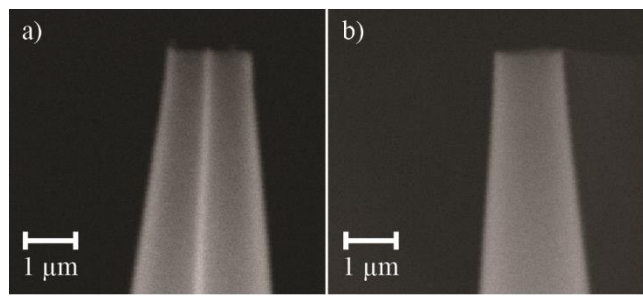


**Figure 2.1.** Electron micrographs of the tips of theta-glass emitters with the inner divider (a) perpendicular to and (b) parallel to the sample stand.

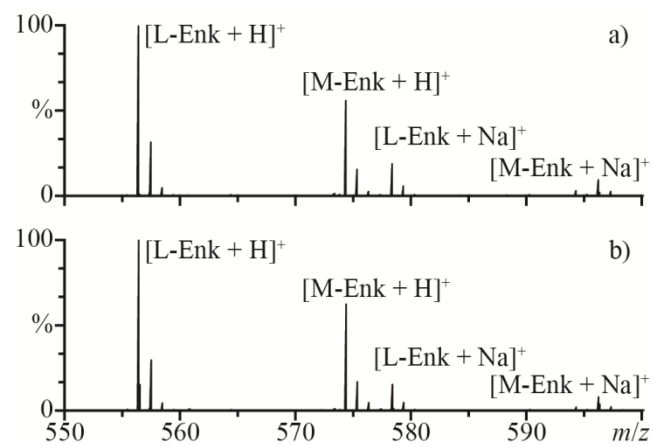


**Figure 2.2.** Representative ESI mass spectra of L-Enk and M-Enk solutions (a) loaded into separate barrels of a theta-glass emitter and (b) premixed and loaded into both barrels.

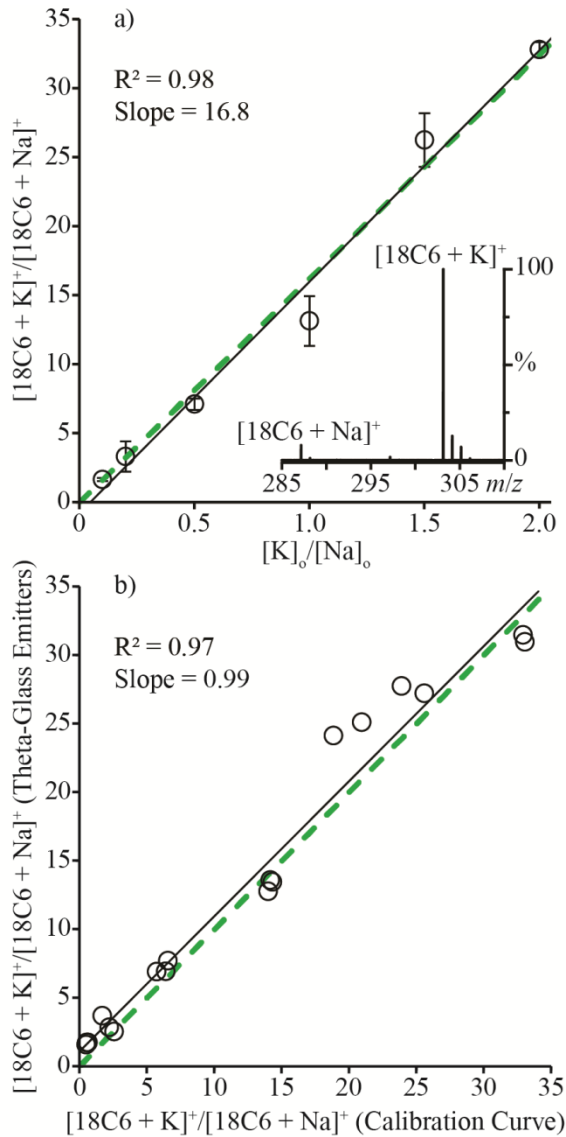


**Figure 2.3.** (a) The ratio,  $[18\text{C}6 + \text{K}]^+ / [18\text{C}6 + \text{Na}]^+$ , in the mass spectra of premixed solutions (circles) and predicted by Eq. 2 (dashed green line), both as functions of the ratio,  $[\text{K}]_o / [\text{Na}]_o$ . The inset is a representative mass spectrum of a solution containing  $\text{Na}^+ : \text{K}^+ : 18\text{C}6$  at a ratio of 1:1:0.05. (b) The ratio,  $[18\text{C}6 + \text{K}]^+ / [18\text{C}6 + \text{Na}]^+$ , in the mass spectra from the theta-glass emitters as a function of the same ratio predicted by a linear fit to the calibration curve data (open circles). The dashed green line is a 1:1 correspondence between the axes. Black lines in both (a) and (b) are linear fits to the data.

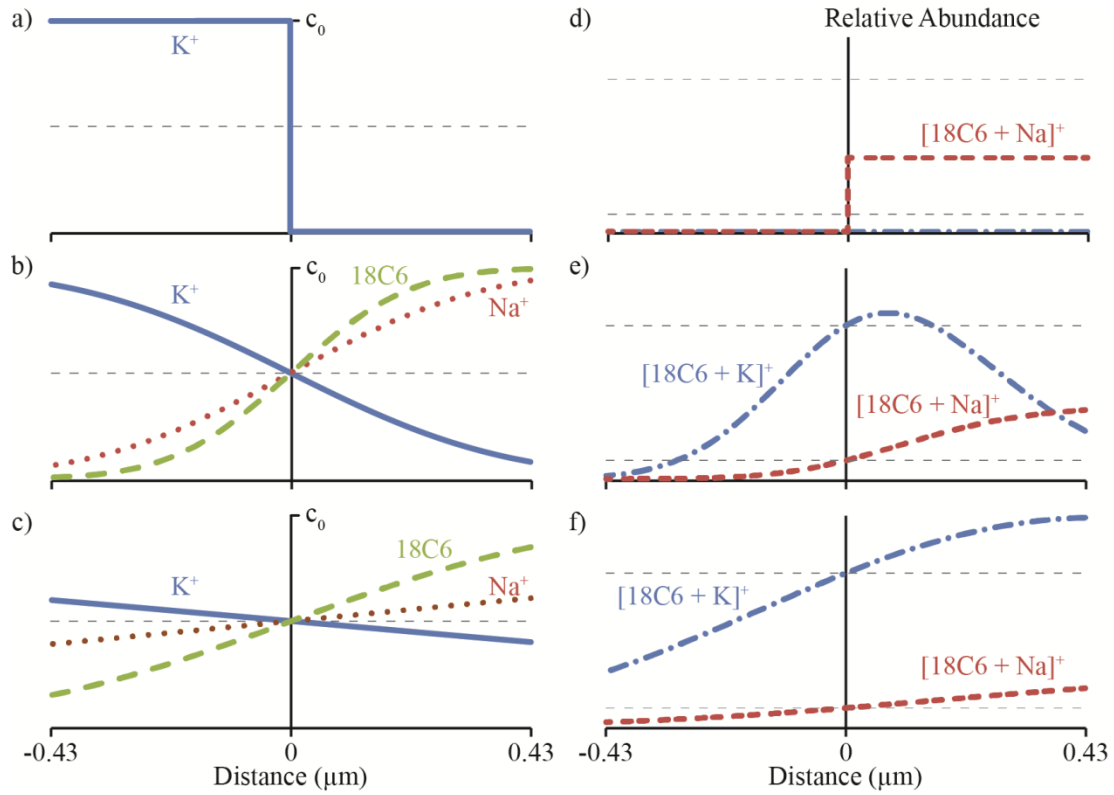


**Figure 2.4.** Concentrations of  $K^+$  (blue line),  $Na^+$  (red dots), and  $18C6$  (green dashes) as a function of the distance from the center of a 0.86  $\mu m$  droplet at (a) 0, (b) 23, and (c) 732  $\mu s$ . Relative abundances of  $[18C6 + K]^+$  (blue dots and dashes) and  $[18C6 + Na]^+$  (red double-dashes) as a function of the distance from the center of the droplet at (d) 0, (e) 23, and (f) 732  $\mu s$ . Initial concentrations used to calculate relative abundances are 500  $\mu M$   $Na^+$  and 100  $\mu M$   $18C6$  in solution A and 250  $\mu M$   $K^+$  in solution B. Horizontal dashed, grey lines represent equilibrium concentrations (a-c) and abundances (d-f).

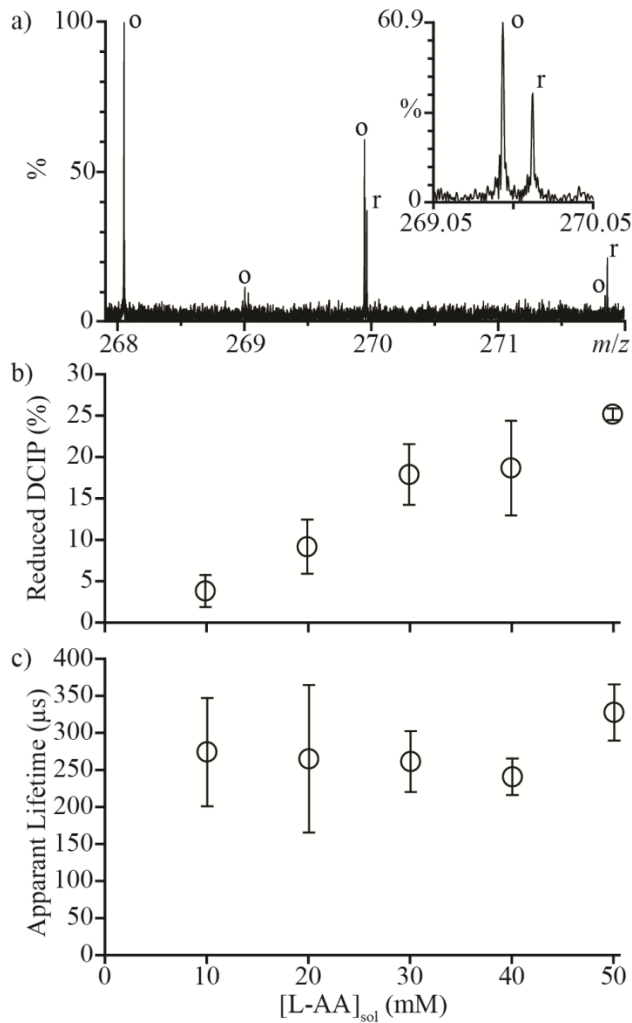
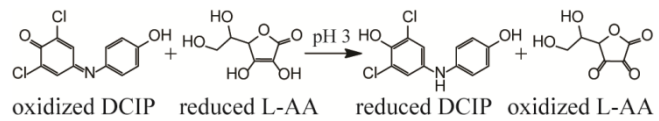


**Figure 2.5.** (a) A representative mass spectrum of a  $10 \mu\text{M}$  DCIP solution mixed with a  $50 \text{ mM}$  L-AA solution (both  $\text{pH} = 3$ ) from a theta-glass emitter. The inset shows the third isotope peak of oxidized DCIP and the first isotope peak of reduced DCIP. (b) The fraction of DCIP reduced as a function of the concentration of L-AA in the opposite barrel. (c) Reaction times calculated from the relative abundances of oxidized and reduced DCIP using eq. 6 as a function of the initial concentration of L-AA in solution.



**Scheme 2.1.** The reduction of 2,6-dichloroindophenol by L-ascorbic acid.

## Chapter 3

# Investigating Protein Folding and Unfolding in Electrospray Nanodrops Upon Rapid Mixing Using Theta-Glass Emitters

This Chapter is reproduced with permission from

Mortensen, D.M.; Williams, E.R.

“Investigating Protein Folding and Unfolding in Electrospray Nanodrops Upon Rapid Mixing Using Theta-Glass Emitters”

*Analytical Chemistry* **2015**, *87*, 1281–1287

© 2014 American Chemical Society

### 3.1 Introduction

Electrospray ionization (ESI) mass spectrometry (MS) is widely used to obtain information about protein structure, including protein identification and analysis of posttranslational modifications.<sup>1–3</sup> Information about protein conformation can also be obtained from charge state distributions in ESI mass spectra.<sup>4–8</sup> Gaseous ions formed from solutions in which a protein has a native or globular conformation are less highly charged than the corresponding ions formed from solutions in which the protein is unfolded. The relative abundances of different conformations of a protein in solution have been obtained by modeling the resulting charge-state distributions observed in ESI mass spectra.<sup>6</sup> Charge-state distributions have been used to monitor protein unfolding both as a function of temperature by heating the sample solution during ESI<sup>4,7,8</sup> and as a function of solution pH by inducing a pH change in the sample solution using the electrolytic oxidation of water that occurs at the metal-liquid interface in an ESI emitter.<sup>5</sup>

Protein conformational changes can also take place during the ESI process. McLuckey and co-workers demonstrated that exposing aqueous ESI droplets containing folded proteins to either gaseous acids<sup>9</sup> or bases<sup>10</sup> in an ESI interface can result in a bimodal charge-state distribution of ions, indicating that a fraction of the protein population unfolds in the ESI droplet. ESI droplets generated from “native” protein solutions have also been exposed to acids and supercharging reagents in solution by flowing a continuous stream of solution from a hypodermic needle into the ESI plume.<sup>11</sup> The stream-droplet interactions in these experiments result in bimodal charge-state distributions of the resulting protein ions, indicative of protein unfolding. Protein unfolding in ESI droplets can also be induced thermally, which is the likely mechanism of electrothermal supercharging,<sup>12,13</sup> wherein high charge states are obtained from buffered aqueous protein solutions by raising the electrospray potential to collisionally activate and heat the ESI droplets.

In contrast to the many studies of protein unfolding during ESI, there are fewer reports of protein folding during ESI. Acid-denatured proteins in ESI droplets have been exposed to gaseous bases in an ESI interface, resulting in a bimodal distribution of charge states for some proteins.<sup>14</sup> Although gas-phase proton transfer reactions may contribute to lower charging in these experiments, the bimodal charge-state distributions indicate that a fraction of the protein population folds as a result of an increase in the droplet pH. However, comparisons of the results obtained from these experiments to those from bulk-solution experiments are complicated because of the dynamic nature of ESI. A low charge-state distribution of myoglobin that was

thermally denatured was observed in nanoESI, which suggests that protein folding occurred in the droplets upon rapid evaporative cooling.<sup>8</sup>

Quantitative information about protein folding kinetics can be obtained in mixing experiments, and ESI MS has been combined with a variety of rapid mixers, including continuous,<sup>15,16</sup> stopped,<sup>17</sup> and laminar flow<sup>18,19</sup> mixers, to measure the kinetics of protein folding<sup>17-19</sup> and unfolding<sup>16</sup> and the reincorporation rates of noncovalent cofactors into the protein structure.<sup>15</sup> In conventional mixers, faster kinetic processes can be measured by increasing the flow rates of the solutions. A dead time of 200 µs has been reported for a laminar flow mixer coupled with MS operating at a flow rate of 10 µL/s.<sup>19</sup> This setup was used to study the subms folding steps that occur after the initial collapse, or “burst-phase,” of apo-myoglobin that takes place on an even shorter time scale (~7 µs time constant).<sup>20</sup> Rapid mixing of two solutions during ESI has also been used to unfold proteins during ESI. Microfabricated dual sprayers have been used to mix solutions containing peptides or proteins with solutions containing supercharging reagents,<sup>21</sup> resulting in increased charging indicative of protein unfolding.

Double-barrel wire-in-a-capillary emitters made from theta glass (theta-glass emitters) have also been used to mix solutions during ESI. Rapid mixing from theta-glass emitters was first used to form a noncovalent complex between a short peptide (KAA) and a glycopeptide (vancomycin) and to exchange hydrogen and deuterium with undeuterated and partially deuterated vancomycin during ESI.<sup>22</sup> Substantial mixing was reported to occur in the Taylor cone prior to droplet formation.<sup>22</sup> Solutions containing folded proteins were mixed with acidic solutions using theta-glass emitters, which produced bimodal charge-state distributions and loss of the heme group for myoglobin.<sup>23</sup> These results indicate that protein unfolding occurred during ESI.<sup>23</sup> Supercharging reagents were mixed into solutions containing folded proteins during ESI using theta-glass emitters which resulted in higher charging and loss of heme for myoglobin, consistent with unfolding of the proteins in the ESI droplets induced by the supercharging reagents.<sup>23</sup> A fast complexation reaction was used to show that complete mixing can occur between two different solutions in the theta-glass emitters during nanoESI.<sup>24</sup> An estimate of the droplet lifetime of <27 µs was determined<sup>24</sup> from the reaction kinetics between L-ascorbic acid and 2,6-dichloroindophenol using theta-glass emitters with ~1.5 µm o.d. tips and from the faster reaction rates observed in droplets over those in bulk solution.<sup>25,26</sup> The very short time scale for mixing and droplet lifetimes indicates that fast protein folding could be observed by rapidly mixing solutions in theta-glass emitters coupled with MS.<sup>24</sup> Investigation of protein folding by mixing solutions using theta-glass emitters has the advantage of very low flow rates, e.g., as low as 1.4 nL/s, resulting in low sample consumption.<sup>24</sup>

Here, theta-glass emitters are used to investigate protein folding and unfolding during nanoESI by inducing a pH change in the electrospray solution by rapidly mixing two solutions at the emitter tip. The relative flow rates of these solutions are measured using peptides as standards. From the measured extents of myoglobin and cytochrome c folding and known protein-folding time constants, a time of between 7 and 25 µs, depending on solution composition, is obtained as an upper limit for the lifetime of nanoESI droplets. Significantly fewer sodium ions are adducted to the ions generated from the native-like conformer when native myoglobin is mixed with acid using the theta-glass emitters than to these ions generated from a native solution. This is likely the result of a higher concentration of protons and the short time available for protein unfolding to occur. These results suggest that rapid mixing from theta-glass emitters may be useful in reducing sodium adduction in native MS.

## 3.2 Experimental Section

Experiments were performed using a 9.4 T Fourier-transform ion cyclotron resonance mass spectrometer that is described elsewhere.<sup>27</sup> Theta glass capillaries (Warner Instruments, LLC, Hamden, CT) were pulled using a model p-87 Flaming/Brown micropipette puller (Sutter Instruments Co., Novato, CA) into tips with an o.d. of  $1.36 \pm 0.02 \mu\text{m}$  parallel to and  $1.71 \pm 0.04 \mu\text{m}$  perpendicular to the central divider.<sup>24</sup> A grounded platinum wire is brought into contact with the solution that is loaded into each barrel, and a backing pressure of ~10 psi is applied to the back end of the capillary. Ion formation is initiated by applying a potential of ~-700 V to the heated capillary of the mass spectrometer interface. All data were acquired using a Predator data station (National High Magnetic Field Laboratory, Tallahassee, FL) and mass spectra were background subtracted. Average charge states are computed as the abundance weighted sum of individual charge states in a distribution. All reported uncertainties are standard deviations determined from three replicate measurements.

Leu-enkephalin acetate salt hydrate, Met-enkephalin acetate salt hydrate, ammonium acetate, formic acid, equine apo- and holo-myoglobin, equine cytochrome *c*, and polypropylenimine hexadecaamine dendrimer, generation 3.0 were obtained from Sigma-Aldrich (St. Louis, MO). Glacial acetic acid was obtained from Fisher Scientific (Fair Lawn, NJ). Solutions were prepared with an analyte concentration of 10  $\mu\text{M}$  in 18.2  $\text{M}\Omega$  water from a Milli-Q water purification system (Millipore, Billerica, MA).

The initial pH of droplets formed when two solutions are mixed using the theta-glass emitters is determined from the  $pK_b$  value of ammonia (4.8), the  $pK_a$  values of acetic and formic acid (4.8 and 3.8, respectively; all values at 25 °C),<sup>28</sup> and the initial concentrations of these species in the droplets. Initial concentrations are determined from the initial concentrations of the analytes in the solutions in both barrels of the theta-glass emitters and from the relative flow rates of these solutions during nanoESI. Relative flow rates are measured using Leu-enkephalin and Met-enkephalin as internal standards (1.0  $\mu\text{M}$ ) as described elsewhere.<sup>24</sup>

## 3.3 Results and Discussion

**3.3.1 Unfolding Holo-Myoglobin During NanoESI.** In low-ionic-strength aqueous solutions (salt concentrations of less than ~0.02 M), holo-myoglobin (holo-Mb) has a native conformation between pH = 5 and 7,<sup>29</sup> a less-compact globular structure around pH = 3,<sup>29</sup> and an unfolded structure with no heme group attached at lower pH.<sup>30</sup> A representative nanoESI mass spectrum of holo-Mb in a 1.0 mM aqueous ammonium acetate solution (pH = 6.4) is shown in Figure 3.1a. The charge states (7 – 9+) are indicative of forming these ions from an aqueous solution in which the protein has a native structure.<sup>6</sup> A nanoESI mass spectrum obtained by mixing this solution with a 1.0 M aqueous acetic acid solution at a 1:1 ratio (pH = 2.6) is shown in Figure 3.1b. The 10 – 26+ charge states of apo-myoglobin (apo-Mb) are formed and no holo-Mb is observed, indicating that extensive unfolding of the protein and concomitant loss of the heme group has occurred in solution.

A nanoESI mass spectrum resulting from mixing these two solutions using the theta-glass emitters is shown in Figure 3.1c. The charge-state distribution of holo-Mb is bimodal, with a high abundance distribution between 8+ and 12+ (comprising  $86 \pm 3\%$  of myoglobin) and a low abundance distribution between 13+ and 19+ (comprising  $11 \pm 1\%$  of myoglobin). The

distribution between 13+ and 19+ corresponds to more open structures resulting from protein unfolding during nanoESI. The 13 – 17+ charge states of apo-Mb are also observed (comprising  $3 \pm 2\%$  of myoglobin), indicating that some heme loss accompanies unfolding of the protein in the nanoESI droplet.

The average charge state of the distribution between 8+ and 12+ in the rapid mixing experiments ( $9.8 \pm 0.2$ ) is higher than the average charge state of holo-Mb in the mass spectra obtained from the pH = 6.4 solution ( $8.0 \pm 0.1$ ). The higher charging obtained for the folded form of the protein in the rapid mixing experiments may be a result of a small change in the conformation, or it could be due to effects of solution composition on charging. To determine the role of solution composition on charging in these experiments, nanoESI mass spectra of polypropylenimine hexadecaamine dendrimer, generation 3.0 (DAB-16), were obtained under similar conditions. NanoESI of DAB-16 in a 1.0 mM aqueous ammonium acetate solution adjusted to pH = 6.4 with acetic acid results in an average charge state of  $3.6 \pm 0.1$  (Figure 3.2a). This solution was mixed with a 1.0 M aqueous acetic acid solution at a 1:1 ratio (pH = 2.6), and in the nanoESI mass spectra of the resulting solution, the average charge state is  $4.0 \pm 0.1$  (Figure 3.2b). Results from small-angle neutron scattering, viscosimetry, and molecular dynamics studies indicate that the conformation of DAB-16 does not strongly depend on solution composition.<sup>31</sup> Thus, the slightly higher charging obtained from this solution is likely a result of the different solution composition, although it may also reflect small changes to the shape of DAB-16. These results suggest that the shift in charging of the folded form of myoglobin in the rapid mixing experiments may be due, at least in part, to the different solution composition as well as any potential change to the native protein structure.

Fisher et al.<sup>23</sup> also reported that myoglobin unfolds when aqueous holo-Mb is mixed with an aqueous solution of 1% acetic acid (~174 mM) using theta-glass emitters, resulting in the formation of 7% apo-Mb. In our experiment, a 5-fold higher concentration of acetic acid is used, yet only 3% apo-Mb is produced (Figure 3.1c). The different extents of unfolding and heme loss in these two experiments are likely a result of different reaction times. The reaction time is limited by the droplet lifetime, which depends on the initial droplet diameter<sup>32</sup> and thus, on the diameter of the electrospray capillary.<sup>33</sup> Fisher et al. used theta-glass emitters with ~10 μm o.d. tips, whereas ~1.5 μm o.d. tips were used here, which results in smaller initial droplets and less time for protein unfolding to occur.

It is also interesting that there is less sodium ion adduction on the folded holo-Mb ions formed after mixing the two solutions using the theta-glass emitters (Figure 3.1c) than on those formed directly from the ammonium acetate solution (Figure 3.1a). For example, the average number of sodium ions adducted to the 8+ charge state is  $3.1 \pm 0.8$  in the nanoESI mass spectra of the ammonium acetate solution and only  $0.7 \pm 0.2$  in those resulting from the solutions mixed using the theta-glass emitters. The lower average number of sodium adducts upon mixing likely results from the >1000 fold increase in the initial concentration of protons in the droplet, which can displace sodium ions near the surface of the protein during droplet evaporation.

**3.3.2 Folding Apo-Myoglobin During NanoESI.** There are at least three conformers of apo-myoglobin (apo-Mb) that exist in aqueous solution. Between pH = 5 and 7, apo-Mb adopts a conformation similar to that of native holo-Mb; at pH = 4, it has a less compact globular structure, and below pH = 3, it is unfolded.<sup>34</sup> NanoESI of acid-denatured apo-Mb (pH = 2.9; Figure 3.3a) results in a charge-state distribution between 11+ and 28+. This high charging is consistent with an unfolded form of apo-Mb in solution. Results from raising the pH of this

solution using a 100 mM aqueous ammonium acetate solution are shown in Figure 3.3b-d. The addition of ammonium acetate results in the elimination of the highest charge states, and a second charge-state distribution between 7+ and 9+ becomes more abundant with increasing pH. This charge-state distribution is consistent with a globular conformer in solution and comprises 13 ± 4%, 25 ± 5%, and 35 ± 7% of myoglobin at pH = 3.9, 4.4, and 4.7, respectively (Figure 3.3b-d). The 11+ charge state is slightly more abundant than the 10+ and 12+ charge states, suggesting that a partially folded intermediate structure may also be present.

Mixing the initial acidified solution (Figure 3.3a) with the 100 mM aqueous ammonium acetate solution using the theta-glass emitters produces droplets with an initial pH of ~4.7. In the nanoESI mass spectra resulting from this experiment (Figure 3.3e), there are at least two charge-state distributions for apo-Mb: one between 10+ and 21+ corresponding to an unfolded conformer and another between 7+ and 9+ corresponding to the fraction of apo-Mb that is folded into a globular conformer during nanoESI (25 ± 2% of apo-Mb). The 11+ charge state is again more abundant than the 10+ and 12+, possibly suggesting the presence of a partially folded intermediate structure. At pH = 4.7, the equilibrium distribution of folded protein (7–9+) constitutes 35 ± 7% of apo-Mb (Figure 3.3d). However, the abundance of this distribution in the rapid mixing experiments (estimated initial droplet pH = 4.7) more closely resembles that in the nanoESI mass spectra of a pH = 4.4 solution at equilibrium, wherein it compromises 25 ± 5% of apo-Mb (Figure 3.3c). This result indicates that the droplet lifetime is sufficiently short so that equilibrium is not reached during nanoESI and that protein folding is incomplete.

The initial collapse of apo-Mb from an unfolded to a globular structure occurs with a time constant of ~7 μs,<sup>20</sup> and the subsequent formation of a structure similar to that of native holo-Mb takes more than a ms to occur.<sup>35</sup> In previous mixing experiments using these same theta-glass emitters, a <27 μs droplet lifetime was deduced from the extent of product formation of a fast reaction with a known rate constant in bulk solution.<sup>24</sup> The short droplet lifetime established in those experiments indicates that only the initial collapse of apo-Mb is likely to occur to a significant extent in the droplets.

An estimate of the time scale for protein folding in this study is obtained by modeling the initial collapse of apo-Mb as an independent, two-state folding reaction.<sup>36,37</sup> The integrated rate law for a two-state folding reaction is given in eq 1:

$$t = \tau \ln\left(\frac{A_e - A_o}{A_e - A_t}\right) \quad (1)$$

where  $t$  is the reaction time,  $\tau$  is the protein folding time constant,  $A_e$  is the abundance of the folded protein conformer at equilibrium, and  $A_o$  and  $A_t$  are the abundances of the folded protein conformer at times 0 and  $t$ , respectively. From the relative abundances of the globular apo-Mb conformer in the unmixed, equilibrium, and rapid mixing experiments (Figure 3.3 a, d, and e, respectively) and the 7 μs time constant of the initial collapse of apo-Mb,<sup>20</sup> a reaction time of 9 ± 2 μs is obtained. This reaction time is consistent with the <27 μs droplet lifetime reported previously that was deduced on the basis of the extent of product formation for a bimolecular reaction and a known solution reaction rate constant.<sup>24</sup> Because the concentrations of the reagents increase to an unknown extent as droplets evaporate and bimolecular reaction rates depend on concentration, there is a significant uncertainty in the true droplet lifetime obtained from previous measurements. In contrast, folding of apo-Mb is a unimolecular process that does not depend on protein concentration at the concentrations used. Surface effects as a result of the

high surface-to-volume ratios of small droplets compared to that of bulk solution may influence protein folding rates in droplets.<sup>26</sup> However, similarity between the droplet lifetimes obtained by both methods indicate that surface effects may be small in these protein folding experiments.

**3.3.3 Folding and Reincorporation of the Heme.** Although folding of apo-Mb occurs quickly,<sup>20,35</sup> reincorporation of the heme group into the protein structure requires considerably more time (hundreds of milliseconds to seconds).<sup>15</sup> In order to determine if heme reincorporation can occur during nanoESI, solutions that result in heme reincorporation at equilibrium when mixed at a 1:1 ratio were mixed using the theta-glass emitters. A mass spectrum resulting from mixing a solution of acid-denatured holo-Mb (pH = 2.9; Figure 3.4a) and a solution of 100 mM aqueous ammonium acetate at a 1:1 ratio is shown in Figure 3.4b. There is a bimodal charge-state distribution of apo-Mb centered at 15+ and at 9+ as well as a distribution of holo-Mb in the 9+ and 8+ charge states. The relative abundances of unfolded and folded apo-Mb and folded holo-Mb are 50 ± 3%, 13 ± 3%, and 37 ± 4%, respectively.

A nanoESI mass spectrum resulting from mixing the acidified solution (Figure 3.4a) with the 100 mM aqueous ammonium acetate solution using a theta-glass emitter is shown in Figure 3.4c. There is a bimodal charge-state distribution of apo-Mb centered at 16+ and ~8+, corresponding to unfolded and folded forms of the protein, respectively. The initial pH of the mixed droplets is ~4.9, and the folded form of the protein comprises 25 ± 9% of myoglobin, consistent with the results from solutions without heme present (25 ± 2%, Figure 3.3e). No holo-Mb is observed despite the presence of both a globular apo-Mb conformer and the heme group in solution. This result indicates that heme reincorporation does not occur to an appreciable extent within the nanoESI droplet, which is consistent with the droplet lifetime of ~9 µs measured using the refolding of apo-Mb and the heme reincorporation time constant on the order of hundreds of milliseconds to seconds.<sup>15</sup>

**3.3.4 Temperature of NanoESI Droplets.** Fragments of ions formed by ESI can be observed in some ESI mass spectra, and this has led some to conclude that the ESI process itself activates ions.<sup>38-42</sup> For example, Vékey and co-workers concluded from the extent of fragmentation of benzylpyridinium salts during ESI compared to that predicted by RRKM calculations at various temperatures that electrospray ionization produces ions with internal temperatures greater than 200 °C.<sup>38,39</sup> The potential used to produce ions in ESI can result in droplet heating, such as in electrothermal supercharging, wherein high charge states of protein ions are formed from buffered aqueous solutions.<sup>12,13</sup> However, extensively hydrated ions can also be directly produced using ESI, and evaporative cooling significantly reduces the temperatures of these clusters.<sup>43-46</sup> Results for trivalent atomic ions show that these ions require approximately 18 water molecules to be stable, indicating that these clusters are formed by evaporative cooling of even larger clusters and not by condensation of water onto minimally solvated or bare ions.<sup>46</sup> Because preservation of weakly bound water molecules can only occur in ESI droplets that are not significantly heated, these results show that the ESI process itself is not activating, although activation can occur either in the ESI droplet or after ion formation as a result of instrumental conditions.

Apo-Mb thermally denatures between about 60 and 70 °C in unbuffered aqueous solutions.<sup>20</sup> The folding of this protein during nanoESI shown here (Figures 2e and 3c) indicates that the droplet temperature in these experiments must be less than 70 °C. This result shows that the droplet temperature in ESI can be lower than the melting point of some proteins. In sum,

these results indicate that ESI droplets can have low temperatures and that ion formation by ESI is intrinsically soft under appropriate experimental conditions.

**3.3.5 Folding Cytochrome *c* During NanoESI.** In low ionic strength aqueous solutions, cytochrome *c* (cyt *c*) is unfolded with little secondary structure at pH = 2 but has a native folded structure between pH = 3 and 7.<sup>47,48</sup> A globular form, known as the A state, can form at high salt concentrations (0.2 M),<sup>49,50</sup> and a partially folded intermediate structure may also form during folding in salt-free solutions.<sup>51,52</sup> A mass spectrum of cyt *c* in an aqueous solution with 2.5% formic acid (pH = 2.0) is shown in Figure 3.5a. The charge-state distribution is bimodal, with a low-abundance distribution between 7+ and 9+ corresponding to a folded structure ( $11 \pm 4\%$  of cyt *c*) and a high-abundance distribution between 10+ and 18+ corresponding to unfolded structures in solution. This solution was mixed with a solution of 500 mM aqueous ammonium acetate at a 1:1 ratio (pH = 4.2), and a mass spectrum of the resulting solution is shown in Figure 3.5b. The 6 – 8+ charge states are formed and comprise  $98 \pm 0\%$  of cyt *c* in the mass spectra. The 14+ charge state is also present at low abundance. These results indicate that cyt *c* has predominantly adopted a folded structure in this solution at equilibrium.

A mass spectrum resulting from mixing these two solutions using a theta-glass emitter is shown in Figure 3.5c. The charge state distribution is bimodal, with one distribution between 6+ and 8+ corresponding to a folded structure ( $21 \pm 1\%$  of cyt *c*) and another between 9+ and 17+ corresponding to an unfolded structure. The initial folding step of cyt *c* occurs with a time constant of  $\sim 57 \mu\text{s}$ <sup>47</sup> and other steps may also occur with time constants at or above  $600 \mu\text{s}$ .<sup>52-54</sup> The droplet lifetime of  $<27 \mu\text{s}$  reported previously<sup>24</sup> and the  $9 \mu\text{s}$  lifetime obtained here for the folding of apo-Mb indicate that only the  $57 \mu\text{s}$  folding step of cyt *c* is likely to occur to a significant extent in these experiments. The abundances of the folded cyt *c* conformer in the unmixed, equilibrium, and rapid mixing experiments (Figure 3.5a-c, respectively) and the  $57 \mu\text{s}$  time constant are used to obtain a reaction time of  $7 \pm 3 \mu\text{s}$  from eq 1. This result is remarkably similar to the reaction time of  $9 \pm 2 \mu\text{s}$  obtained for the folding of apo-Mb during the nanoESI process.

Slightly different solution conditions were used in these experiments than those in which the protein folding time constants were obtained, which may affect the droplet lifetimes reported here. The time constant for the initial collapse of apo-Mb was measured in a pH = 5.9 solution containing 10 mM sodium acetate<sup>20</sup> and the folding time constant of cyt *c* in a pH = 4.5 solution containing 25 mM sodium phosphate and 25 mM sodium acetate.<sup>47</sup> In this study, apo-Mb and cyt *c* were folded in droplets containing higher salt concentrations (~50 and ~250 mM ammonium acetate, respectively) and slightly lower initial pHs (pH = 4.7 and 4.2, respectively). The different solution compositions likely result in slightly different protein-folding time constants in the nanoESI droplets than were measured in those bulk solution experiments. However, the remarkable agreement in reaction times obtained for apo-Mb and cyt *c* in the rapid mixing experiments indicates a relatively small uncertainty in the measured reaction times despite the different solution conditions used to obtain the folding time constants.

Between pH = 2 and 3, the unfolded and globular forms of cyt *c* co-exist in equilibrium.<sup>48</sup> The equilibrium distribution of partially acid-denatured cyt *c* can be shifted towards the folded conformer by diluting the solution with water. In the nanoESI mass spectrum of cyt *c* at pH = 2.8 (1.0% acetic acid in water, Figure 3.5d), the charge-state distribution is bimodal, with one distribution centered at 8+ corresponding to a folded structure ( $34 \pm 7\%$  of cyt *c*) and another distribution centered at 16+ corresponding to an unfolded structure. Results from mixing this

solution with water at a 1:1 ratio ( $\text{pH} = 2.9$ ) are shown in Figure 3.5e. The same charge-state distributions are observed, but the relative abundances of these distributions indicate that  $76 \pm 5\%$  of cyt *c* is in the folded form. This result shows that the equilibrium distribution between the two forms of cyt *c* shifts toward the globular structure in this solution.

A nanoESI mass spectrum resulting from mixing these two solutions using a theta-glass emitter is shown in Figure 3.5f. The same charge-state distributions are observed, and the relative abundances of these distributions indicate that the folded form comprises  $49 \pm 7\%$  of cyt *c*. From the abundances of the globular cyt *c* conformer in the unmixed, equilibrium, and rapid mixing experiments (Figure 3.5d-f, respectively) and a folding time constant of  $57 \mu\text{s}$  for cyt *c*,<sup>47</sup> a reaction time of  $25 \pm 7 \mu\text{s}$  is obtained from eq 1. This reaction time is about 3-fold higher than the reaction times for the folding of myoglobin ( $9 \pm 2 \mu\text{s}$ ) and of cyt *c* from the acidified solution mixed with 500 mM aqueous ammonium acetate ( $7 \pm 3 \mu\text{s}$ ).

The shorter droplet lifetime deduced from the experiments in which ammonium acetate is used to increase the initial pH of the droplets may be due to uncertainties associated with the folding time constants measured under slightly different conditions. It may also be a result of faster water evaporation or of differences in the temperatures of the nanodrops. Emission of water-solvated ammonium ions from the droplet<sup>55,56</sup> could result in an increased rate of droplet evaporation and, hence, a shorter droplet lifetime. The presence of ammonium acetate may also affect the droplet temperature,<sup>57</sup> which would affect the protein-folding time constants.<sup>37,58</sup>

### 3.4 Conclusions

Theta-glass emitters were used to rapidly mix two solutions in order to induce either protein folding or unfolding during nanoESI. Acid-denatured myoglobin was mixed with a solution of ammonium acetate to increase pH and induce folding both with and without heme present in solution. The extents of folding in these experiments compared to those obtained at equilibrium indicates a reaction time of  $9 \pm 2 \mu\text{s}$ , which is an upper limit to the droplet lifetime because some folding will occur in the Taylor cone prior to droplet formation. Reincorporation of the heme into the folded protein structure does not occur, consistent with the much longer time constant of hundreds of milliseconds to seconds for this process.<sup>15</sup> Similarly, droplet lifetimes of  $7 \pm 3$  and  $25 \pm 7 \mu\text{s}$ , depending on solution compositions, were obtained from folding experiments with cyt *c*. These results indicate that the nanoESI droplet lifetime can be very short and that the droplets are not heated past the melting points of many proteins<sup>7,20</sup> under appropriate experimental conditions.

The extent of unfolding of holo-Mb obtained in the rapid mixing experiments in this study is less than that reported earlier,<sup>23</sup> a result that is consistent with the much smaller tips used in the current experiments. These results indicate that the time frame for reactions to occur during the nanoESI process can be readily controlled by changing the emitter tip diameter or other properties that affect the initial size of the nanoESI droplets. Thus, it should be possible to acquire “snapshots” of protein folding or unfolding at various time points by varying the diameter of the tips of the theta-glass emitters.

The extent of sodium ion adduction to the folded forms of protein ions resulting from rapidly mixing proteins in buffered aqueous solutions with acidified solutions using the theta-glass emitters is less than in protein ions generated from native solutions. This is likely the result of the much higher concentration of protons that can displace sodium ions at the protein surface during nanoESI. This may be an effective way to reduce sodium adduction in native MS without

significantly affecting the resulting protein ion structure if the unfolding time of the protein is significantly greater than the time frame for ion formation in nanoESI.

### 3.5 References

- (1) Aebersold, R.; Mann, M. *Nature* **2003**, *422*, 198-207.
- (2) Siuti, N.; Kelleher, N. L. *Nat. Methods* **2007**, *4*, 817-821.
- (3) Pan, J.; Borchers, C. H. *Proteomics* **2013**, *13*, 974-981.
- (4) Mirza, U.; Cohen, S.; Chait, B. *Anal. Chem.* **1993**, *65*, 1-6.
- (5) Konermann, L.; Silva, E.; Sogbein, O. *Anal. Chem.* **2001**, *73*, 4836-4844.
- (6) Kaltashov, I.; Eyles, S. *Mass Spectrom. Rev.* **2002**, *21*, 37-71.
- (7) Liu, J.; Konermann, L. *J. Am. Soc. Mass Spectrom.* **2009**, *20*, 819-828.
- (8) Sterling, H. J.; Williams, E. R. *J. Am. Soc. Mass Spectrom.* **2009**, *20*, 1933-1943.
- (9) Kharlamova, A.; Prentice, B. M.; Huang, T.; McLuckey, S. A. *Anal. Chem.* **2010**, *82*, 7422-7429.
- (10) Kharlamova, A.; McLuckey, S. A. *Anal. Chem.* **2011**, *83*, 431-437.
- (11) Yang, S. H.; Wijeratne, A. B.; Li, L.; Edwards, B. L.; Schug, K. A. *Anal. Chem.* **2011**, *83*, 643-647.
- (12) Sterling, H. J.; Cassou, C. A.; SU. S. A., A. C.; Williams, E. R. *Anal. Chem.* **2012**, *84*, 3795-3801.
- (13) Cassou, C. A.; Sterling, H. J.; SU. S. A., A. C.; Williams, E. R. *Anal. Chem.* **2013**, *85*, 138-146.
- (14) Kharlamova, A.; DeMuth, J. C.; McLuckey, S. A. *J. Am. Soc. Mass Spectrom.* **2012**, *23*, 88-101.
- (15) Simmons, D. A.; Konermann, L. *Biochemistry* **2002**, *41*, 1906-1914.
- (16) Zinck, N.; Stark, A.; Wilson, D. J.; Sharon, M. *ChemistryOpen* **2014**, *3*, 109-114.
- (17) Kolakowski, B.; Konermann, L. *Anal. Biochem.* **2001**, *292*, 107-114.
- (18) Wu, L.; Lapidus, L. *J. Anal. Chem.* **2013**, *85*, 4920-4924.
- (19) Vahidi, S.; Stocks, B. B.; Liaghati-Mobarhan, Y.; Konermann, L. *Anal. Chem.* **2013**, *85*, 8618-8625.
- (20) Ballew, R.; Sabelko, J.; Gruebele, M. *Proc. Natl. Acad. Sci. U. S. A.* **1996**, *93*, 5759-5764.
- (21) Miladinovic, S. M.; Fornelli, L.; Lu, Y.; Piech, K. M.; Girault, H. H.; Tsybin, Y. O. *Anal. Chem.* **2012**, *84*, 4647-4651.
- (22) Mark, L. P.; Gill, M. C.; Mahut, M.; Derrick, P. J. *Eur. J. Mass Spectrom.* **2012**, *18*, 439-446.
- (23) Fisher, C. M.; Kharlamova, A.; McLuckey, S. A. *Anal. Chem.* **2014**, *86*, 4581-4588.
- (24) Mortensen, D. N.; Williams, E. R. *Anal. Chem.* **2014**, *86*, 9315-9321.
- (25) Girod, M.; Moyano, E.; Campbell, D. I.; Cooks, R. G. *Chem. Sci.* **2011**, *2*, 501-510.
- (26) Badu-Tawiah, A. K.; Campbell, D. I.; Cooks, R. G. *J. Am. Soc. Mass Spectrom.* **2012**, *23*, 1461-1468.
- (27) Jurchen, J. C.; Williams, E. R. *J. Am. Chem. Soc.* **2003**, *125*, 2817-2826.
- (28) *CRC Handbook of Chemistry and Physics*, 55th ed.; Weast, R. C., Ed.; CRC Press: Boca Raton, FL, 1974.
- (29) Sage, J. T.; Morikis, D.; Champion, P. M. *Biochemistry* **1991**, *30*, 1227-1237.
- (30) Griko, Y. V.; Privalov, P. L.; Venyaminov, S. Y.; Kutyshenko, V. P. *J. Mol. Biol.* **1988**, *202*, 127-138.
- (31) Scherrenberg, R.; Coussens, B.; van Vliet, P.; Edouard, G.; Brackman, J.; de Brabander, E.; Mortensen, K. *Macromolecules* **1998**, *31*, 456-461.

- (32) Grimm, R. L.; Beauchamp, J. L. *Anal. Chem.* **2002**, *74*, 6291-6297.
- (33) Schmidt, A.; Karas, M.; Dülcks, T. *J. Am. Soc. Mass Spectrom.* **2003**, *14*, 492-500.
- (34) Goto, Y.; Fink, A. L. *J. Mol. Biol.* **1990**, *214*, 803-805.
- (35) Callender, R.; Dyer, R.; Gilmanshin, R.; Woodruff, W. *Annu. Rev. Phys. Chem.* **1998**, *49*, 173-202.
- (36) Gilmanshin, R.; Williams, S.; Callender, R.; Woodruff, W.; Dyer, R. *Proc. Natl. Acad. Sci. U. S. A.* **1997**, *94*, 3709-3713.
- (37) Gilmanshin, R.; Callender, R.; Dyer, R. *Nat. Struct. Biol.* **1998**, *5*, 363-365.
- (38) Drahos, L.; Heeren, R. M. A.; Collette, C.; De Pauw, E.; Vékey, K. *J. Mass Spectrom.* **1999**, *34*, 1373-1379.
- (39) Takáts, Z.; Drahos, L.; Schlosser, G.; Vékey, K. *Anal. Chem.* **2002**, *74*, 6427-6429.
- (40) Naban-Maillet, J.; Lesage, D.; Bossee, A.; Gimbert, Y.; Sztaray, J.; Vekey, K.; Tabet, J. *J. Mass Spectrom.* **2005**, *40*, 1-8.
- (41) Gabelica, V.; De Pauw, E. *Mass Spectrom. Rev.* **2005**, *24*, 566-587.
- (42) Huang, Y.; Yoon, S. H.; Heron, S. R.; Masselon, C. D.; Edgar, J. S.; Turecek, F.; Goodlett, D. R. *J. Am. Soc. Mass Spectrom.* **2012**, *23*, 1062-1070.
- (43) Rodriguez-Cruz, S. E.; Klassen, J. S.; Williams, E. R. *J. Am. Soc. Mass Spectrom.* **1999**, *10*, 958-968.
- (44) Prell, J. S.; O'Brien, J. T.; Holm, A. I. S.; Leib, R. D.; Donald, W. A.; Williams, E. R. *J. Am. Chem. Soc.* **2008**, *130*, 12680-12689.
- (45) Lee, S.; Freivogel, P.; Schindler, T.; Beauchamp, J. L. *J. Am. Chem. Soc.* **1998**, *120*, 11758-11765.
- (46) Bush, M. F.; Saykally, R. J.; Williams, E. R. *J. Am. Chem. Soc.* **2008**, *130*, 9122-9128.
- (47) Shastry, R. M. C.; Luck, S. D.; Roder, H. *Biophys. J.* **1998**, *74*, 2714-2721.
- (48) Konno, T. *Protein Sci.* **1998**, *7*, 975-982.
- (49) Stellwagen, E.; Babul, J. *Biochemistry* **1975**, *14*, 5135-5140.
- (50) Pletneva, E.; Gray, H.; Winkler, J. *J. Am. Chem. Soc.* **2005**, *127*, 15370-15371.
- (51) Krantz, B.; Mayne, L.; Rumbley, J.; Englander, S.; Sosnick, T. *J. Mol. Biol.* **2002**, *324*, 359-371.
- (52) Kathuria, S. V.; Chan, A.; Graceffa, R.; Nobrega, R. P.; Matthews, C. R.; Irving, T. C.; Perot, B.; Bilsel, O. *Biopolymers* **2013**, *99*, 888-896.
- (53) Takahashi, S.; Yeh, S.; Das, T.; Chan, C.; Gottfried, D.; Rousseau, D. *Nat. Struct. Biol.* **1997**, *4*, 44-50.
- (54) Chan, C.; Hu, Y.; Takahashi, S.; Rousseau, D.; Eaton, W.; Hofrichter, J. *Proc. Natl. Acad. Sci. U. S. A.* **1997**, *94*, 1779-1784.
- (55) Labowsky, M. *Rapid Commun. Mass Spectrom.* **2010**, *24*, 3079-3091.
- (56) Ahadi, E.; Konermann, L. *J. Am. Chem. Soc.* **2011**, *133*, 9354-9363.
- (57) Mirza, U.; Chait, B. *Int. J. Mass Spectrom. Ion Process.* **1997**, *162*, 173-181.
- (58) Pascher, T. *Biochemistry* **2001**, *40*, 5812-5820.

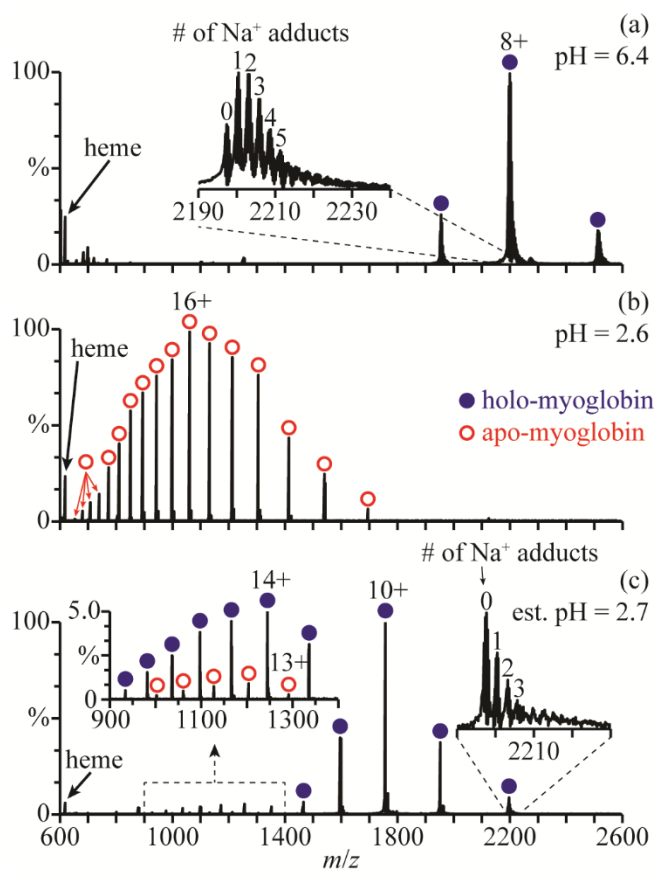


**Figure 3.1.** NanoESI mass spectra of (a) holo-Mb in a 1.0 mM aqueous ammonium acetate solution ( $\text{pH} = 6.4$ ), (b) this ammonium acetate solution mixed with a 1.0 M aqueous acetic acid solution at a 1:1 ratio ( $\text{pH} = 2.6$ ), and (c) this ammonium acetate solution mixed with the acetic acid solution using a theta-glass emitter (estimated  $\text{pH} = 2.7$ ). Insets in (a) and (c) show the extent of  $\text{Na}^+$  addition to the 8+ charge states and, in (c), the distributions of apo- and holo-Mb between  $m/z$  900 and 1400.

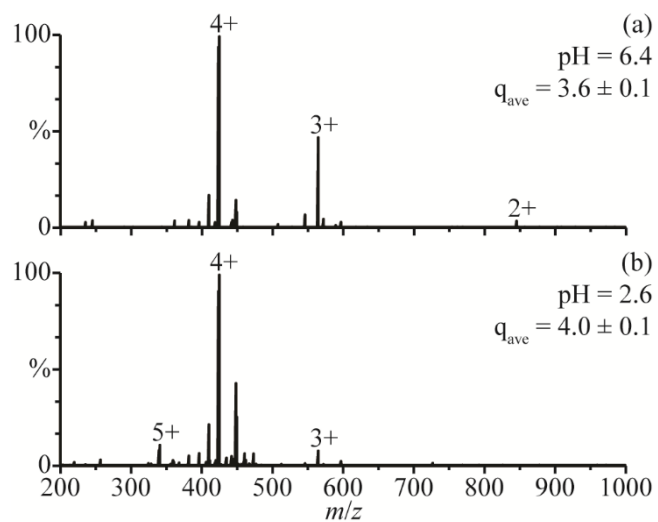


**Figure 3.2.** NanoESI mass spectra of (a) DAB-16 in a 1.0 mM aqueous ammonium acetate solution adjusted to pH = 6.4 with acetic acid and (b) this solution adjusted to pH = 2.6 by mixing with a 1.0 M aqueous acetic acid solution at a 1:1 ratio.  $q_{ave}$  denotes the average charge state.

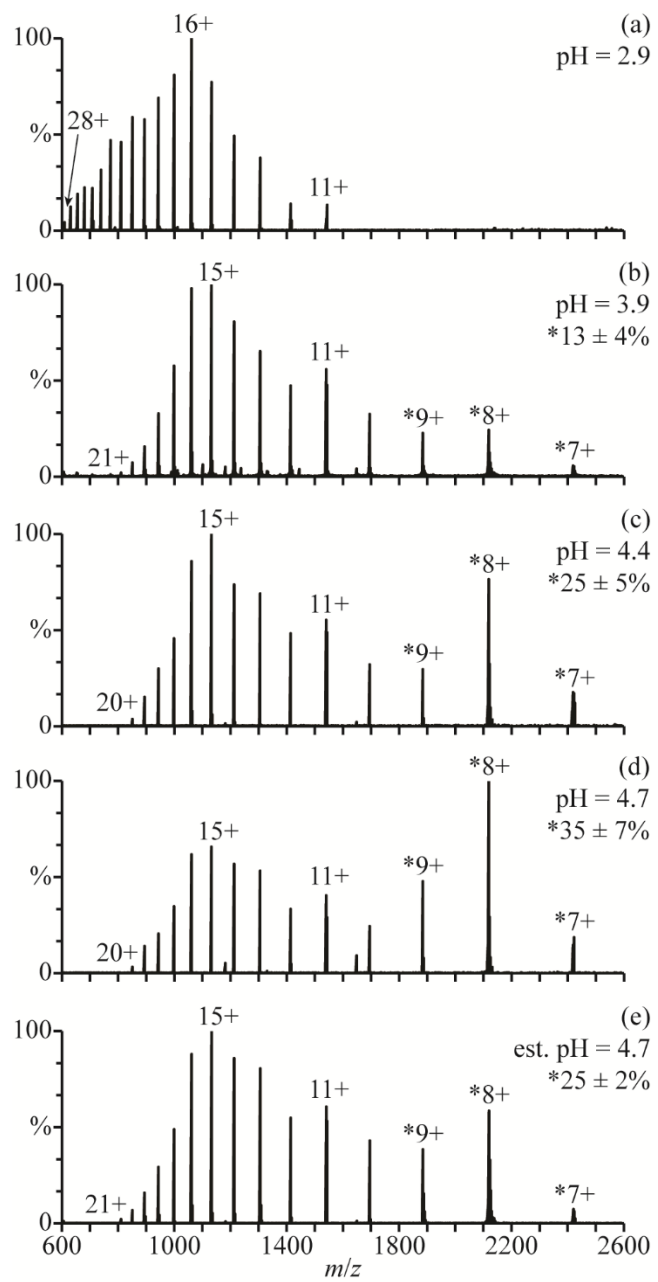


**Figure 3.3.** NanoESI mass spectra of (a) acid-denatured apo-Mb ( $\text{pH} = 2.9$ ), acid-denatured apo-Mb mixed with a 100 mM aqueous ammonium acetate solution at ratios of (b) 10:1 ( $\text{pH} = 3.9$ ), (c) 2:1 ( $\text{pH} = 4.4$ ), and (d) 1:1 ( $\text{pH} = 4.7$ ), and (e) acid-denatured apo-Mb mixed with this ammonium acetate solution using a theta-glass emitter (estimated  $\text{pH} = 4.7$ ). Percentages are the relative abundances of the folded fractions (7–9+ charge states) of apo-Mb.

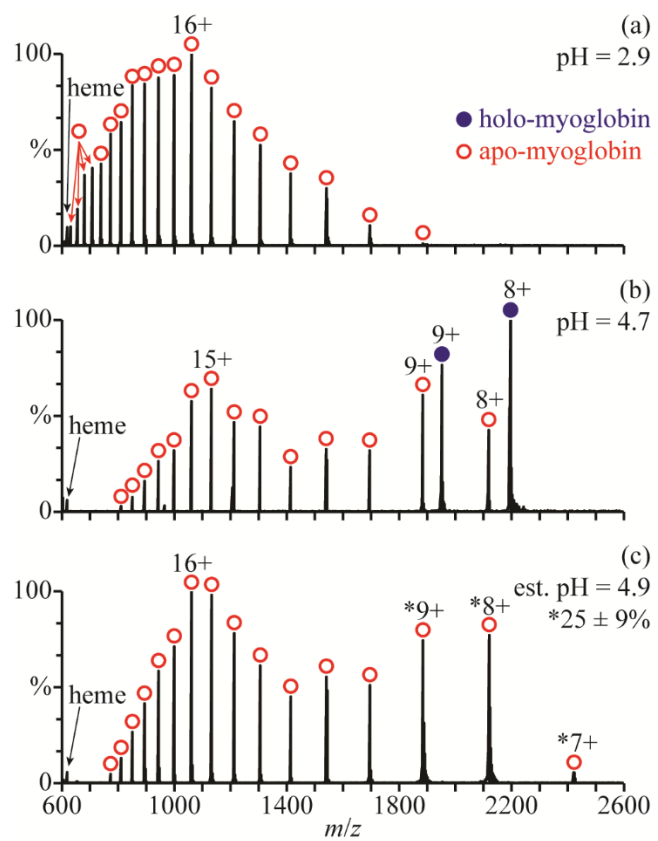


**Figure 3.4.** Mass spectra of (a) acid-denatured holo-Mb (pH = 2.9), (b) acid-denatured holo-Mb mixed with a 100 mM aqueous ammonium acetate solution at a 1:1 ratio (pH = 4.7), and (c) acid-denatured holo-Mb mixed with the ammonium acetate solution using a theta-glass emitter (estimated pH = 4.9). The percentage in (c) is the relative abundance of the folded fraction (7 – 9+ charge states) of apo-Mb.

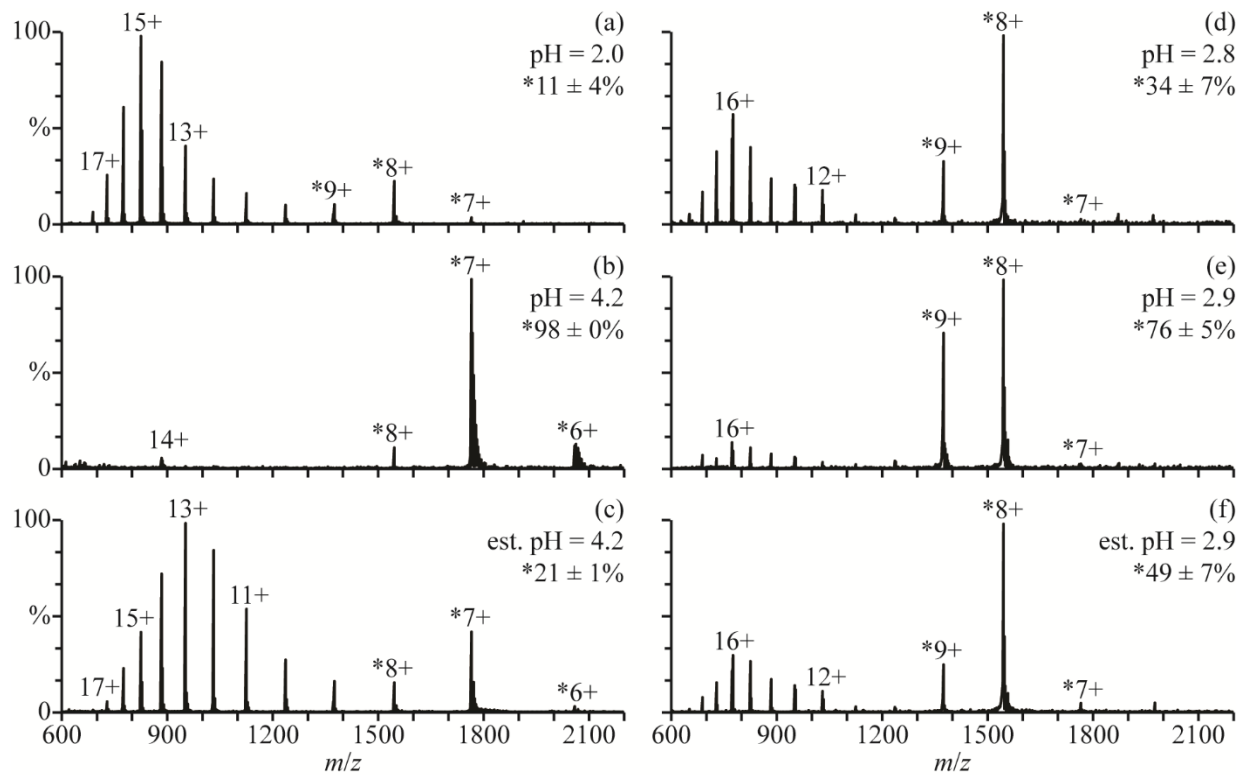


**Figure 3.5.** Mass spectra of (a) cyt *c* in an aqueous solution of 2.5% formic acid (pH = 2.0), (b) this formic acid solution mixed with a 500 mM aqueous ammonium acetate solution at a 1:1 ratio (pH = 4.2), and (c) this formic acid solution mixed with the ammonium acetate solution using a theta-glass emitter (estimated pH = 4.2). Mass spectra of (d) cyt *c* in an aqueous solution of 1.0% acetic acid (pH = 2.8), (e) this acetic acid solution mixed with water at a 1:1 ratio (pH = 2.9), and (f) this acetic acid solution mixed with water using a theta-glass emitter (estimated pH = 2.9). Percentages are the relative abundances of the fraction of cyt *c* in charge states corresponding to folded conformers (denoted with \*).

## Chapter 4

# Ultrafast (1 $\mu$ s) Mixing and Fast Protein Folding in Nanodrops Monitored by Mass Spectrometry

This Chapter is reproduced with permission from  
Mortensen, D.M.; Williams, E.R.  
“Ultrafast (1  $\mu$ s) Mixing and Fast Protein Folding in  
Nanodrops Monitored by Mass Spectrometry”  
Journal of the American Chemical Society **2016**, *138*, 3453–3460  
© 2016 American Chemical Society

### 4.1 Introduction

Information about reaction kinetics, including protein folding<sup>1–3</sup> and unfolding,<sup>4</sup> is often obtained by rapidly mixing two or more solutions. Conventional mixing devices include chaotic,<sup>5</sup> turbulent,<sup>6</sup> and laminar<sup>2,3</sup> flow mixers. Shorter reaction times are often obtained by increasing the solution flow rate. The shortest reaction time achieved with a conventional mixer is 8  $\mu$ s using a laminar flow mixer with a ~100 nL/s flow rate.<sup>2</sup> This mixing time is insufficient to observe some fast protein folding events, such as the folding of the 20-residue “mini-protein” Trp-cage, which has a folding time constant of 4.1  $\mu$ s.<sup>7</sup> Mass spectrometry (MS) is an excellent detector for measuring reaction products resulting from rapid mixing experiments owing to its high sensitivity, high chemical specificity, and rapid speed of analysis.<sup>8</sup> Several different in-line mixers have been coupled with MS, including stopped,<sup>1</sup> continuous,<sup>4,9</sup> and laminar<sup>2,3</sup> flow devices. The shortest reaction time achieved using a conventional mixer coupled with MS is 200  $\mu$ s with a laminar flow mixer and a 10  $\mu$ L/s flow rate.<sup>3</sup>

Solutions can be mixed prior to MS during electrospray ionization (ESI), which has been done using multiple channel electrospray,<sup>10,11</sup> fused-droplet electrospray,<sup>12</sup> extractive electrospray,<sup>13,14</sup> and dual-sprayer microchips.<sup>15,16</sup> Solution-phase reactions have also been carried out in charged microdroplets and monitored with MS using desorption electrospray ionization,<sup>17,18</sup> ambient ion soft landing,<sup>19</sup> and microdroplet fusion, which is accomplished by orthogonally colliding ESI droplets.<sup>20</sup> Microdroplet fusion MS has been used to measure bimolecular reduction-oxidation, protein unfolding, and hydrogen/deuterium exchange at reaction times of >13  $\mu$ s.<sup>20</sup> This reaction time was obtained from the droplet velocity and the distance between the droplet collision point and the entrance to the mass spectrometer. Mixing times in these experiments were estimated to be less than a few microseconds.

Recently, theta-glass emitters (double-barrel wire-in-a-capillary emitters that resemble the Greek letter θ “theta” when turned on end) have been used to mix solutions during the ESI process. Mixing with theta-glass emitters likely occurs in a few microseconds or less<sup>21</sup> and has been used to measure noncovalent complexation,<sup>21,22</sup> hydrogen/deuterium exchange,<sup>22</sup> bimolecular reduction-oxidation,<sup>21</sup> protein folding<sup>23</sup> and unfolding<sup>23,24</sup> and to introduce supercharging reagents to protein solutions during ESI.<sup>24</sup>

The lifetime of the droplets formed using the theta-glass emitters controls the extent to which solution-phase reactions can occur in these droplets.<sup>21,23</sup> The ESI droplet lifetime depends on several factors including the solution composition<sup>23,25</sup> and the initial droplet diameter.<sup>25</sup> The initial droplet diameter can be varied by changing the solution flow rate,<sup>26–29</sup> which depends on

both the inner diameters of the electrospray emitter tips and the backing pressure applied to the solutions inside the emitters.<sup>29,30</sup> Reaction times between 7 and 25  $\mu$ s, depending on solution composition, have been obtained for droplets formed from theta-glass emitters operating at a flow rate of  $\sim$ 1 nL/s.<sup>23</sup> These reaction times were obtained from the extent of protein folding that occurs during nanoESI and known protein folding time constants obtained in bulk solution. Information about the conformation of proteins in solution is obtained from the charge-state distributions of the protein ions formed by ESI. Folded globular conformers are less highly charged than unfolded conformers,<sup>31-34</sup> and the relative abundances of different protein conformers can be obtained by modeling the bimodal or multimodal charge-state distributions.<sup>34,35</sup> The short reaction times obtained using rapid mixing from theta-glass emitters indicate that this technique can be used to access fast reaction times while consuming substantially less sample than is used in conventional mixing apparatus. However, methods for varying the reaction time at short time scales using rapid mixing from theta-glass emitters have not previously been demonstrated.

Here, theta-glass emitters are used to mix acidified aqueous solutions containing a protein with aqueous ammonium acetate to increase the solution pH and induce protein folding during nanoESI. The extent of protein folding that occurs in these experiments is controlled by varying the solution flow rate, and reaction times between 1.0  $\mu$ s at 48 pL/s and 22  $\mu$ s at 2880 pL/s are obtained from the extent of folding that occurs in these experiments and known folding time constants of different proteins. The 1.0  $\mu$ s reaction time is significantly less than the 8  $\mu$ s reaction time reported for a conventional mixer.<sup>2</sup> The 1.0  $\mu$ s reaction time is obtained using a flow rate (48 pL/s) that is 2000-fold less than that required to obtain the 8  $\mu$ s reaction time using a conventional mixer ( $\sim$ 100 nL/s). Results from this study demonstrate that ultrafast (1  $\mu$ s) protein folding reactions can be readily investigated using rapid mixing from theta-glass emitters coupled with MS and that substantially less sample is required compared to conventional mixing apparatus. This method should enable a wide range of fast reactions to be measured including complex reactions with multiple reaction products.

## 4.2 Experimental Section

Mass spectra are acquired using a 9.4 T Fourier-transform ion cyclotron resonance mass spectrometer that is described elsewhere.<sup>36</sup> Rapid mixing is performed using theta-glass capillaries (Warner Instruments, LLC; Hamden, CT) that have tips that are pulled using a model p-87 Flaming/Brown micropipette puller (Sutter Instruments Co.; Novato, CA). The tips of the capillaries are imaged on carbon tape at 10 000-times magnification using a TM-1000 scanning electron microscope (Hitachi High-Technologies Co.; Tokyo, Japan). Grounded platinum wires are inserted into the capillaries so as to contact the solutions in each barrel, and a backing pressure is applied to the back end of the capillaries. NanoESI is initiated by applying a potential of about -700 V to the heated capillary of the ESI interface. Data are acquired using a Predator data station,<sup>37</sup> and mass spectra are background subtracted. To determine flow rates, the theta-glass emitters are weighed before and after electrospraying for a fixed time using an A-200DS analytical balance (Denver Instrument Company, Bohemia, NY) with a lower mass range of 0.01 mg and a reproducibility (standard deviation) of 0.02 mg. Temperature dependent studies are conducted using single-barrel wire-in-a-capillary electrospray emitters prepared by pulling borosilicate capillaries (Warner Instruments) into  $1.83 \pm 0.04$   $\mu$ m o.d. tips. A NiCr wire is wrapped around a cylindrical aluminum jacket that holds the capillaries and is used to resistively

heat the capillaries during nanoESI. The temperature of the aluminum jacket is measured using a thermocouple (Omega, Stamford, CT). This device is described elsewhere.<sup>34</sup> Traveling wave ion mobility spectrometry drift times in nitrogen gas are measured using a Synapt G2-Si High Definition Mass Spectrometer (Waters, Milford, MA, U. S. A.) with a wave velocity of 500 m/s, a wave height of 40 V, and helium and nitrogen flow rates of 180 and 90 mL/s, respectively.

Average charge states are computed as abundance weighted sums of the individual charge states. All uncertainties reported are standard deviations determined from triplicate measurements. The initial pH values of droplets formed upon rapid mixing of two solutions from the theta-glass emitters are estimated to be within  $\pm 0.2$  of the pH of those solutions mixed at a 1:1 ratio. This estimate is determined using the initial concentrations of acetic acid ( $pK_a = 4.8$ ) and ammonia ( $pK_b = 4.8$ , both at 25 °C)<sup>38</sup> in the droplets. Initial droplet concentrations are determined from the initial concentrations of the solutions in each barrel and the relative flow rates of these solutions during nanoESI. Relative flow rates are monitored using Leu- and Met-enkephalin as internal standards as described previously.<sup>21</sup>

Ammonium acetate, 18-crown-6, Leu- and Met-enkephalin acetate salt hydrates, equine apo-myoglobin and cytochrome *c*, and renin substrate tetradecapeptide are obtained from Sigma-Aldrich (St. Louis, MO), glacial acetic acid and NaCl from Fisher Scientific (Fair Lawn, NJ), KCl from Mallinckrodt Baker, Inc. (Phillipsburg, NJ), and Trp-cage from AnaSpec Inc. (Fremont, CA).

## 4.3 Results and Discussion

**4.3.1 Controlling Solution Flow Rates.** The solution flow rates in the theta-glass emitters can be varied by changing the backing pressure applied to the solutions in the emitters and by making emitters with tips that have different outer diameters (o.d.).<sup>29,30</sup> Smaller initial droplet sizes are formed with lower solution flow rates<sup>29</sup> and with smaller tip sizes.<sup>39</sup> The effect of the backing pressure on the flow rate was investigated by varying the pressure between 5 and 40 psi using theta-glass emitters with ~1465 nm o.d. tips. Flow rates are obtained by spraying an aqueous solution of 500 μm 18C6 and 500 μm NaCl until the mass of the solution in the tip decreases by at least 0.5 mg and by measuring the change of mass with time (between ~10 min and ~2 h, depending on the flow rate). These measurements show that the flow rate increases linearly with increasing backing pressure from 383 pL/s at 5 psi to 2880 pL/s at 40 psi (Figure 4.1a).

The effect of the size of the o.d. of the tips of the theta-glass emitters on the flow rate was investigated by varying the o.d. of the tips between  $244 \pm 61$  and  $1465 \pm 134$  nm and using a 10 psi backing pressure. Electron micrographs of the various size tips are provided in Appendix B (Figure B.1). The flow rate increases linearly with increasing tip o.d., from 48 pL/s at ~244 nm to 913 pL/s at ~1465 nm (Figure 4.1b), even though the cross-sectional area of the tips increases quadratically with the tip diameter. The linear relationship between tip size and flow rate is consistent with results reported for single-barrel emitters with tip o.d.s of between 1 and 5 μm.<sup>30</sup> The relationship between flow rate and cross-sectional area of the tip indicates that the velocity of the solution exiting an emitter changes with tip size. The velocity of a solution as it exits the emitter was obtained by dividing the solution flow rate by the emitter tip orifice area. The latter value was estimated as an ellipse with diameters equal to the i.d. of the tips perpendicular to and parallel to the inner divider less the area occupied by the inner divider. Solution velocities were not estimated for the smallest (~244 nm o.d.) tips because the i.d. and central divider were not

resolvable. The velocity of the solution at the tip of the theta-glass emitters as a function of the tip o.d. is shown in Figure 4.1, panel c. The solution velocity increases significantly with decreasing tip size. The electric field at the tip of the emitter also increases with decreasing tip size, and this may play a role in the increasing velocity with decreasing tip size.

To determine whether complete mixing between the solutions in the two channels of the theta-glass emitters occurs during nanoESI, a solution containing 18-crown-6 (18C6) was mixed with a solution containing KCl, and the rapid equilibration complexation reaction between 18C6 and K<sup>+</sup> was measured. The extent of complexation reaction that occurs in these experiments is obtained from the abundance of the complex [18C6 + K]<sup>+</sup> relative to that of the complex [18C6 + Na]<sup>+</sup> as described previously<sup>21</sup> (Appendix B, Figure B.2). This reaction reaches equilibrium during nanoESI at each flow rate, indicating that the solutions loaded into the different barrels of the theta-glass emitters mix completely in these experiments.

**4.3.2 Reaction Times and Backing Pressure.** To determine the reaction times that are accessible with these theta-glass emitters, the folding of proteins with known folding rate constants was investigated. In aqueous solution, apo-myoglobin (aMb) is unfolded below pH = 3, has a partially unfolded globular structure at pH = 4, and has a compact globular structure similar to that of native holo-myoglobin between pH = 5 and 7.<sup>40</sup> NanoESI of an acidified aqueous aMb solution (pH = 2.9) results in the production of the 11–26+ charge states (Figure 4.2a), consistent with this protein adopting unfolded conformations in this solution. Results from mixing this acidified aMb solution with a 100 mM aqueous ammonium acetate solution at a 1:1 ratio prior to nanoESI (equilibrium; pH = 4.7) are shown in Figure 4.2, panel b. The charge-state distribution is bimodal, and the high charge state distribution corresponding to unfolded structures is shifted to slightly lower charge. The 7–10+ charge states correspond to folded conformers and constitute 36 ± 5% of aMb. The 11+ charge state is more abundant than the 10+ and 12+ charge states, suggesting that a partially folded, perhaps intermediate conformer, may also be present.

The effects of the solution flow rate on the extent of folding that occurs during nanoESI were determined by mixing the acidified aMb solution with the ammonium acetate solution using the theta-glass emitters with backing pressures of between 5 and 40 psi (Figure 4.2c–f, in order of increasing backing pressure). The same charge states are observed as those measured when these solutions are at equilibrium (Figure 4.2b), but the relative abundance of the folded fraction of aMb (7–10+) increases with backing pressure from 17 ± 6% at 5 psi to 34 ± 2% at 40 psi. These results indicate that the extent of folding that occurs during the nanoESI process increases with increasing backing pressure. Interestingly, the relative abundance of the 11+ charge state also increases with increasing backing pressure, consistent with this charge state corresponding to a short-lived folding intermediate. The reaction time upon rapid mixing using the theta-glass emitters can be obtained from the extent of protein folding that occurs by modeling this as a two-state folding reaction.<sup>41</sup> The integrated rate law for a two-state folding reaction is

$$t = \tau \ln \left( \frac{A_e - A_o}{A_e - A_t} \right) \quad (1)$$

where  $t$  is time,  $\tau$  is the protein folding time constant, and  $A_e$ ,  $A_o$ , and  $A_t$  are the relative abundances of the folded protein conformer at equilibrium and at times 0 and  $t$ , respectively. The

initial collapse of unfolded aMb to a globular conformer occurs with a 7  $\mu$ s time constant,<sup>42</sup> and the formation of a conformer similar to that of native holo-myoglobin occurs in greater than 1 ms.<sup>43</sup> Previous results using theta-glass emitters with ~1 nL/s flow rates indicated a 9  $\mu$ s reaction time.<sup>23</sup> Thus, only the initial collapse of aMb is likely to occur to a significant extent in the droplets formed here.

To determine the extent to which the folded structures from the equilibrium and rapid mixing experiments are similar, drift times of the corresponding charge states (8–10+) are obtained using traveling wave ion mobility spectrometry (TWIMS). Drift times obtained for the 8–10+ charge states of aMb resulting from the rapid mixing experiments are between 1 and 3% longer than those obtained for the same charge states resulting from the equilibrium experiments (Appendix B, Figure B.3a-c). These results suggest that the 8–10+ charge states resulting from the rapid mixing experiments correspond to slightly less compact structures than those resulting from the equilibrium experiments, consistent with the initial collapse expected on this fast time scale.

The reaction times in these rapid mixing experiments are obtained from the relative abundances of the folded fraction of aMb obtained in the unmixed, equilibrium, and rapid mixing experiments and the 7  $\mu$ s time constant of the initial collapse of aMb using eq 1. These reaction times are indicated on the corresponding mass spectra (Figure 4.2c–f). The reaction time increases with increasing backing pressure from 5  $\pm$  2  $\mu$ s at 5 psi to 20  $\pm$  3  $\mu$ s at 40 psi.

To determine the accuracy of these reaction times, another protein with a significantly different folding time constant was investigated. In aqueous solution, cytochrome *c* (cyt *c*) adopts a native folded conformer between pH = 3 and 7 and is unfolded at pH = 2.<sup>44,45</sup> Cyt *c* also adopts a globular “A” state at salt concentrations of  $\geq$ 0.2 M,<sup>46</sup> and a partially folded intermediate may form in solutions with lower salt concentrations.<sup>47,48</sup> NanoESI of an aqueous cyt *c* solution at pH = 2.8 results in a bimodal charge-state distribution (Figure 4.2g), indicating that both folded (6–10+) and unfolded (11–19+) conformers exist in solution at this pH and that the folded form comprises 34  $\pm$  5% of the population. Results from mixing this acidified cyt *c* solution with a 100 mM aqueous ammonium acetate solution at a 1:1 ratio prior to nanoESI (equilibrium; pH = 4.4) are shown in Figure 4.2, panel h. Only the 7+ and 8+ charge states are observed, indicating that cyt *c* is predominantly folded in this solution. The slightly lower charging of the folded form resulting from this solution (Figure 4.2h) compared to that from the unmixed cyt *c* solution (Figure 4.2g) may be a result of the different solution composition or of changes to the structure of the folded conformer. The mixed solution has a higher ionic strength and thus may result in more compact conformers. Results from mixing the acidified cyt *c* solution with the ammonium acetate solution using the theta-glass emitters with backing pressures of between 5 and 40 psi are shown in Figure 4.2, panels i-l in order of increasing backing pressure. There are charge states corresponding to both folded (6–8+) and unfolded (9–16+) structures in each spectrum, and the relative abundance of the folded form increases with backing pressure from 40  $\pm$  2% at 5 psi to 55  $\pm$  3% at 40 psi.

The initial folding of cyt *c* occurs with a 57  $\mu$ s time constant,<sup>44</sup> and other folding steps may occur with time constants of  $\geq$ 600  $\mu$ s.<sup>48–50</sup> The TWIMS ion mobility drift times for the 6–8+ charge states of cyt *c* formed in the rapid mixing and equilibrium experiments are indistinguishable (Appendix B, Figure B.3d-f). This result indicates that any differences in structure are indistinguishable based on the collisional cross section alone. On the basis of the 5–20  $\mu$ s reaction times obtained here for aMb, only the initial folding step of cyt *c* is likely to occur to a significant extent in these experiments. Thus, only the 57  $\mu$ s time constant for the initial

folding step of cyt *c* is considered in obtaining the reaction times for these experiments, which are indicated on the respective mass spectra (Figure 4.2i-l). The reaction time increases with backing pressure from  $5.5 \pm 0.9 \mu\text{s}$  at 5 psi to  $22 \pm 4 \mu\text{s}$  at 40 psi. All of these reaction times are the same as those obtained for aMb at the same backing pressures. These results indicate that the reaction times obtained using rapid mixing from theta-glass emitters are independent of the different folding time constants for these two proteins and any uncertainties in the protein folding time constants do not contribute substantially to uncertainties in the reaction times measured here. A reaction time of  $7 \pm 3 \mu\text{s}$  was reported<sup>23</sup> from cyt *c* folding using the same tip size and backing pressure as that used to obtain the  $9 \pm 2 \mu\text{s}$  reaction time reported here. A significantly more concentrated aqueous ammonium acetate solution (500 mM) was used in the earlier study compared to the 100 mM aqueous ammonium acetate solution used here. The similar reaction times indicate that the initial concentration of ammonium acetate in the droplets has no measurable effect on the measured reaction times within this range of concentrations.

**4.3.3 Reaction Times and Tip Size.** Reducing the o.d. of the tips of the theta-glass emitters results in lower flow rates, smaller initial droplet sizes,<sup>39</sup> and shorter droplet lifetimes. The data in Figure 4.2 were acquired using ~1465 nm o.d. tips. A nanoESI mass spectrum of the acidified aqueous aMb solution (pH = 2.9) acquired using a theta-glass emitter with a significantly smaller ~305 nm o.d. tip is shown in Figure 4.3, panel a. The charge-state distribution is bimodal, with one distribution between the 12–21+ charge states and the other between the 22–27+ charge states, which comprise  $18 \pm 3\%$  of the population. The distribution between the 12–21+ charge states is significantly narrower than the distribution corresponding to unfolded conformers (11–26+) obtained with the larger ~1465 nm o.d. tips (Figure 4.2a). This is possibly a result of a narrower distribution of droplet sizes being formed from the smaller tips. Narrower charge-state distributions have also been reported for cyt *c* and ubiquitin ions generated from <100 nm o.d. tips compared to those generated from ~1 μm o.d. tips.<sup>51</sup> The 22–27+ charge states observed here may correspond to an even more highly unfolded conformer. Smaller tips have a higher surface area relative to the solution volume, and the surface may cause some changes to the protein conformation prior to droplet formation. Similar results are obtained when either a single barrel or both barrels of the theta-glass emitters are used, indicating that this distribution is not a result of different droplet size distributions being formed from the different barrels of the theta-glass emitters. The relative abundance of this distribution remains nominally constant when the spray potential is varied between -450 and -1050 V, indicating that this distribution does not result from the increased electric field resulting from the smaller tip size. Charging of protein and peptide ions formed by nanoESI from methanol/water/acid solutions in which proteins are denatured also increases with decreasing tip size.<sup>30,51</sup> This was attributed to the smaller droplets having high charge densities. However, formation of high charge density droplets would not likely result in the bimodal charge state distributions observed here.

Results obtained for the acidified aMb solution mixed with the 100 mM aqueous ammonium acetate solution at a 1:1 ratio prior to nanoESI acquired using a ~305 nm o.d. tip are shown in Figure 4.3, panel b. Charge states corresponding to folded (8–10+) and unfolded (11–19+) conformers are present, and the folded conformer comprises  $36 \pm 3\%$  of aMb. There is not a charge-state distribution corresponding to a highly unfolded structure, suggesting that if this structure exists, it is not stable at pH = 4.7. The 8–10+ and 11–19+ charge state distributions are narrower than those corresponding to the folded (7–10+) and unfolded (11–23+) conformers formed with the ~1465 nm o.d. tips (Figure 4.2b), consistent with the charge-state distribution

narrowing observed for the acidified aMb solution in Figure 4.3, panel a. The acidified aMb solution and the aqueous ammonium acetate solution were mixed using theta-glass emitters with ~305 nm o.d. tips (Figure 4.3c), but no charge states corresponding to folded structures were apparent given the low signal-to-noise ratio. On the basis of the noise level, an upper limit to the reaction time of  $2.8 \pm 0.6 \mu\text{s}$  is established.

To more effectively measure reaction times when using the small tip sizes, a protein that has a shorter folding time constant than that of the initial collapse of aMb ( $7 \mu\text{s}$ ) was used. Trp-cage folds from an open structure to a globular loop structure with a  $4.1 \mu\text{s}$  folding time constant at  $22.7^\circ\text{C}$ .<sup>7</sup> Mass spectra of an acidified aqueous Trp-cage solution ( $\text{pH} = 3.4$ ) obtained using theta-glass emitters with ~244 and ~1465 nm o.d. tips are shown in Figure 4.4, panels a and b, respectively. Both the 2+ and 3+ charge states are formed, and the 3+ is the most abundant in both spectra, though the average charge state is higher from the ~244 nm tips ( $2.98 \pm 0.01$ , Figure 4.4a) than from the ~1465 nm tips ( $2.83 \pm 0.06$ , Figure 4.4b). This result is consistent with the narrower charge-state distributions observed for aMb conformers when using the smaller tips. Results acquired for the acidified Trp-cage solution mixed with a 100 mM aqueous ammonium acetate solution at a 1:1 ratio prior to nanoESI (equilibrium;  $\text{pH} = 5.7$ ) using ~244 and ~1465 nm o.d. tips are shown in Figure 4.4, panels c and d, respectively. The 2+ charge state is most abundant, consistent with a change from an unfolded to a folded structure in solution, and the average charge state of Trp-cage is the same to within error for each tip size ( $2.22 \pm 0.07$  and  $2.23 \pm 0.02$  in Figure 4.4c,d, respectively).

The acidified Trp-cage solution was mixed with the ammonium acetate solution using the theta-glass emitters at flow rates of 48–913 pL/s. These flow rates were obtained using various tip sizes and backing pressures. Results from these experiments are shown in Figure 4.4, panels e–h in order of increasing flow rate. The average charge state decreases with increasing flow rate from  $2.81 \pm 0.05$  at 48 pL/s to  $2.25 \pm 0.00$  at 913 pL/s. These results indicate that the extent of folding occurring in these experiments increases with increasing flow rate. Because the charge state distribution is not bimodal, reaction times for these experiments are obtained from the average charge states (instead of the folded fractions of the protein) using eq 2:

$$t = \tau \ln \left( \frac{q_e - q_o}{q_e - q_t} \right) \quad (2)$$

which is derived from eq 1 by substituting the average charge states at equilibrium and times 0 and  $t$  ( $q_e$ ,  $q_o$ , and  $q_t$ , respectively) for the relative abundances of the folded protein conformer at these times. Reaction times obtained using eq 2 and the  $4.1 \mu\text{s}$  folding time constant of Trp-cage are indicated on the corresponding mass spectra (Figure 4.4e–h). The reaction time increases with increasing flow rate from  $1.01 \pm 0.04 \mu\text{s}$  at 48 pL/s to  $5.3 \pm 0.2 \mu\text{s}$  at 383 pL/s. The  $1.0 \mu\text{s}$  reaction time is significantly less than the shortest reaction time ( $8 \mu\text{s}$ ) reported for a conventional mixer.<sup>2</sup> This  $1.0 \mu\text{s}$  reaction time is obtained using a 48 pL/s flow rate, which is ~2000 times less than the ~100 nL/s flow rate used to obtain the  $8 \mu\text{s}$  reaction time using a conventional mixer. This reaction time is also more than an order of magnitude less than the shortest reaction time ( $>13 \mu\text{s}$ ) reported for a time resolvable mixing experiment coupled with MS<sup>20</sup> and more than two orders of magnitude less than that for a conventional mixer ( $200 \mu\text{s}$ ) coupled with MS.<sup>3</sup> At a flow rate of 383 pL/s, a reaction time of  $5.3 \mu\text{s}$  is obtained, which is essentially the same as the  $5 \pm 2$  and  $5.5 \pm 0.9 \mu\text{s}$  reaction times obtained for aMb and cyt *c*, respectively, using this same flow rate. This result indicates that the average charge state can be

used to monitor protein folding in cases where bimodal charge-state distributions are not produced. At 913 pL/s, the folding of Trp-cage reaches equilibrium during nanoESI. Results from laser-induced temperature-jump experiments indicate that Trp-cage folding reaches equilibrium in about 9–10 μs at 25 °C.<sup>7</sup> This result suggests a lower limit of about 9–10 μs for the reaction time at 913 pL/s, consistent with the 9 ± 2 μs reaction time obtained for both aMb and cyt c using this same flow rate. The 9–10 μs equilibration time for Trp-cage folding indicates that this reaction would be near equilibrium within the 8 μs reaction time reported for a conventional mixer, but results reported here illustrate that this fast folding reaction can be readily investigated with mass spectrometry using rapid mixing from theta-glass emitters.

**4.3.4 Kinetics of a β-hairpin Formation.** β-hairpin formation can occur quickly. The formation of the β-hairpin structure of a 16 residue peptide (protein G B1, fragment 41–56) at room temperature, measured using nanosecond laser temperature-jump experiments, occurs with a time constant of 6 μs.<sup>52</sup> Folding time constants between 0.8 and 20 μs have been estimated for the formation of similar structures for three different 15–17 residue peptides based on computer simulations.<sup>53</sup> To determine if the formation of a β-hairpin structure can be monitored using rapid mixing from theta-glass emitters, the folding of renin substrate tetradecapeptide (RST) was investigated. RST is a 14 residue peptide that adopts a β-hairpin structure in aqueous solutions between pH = 4.0 and 6.0 and is unfolded between pH = 2.5 and 3.6.<sup>54</sup> The rate at which RST folds from an unfolded structure to the β-hairpin structure has not been previously measured. To measure this rate, acid denatured RST is mixed with aqueous ammonium acetate to induce folding using the theta-glass emitters at various reaction times. Mass spectra of an acidified aqueous RST solution (pH = 2.9) obtained using theta-glass emitters with ~244 and ~1465 nm o.d. tips are shown in Figure 4.5, panels a and b, respectively. Only the 3+ charge state is formed when the smaller ~244 nm tips are used (Figure 4.5a), but the 2+ charge state is also present at low abundance with the larger ~1465 nm tips (Figure 4.5b, average charge state = 2.89 ± 0.03). These results are consistent with the narrower charge state distributions observed for aMb and Trp-cage conformers when the smaller tips are used. Results from mixing the acidified RST solution with a 100 mM aqueous ammonium acetate solution at a 1:1 ratio prior to nanoESI (equilibrium; pH = 4.7) obtained using ~244 and ~1465 nm o.d. tips are shown in Figure 4.5, panels c and d, respectively. The 2+ charge state is predominantly formed (>93% of RST), resulting in an average charge state of 2.06 ± 0.00 and 2.04 ± 0.01 for the ~244 and ~1465 nm o.d. tips, respectively. The change in charge state from predominantly a 3+ (Figure 4.5a,b) to predominantly a 2+ (Figure 4.5c,d) is consistent with a change from an unfolded to a folded structure in solution.

Results from mixing the acidified RST solution with the ammonium acetate solution using the theta-glass emitters with flow rates that result in reaction times of between 1.0 and 9.1 μs (average of values obtained for aMb, cyt c, and Trp-cage) are shown in Figure 4.5, panels e–h in order of increasing reaction time. The average charge state decreases with increasing reaction time from 2.62 ± 0.04 at 1.0 μs to 2.04 ± 0.01 at 9.1 μs. For reaction times of 1.0–5.3 μs (Figures 4.5e–g), the average charge state of RST is higher than that resulting from the premixed solution at equilibrium (Figure 4.5c,d), but at 9.1 μs (Figure 4.5h), the average charge state is the same as that resulting from the premixed solution at equilibrium. These results indicate that the folding of RST does not reach equilibrium within ≤5.3 μs but does reach equilibrium within 9.1 μs. The folding time constant for the formation of the β-hairpin structure is obtained from the rapid mixing data at short times (Figure 4.5e–g) using eq 2. Folding time constants of 2.0 ± 0.3, 2.3 ±

0.2, and  $2.2 \pm 0.2$   $\mu$ s are obtained at reaction times of 1.0, 3.0, and 5.3  $\mu$ s, respectively. These values are the same to within error, and the average value is  $2.2 \pm 0.3$   $\mu$ s. These results indicate that RST folds from an unfolded structure to a  $\beta$ -hairpin structure within a few  $\mu$ s. To the best of our knowledge, this is the fastest folding event that has been directly monitored using a rapid mixing technique. These results indicate that fast folding events that occur on the low  $\mu$ s time scale can be readily investigated using rapid mixing from theta-glass emitters with mass spectrometry detection.

**4.3.5 Reaction Temperature.** Protein conformation and folding time constants depend on temperature.<sup>7,41</sup> Temperature regulated ESI capillaries have been used to measure the thermal stabilities of folded forms of proteins at equilibrium<sup>34,55-58</sup> as well as to investigate protein complexation<sup>59</sup> and aggregation<sup>57</sup> as a function of temperature. Thermal unfolding midpoint temperatures and association constants have been obtained using temperature regulated ESI capillaries that are the same as those obtained using traditional solution-phase techniques, such as fluorescence spectroscopy,<sup>55,56</sup> isothermal titration calorimetry,<sup>59</sup> and differential scanning calorimetry.<sup>57</sup> These results suggest that the temperature of the ESI droplets reflects that of the original solution. To obtain information about the droplet temperature in our rapid mixing experiments, the fraction of Trp-cage that is unfolded as a function of temperature was measured using temperature regulated ESI capillaries.<sup>34</sup> Mass spectra of the acidified Trp-cage solution mixed with the ammonium acetate solution at a 1:1 ratio prior to nanoESI (equilibrium; pH = 5.7) acquired at capillary temperatures of 25, 45, and 65 °C are shown in Figure 4.6, panel a. The relative abundance of the 3+ charge state increases with increasing solution temperature, consistent with thermal denaturation of Trp-cage in solution prior to nanoESI.

The relative ion abundances in a bimodal charge-state distribution directly reflect the populations of folded and unfolded structures. In cases where a bimodal charge-state distribution is not formed, information about folding is deduced from changes in the average charge state, but the abundances of the folded and unfolded populations are not obtained. The charge-state distribution of Trp-cage is not bimodal. Thus, it is not possible to obtain the abundances of the folded and unfolded forms of Trp-cage from these temperature-dependent experiments alone. This information can be obtained from the average charge state by comparing our results to those measured in solution using more conventional structural methods. The fraction of Trp-cage that is unfolded at 25 °C is 28% in aqueous buffer solutions.<sup>7</sup> If the solution temperature and the droplet temperature are similar, our results measured at 25 °C (Figure 4.6a) indicates that a 28% unfolded population corresponds to an average charge state of  $2.21 \pm 0.06$ . If Trp-cage is fully unfolded at pH = 3.4, then the fully unfolded form has an average charge state of  $2.83 \pm 0.06$  (Figure 4.4b). Assuming that the average charge state is a linear superposition of the charge states corresponding to the folded and unfolded conformers, the temperature dependent charge-state distributions in Figure 4.6, panel a can be used to obtain the relative abundances of these two conformers in these experiments. The average charge state (left axis) and the resulting fraction unfolded (right axis) of Trp-cage as a function of temperature are shown in Figure 4.6, panel b. The fraction of Trp-cage that is unfolded increases from 34% at 30 °C to 77% at 65 °C. The fraction of Trp-cage that is unfolded at 30 and 65 °C measured in solution previously is 35% and 80%, respectively.<sup>7</sup> All of the data measured in solution<sup>7</sup> and the data obtained using the average charge states reported here are the same to within 4% over this temperature range. The Trp-cage data were obtained using a flow rate that results in a 9.1  $\mu$ s reaction time. Thus, Trp-cage could fold or unfold if the droplet temperature was significantly lower or higher,

respectively, than the initial solution temperature. The close agreement between the extent of unfolding observed in our temperature-dependent theta-glass emitter experiments and those measured in solution using conventional structural methods indicates that the droplet temperature is similar to the temperature of the initial solution, and that any changes in the droplet temperature that may occur do not significantly affect folding time constants measured using our rapid mixing technique at room temperature.

#### 4.4 Conclusions

Rapid mixing of two solutions to measure reaction times as short as 1.0  $\mu$ s is demonstrated using theta-glass emitters combined with MS detection. Reaction times were measured by monitoring the pH induced folding of three proteins with folding time constants ranging from 4.1 to 57  $\mu$ s. The extent of folding that occurs in these experiments depends on the initial droplet size, which was controlled by varying the solution flow rate from 48–2880 pL/s, resulting in reaction times of between 1.0 and 22  $\mu$ s. The reaction times obtained for all three proteins at the same flow rates are nearly identical, indicating that reaction times can be accurately obtained from these protein folding measurements. These reaction times are upper limits to the lifetimes of the ESI droplets because some product formation likely occurs in the Taylor cone prior to droplet formation.<sup>21,22</sup> The shortest reaction time (1  $\mu$ s) achieved in these experiments is significantly shorter than that achieved using conventional mixers (8  $\mu$ s).<sup>2</sup> This 1.0  $\mu$ s reaction time is obtained using a 48 pL/s flow rate, which is 2000-fold less than the flow rate used to obtain the 8  $\mu$ s reaction time using a conventional mixer (~100 nL/s), demonstrating that substantially less sample is required to perform these fast mixing experiments.

A folding time constant of 2.2  $\mu$ s for the formation of the  $\beta$ -hairpin structure of RST was measured using rapid mixing with theta-glass emitters. This is the fastest folding event that has been directly monitored using a rapid mixing technique. Results from this experiment demonstrate that fast folding events that occur in as fast as a few microseconds can be readily investigated using rapid mixing from theta-glass emitters. Rapid mixing from theta-glass emitters also has the advantage of high chemical specificity and sensitivity provided by the MS detection, which should make it possible to measure complex reactions with multiple reaction products. This capability should make these devices generally applicable to measuring kinetic parameters for a diverse range of fast reactions. By using unimolecular reaction processes, such as protein folding, to establish reaction times at different flow rates, quantitative information about enhanced reaction rates for bimolecular or more complex reactions as a result of droplet evaporation<sup>60</sup> and droplet surface effects could be obtained.

## 4.5 References

- (1) Kolakowski, B.; Konermann, L. *Anal. Biochem.* **2001**, *292*, 107-114.
- (2) Wu, L.; Lapidus, L. *J. Anal. Chem.* **2013**, *85*, 4920-4924.
- (3) Vahidi, S.; Stocks, B. B.; Liaghati-Mobarhan, Y.; Konermann, L. *Anal. Chem.* **2013**, *85*, 8618-8625.
- (4) Zinck, N.; Stark, A.; Wilson, D. J.; Sharon, M. *ChemistryOpen* **2014**, *3*, 109-114.
- (5) Li, Y.; Zhang, D.; Feng, X.; Xu, Y.; Liu, B. *Talanta* **2012**, *88*, 175-180.
- (6) Matsumoto, S.; Yane, A.; Nakashima, S.; Hashida, M.; Fujita, M.; Goto, Y.; Takahashi, S. *J. Am. Chem. Soc.* **2007**, *129*, 3840-3841.
- (7) Qiu, L.; Pabit, S.; Roitberg, A.; Hagen, S. *J. Am. Chem. Soc.* **2002**, *124*, 12952-12953.
- (8) Lee, E. D.; Muck, W.; Henion, J. D.; Covey, T. R. *J. Am. Chem. Soc.* **1989**, *111*, 4600-4604.
- (9) Simmons, D. A.; Konermann, L. *Biochemistry* **2002**, *41*, 1906-1914.
- (10) Hong, C.; Tsai, F.; Shiea, J. *Anal. Chem.* **2000**, *72*, 1175-1178.
- (11) Shiea, J.; Chang, D.; Lin, C.; Jiang, S. *Anal. Chem.* **2001**, *73*, 4983-4987.
- (12) Shieh, I.; Lee, C.; Shiea, J. *J. Proteome Res.* **2005**, *4*, 606-612.
- (13) Chen, H.; Venter, A.; Cooks, R. G. *Chem. Commun.* **2006**, *19*, 2042-2044.
- (14) Tian, Y.; Chen, J.; Ouyang, Y.; Qu, G.; Liu, A.; Wang, X.; Liu, C.; Shi, J.; Chen, H.; Jiang, G. *Anal. Chim. Acta* **2014**, *814*, 49-54.
- (15) Prudent, M.; Rossier, J. S.; Lion, N.; Girault, H. H. *Anal. Chem.* **2008**, *80*, 2531-2538.
- (16) Miladinovic, S. M.; Fornelli, L.; Lu, Y.; Piech, K. M.; Girault, H. H.; Tsypin, Y. O. *Anal. Chem.* **2012**, *84*, 4647-4651.
- (17) Girod, M.; Moyano, E.; Campbell, D. I.; Cooks, R. G. *Chem. Sci.* **2011**, *2*, 501-510.
- (18) Miao, Z.; Chen, H.; Liu, P.; Liu, Y. *Anal. Chem.* **2011**, *83*, 3994-3997.
- (19) Badu-Tawiah, A. K.; Campbell, D. I.; Cooks, R. G. *J. Am. Soc. Mass Spectrom.* **2012**, *23*, 1077-1094.
- (20) Lee, J. K.; Kim, S.; Nam, H. G.; Zare, R. N. *Proc. Natl. Acad. Sci. U. S. A.* **2015**, *112*, 3898-3903.
- (21) Mortensen, D. N.; Williams, E. R. *Anal. Chem.* **2014**, *86*, 9315-9321.
- (22) Mark, L. P.; Gill, M. C.; Mahut, M.; Derrick, P. J. *Eur. J. Mass Spectrom.* **2012**, *18*, 439-446.
- (23) Mortensen, D. N.; Williams, E. R. *Anal. Chem.* **2015**, *87*, 1281-1287.
- (24) Fisher, C. M.; Kharlamova, A.; McLuckey, S. A. *Anal. Chem.* **2014**, *86*, 4581-4588.
- (25) Grimm, R. L.; Beauchamp, J. L. *Anal. Chem.* **2002**, *74*, 6291-6297.
- (26) Pfeifer, R. J.; Hendricks, C. D. *AIAA J.* **1968**, *6*, 496-502.
- (27) De La Mora J. F.; Loscertales, I. G. *J. Fluid Mech.* **1994**, *260*, 155-184.
- (28) Wilm, M. S.; Mann, M. *Int. J. Mass Spectrom. Ion Processes* **1994**, *136*, 167-180.
- (29) Tang, K.; Gomez, A. *J. Colloid Interface Sci.* **1996**, *184*, 500-511.
- (30) Li, Y.; Cole, R. B. *Anal. Chem.* **2003**, *75*, 5739-5746.
- (31) Mirza, U.; Cohen, S.; Chait, B. *Anal. Chem.* **1993**, *65*, 1-6.
- (32) Kaltashov, I.; Eyles, S. *Mass Spectrom. Rev.* **2002**, *21*, 37-71.
- (33) Liu, J.; Konermann, L. *J. Am. Soc. Mass Spectrom.* **2009**, *20*, 819-828.
- (34) Sterling, H. J.; Williams, E. R. *J. Am. Soc. Mass Spectrom.* **2009**, *20*, 1933-1943.
- (35) Konermann, L.; Rosell, F. I.; Mauk, A. G.; Douglas, D. J. *Biochemistry* **1997**, *36*, 6448-6454.

- (36) Jurchen, J. C.; Williams, E. R. *J. Am. Chem. Soc.* **2003**, *125*, 2817-2826.
- (37) Blakney, G. T.; Hendrickson, C. L.; Marshall, A. G. *Int. J. Mass Spectrom.* **2011**, *306*, 246-252.
- (38) *CRC Handbook of Chemistry and Physics*, 55th ed.; Weast, R. C., Ed.; CRC Press: Boca Raton, FL, 1974.
- (39) Schmidt, A.; Karas, M.; Dülcks, T. *J. Am. Soc. Mass Spectrom.* **2003**, *14*, 492-500.
- (40) Goto, Y.; Fink, A. L. P. *J. Mol. Biol.* **1990**, *214*, 803-805.
- (41) Gilmanshin, R.; Callender, R.; Dyer, R. *Nat. Struct. Biol.* **1998**, *5*, 363-365.
- (42) Ballew, R.; Sabelko, J.; Gruebele, M. *Proc. Natl. Acad. Sci. U. S. A.* **1996**, *93*, 5759-5764.
- (43) Callender, R.; Dyer, R.; Gilmanshin, R.; Woodruff, W. *Annu. Rev. Phys. Chem.* **1998**, *49*, 173-202.
- (44) Shastry, R. M. C.; Luck, S. D.; Roder, H. *Biophys. J.* **1998**, *74*, 2714-2721.
- (45) Konno, T. *Protein Sci.* **1998**, *7*, 975-982.
- (46) Stellwagen, E.; Babul, J. *Biochemistry* **1975**, *14*, 5135-5140.
- (47) Krantz, B.; Mayne, L.; Rumbley, J.; Englander, S.; Sosnick, T. *J. Mol. Biol.* **2002**, *324*, 359-371.
- (48) Kathuria, S. V.; Chan, A.; Graceffa, R.; Nobrega, R. P.; Matthews, C. R.; Irving, T. C.; Perot, B.; Bilsel, O. *Biopolymers* **2013**, *99*, 888-896.
- (49) Takahashi, S.; Yeh, S.; Das, T.; Chan, C.; Gottfried, D.; Rousseau, D. *Nat. Struct. Biol.* **1997**, *4*, 44-50.
- (50) Chan, C.; Hu, Y.; Takahashi, S.; Rousseau, D.; Eaton, W.; Hofrichter, J. *Proc. Natl. Acad. Sci. U. S. A.* **1997**, *94*, 1779-1784.
- (51) Yuill, E. M.; Sa, N.; Ray, S. J.; Hieftje, G. M.; Baker, L. A. *Anal. Chem.* **2013**, *85*, 8498-8502.
- (52) Munoz, V.; Thompson, P. A.; Hofrichter, J.; Eaton, W. A. *Nature* **1997**, *390*, 196-199.
- (53) Kubelka, J.; Hofrichter, J.; Eaton, W. A. *Curr. Opin. Struct. Biol.* **2004**, *14*, 76-88.
- (54) Oliveira, M. C. F.; Juliano, L.; Paiva, A. C. M. *Biochemistry* **1977**, *16*, 2606-2611.
- (55) Benesch, J.; Sobott, F.; Robinson, C. *Anal. Chem.* **2003**, *75*, 2208-2214.
- (56) Geels, R. B. J.; Calmat, S.; Heck, A. J. R.; van der Vies, S. M.; Heeren, R. M. A. *Rapid Commun. Mass Spectrom.* **2008**, *22*, 3633-3641.
- (57) Wang, G.; Abzalimov, R. R.; Kaltashov, I. A. *Anal. Chem.* **2011**, *83*, 2870-2876.
- (58) Chen, L. C.; Rahman, M. M.; Hiraoka, K. *J. Am. Soc. Mass Spectrom.* **2014**, *25*, 1862-1869.
- (59) Daneshfar, R.; Kitova, E. N.; Klassen, J. S. *J. Am. Chem. Soc.* **2004**, *126*, 4786-4787.
- (60) Badu-Tawiah, A. K.; Campbell, D. I.; Cooks, R. G. *J. Am. Soc. Mass Spectrom.* **2012**, *23*, 1461-1468.

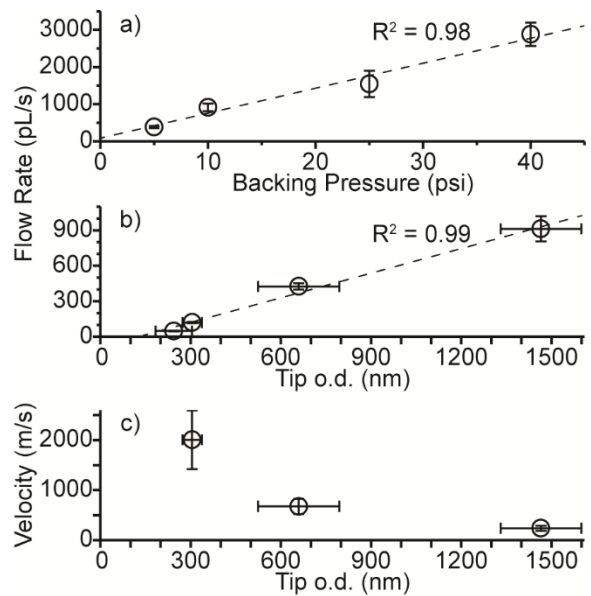


**Figure 4.1.** Solution flow rates as a function of (a) the backing pressure applied to the solutions during nanoESI using theta-glass emitters with ~1465 nm o.d. tips and (b) the o.d. of the tips of the theta-glass emitters using a 10 psi backing pressure. Dashed lines are linear fits to the data. (c) Solution velocities at the tips of the theta-glass emitters as a function of the tip o.d.

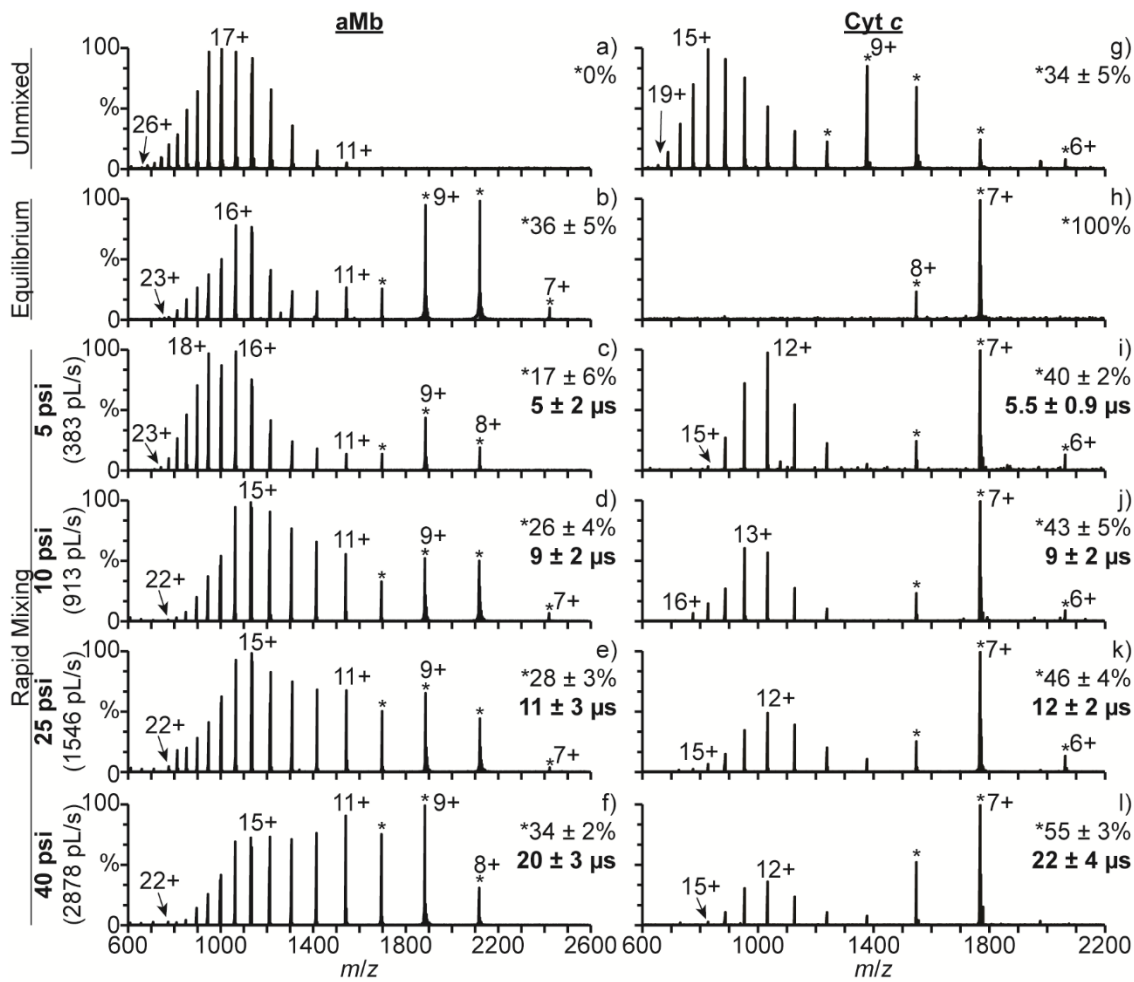


**Figure 4.2.** Mass spectra of (a) an acidified aqueous aMb solution ( $\text{pH} = 2.9$ ), (b) the acidified aMb solution mixed with a 100 mM aqueous ammonium acetate solution at a 1:1 ratio prior to nanoESI (equilibrium;  $\text{pH} = 4.7$ ), the acidified aMb solution mixed with the ammonium acetate solution using the theta-glass emitters and backing pressures of (c) 5, (d) 10, (e) 25, and (f) 40 psi, (g) an acidified aqueous cyt c solution ( $\text{pH} = 2.8$ ), (h) the acidified cyt c solution mixed with the ammonium acetate solution at a 1:1 ratio prior to nanoESI (equilibrium;  $\text{pH} = 4.4$ ), and the acidified cyt c solution mixed with the ammonium acetate solution using the theta-glass emitters and backing pressures of (i) 5, (j) 10, (k) 25, and (l) 40 psi. Inset percentages are the relative abundances of the charge states corresponding to folded protein conformers (denoted with \*).

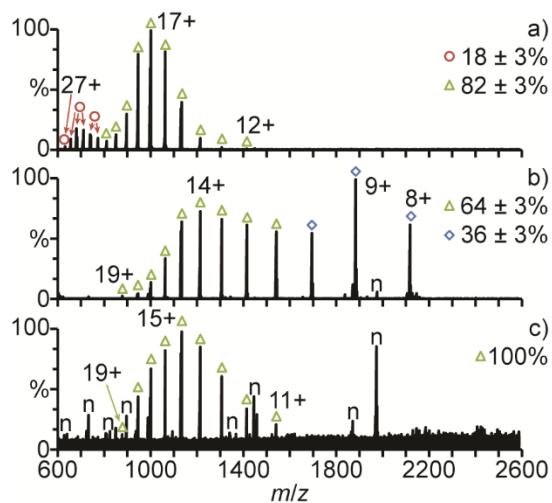


**Figure 4.3.** Mass spectra of (a) an acidified aqueous aMb solution ( $\text{pH} = 2.9$ ) and the acidified aMb solution mixed with a 100 mM aqueous ammonium acetate solution (b) at a 1:1 ratio prior to nanoESI (equilibrium;  $\text{pH} = 4.7$ ) and (c) using the theta-glass emitters. (n) denotes noise. All data were acquired using  $\sim 305$  nm o.d. tips.

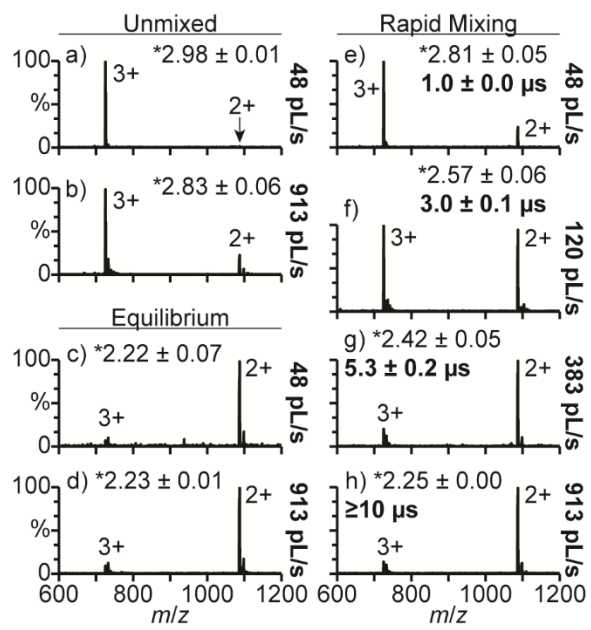


**Figure 4.4.** Mass spectra of (a,b) an acidified aqueous Trp-cage solution ( $\text{pH} = 3.4$ ) and (c,d) the acidified Trp-cage solution mixed with a 100 mM aqueous ammonium acetate solution at a 1:1 ratio prior to nanoESI (equilibrium;  $\text{pH} = 5.7$ ) acquired using (a,c)  $\sim 244$  and (b,d)  $\sim 1465$  nm o.d. tips. Mass spectra of the acidified Trp-cage solution mixed with the ammonium acetate solution using the theta-glass emitters at flow rates of (e) 48, (f) 120, (g) 383, and (h) 913  $\text{pL/s}$ . (\*) denotes average charge state.

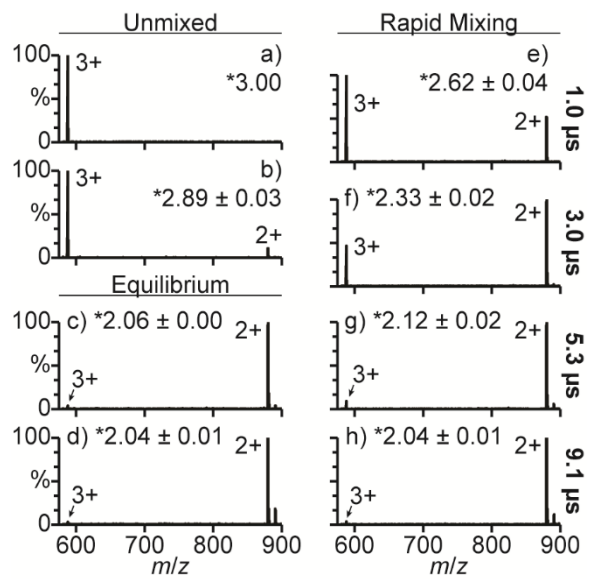


**Figure 4.5.** Mass spectra of (a,b) an acidified aqueous RST solution ( $\text{pH} = 2.9$ ) and (c,d) the acidified RST solution mixed with a 100 mM aqueous ammonium acetate solution at a 1:1 ratio prior to nanoESI (equilibrium;  $\text{pH} = 4.7$ ) acquired using (a,c)  $\sim 244$  and (b,d)  $\sim 1465$  nm o.d. tips. Mass spectra of the acidified RST solution mixed with the ammonium acetate solution using the theta-glass emitters with flow rates that result in reaction times of (e) 1.0, (f) 3.0, (g) 5.3, and (h) 9.1  $\mu\text{s}$ . (\*) denotes average charge state.

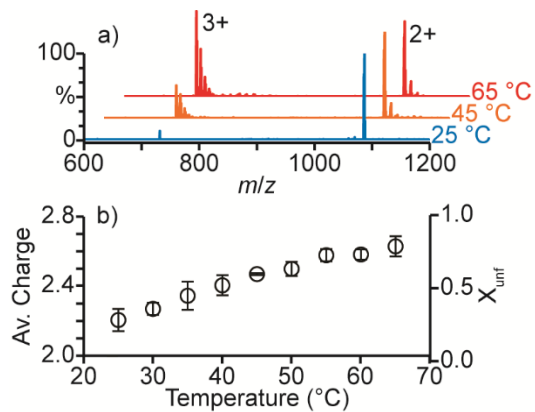


**Figure 4.6.** (a) Mass spectra of an acidified aqueous Trp-cage solution mixed with a 100 mM aqueous ammonium acetate solution at a 1:1 ratio prior to nanoESI (equilibrium, pH = 5.7) acquired at capillary temperatures of 25 (blue), 45 (orange), and 65 (red) °C. (b) The average charge state (left axis) and fraction unfolded ( $X_{unf}$ , right axis) of Trp-cage resulting from this solution as a function of the capillary temperature.

## Chapter 5

# Surface-Induced Protein Unfolding in Submicron Electrospray Emitters

This Chapter is reproduced with permission from  
Mortensen, D.M.; Williams, E.R.  
“Surface-Induced Protein Unfolding in  
Submicron Electrospray Emitters”  
*Submitted to Analytical Chemistry 2016*  
© 2016 Royal Society of Chemistry

### 5.1 Introduction

Electrospray ionization (ESI) mass spectrometry (MS) is widely used for protein identification and structural analysis, including identifying sites of posttranslational modifications.<sup>1-3</sup> Information about protein conformation can be obtained from the charge-state distributions produced by ESI. Ions formed from solutions in which proteins have folded globular structures are less highly charged than those formed from solutions in which proteins are unfolded.<sup>4,5</sup> The relative abundances of different protein conformers in solution can be obtained by modelling the different charge-state distributions resulting from these conformers.<sup>4,6</sup> Other factors that affect the extent of charging in ESI include the solution pH and protein isoelectric point (pI),<sup>7</sup> the solution surface tension,<sup>8,9</sup> the solvent and analyte basicities,<sup>10-12</sup> and instrumental parameters.<sup>13,14</sup>

High charge state ions produced by ESI are advantageous because they can be detected more readily on charge detection mass spectrometers, such as FTMS instruments,<sup>15,16</sup> and they fragment more readily, often resulting in increased structural information in tandem MS.<sup>17-19</sup> High charge state protein ions can be obtained by adding supercharging reagents to solutions in which proteins have either denatured<sup>8,20-26</sup> or native<sup>9,26-32</sup> structures. In native MS, high charge states can also be obtained by adding trivalent metal ions to the analyte solution,<sup>33</sup> by exposing the ESI droplets to either acidic<sup>34</sup> or basic<sup>35</sup> vapors, or by electrothermal supercharging.<sup>36-38</sup> In electrothermal supercharging, ions are formed from buffered aqueous solutions using high spray potentials which result in collisional heating of the ESI droplets and protein unfolding inside the ESI droplet.<sup>36,38</sup>

Increased charging has also been reported for protein and peptide ions when the outer diameter (o.d.) of the tips of the ESI emitters is reduced. For example, the average charge state of angiotensin I ions formed from a denaturing solution increased from ~1.7 to ~2.8 when the tip o.d. was decreased from ~5 µm to ~1 µm.<sup>39</sup> Increased charging and narrower charge-state distributions were also reported for cytochrome *c* and ubiquitin ions formed from acidified denaturing solutions with <100 nm o.d. tips compared to those generated with ~1 µm o.d. tips.<sup>40</sup> The increased charging obtained with decreasing tip o.d. was attributed to smaller droplets with higher charge densities being formed from the smaller tips.<sup>39,40</sup> Electrospray emitters with adjustable orifice sizes have also been reported.<sup>41,42</sup> The horizontal gap width was varied between 1 and >10 µm by adjusting the positions of two triangular-shaped silicon chips.

Improved signal-to-noise ratios and higher charging with decreasing orifice size were reported for angiotensin I<sup>42</sup> and insulin chain B<sup>41</sup> ions formed from acidified denaturing solutions.

Recently, increased charging and narrower charge-state distributions with decreased tip o.d. were reported for apo-myoglobin and Trp-cage ions formed from acidified aqueous solutions using double-barrel wire-in-a-capillary emitters (theta-glass emitters) with ~1.5 μm to ~250 nm o.d. tips.<sup>43</sup> Bimodal charging was also reported for apo-myoglobin ions with the smaller tips, consistent with a fraction of the protein population adopting a highly unfolded structure.<sup>43</sup> The formation of this highly unfolded conformer was attributed to protein molecules in solution interacting with the surface of the tips of the emitters prior to nanoESI.<sup>43</sup> The relative abundance of this highly unfolded conformer was constant with spray potential between 450 and 1050 V, indicating that this conformer was not formed as a result of the higher electric field obtained with the smaller tip size.<sup>43</sup>

Nano-ESI emitters are generally prepared from borosilicate glass capillaries<sup>39,40,43</sup> or other forms of silicon<sup>41,42</sup> that contain silanol groups at the surface.<sup>44</sup> In aqueous solutions, a fraction of the silanol groups is deprotonated, resulting in a net negative charge on the glass surface that depends on the solution pH.<sup>44</sup> Interactions between positively charged proteins in solution and negatively charged glass surfaces result in longer transport times for protein and DNA molecules than for solvent molecules through 5 to 96 nm diameter nanochannels in silica membranes.<sup>45-48</sup> In these experiments, the solutions are electrokinetically transported, and the transport time of molecules through the pores depends on the charge of the molecules and on the charge density on the surface of the nanochannels.<sup>48</sup> This technique has been used to detect single protein and DNA molecules.<sup>45-48</sup>

Here, theta-glass emitters with micron and submicron o.d. tips prepared from borosilicate glass capillaries are used to form protein ions from aqueous solutions using nanoESI. With the submicron o.d. tips, distributions of highly charged ions are formed for proteins that are positively charged in solution but not for proteins that are negatively charged in solution. These results indicate that Coulombic attraction between the positively charged proteins and the negatively charged glass surfaces in the small tips of these emitters results in unfolding of a fraction of the protein population prior to nanoESI. These results show another way to produce highly charged ions that does not require the addition of other chemicals either to the analyte solution or in the gas phase.

## 5.2 Experimental Section

Experiments were performed using a 9.4 T Fourier-transform ion cyclotron resonance mass spectrometer that is described elsewhere.<sup>49</sup> Ions are formed by nanoelectrospray ionization using theta glass capillaries (Warner Instruments, LLC, Hamden, CT) with tips pulled to a small o.d. using a model p-87 Flaming/Brown micropipette puller (Sutter Instruments Co., Novato, CA). Electron micrographs of the tips of the emitters mounted on carbon tape (Figure 5.1) are obtained at 10,000-times magnification with a TM-1000 scanning electron microscope (Hitachi High-Technologies Co., Tokyo, Japan). Grounded platinum wires are brought into contact with the solutions in the emitters, and nanoESI is initiated by applying about a -700 V potential to the heated capillary of the ESI interface. Data are acquired using a Predator data station,<sup>50</sup> and mass spectra are background subtracted. Average charge states are computed as abundance weighted sums of the individual charge states. All reported uncertainties are standard deviations determined from triplicate measurements.

Ammonium acetate, equine apo- and holo-myoglobin, equine cytochrome *c*, and bovine  $\beta$ -lactoglobulin A are obtained from Sigma-Aldrich (St. Louis, MO), and glacial acetic acid is from Fisher Scientific (Fair Lawn, NJ). Solutions are prepared with a 10  $\mu\text{M}$  analyte concentration in 18.2 M $\Omega$  water from a Milli-Q water purification system (Millipore, Billerica, MA).

### 5.3 Results and Discussion

**5.3.1 Charging of apo-Myoglobin and Tip Size.** Mass spectra of an acidified aqueous aMb solution ( $\text{pH} = 2.9$ ) obtained using theta-glass emitters with  $1465 \pm 134$ ,  $305 \pm 32$ , and  $244 \pm 61$  nm o.d. tips are shown in Figure 5.2a-c, respectively. In aqueous solutions, apo-myoglobin (aMb) adopts a globular structure similar to that of native holo-myoglobin between  $\text{pH} = 5$  and 7, a less compact globular structure at  $\text{pH} = 4$ , and a partially unfolded structure below  $\text{pH} = 3$ .<sup>51</sup> A single charge-state distribution center at  $17^+$  is formed with the  $\sim 1465$  nm o.d. tips (Figure 5.2a). The breadth and position of this distribution is consistent with aMb adopting a range of unfolded structures in this solution. With the smaller  $\sim 305$  nm o.d. tips (Figure 5.2b), the charge-state distribution is bimodal, with one distribution centered at  $17^+$ , corresponding to partially unfolded conformers and comprising  $82 \pm 2\%$  of aMb, and another distribution centered at  $25^+$ , comprising  $18 \pm 2\%$ . The distribution centered at  $25^+$  is consistent with the formation of a distribution of more highly unfolded conformers. With the even smaller  $\sim 244$  nm o.d. tips (Figure 5.2c), the relative abundance and maximum charge state of the highly unfolded conformers increase to  $37 \pm 2\%$  and to the  $29^+$  charge state, respectively. The surface area relative to the solution volume in the tips of the nanoESI emitters increases with decreasing tip size, and the surfaces in these tips likely cause changes to the protein structure for a fraction of the population prior to nanoESI.

To compare the charging obtained with single-barrel emitters and theta-glass emitters, single-barrel borosilicate emitters with  $1448 \pm 135$  and  $269 \pm 29$  nm o.d. tips were prepared (Figure 5.3a and 5.3b, respectively). In the mass spectra of aMb in acidified solution ( $\text{pH} = 2.9$ ) obtained with the  $1448 \pm 135$  nm o.d. tips (Figure 5.3c), only a single charge-state distribution centered at  $17^+$  is observed. This distribution is consistent with aMb adopting a range of unfolded conformers in this solution and is very similar to the charge-state distribution centered at  $17^+$  obtained with the  $\sim 1465$  nm o.d. tip theta-glass emitters (Figure 5.2a). With the  $269 \pm 29$  nm o.d. tips (Figure 5.3d), the charge-state distribution is bimodal, with distributions centered at  $17^+$  and  $23^+$ , comprising  $81 \pm 3\%$  and  $19 \pm 3\%$  of aMb, respectively. These charge-state distributions are consistent with partially and highly unfolded conformers, respectively. The relative abundance of the highly unfolded conformers obtained with the single-barrel emitters with  $269 \pm 29$  nm o.d. tips ( $19 \pm 3\%$ , Figure 5.3d) is less than that obtained with the theta-glass emitters with the  $\sim 244$  nm o.d. tips ( $37 \pm 2\%$ , Figure 5.2c). The greater extent of highly unfolded conformers obtained with the theta-glass emitters is likely due to the central divider resulting in a greater surface area in the tips of these emitters compared to that in the tips of single-barrel emitters with similar tip sizes. This result is consistent with protein-surface interactions resulting in protein unfolding prior to nanoESI.

**5.3.2 Charging of Cytochrome *c* and Tip Size.** To determine if high charge state distributions of other proteins can also be produced with the smaller tip sizes, similar experiments were performed with cytochrome *c* (cyt *c*). In aqueous solutions containing  $<0.2$  M

salt concentrations, cyt *c* has a native folded structure between pH = 3 and 7 and is partially unfolded at pH = 2.<sup>52,53</sup> Between pH = 2 and 3, the folded and partially unfolded structures exist in equilibrium.<sup>53</sup> Mass spectra of an acidified aqueous cyt *c* solution (pH = 2.8) obtained using theta-glass emitters with ~1465, ~305, and ~244 nm o.d. tips are shown in Figure 5.4a-c, respectively. The charge-state distribution is bimodal with the ~1465 nm o.d. tips (Figure 5.4a), with charge-state distributions centered at 9+ and 15+, comprising 34 ± 5% and 66 ± 5% of the population, respectively. These distributions are consistent with folded and partially unfolded structures, respectively. With the smaller ~305 nm o.d. tips (Figure 5.4b), charge-state distributions centered at 9+ and 14+ are observed, comprising 31 ± 3% and 41 ± 3% of cyt *c*, respectively. These distributions are similar to those obtained with the larger ~1465 nm o.d. tips (Figure 5.4a) and are consistent with folded and partially unfolded conformers, respectively. In addition, a third distribution centered at 18+ is formed, comprising 28 ± 5% of the population. This third distribution is consistent with the formation of more highly unfolded cyt *c* conformers. With the smallest ~244 nm o.d. tips (Figure 5.4c), the relative abundance and maximum charge state of the highly unfolded conformers increase to 37 ± 4% and to the 21+ charge state, respectively. These results are consistent with an increase in the extent of protein-surface interactions occurring as a result of decreasing the tip o.d.

The relative abundance of the folded cyt *c* conformer decreases by only ~6% when the tip o.d. is reduced from ~1465 nm (34 ± 5%, Figure 5.4a) to ~244 nm (28 ± 5%, Figure 5.4c), but the relative abundance of the partially unfolded conformers decreases by ~31% with this reduction in tip size (66 ± 5% and 35 ± 9% in Figure 5.4a and 5.4c, respectively). These results indicate that the population of highly unfolded conformers is formed predominantly from the partially unfolded conformers and that only a small fraction of the folded conformer is unfolded by the surfaces in these experiments. Partially unfolded proteins may interact more strongly with the glass surfaces than fully folded proteins because of their greater surface areas, which may result in even more unfolding. The transition from a folded form to an unfolded form may also have a higher activation barrier compared to the transition from a partially unfolded form to a highly unfolded form of the population.

The charge-state distribution corresponding to partially unfolded structures is centered at 15+ with the ~1465 nm o.d. tips (Figure 5.4a). With the smaller ~305 and ~244 nm o.d. tips (Figure 5.4b and 5.4c, respectively), this distribution is centered at 14+. This shift to lower charge with decreasing tip size may suggest that the broad charge-state distribution obtained for the partially unfolded conformers with the larger ~1465 nm o.d. tips is composed of unresolved charge-state distributions resulting from a distribution of partially unfolded conformers. The partially unfolded conformers that result in higher charging with the larger tips likely unfold more readily with the smaller tips, resulting in a shift in the partially folded distribution in Figure 5.4b to slightly lower charge. These results suggest that more information about the number of solution-phase protein conformers can be obtained with multiple tip sizes than with a single tip size.

**5.3.3 Mechanism of Increased Charging with Decreasing Tip Size.** To confirm that the high charge-state distributions obtained with the submicron o.d. tips result from protein unfolding, experiments were performed with holo-myoglobin (hMb). In aqueous solutions, hMb adopts a native structure between pH = 5 and 7,<sup>54</sup> a less-compact globular structure around pH = 3,<sup>54</sup> and a partially unfolded structure with no heme group attached at lower pH.<sup>55</sup> NanoESI of hMb in a slightly acidified aqueous solution (pH = 4.1) with a ~1465 nm o.d. tip (Figure 5.5a)

results in the 7–12+ charge states with an average charge state of  $9.2 \pm 0.1$ . These results are consistent with hMb adopting folded conformations in this solution. With smaller ~305 nm o.d. tips (Figure 5.5b), the average charge state of hMb increases to  $10.6 \pm 0.3$  and the 8–12+ charge states of aMb are formed, comprising  $5 \pm 2\%$  of myoglobin. Some structural changes to hMb must occur in order for loss of the heme to occur with the smaller tips. The presence of aMb, which is formed by loss of the heme group from hMb, indicates that a fraction of myoglobin is partially unfolded with the ~305 nm o.d. tips. Both the higher charging and the loss of heme that occur with the smaller tips indicate that the smaller tips induce a structural change in the protein. The similar distributions of charge states for hMb and aMb suggest that the formation of higher charge states and the loss of heme are related. These results also indicate that extensive unfolding of the protein does not occur. The production of aMb observed here with the small ~305 nm o.d. tips but not with the large ~1465 nm o.d. tips is consistent with the high charge states obtained with the small tip sizes for aMb (Figures 5.2b, 5.2c, and 5.3d) and for cyt c (Figure 5.4b and 5.4c) forming as a result of destabilization and some unfolding of the proteins in the tips of the emitters.

Results with  $\beta$ -lactoglobulin A ( $\beta$ -lac A), which aggregates upon denaturation,<sup>56,57</sup> provide additional support for increased charging at small tip size resulting from protein unfolding. Mass spectra of  $\beta$ -lac A in a slightly acidified aqueous solution ( $\text{pH} = 4.1$ ) with ~1465 and ~305 nm o.d. tips are shown in Figure 5.5c and 5.5d, respectively. With the larger ~1465 nm o.d. tips (Figure 5.5c), the 8–12+ charge states of  $\beta$ -lac A are formed and the average charge state is  $9.4 \pm 0.0$ . With the smaller ~305 nm o.d. tips (Figure 5.5d), the average charge state is  $10.9 \pm 0.1$  (8–15+ charge states), and the 14–16+ charge states of  $\beta$ -lac A dimers are formed, comprising  $17 \pm 8\%$  of the population. The formation of these dimers likely results from the aggregation of unfolded monomers, consistent with protein unfolding occurring with the smaller tips.

Both myoglobin ( $\text{pI} = 7.4$ )<sup>58</sup> and cyt c ( $\text{pI} = 10.3$ )<sup>59</sup> have net positive charge in the  $\text{pH} \leq 4.1$  solutions used to obtain the data in Figures 5.2–5. The nanoESI emitters are borosilicate glass, which has a surface that is negatively charged in these aqueous solutions.<sup>44</sup> Coulombic attraction between positively charged protein molecules in solution and the negatively charged glass surfaces in the tips of the nanoESI emitters likely leads to protein-surface interactions that destabilize protein structure, an effect that should be more pronounced with smaller tip sizes owing to the higher surface-to-volume ratios. To provide evidence for this mechanism, results are obtained from buffered aqueous solutions with  $\text{pH}$  values both above and below the  $\text{pI} = 7.4$  of hMb. In a 100 mM aqueous ammonium acetate solution ( $\text{pH} = 6.7$ ), hMb has a net positive charge. NanoESI of this solution with a ~1465 nm o.d. tip (Figure 5.6a) results in the 7–9+ charge states with an average charge state of  $8.0 \pm 0.1$ . These results are consistent with hMb adopting a folded native-like structure in solution. With a smaller ~305 nm o.d. tip (Figure 5.6b), there is no 7+ charge state and the average charge state is shifted higher to  $8.5 \pm 0.0$ . These results are consistent with a change to a slightly unfolded protein structure occurring with the smaller tips.

In a 100 mM aqueous ammonium bicarbonate solution ( $\text{pH} = 8.3$ ), hMb is predominantly negatively charged. Results obtained for this solution with ~1465 and ~305 nm o.d. tips are shown in Figure 5.6c and 5.6d, respectively. The 7–9+ charge states are formed and the average charge state is the same to within error for each tip size ( $8.2 \pm 0.1$  and  $8.1 \pm 0.2$  in Figure 5.6c and 5.6d, respectively). These results are nearly identical to those obtained for the ammonium acetate solution with the larger tip size (Figure 5.6a) and are consistent with hMb adopting a

folded native-like structure in solution. These results indicate that reducing the tip o.d. within this range of tip sizes does not result in a measurable change to the protein structure when the solution pH (8.3) is greater than the protein pI (7.4). The stability of the folded hMb conformer in aqueous ammonium bicarbonate solutions is the same as that in aqueous ammonium acetate solutions with similar buffer concentrations.<sup>37</sup> Thus, the effects of tip size on the charge state distribution at pH = 6.7 but not at pH = 8.3 is not due to a difference in protein stability in these solutions. These results are consistent with the increased charging and protein unfolding obtained by decreasing the tip o.d. resulting from Coulombic attraction between positively charged protein molecules in solution and the negatively charged glass surfaces in the tips of the nanoESI emitters.

Effects of ionic strength on the increased charging at small tip size was investigated. Mass spectra of hMb with the ~1465 and ~305 nm o.d. tips were acquired from 10, 100 and 500 mM aqueous ammonium acetate solutions in which hMb has a net positive charge. The average charge state is  $8.0 \pm 0.1$  for each ammonium acetate solution with the ~1465 nm o.d. tips (Appendix C, Figure C.1a-c, respectively). With the ~305 nm o.d. tips, the average charge state is  $8.5 \pm 0.0$ ,  $8.5 \pm 0.0$  and  $8.3 \pm 0.1$  for the 10, 100 and 500 mM ammonium acetate solutions, respectively (Appendix C, Figure C.1d-f). The slightly lower average charge with the 500 mM solution may be due to increased ammonium-surface interactions in the tips of the emitters. Ammonium-surface interactions could lower the effective net charge on the surface of the emitters,<sup>60</sup> which could result in less unfolding occurring prior to nanoESI. The higher ammonium acetate concentration may also increase the stability of the folded conformation, resulting in less conformational changes occurring. Spectra were also acquired from 10, 100 and 500 mM aqueous ammonium bicarbonate solutions in which hMb has a net negative charge (Appendix C, Figure C.2). The average charge state of hMb ions is the same to within error at each concentration and with both tip sizes, consistent with no destabilizing interactions between the negatively charged proteins and tip surfaces occurring.

Support for protein unfolding as a result of Coulombic attraction between the proteins and the glass surfaces is also obtained using 100 mM aqueous ammonium acetate solutions (pH = 6.7) containing either predominantly negatively or positively charged proteins.  $\beta$ -lac A (pI = 5.1)<sup>61</sup> is predominantly negatively charged in aqueous solutions at pH = 6.7. Results obtained for  $\beta$ -lac A in aqueous ammonium acetate with ~1465 and ~305 nm o.d. tips are shown in Figure 5.7a and 5.7b, respectively. The 7–9+ charge states are formed and the average charge state is the same at each tip size ( $8.0 \pm 0.3$  and  $8.0 \pm 0.2$  in Figure 5.7a and 5.7b, respectively).  $\beta$ -lac A adopts a globular native structure between pH = 2.0 and 6.2 and a slightly unfolded globular structure at pH = 7.5.<sup>62</sup> The results in Figure 5.7a and 5.7b are consistent with  $\beta$ -lac A adopting a folded conformation in solution. The similar results obtained with the different tip sizes indicate that reducing the tip o.d. from ~1465 to ~305 nm does not result in measurable unfolding occurring for  $\beta$ -lac A in this solution.

Cyt c (pI = 10.3)<sup>59</sup> is predominantly positively charged in aqueous solutions at pH = 6.7. Results obtained for cyt c in a 100 mM aqueous ammonium acetate solution with ~1465 and ~305 nm o.d. tips are shown in Figure 5.7c and 5.7d, respectively. The 6–8+ charge states are formed with the ~1465 nm o.d. tips (Figure 5.7c), consistent with cyt c adopting a folded conformation in solution. With the ~305 nm o.d. tips (Figure 5.7d), charge states corresponding to both folded (6–8+) and unfolded (9–13+) conformers are formed, and the unfolded conformers comprise  $9 \pm 6\%$  of the population. The formation of ions corresponding to unfolded cyt c with the ~305 nm o.d. tips is consistent with the positively charged cyt c molecules

interacting with the negatively charged glass surfaces in the smaller tips of these emitters, which results in some protein unfolding.

**5.3.4 Comparison with Previous Results.** Increased charging with decreasing tip size has previously been attributed to smaller droplets with higher charge densities being formed with decreasing tip size.<sup>39,40</sup> However, the results from those studies are also consistent with surface-induced unfolding in the tips of the emitters. For example, nanoESI mass spectra of cyt *c* in a denaturing solution obtained with ~1  $\mu\text{m}$  and 58 nm o.d. tips were reported.<sup>40</sup> The mass spectrum obtained with the larger ~1  $\mu\text{m}$  o.d. tip shows a single charge-state distribution centered at 15+, whereas there is a bimodal charge-state distribution centered at 11+ and 17+ with the smaller 58 nm o.d. tip. The formation of highly charged droplets with the smaller tip size would not likely result in the formation of a distribution centered at a lower charge state (11+) than that obtained with the larger tip size (15+), nor would a bimodal charge-state distribution be expected. It is likely that the distribution centered at 15+ with the ~1  $\mu\text{m}$  o.d. tip corresponds to a distribution of partially unfolded conformers. The distribution centered at 17+ obtained with the 58 nm o.d. tip may correspond to highly unfolded structures resulting from surface-induced unfolding in the tip of the emitter prior to nanoESI, which shift the other distribution lower to 11+ due to partially unfolded conformers that are not substantially unfolded by the surface in the tip of the emitter.

It is interesting to note the differences in the results obtained for cyt *c* in a denaturing solution in the previous study to those obtained here with the 1% aqueous acetic acid solution (Figure 5.4). A bimodal charge-state distribution is obtained here with the micron o.d. tips, whereas a highly charged single distribution was reported with a micron o.d. tip previously,<sup>40</sup> indicating that the solution used here is less denaturing than that used previously. However, the charge-state distribution obtained here for the highly unfolded conformers with the ~244 nm o.d. tips (Figure 5.4c) is centered at a higher charge state (19+) and has a higher maximum charge state (21+) than that obtained previously with the more denaturing solution and an even smaller 58 nm o.d. tip (high charge state distribution centered at 17+ with a maximum charge state of 20+).<sup>40</sup> Higher charging is likely obtained here because the surface tension of the 1% aqueous acetic acid solution used here (~65 dyn cm<sup>-1</sup>)<sup>63</sup> is higher than that of the 30/70/0.1 water, methanol, acetic acid solution used previously (~27 dyn cm<sup>-1</sup>).<sup>64</sup> Preferential evaporation of the more volatile solvents will enrich both solutions in acetic acid, and pure acetic acid has a surface tension of ~27 dyn cm<sup>-1</sup>.<sup>63</sup> These results indicate that the average surface tension in the droplets formed from the solution used here is higher than the average surface tension in the droplets formed from the solution used previously. Charging in ESI increases with increasing surface tension of the droplets.<sup>8,9</sup>

It was argued previously that the increased charging obtained with decreasing tip size for protein and peptide ions does not result from conformational changes because increased charging with decreasing tip size was obtained for angiotensin I, a 10 residue peptide, and it was assumed that this peptide is too small to have significant secondary structure.<sup>39,65</sup> However, angiotensin I has a solution-phase structure containing a hydrophobic core,<sup>66</sup> and structural transitions have been reported for peptides containing as few as 5 residues.<sup>67</sup> Similar shifts in charge reported for angiotensin I with ~1 and ~5  $\mu\text{m}$  o.d. tips<sup>39</sup> were used to monitor changes to the solution-phase structures of both the 20 residue “mini-protein” Trp-cage and the 14 residue peptide renin substrate tetradecapeptide.<sup>43</sup> These results indicate that the increased charging with decreasing tip size obtained for angiotensin I likely results from surface-induced unfolding in the tips of the emitters prior to nanoESI.

## 5.4 Conclusions

The charge-state distributions of protein ions formed by nanoESI with borosilicate glass capillary emitters with micron and submicron o.d. tips are compared. High charge states are formed with the submicron o.d. tips for proteins that are positively charged in solution, and additional high-charge-state distributions are often observed. There is a single charge-state distribution for hMb with the micron o.d. tips that is consistent with a folded hMb structure, but with the submicron o.d. tips, the average charge state of the hMb ions increases and some aMb is produced. These results indicate that a fraction of the protein population is partially unfolded with the smaller tips. Higher charging with smaller emitter tips occurs for proteins that are positively charged in solution but not for proteins that are negatively charged in solution. These results indicate that the increased charging and protein unfolding obtained with decreasing tip size for proteins that are positively charged in solution results from Coulombic attraction to the negatively charged glass surfaces in the submicron o.d. tips prior to nanoESI. More unfolding occurs for proteins that are partially unfolded than for proteins that are folded. Partially unfolded proteins may interact more with the glass surfaces than folded proteins as a result of their greater surface areas, which may result in even more unfolding. The transition from a folded structure to an unfolded structure may also have a higher activation barrier than the transition from a partially unfolded structure to a highly unfolded structure.

Results from these experiments demonstrate a novel method for producing highly charged protein ions from aqueous solutions that does not require exposing the proteins to additional chemicals, either in solution or in the gas phase. These results also clearly show that investigations into how various factors affect charging of gaseous protein ions formed by ESI, such as addition of supercharging reagents, must take into account the effects of ESI emitter tip size on destabilizing protein conformation in solution prior to droplet formation. Protein-surface interactions may also play a role in the commonly reported phenomenon that more highly charged protein ions are often produced as positive ions rather than negative ions.

## 5.5 References

- (1) Kruppa, G.; Schoeniger, J.; Young, M. *Rapid Commun. Mass Spectrom.* **2003**, *17*, 155-162.
- (2) Aebersold, R.; Mann, M. *Nature* **2003**, *422*, 198-207.
- (3) Pan, J.; Borchers, C. H. *Proteomics* **2013**, *13*, 974-981.
- (4) Kaltashov, I.; Eyles, S. *Mass Spectrom. Rev.* **2002**, *21*, 37-71.
- (5) Liu, J.; Konermann, L. *J. Am. Soc. Mass Spectrom.* **2009**, *20*, 819-828.
- (6) Konermann, L.; Rosell, F. I.; Mauk, A. G.; Douglas, D. J. *Biochemistry* **1997**, *36*, 6448-6454.
- (7) Pan, P.; Gunawardena, H. P.; Xia, Y.; McLuckey, S. A. *Anal. Chem.* **2004**, *76*, 1165-1174.
- (8) Iavarone, A. T.; Williams, E. R. *J. Am. Chem. Soc.* **2003**, *125*, 2319-2327.
- (9) Sterling, H. J.; Cassou, C. A.; Trnka, M. J.; Burlingame, A. L.; Krantz, B. A.; Williams, E. R. *Phys. Chem. Chem. Phys.* **2011**, *13*, 18288-18296.
- (10) Loo, R. R. O.; Smith, R. D. *J. Mass Spectrom.* **1995**, *30*, 339-347.
- (11) Williams, E. R. *J. Mass Spectrom.* **1996**, *31*, 831-842.
- (12) Iavarone, A. T.; Jurchen, J. C.; Williams, E. R. *J. Am. Soc. Mass Spectrom.* **2000**, *11*, 976-985.
- (13) Thomson, B. *J. Am. Soc. Mass Spectrom.* **1997**, *8*, 1053-1058.
- (14) Page, J. S.; Kelly, R. T.; Tang, K.; Smith, R. D. *J. Am. Soc. Mass Spectrom.* **2007**, *18*, 1582-1590.
- (15) Marshall, A. G.; Hendrickson, C. L.; Jackson, G. S. *Mass Spectrom. Rev.* **1998**, *17*, 1-35.
- (16) Zubarev, R. A.; Makarov, A. *Anal. Chem.* **2013**, *85*, 5288-5296.
- (17) Zubarev, R.; Kelleher, N.; McLafferty, F. *J. Am. Chem. Soc.* **1998**, *120*, 3265-3266.
- (18) Iavarone, A. T.; Williams, E. R. *Anal. Chem.* **2003**, *75*, 4525-4533.
- (19) Madsen, J. A.; Brodbelt, J. S. *J. Am. Soc. Mass Spectrom.* **2009**, *20*, 349-358.
- (20) Iavarone, A. T.; Jurchen, J. C.; Williams, E. R. *Anal. Chem.* **2001**, *73*, 1455-1460.
- (21) Davies, N. W.; Wiese, M. D.; Browne, S. G. A. *Toxicon* **2004**, *43*, 173-183.
- (22) Kjeldsen, F.; Giessing, A. M. B.; Ingrell, C. R.; Jensen, O. N. *Anal. Chem.* **2007**, *79*, 9243-9252.
- (23) Valeja, S. G.; Tipton, J. D.; Emmett, M. R.; Marshall, A. G. *Anal. Chem.* **2010**, *82*, 7515-7519.
- (24) Miladinovic, S. M.; Fornelli, L.; Lu, Y.; Piech, K. M.; Girault, H. H.; Tsybin, Y. O. *Anal. Chem.* **2012**, *84*, 4647-4651.
- (25) Teo, C. A.; Donald, W. A. *Anal. Chem.* **2014**, *86*, 4455-4462.
- (26) Going, C. C.; Williams, E. R. *Anal. Chem.* **2015**, *87*, 3973-3980.
- (27) Lomeli, S. H.; Yin, S.; Loo, R. R. O.; Loo, J. A. *J. Am. Soc. Mass Spectrom.* **2009**, *20*, 593-596.
- (28) Sterling, H. J.; Williams, E. R. *Anal. Chem.* **2010**, *82*, 9050-9057.
- (29) Hogan, C. J.; Loo, R. R. O.; Loo, J. A.; de la Mora, J. F. *PCCP* **2010**, *12*, 13476-13483.
- (30) Yin, S.; Loo, J. A. *Int. J. Mass Spectrom.* **2011**, *300*, 118-122.
- (31) Sterling, H. J.; Kintzer, A. F.; Feld, G. K.; Cassou, C. A.; Krantz, B. A.; Williams, E. R. *J. Am. Soc. Mass Spectrom.* **2012**, *23*, 191-200.
- (32) Metwally, H.; McAllister, R. G.; Popa, V.; Konermann, L. *Anal. Chem.* **2016**, *88*, 5345-5354.

- (33) Flick, T. G.; Williams, E. R. *J. Am. Soc. Mass Spectrom.* **2012**, *23*, 1885-1895.
- (34) Kharlamova, A.; Prentice, B. M.; Huang, T.; McLuckey, S. A. *Anal. Chem.* **2010**, *82*, 7422-7429.
- (35) Kharlamova, A.; McLuckey, S. A. *Anal. Chem.* **2011**, *83*, 431-437.
- (36) Sterling, H. J.; Cassou, C. A.; Susa, A. C.; Williams, E. R. *Anal. Chem.* **2012**, *84*, 3795-3801.
- (37) Hedges, J. B.; Vahidi, S.; Yue, X.; Konermann, L. *Anal. Chem.* **2013**, *85*, 6469-6476.
- (38) Cassou, C. A.; Williams, E. R. *Anal. Chem.* **2014**, *86*, 1640-1647.
- (39) Li, Y.; Cole, R. B. *Anal. Chem.* **2003**, *75*, 5739-5746.
- (40) Yuill, E. M.; Sa, N.; Ray, S. J.; Hieftje, G. M.; Baker, L. A. *Anal. Chem.* **2013**, *85*, 8498-8502.
- (41) Ek, P.; Schonberg, T.; Sjodahl, J.; Jacksen, J.; Vieider, C.; Emmer, A.; Roeraade, J. *J. Mass Spectrom.* **2009**, *44*, 171-181.
- (42) Ek, P.; Sjodahl, J.; Roeraade, J. *Rapid Commun. Mass Spectrom.* **2006**, *20*, 3176-3182.
- (43) Mortensen, D. N.; Williams, E. R. *J. Am. Chem. Soc.* **2016**, *138*, 3453-3460.
- (44) Behrens, S. H.; Grier, D. G. *J. Chem. Phys.* **2001**, *115*, 6716-6721.
- (45) Pennathur, S.; Santiago, J. *Anal. Chem.* **2005**, *77*, 6782-6789.
- (46) Freedman, K. J.; Jurgens, M.; Prabhu, A.; Ahn, C. W.; Jemth, P.; Edel, J. B.; Kim, M. J. *Anal. Chem.* **2011**, *83*, 5137-5144.
- (47) Yusko, E. C.; Johnson, J. M.; Majd, S.; Prangkio, P.; Rollings, R. C.; Li, J.; Yang, J.; Mayer, M. *Nat. Nanotechnol.* **2011**, *6*, 253-260.
- (48) Anderson, B. N.; Muthukumar, M.; Meller, A. *ACS Nano* **2013**, *7*, 1408-1414.
- (49) Jurchen, J. C.; Williams, E. R. *J. Am. Chem. Soc.* **2003**, *125*, 2817-2826.
- (50) Blakney, G. T.; Hendrickson, C. L.; Marshall, A. G. *Int. J. Mass Spectrom.* **2011**, *306*, 246-252.
- (51) Goto, Y.; Fink, A. L. *J. Mol. Biol.* **1990**, *214*, 803-805.
- (52) Shastry, R. M. C.; Luck, S. D.; Roder, H. *Biophys. J.* **1998**, *74*, 2714-2721.
- (53) Konno, T. *Protein Sci.* **1998**, *7*, 975-982.
- (54) Sage, J. T.; Morikis, D.; Champion, P. M. *Biochemistry* **1991**, *30*, 1227-1237.
- (55) Griko, Y. V.; Privalov, P. L.; Venyaminov, S. Y.; Kutyshenko, V. P. *J. Mol. Biol.* **1988**, *202*, 127-138.
- (56) Aymard, P.; Nicolai, T.; Durand, D.; Clark, A. *Macromolecules* **1999**, *32*, 2542-2552.
- (57) Bouhallab, S.; Morgan, F.; Henry, G.; Molle, D.; Leonil, J. *J. Agric. Food Chem.* **1999**, *47*, 1489-1494.
- (58) Bergers, J. J.; Vingerhoeds, M. H.; Vanbloois, L.; Herron, J. N.; Janssen, L. H. M.; Fischer, M. J. E.; Crommelin, D. J. A. *Biochemistry* **1993**, *32*, 4641-4649.
- (59) Hemdan, E. S.; Zhao, Y. J.; Sulkowski, E.; Porath, J. *Proc. Natl. Acad. Sci. U. S. A.* **1989**, *86*, 1811-1815.
- (60) Stein, D.; Kruithof, M.; Dekker, C. *Phys. Rev. Lett.* **2004**, *93*, 035901.
- (61) Kuroda, Y.; Yukinaga, H.; Kitano, M.; Noguchi, T.; Nemati, M.; Shibukawa, A.; Nakagawa, T.; Matsuzaki, K. *J. Pharm. Biomed. Anal.* **2005**, *37*, 423-428.
- (62) Kuwata, K.; Hoshino, M.; Forge, V.; Era, S.; Batt, C. A.; Goto, Y. *Protein Sci.* **1999**, *8*, 2541-2545.
- (63) Alvarez, E.; Vazquez, G.; Sanchez-Vilas, M.; Sanjurjo, B.; Navaza, J. *J. Chem. Eng. Data* **1997**, *42*, 957-960.
- (64) Vazquez, G.; Alvarez, E.; Navaza, J. M. *J. Chem. Eng. Data* **1995**, *40*, 611-614.

- (65) Loo, R. R. O.; Lakshmanan, R.; Loo, J. A. *J. Am. Soc. Mass Spectrom.* **2014**, *25*, 1675-1693.
- (66) Spyroulias, G.; Nikolakopoulou, P.; Tzakos, A.; Gerohanassis, I.; Magafa, V.; Manessi-Zoupa, E.; Cordopatis, P. *Eur. J. Biochem.* **2003**, *270*, 2163-2173.
- (67) Kubelka, J.; Hofrichter, J.; Eaton, W. *Curr. Opin. Struct. Biol.* **2004**, *14*, 76-88.
- (68) Leonil, J.; Molle, D.; Fauquant, J.; Maubois, J. L.; Pearce, R. J.; Bouhallab, S. *J. Dairy Sci.* **1997**, *80*, 2270-2281.

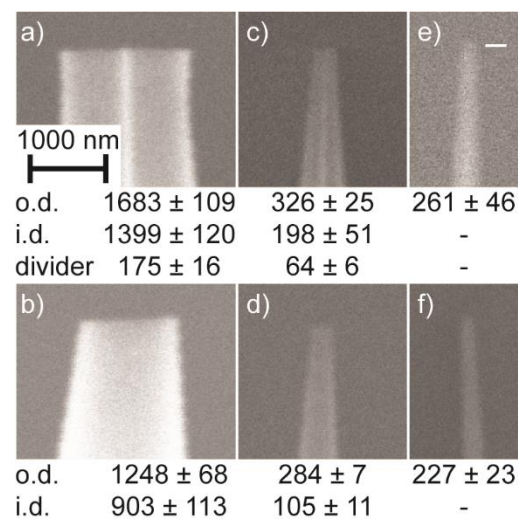


**Figure 5.1.** Electron micrographs of the tips of the theta-glass emitters with average outer diameters of (a,b)  $1465 \pm 134$ , (c,d)  $305 \pm 32$ , and (e,f)  $244 \pm 61$  nm with the inner divider perpendicular to and parallel to the sample stand in the upper and lower panels, respectively. A white line was added to (e) to indicate where the tip ends.

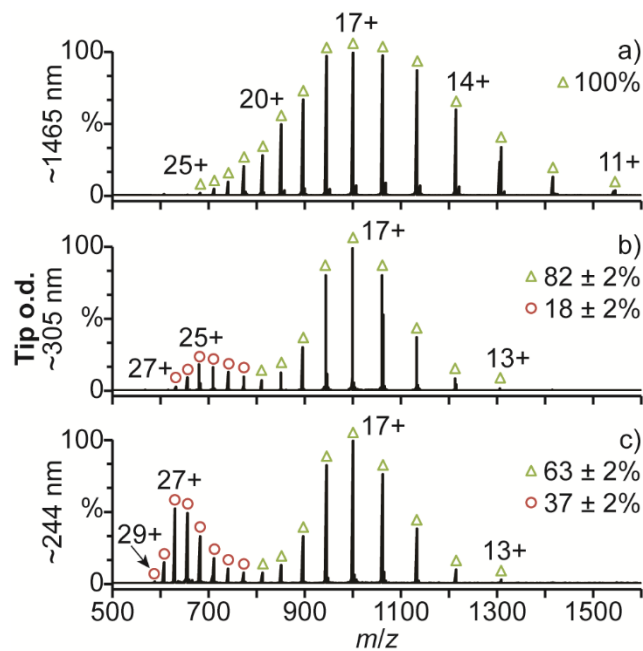


**Figure 5.2.** Mass spectra of aMb in an acidified aqueous solution ( $\text{pH} = 2.9$ ) acquired with theta-glass emitters with (a)  $\sim 1465$ , (b)  $\sim 305$ , and (c)  $\sim 244$  nm o.d. tips.

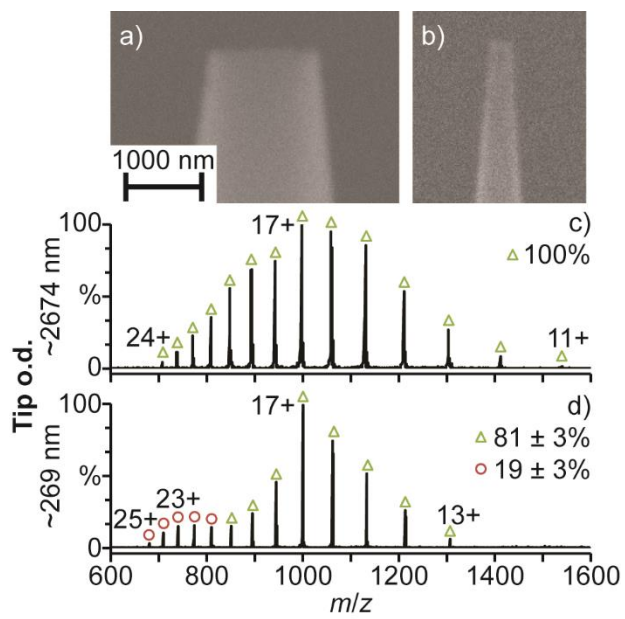


**Figure 5.3.** Electron micrographs of the tips of the single-barrel emitters with average outer diameters of (a)  $1448 \pm 135$  and (b)  $269 \pm 29$  nm. Mass spectra of aMb in an acidified aqueous solution ( $\text{pH} = 2.9$ ) acquired with single-barrel emitters with (c)  $\sim 2674$  and (d)  $\sim 269$  nm o.d. tips.

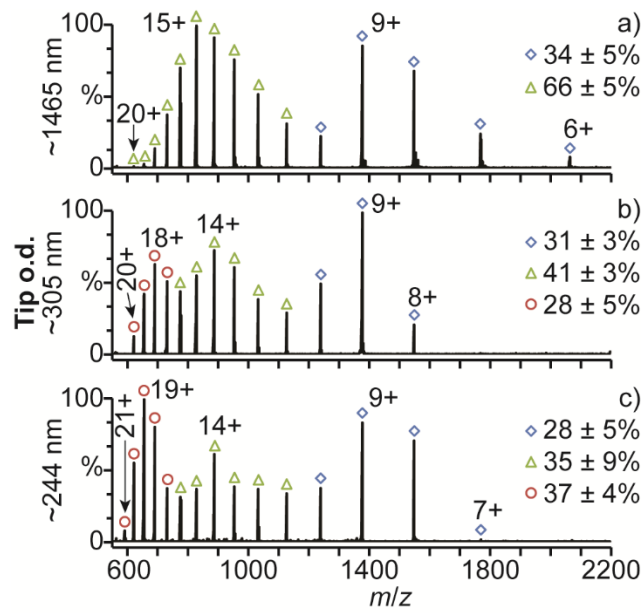


**Figure 5.4.** Mass spectra of cyt *c* in an acidified aqueous solution (pH = 2.8) acquired with (a)  $\sim 1465$ , (b)  $\sim 305$ , and (c)  $\sim 244$  nm o.d. tips.

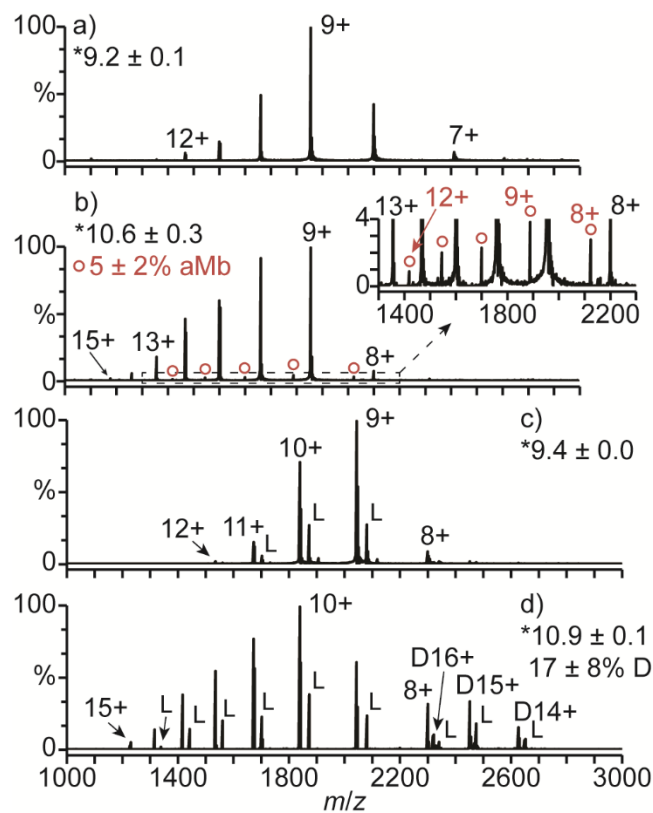


**Figure 5.5.** Mass spectra of (a,b) hMb and (c,d)  $\beta$ -lac A in slightly acidified aqueous solutions ( $\text{pH} = 4.1$ ) acquired with (a,c)  $\sim 1465$  and (b,d)  $\sim 305$  nm o.d. tips. (\*) denotes average charge state. (L) denotes  $\beta$ -lac A with a covalently bound lactosyl molecule.<sup>57,68</sup> (D) denotes dimers.

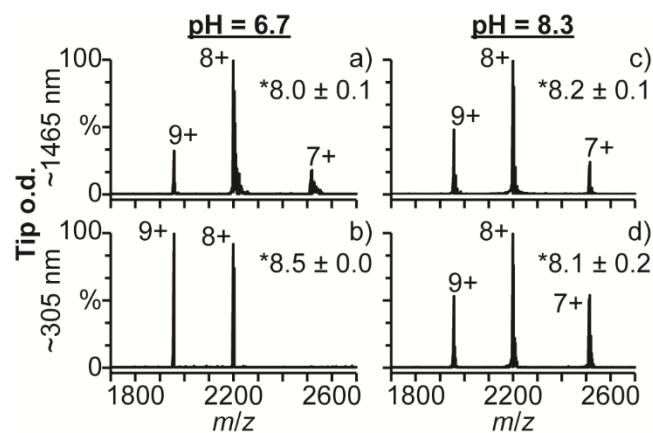


**Figure 5.6.** Mass spectra of hMb ( $pI = 7.4$ ) in aqueous solutions containing (a,b) 100 mM ammonium acetate ( $pH = 6.7$ ) and (c,d) 100 mM ammonium bicarbonate ( $pH = 8.3$ ) acquired with (a,c)  $\sim 1465$  and (b,d)  $\sim 305$  nm o.d. tips. (\*) denotes average charge state.

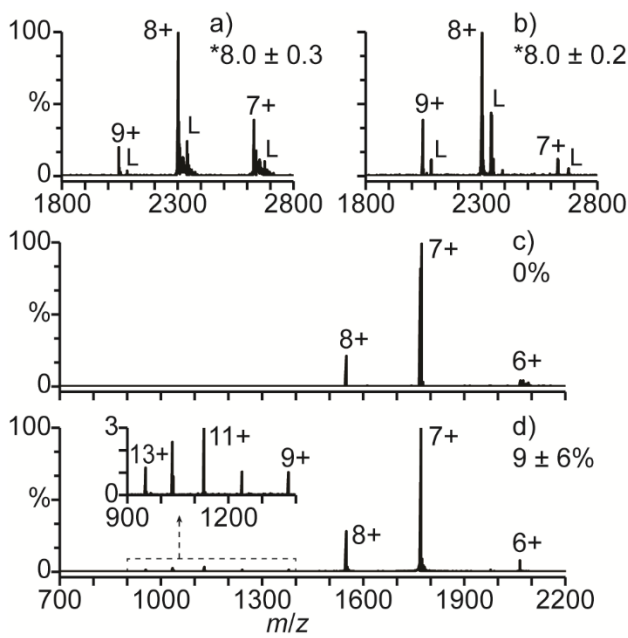


**Figure 5.7.** Mass spectra of (a,b)  $\beta$ -lac A ( $pI = 5.1$ ) and (c,d) cyt c ( $pI = 10.3$ ) in 100 mM aqueous ammonium acetate solutions ( $pH = 6.7$ ) acquired with (a,c)  $\sim 1465$  and (b,d)  $\sim 305$  nm o.d. tips. (\*) denotes average charge state. (L) denotes  $\beta$ -lac A with a covalently bound lactosyl molecule.<sup>57,68</sup> Percentages are the relative abundances of the unfolded fractions (9–13+ charge states) of cyt c.

# Chapter 6

## Electrothermal Supercharging of Proteins in Native MS: Effects of Protein Isoelectric Point, Buffer, and nanoESI- Emitter Tip Size

This Chapter is reproduced with permission from  
Mortensen, D.M.; Williams, E.R.

“Electrothermal Supercharging of Proteins in Native  
MS: Effects of Protein Isoelectric Point, Buffer,  
and nanoESI-Emitter Tip Size”  
*Analyst* **2016**, DOI: 10.1039/c6an01380e  
© 2016 Royal Society of Chemistry

### 6.1 Introduction

Electrospray ionization (ESI) mass spectrometry (MS) is a powerful tool for identifying proteins and for obtaining information about protein structure, including posttranslational modifications.<sup>1-3</sup> Native MS,<sup>4,5</sup> where protein ions are formed by ESI from buffered aqueous solutions in which the proteins have folded native or native-like conformations and activities, is useful for measuring protein-ligand binding affinities,<sup>6,7</sup> stoichiometries of protein complexes,<sup>8,9</sup> and thermodynamics and kinetics of protein complex assembly.<sup>10,11</sup> Native MS typically produces compact gaseous ions with low charge states.<sup>8,9</sup> However, the formation of high charge state ions can increase both sensitivity and resolution for charge detection instruments, such as orbitrap and ion cyclotron resonance mass spectrometers.<sup>12,13</sup> Higher charge states fragment more readily, often resulting in increased structural information in tandem MS.<sup>14-16</sup> Fewer cations adduct to higher charge states,<sup>17,18</sup> and unresolved adducts can broaden ion peaks in ESI mass spectra, resulting in lower resolution and mass measuring accuracy.<sup>19</sup>

High charge state ions are most often formed from solutions containing acids and organic solvents in which proteins are denatured. High charge states can also be formed in native MS by adding supercharging reagents<sup>20-27</sup> or trivalent metal ions<sup>28</sup> to the analyte solution prior to ESI, by exposing the ESI droplets to acidic<sup>29</sup> or basic<sup>30</sup> vapors, or by using electrothermal supercharging (ETS).<sup>31-33</sup> In ETS, protein ions are formed from buffered aqueous solutions using high spray potentials, which results in collisional heating of the ESI droplets and thermal denaturation of the proteins inside the droplets prior to ion formation,<sup>31,33</sup> although other possibly contributing mechanisms have been proposed.<sup>32</sup> ETS does not scramble H/D information encoded in the solution, making it well suited to top-down H/D exchange experiments.<sup>34</sup> Charge states as high or higher than those obtained from denaturing solution can be obtained with ETS.<sup>35</sup> The effectiveness of ammonium and sodium salts at forming high charge states with ETS increases with increasing propensity to induce protein aggregation in solution.<sup>33</sup> Electron capture dissociation of the 16+ cytochrome *c* ions formed from ETS and from denaturing solutions resulted in the same extent of sequence coverage, but there were differences in the cleavage sites, indicating that different ion conformers of the same charge state can be formed by ETS and from denaturing solutions.<sup>35</sup> The effects of protein isoelectric point (pI) on ETS have been investigated,<sup>33,35</sup> and ETS is generally slightly more effective for proteins that are positively charged compared to those that are negatively charged in solution.<sup>35</sup>

Higher charging can also be obtained by using ESI emitters with smaller tips. For example, the average charge of ubiquitin ions formed from a 50/50 water/methanol solution increases from ~7 to ~7.5 when the tip outer diameters (o.d.) is reduced from ~45 µm to ~2 µm.<sup>36</sup> Higher charging and narrower charge-state distributions were also reported for cytochrome *c* and ubiquitin ions formed from denaturing solutions with <100 nm o.d. tips compared to that obtained with ~1 µm o.d. tips.<sup>37</sup> Improved signal-to-noise ratios and higher charging with decreasing tip size have also been reported for angiotensin I<sup>38</sup> and insulin chain B<sup>39</sup> ions formed using ESI emitters with adjustable orifice sizes.<sup>38,39</sup> In these devices, the orifice width is varied between 1 and 10's of microns by adjusting the position of silicon chips.

Recently, increased charging with decreasing tip size was reported for several proteins and a 14 residue peptide using double-barrel wire-in-a-capillary emitters (theta-glass emitters) with tips between ~1.5 µm and ~240 nm o.d.<sup>40,41</sup> Additional high charge-state distributions in the ESI spectrum were often formed with the smaller tip sizes.<sup>40,41</sup> Loss of heme occurred for holo-myoglobin ions formed from a slightly acidified aqueous solution with submicron o.d. tips, whereas the heme is retained for ions formed from this solution with micron o.d. tips.<sup>41</sup> The formation of high charge-state distributions and the loss of heme for myoglobin indicate that fractions of these protein populations are unfolded with the submicron o.d. tips.<sup>40,41</sup> More unfolding occurs with decreasing tip size for partially unfolded proteins than for folded proteins.<sup>41</sup>

Increased charging with decreasing tip size has only been reported for proteins that are positively charged in solution.<sup>36-41</sup> For proteins that are negatively charged in solution, changes in tip o.d. between ~1.5 µm and ~310 nm did not result in measurable changes to the average charge of protein ions.<sup>41</sup> Nano-ESI emitters are typically prepared from borosilicate glass<sup>36,37,40,41</sup> or other forms of silicon<sup>38,39</sup> that contain silanol groups on their surfaces.<sup>42</sup> In aqueous solutions, a fraction of the silanol groups are deprotonated, resulting in a net negative charge on glass surfaces that depends on the solution pH.<sup>42</sup> The increased charging obtained with decreasing tip size for positively charged proteins but not for negatively charged proteins suggests that the increased charging with decreasing tip size results from Coulombic attraction between positively charged protein molecules and the negatively charged glass surfaces in the tips of the nanoESI emitters, which results in protein destabilization and unfolding prior to nanoESI.<sup>41</sup>

Here, ETS is performed using emitters with micron and submicron o.d. tips prepared from borosilicate theta-glass capillaries. The efficiency of ETS at producing high charge state ions increases with decreasing tip size for proteins that are positively charged in solution but decreases with decreasing tip size for proteins that are negatively charged in solution. These results indicate that when surface-induced destabilization of the protein conformation occurs in the tips of the emitters prior to nanoESI, charging with ETS is enhanced in the droplets. When surface interactions do not occur in the tips of the nanoESI emitters, such as with negatively charged protein molecules, the extent to which high charge states are formed with ETS decreases with decreasing tip size. This reduced charging with decreased tip size likely results from droplets with smaller initial diameters that are formed with the smaller tips. Smaller droplets have shorter lifetimes,<sup>40,43</sup> which limit the extent to which protein unfolding can occur in the nanoESI droplets prior to gaseous ion formation. These results demonstrate a simple method for increasing the extent of charging obtained with ETS, which should be useful for obtaining more structural information in tandem MS.

## 6.2 Experimental Section

Experiments are performed with a 9.4 T Fourier-transform ion cyclotron resonance mass spectrometer that is described elsewhere.<sup>44</sup> Ions are formed by nanoESI using theta glass capillaries (Warner Instruments, LLC, Hamden, CT) with tips pulled to a small o.d. using a model p-87 Flaming/Brown micropipette puller (Sutter Instruments Co., Novato, CA). The tips of these emitters are imaged on carbon tape at 10,000-times magnification (Appendix D, Figure D.1) with a TM-1000 scanning electron microscope (Hitachi High-Technologies Co., Tokyo, Japan). Grounded platinum wires are inserted to within ~1 cm of the tips of the emitters and are in contact with the solutions. The distance between the platinum wires and the tips of the emitters does not affect the extent of charging resulting from nanoESI as long as contact is made between the wires and the solutions. The emitters are positioned ~1 mm from the mass spectrometer inlet, and nanoESI is initiated by applying a negative potential to the heated capillary of the ESI interface. Native MS and ETS were performed with 700 V and 1050 V spray potentials, respectively. Data are acquired with a Predator data station,<sup>45</sup> and mass spectra are background subtracted. To determine flow rates, the emitters are weighed before and after ~20 min of electrospray using an A-200DS analytical balance (Denver Instrument Company, Bohemia, NY) with a lower mass limit of 10 µg. Spray currents are measured with a model 485 autoranging picoammeter (Keithley Instruments, Cleveland, OH) with a 2 Hz refresh rate. Average charge is computed as abundance weighted sums of the individual charge states, and reported uncertainties are standard deviations determined from triplicate measurements.

Ammonium acetate, ammonium formate, ammonium bicarbonate, L-arginine hydrochloride, equine apo- and holo-myoglobin, cytochrome *c*, bovine β-lactoglobulin A, ribonuclease A, ubiquitin, and chicken egg white lysozyme are obtained from Sigma-Aldrich (St. Louis, MO). Solutions are prepared with a 10 µM analyte concentration in 18.2 MΩ water from a Milli-Q water purification system (Millipore, Billerica, MA).

### 6.3 Results and Discussion

**6.3.1 Electrothermal Supercharging of a Noncovalent Complex.** Mass spectra of hMb in 100 mM aqueous ammonium acetate (pH = 6.7), formate (pH = 6.5), and bicarbonate (pH = 8.3) solutions obtained with large ~1465 nm o.d. ESI emitter tips under ETS conditions (1050 V spray potential) are shown in Figure 6.1a-c, respectively. In 100 mM aqueous salt solutions, hMb is in a native conformation between pH = 5 and 7, a slightly unfolded globular conformation around pH = 3,<sup>46</sup> and an unfolded conformation with no heme attached below pH = 3.<sup>47</sup> Only the 7–9+ charge states are formed with the ammonium acetate solution (Figure 6.1a), consistent with hMb adopting a folded conformation in solution. The 7–9+ charge states are also formed with this solution under native MS conditions (700 V spray potential, Appendix D, Figure D.2a), indicating that ETS does not result in a significant increase in charge. With the ammonium formate (Figure 6.1b) and bicarbonate (Figure 6.1c) solutions under ETS conditions, charge states corresponding to both folded (7–9+) and unfolded (10–21+) conformers of hMb are formed. Apo-myoglobin (aMb) ions are also formed, indicating that a fraction of myoglobin is unfolded, and aMb comprises 14 ± 2% and 32 ± 1% of myoglobin in Figure 6.1b and 6.1c, respectively. No aMb or charge states greater than 9+ are formed with these solutions under native MS conditions (Appendix D, Figure D.2b and D.2c, respectively), indicating that the unfolding and resulting increased charging obtained with the high spray potential result from ETS. The relative abundance of aMb produced under ETS conditions is greater with ammonium

bicarbonate ( $32 \pm 1\%$ , Figure 6.1c) than with ammonium formate ( $14 \pm 2\%$ , Figure 6.1b) or ammonium acetate (0%, Figure 6.1a). These results are consistent with the relative effectiveness of these three salts at inducing ETS reported previously.<sup>33</sup>

Results obtained for the ammonium acetate, formate, and bicarbonate solutions with the smaller  $\sim 305$  nm o.d. tips under ETS conditions are shown in Figure 6.1d-f, respectively. Charge states corresponding to both folded (7–9+) and unfolded (10–17+) conformers of hMb and to aMb are observed. With the ammonium acetate solution (Figure 6.1d), aMb comprises  $58 \pm 3\%$  of myoglobin. Neither aMb nor charge states of hMb greater than 9+ are produced with this solution under ETS conditions with the larger tips (Figure 6.1a). With the ammonium formate solution, significantly more aMb is also produced with the smaller  $\sim 305$  nm o.d. tips ( $54 \pm 1\%$ , Figure 6.1e) than with the larger  $\sim 1465$  nm o.d. tips ( $14 \pm 2\%$ , Figure 6.1b). However, with the ammonium bicarbonate solution ( $\text{pH} = 8.3$ ), significantly *less* aMb is produced with the smaller tips ( $11 \pm 2\%$ , Figure 6.1f) than with the larger tips ( $32 \pm 1\%$ , Figure 6.1c).

The pI of hMb is 7.4,<sup>48</sup> so hMb is predominantly positively charged in the  $\text{pH} = 6.7$  ammonium acetate and  $\text{pH} = 6.5$  ammonium formate solutions and predominantly negatively charged in the  $\text{pH} = 8.3$  ammonium bicarbonate solution. The extent of unfolding resulting from ETS increases with decreasing tip size for proteins that are positively charged in solution but decreases with decreasing tip size for proteins that are negatively charged in solution. Glass surfaces are negatively charged in aqueous solution,<sup>42</sup> and Coulombic attraction between positively charged protein molecules and the negatively charged glass surfaces in the tips of nanoESI emitters can result in protein unfolding prior to nanoESI.<sup>40</sup> These results indicate that the increased ETS efficiency obtained with the smaller tips for proteins that are positively charged in solution results from surface-induced unfolding occurring in the tips of these emitters prior to droplet formation by nanoESI.

In order to provide additional evidence for protein unfolding as the origin of increased charging obtained with the smaller tips, experiments were performed with a protein that has intramolecular disulfide bonds and therefore cannot unfold as extensively as a protein without internal linkages. Lysozyme ( $\text{pI} = 11.3$ )<sup>49</sup> has four disulfide bridges. In aqueous solutions, lysozyme adopts a globular conformation between  $\text{pH} = 2$  and 6 and a slightly unfolded conformation above  $\text{pH} = 7$ .<sup>50</sup> NanoESI of lysozyme in a 100 mM aqueous ammonium acetate solution ( $\text{pH} = 6.7$ ) with  $\sim 1465$  nm o.d. tips under ETS conditions results in the 6–9+ charge states (Figure 2a), consistent with a folded conformation in solution. These charge states are also formed from this solution under native MS conditions (Figure 2b), indicating that ETS does not result in measurable unfolding in this experiment. NanoESI of this solution with  $\sim 305$  nm o.d. tips under ETS conditions (Figure 2c) also results in the 6–9+ charge states, as well as the 10+ and 11+ charge states. The higher charge states that are produced with the smaller tips are consistent with the formation of partially unfolded conformers that comprise  $2 \pm 1\%$  of the population. The extent of unfolding obtained for lysozyme with the  $\sim 305$  nm o.d. tips is significantly less than that obtained for myoglobin ( $\sim 58\%$  aMb produced) with the ammonium acetate solution and the same tip size (Figure 1d). The lower extent of unfolding obtained for lysozyme than for myoglobin is consistent with the four disulfide bonds in lysozyme resulting in less structural flexibility for this protein and thus less surface-induced unfolding occurring prior to nanoESI. This result is consistent with the lower extent of supercharging with supercharging reagents for proteins with more disulfide bridges or chemical crosslinks that reduce conformational flexibility.<sup>23</sup>

The decreased charging obtained with decreasing tip size for proteins that are negatively charged in solution likely results from the initial size of the nanoESI droplets, which decreases with decreasing tip o.d.<sup>51</sup> Smaller droplets have shorter lifetimes,<sup>40,43</sup> which reduce the time for protein unfolding to occur in these droplets prior to gaseous ion formation. The electric field at the tip of the emitter increases with decreasing tip size, and the extent of unfolding obtained with ETS generally increases with increasing electric field strength.<sup>31</sup> However, the extent of charging resulting directly from ETS decreases with decreasing tip size. This result indicates that the relationship between tip size and the extent of charging resulting from ETS is affected more by changes to the droplet lifetime than by changes to the electric field strength.

**6.3.2 Electrothermal Supercharging of Positively Charged Proteins.** Mass spectra of cyt *c* in 100 mM aqueous ammonium acetate (pH = 6.7), formate (pH = 6.5), and bicarbonate (pH = 8.3) solutions obtained with ~1465 nm o.d. tips under ETS conditions are shown in Figure 6.3a-c, respectively. In 100 mM aqueous salt solutions, cyt *c* has a native folded conformation between pH = 3 and 7 and is unfolded at pH = 2.<sup>52,53</sup> Only the 6–8+ charge states are formed with the ammonium acetate solution (Figure 6.3a), consistent with cyt *c* adopting a folded conformation in solution. The 6–8+ charge states are also formed with this solution under native MS conditions (Appendix D, Figure D.3a), indicating that ETS does not result in measurable unfolding in this experiment. With the ammonium formate (Figure 6.3b) and bicarbonate (Figure 6.3c) solutions, charge states corresponding to both folded (6–9+) and unfolded (10–18+) conformers are observed with ETS, and the unfolded conformers comprise 9 ± 1% and 26 ± 2% of cyt *c* in Figure 6.3b and 6.3c, respectively. No charge states greater than 9+ are formed with either of these solutions under native MS conditions (Appendix D, Figure D.3b and D.3c, respectively), showing that the high charge states are formed by ETS. The order of effectiveness of these salts at inducing ETS for cyt *c* is the same as that obtained for hMb with the larger tips and that reported previously.<sup>33</sup>

Charge states corresponding to both folded (6–9+) and unfolded (10–15+) conformers are formed by ETS of cyt *c* in the ammonium acetate and formate solutions with the smaller ~305 nm o.d. tips (Figure 6.3d and 6.3e, respectively). With the ammonium acetate solution (Figure 6.3d), 62 ± 2% of cyt *c* is unfolded, compared to no charge states greater than 8+ formed with the larger ~1465 nm o.d. tips (Figure 6.3a). With the ammonium formate solution, ions corresponding to unfolded cyt *c* are also significantly more abundant with the smaller ~305 nm o.d. tips (77 ± 3%, Figure 6.3e) than with the larger ~1465 nm o.d. tips (9 ± 1%, Figure 6.3b). Cyt *c* has a pI = 10.3<sup>49</sup> and is therefore predominantly positively charged in these respective pH = 6.7 and 6.5 solutions. Therefore, the increased unfolding with decreasing tip size obtained for cyt *c* in these solutions is consistent with surface-induced unfolding occurring prior to droplet formation, resulting in enhanced charging with ETS in the droplet. With the ammonium bicarbonate solution and the ~305 nm o.d. tips, there is no ion signal for cyt *c* despite measurable spray current. To confirm that ion formation is occurring, 10 µM hMb was added to this solution. In aqueous solutions at pH = 8.3, hMb (pI = 7.3) is predominantly negatively charged and should not interact with the surfaces of the smaller tips. Results obtained for this spiked solution with ~1465 and ~305 nm o.d. tips are shown in Figure 6.4a and 6.4b, respectively. With the ~1465 nm o.d. tips (Figure 6.4a), both cyt *c* and myoglobin ions are observed. With the smaller ~305 nm o.d. tips (Figure 6.4b), only myoglobin ions are observed. These results indicate that cyt *c* is not being ionized to a measurable extent from the pH = 8.3 ammonium bicarbonate solution with the smaller tips.

NanoESI of cyt *c* in a 100 mM aqueous ammonium bicarbonate solution ( $\text{pH} = 8.3$ ) under ETS conditions with an intermediate  $\sim 656$  nm o.d. tip size (Figure 6.4c) results in the 9–18+ charge states, indicating that  $97 \pm 2\%$  of cyt *c* is unfolded (10–18+ charge states). The relative abundance of the unfolded cyt *c* conformers obtained with this solution is nearly four times greater with the  $\sim 656$  nm o.d. tips ( $97 \pm 2\%$ , Figure 6.4c) than with the  $\sim 1465$  nm o.d. tips ( $26 \pm 2\%$ , Figure 6.3c). The relative abundance of the unfolded conformers also increases with ammonium acetate (from 0% to  $62 \pm 2\%$ ) and ammonium formate (from  $9 \pm 1\%$  to  $77 \pm 3\%$ ) when the tip o.d. is reduced from  $\sim 1465$  to  $\sim 305$  nm, respectively, but the population of unfolded conformers is greatest with ammonium bicarbonate. These results indicate that more surface interactions resulting in protein unfolding occur with the ammonium bicarbonate solution than with the ammonium acetate and formate solutions. The charge density on the surface of the tips of the nanoESI emitters is at least 3 to 4 fold higher with the  $\text{pH} = 8.3$  ammonium bicarbonate solution than with the  $\text{pH} = 6.7$  ammonium acetate and  $\text{pH} = 6.5$  ammonium formate solutions.<sup>42</sup> These results indicate that increasing the charge density on the glass surfaces results in more Coulombic attraction for the positively charged protein molecules, resulting in more surface-induced protein unfolding.

The high charge density on the surface of the tips with the  $\text{pH} = 8.3$  ammonium bicarbonate solution and the inability to form cyt *c* ions from this solution with the small  $\sim 305$  nm o.d. tips suggests that positively charged protein molecules are adducting to the surfaces of these tips. To provide support for this hypothesis, ions were formed from an aqueous  $\text{pH} = 8.3$  solution containing  $10 \mu\text{M}$  cyt *c*, 100 mM ammonium bicarbonate, and 10 mM arginine using a  $\sim 305$  nm o.d. tip (Figure 6.4d). Arginine is predominantly positively charged in aqueous solutions below  $\text{pH} = 10.8$ ,<sup>54</sup> and positive ions can interact with the glass surfaces and reduce the net charge.<sup>55</sup> Singly and doubly protonated arginine clusters and the 6–14+ charge states of cyt *c* are observed. The formation of cyt *c* ions only upon the addition of arginine is consistent with the positively charged arginine molecules interacting with and reducing the net charge on the surfaces in the tips of these emitters, resulting in less adduction and, thus, measurable ionization of cyt *c*.

**6.3.4 Protein Adduction and Solution Flow Rates.** The effects of positively charged protein ions adducting to the surfaces of the emitter tips on solution flow rates during nanoESI was investigated with 100 mM aqueous ammonium bicarbonate solutions ( $\text{pH} = 8.3$ ), each containing a single protein with a pI value either below or above the solution pH (low and high pI proteins, respectively). Flow rates with  $\sim 305$  nm o.d. tips were obtained for these solutions by measuring the change of mass before and after spraying the solutions for  $\sim 20$  min (Figure 6.5a). The flow rates obtained for the solutions containing low pI proteins (average flow rate =  $119 \pm 8$  nL/s) are significantly higher than those obtained for the solutions containing high pI proteins (average flow rate =  $40 \pm 9$  nL/s), indicating that protein adduction drastically reduces the flow rates of the solutions containing high pI proteins. In order to determine if the flow rates change with time within the 20 min used to obtain these data, the solution spray currents, which reflect solution flow rates,<sup>56</sup> were measured (Figure 6.5b). Higher spray currents are obtained for the solutions containing low pI proteins (average spray current =  $929 \pm 66$  nA) than for the solutions containing high pI proteins (average spray current =  $731 \pm 81$  nA). These spray currents were obtained immediately after initiating nanoESI and remained nominally constant with time for the  $\sim 20$  min used to obtain the solution flow rates. These results suggest that the flow rates do not

change with time and that for the solutions containing high pI proteins, adduction to the glass surfaces in the tips of the emitters occurs to a significant extent prior to the initiation of nanoESI.

The lower flow rates of the solutions containing high pI proteins may be attributed to protein adduction resulting in an obstruction of the emitter tip orifice. The average flow rate of the solutions containing high pI proteins ( $40 \pm 9$  nL/s) is about one-third that of the solutions containing low pI proteins ( $119 \pm 8$  nL/s). Solution flow rates in nanoESI are directly proportional to the emitter tip diameter<sup>36,40</sup> and are thus proportional to the square root of the emitter tip orifice area. Therefore, protein molecules would need to occupy a cross sectional area equal to about 81% of the orifice area in order to reduce the solution flow rate by about two-thirds (67%). The orifice area of a single barrel of a ~305 nm o.d. theta-glass emitter tip is ~4820 nm<sup>2</sup>. This value was estimated as the area of half of an ellipse with diameters equal to the i.d. of the tips perpendicular to and parallel to the inner divider less the area occupied by the inner divider. To reduce this orifice area by about 81% would require a ~21 nm thick obstruction along the surface of the tips of the emitters. A single folded cyt c molecule has a diameter of ~4.1 nm, estimated as the maximum diameter of the protein crystal structure of horse heart cyt c (PDB code 1HRC).<sup>57</sup> The ~21 nm obstruction thickness and the ~4.1 nm diameter of cyt c indicate that ~5 layers of cyt c are required to reduce the solution flow rate by about two-thirds if the protein remains folded. The length of a fully extended cyt c molecule is about 40 nm (estimated from the average length of an individual amino acid in a fully extended protein conformation, between 0.34 and 0.40 nm,<sup>58</sup> and the 104 amino acids in cyt c). The length of a fully extended cyt c molecule is greater than the ~21 nm obstruction thickness required to reduce the solution flow rate by about two-thirds. Thus, even a single layer of adducted protein molecules, which are partially or extensively unfolded and extend into the solution, is sufficient to reduce the solution flow rate by about two-thirds.

Protein adduction to the surface of the tips may also result in a change to the solution conductivity, and ESI solution flow rates increase with increasing solution conductivities.<sup>56,59</sup> The conductivity of  $\geq 50$  mM aqueous salt solutions decreases with increasing protein concentration.<sup>60,61</sup> Adduction of proteins to the glass surfaces results in a decrease in the concentration of proteins in solution, which should increase the solution conductivity and flow rate. However, when protein adduction occurs, lower flow rates are obtained (Figure 6.5a). These results indicate that any possible changes to the solution flow rate resulting from changes to the solution conductivity are less significant than those resulting from obstructing the emitter tip orifice.

**6.3.5 Electrothermal Supercharging of Negatively Charged Proteins.** NanoESI of  $\beta$ -lactoglobulin A ( $\beta$ -lac A) in a 100 mM aqueous ammonium acetate solution (pH = 6.7) under ETS conditions results in the formation of the 7–9+ charge states with both the ~1465 and the ~305 nm o.d. tips (Figures 6.6a and 6.5b, respectively).  $\beta$ -lac A has a native conformation between pH = 2.0 and 6.2 and has a slightly unfolded globular conformation at pH = 7.5.<sup>62</sup> The results in Figures 6.6a and 6.5b are consistent with  $\beta$ -lac A adopting a folded conformation in solution. Charge states consistent with a folded confirmation (6–9+) are also formed from a 100 mM aqueous ammonium formate solution (pH = 6.5) with the ~1465 and ~305 nm o.d. tips (Figures 6.6c and 6.5d, respectively). The 6–9+ charge states are also formed from these solutions under native MS conditions (Appendix D, Figure D.4a and D.4b), indicating that ETS does not result in measurable unfolding in these experiments. Results obtained for  $\beta$ -lac A in a 100 mM aqueous ammonium bicarbonate solution with ~1465 and ~305 nm o.d. tips under ETS

conditions are shown in Figure 6.6e and 6.6f, respectively. With the ~1465 nm o.d. tips (Figure 6.6e), charge states corresponding to both folded (7–9+) and unfolded (10–16+) conformers are observed, and the unfolded conformers comprise  $48 \pm 3\%$  of the population. No charge states greater than 9+ are formed with this solution under native MS conditions (Appendix D, Figure D.4c), indicating that the high charge states obtained with the high spray potential result from ETS. With the smaller ~305 nm o.d. tips and ETS conditions (Figure 6.6f), charge states corresponding to both folded (6–9+) and unfolded (10–16+) conformers are again observed, but only  $19 \pm 1\%$  of the population is unfolded. The relative abundance of the unfolded  $\beta$ -lac A conformer is more than two times less with this tip size than with the larger tips under ETS conditions ( $48 \pm 3\%$ , Figure 6.6e), indicating that reducing the tip size results in *less* unfolding with this solution.

$\beta$ -lac A has a pI = 5.1<sup>63</sup> and is therefore predominantly negatively charged in the pH = 6.7 ammonium acetate, pH = 6.5 ammonium formate, and pH = 8.3 ammonium bicarbonate solutions. Therefore, surface-induced unfolding of  $\beta$ -lac A is not likely to occur in the tips of the emitters prior to nanoESI. This result is consistent with the decreased charging obtained with decreasing tip size for  $\beta$ -lac A in the ammonium bicarbonate solution. Because  $\beta$ -lac A has the same charge in the ammonium acetate, formate, and bicarbonate solutions, the order of effectiveness of these solutions at inducing ETS does not change with tip size and is the same as that obtained for hMb and cyt c with the larger tips and that reported previously.<sup>33</sup>

## 6.4 Conclusions

The effects of emitter tip size, protein isoelectric point, and buffer identity on the extent of charging obtained with ETS was investigated. More charging is obtained with smaller tip sizes for proteins that are positively charged in solution but not for proteins that are negatively charged in solution. There is also more charging and loss of the heme group for myoglobin with smaller emitter tips. These results suggest that for positively charged proteins, Coulombic attraction to the negatively charged surfaces in the tips of the emitters destabilizes the folded protein conformation prior to nanoESI, resulting in enhanced charging from ETS occurring in the droplet prior to gaseous ion formation. The extent to which charging is enhanced increases with increasing solution pH as long as the protein is predominantly positively charged in solution. The charge density on the surface of the emitters increases with increasing solution pH, resulting in more protein-surface interactions that cause destabilization of the folded form of the proteins and unfolding prior to nanoESI. Significant protein adduction to the emitter tip surface can occur, which reduces nanoESI solution flow rates and reduces or prevents measurable ionization from occurring at very small tip sizes. These results clearly show that the tip size, the solution pH, and the net charge of the protein in solution can affect the extent of charging in ETS.

For proteins that are negatively charged in solution, there is no Coulombic attraction to the negatively charged glass surfaces and slightly less charging occurs with smaller tips. The lower charging at small tip sizes is likely due to smaller ESI droplets with decreasing tip size.<sup>51</sup> Smaller droplets have shorter lifetimes,<sup>40</sup> and there is less time for protein unfolding to occur during ETS prior to gaseous ion formation. It may be possible to obtain increased charging with decreased tip size for proteins that are negatively charged in solution by using emitters with positively charged surfaces. The glass surfaces of borosilicate glass emitters could be functionalized with positive charge carriers, or emitters could be made from materials that have positively charged surfaces in aqueous solutions, such as silicon nitride.

## 6.5 References

- (1) Kruppa, G.; Schoeniger, J.; Young, M. *Rapid Commun. Mass Spectrom.* **2003**, *17*, 155-162.
- (2) Aebersold, R.; Mann, M. *Nature* **2003**, *422*, 198-207.
- (3) Pan, J.; Borchers, C. H. *Proteomics* **2013**, *13*, 974-981.
- (4) Benesch, J. L.; Robinson, C. V. *Curr. Opin. Struct. Biol.* **2006**, *16*, 245-251.
- (5) Heck, A. J. R. *Nat. Methods* **2008**, *5*, 927-933.
- (6) Rostom, A. A.; Tame, J. R. H.; Ladbury, J. E.; Robinson, C. V. *J. Mol. Biol.* **2000**, *296*, 269-279.
- (7) Shoemaker, G. K.; Soya, N.; Palcic, M. M.; Klassen, J. S. *Glycobiology* **2008**, *18*, 587-592.
- (8) Esteban, O.; Bernal, R. A.; Donohoe, M.; Videler, H.; Sharon, M.; Robinson, C. V.; Stock, D. *J. Biol. Chem.* **2008**, *283*, 2595-2603.
- (9) Lorenzen, K.; Olia, A. S.; Utrecht, C.; Cingolani, G.; Heck, A. J. R. *J. Mol. Biol.* **2008**, *379*, 385-396.
- (10) Painter, A. J.; Jaya, N.; Basha, E.; Vierling, E.; Robinson, C. V.; Benesch, J. L. P. *Chem. Biol.* **2008**, *15*, 246-253.
- (11) Kintzer, A. F.; Sterling, H. J.; Tang, I. I.; Abdul-Gader, A.; Miles, A. J.; Wallace, B. A.; Williams, E. R.; Krantz, B. A. *J. Mol. Biol.* **2010**, *399*, 741-758.
- (12) Marshall, A. G.; Hendrickson, C. L.; Jackson, G. S. *Mass Spectrom. Rev.* **1998**, *17*, 1-35.
- (13) Zubarev, R. A.; Makarov, A. *Anal. Chem.* **2013**, *85*, 5288-5296.
- (14) Iavarone, A. T.; Williams, E. R. *Anal. Chem.* **2003**, *75*, 4525-4533.
- (15) Iavarone, A. T.; Paech, K.; Williams, E. R. *Anal. Chem.* **2004**, *76*, 2231-2238.
- (16) Madsen, J. A.; Brodbelt, J. S. *J. Am. Soc. Mass Spectrom.* **2009**, *20*, 349-358.
- (17) Pan, P.; Gunawardena, H. P.; Xia, Y.; McLuckey, S. A. *Anal. Chem.* **2004**, *76*, 1165-1174.
- (18) Flick, T. G.; Cassou, C. A.; Chang, T. M.; Williams, E. R. *Anal. Chem.* **2012**, *84*, 7511-7517.
- (19) McKay, A. R.; Ruotolo, B. T.; Ilag, L. L.; Robinson, C. V. *J. Am. Chem. Soc.* **2006**, *128*, 11433-11442.
- (20) Lomeli, S. H.; Yin, S.; Loo, R. R. O.; Loo, J. A. *J. Am. Soc. Mass Spectrom.* **2009**, *20*, 593-596.
- (21) Sterling, H. J.; Williams, E. R. *Anal. Chem.* **2010**, *82*, 9050-9057.
- (22) Hogan, C. J.; Loo, R. R. O.; Loo, J. A.; de la Mora, J. F. *PCCP* **2010**, *12*, 13476-13483.
- (23) Sterling, H. J.; Cassou, C. A.; Trnka, M. J.; Burlingame, A. L.; Krantz, B. A.; Williams, E. R. *PCCP* **2011**, *13*, 18288-18296.
- (24) Yin, S.; Loo, J. A. *Int. J. Mass Spectrom.* **2011**, *300*, 118-122.
- (25) Sterling, H. J.; Kintzer, A. F.; Feld, G. K.; Cassou, C. A.; Krantz, B. A.; Williams, E. R. *J. Am. Soc. Mass Spectrom.* **2012**, *23*, 191-200.
- (26) Going, C. C.; Williams, E. R. *Anal. Chem.* **2015**, *87*, 3973-3980.
- (27) Metwally, H.; McAllister, R. G.; Popa, V.; Konermann, L. *Anal. Chem.* **2016**, *88*, 5345-5354.
- (28) Flick, T. G.; Williams, E. R. *J. Am. Soc. Mass Spectrom.* **2012**, *23*, 1885-1895.

- (29) Kharlamova, A.; Prentice, B. M.; Huang, T.; McLuckey, S. A. *Anal. Chem.* **2010**, *82*, 7422-7429.
- (30) Kharlamova, A.; McLuckey, S. A. *Anal. Chem.* **2011**, *83*, 431-437.
- (31) Sterling, H. J.; Cassou, C. A.; Susa, A. C.; Williams, E. R. *Anal. Chem.* **2012**, *84*, 3795-3801.
- (32) Hedges, J. B.; Vahidi, S.; Yue, X.; Konermann, L. *Anal. Chem.* **2013**, *85*, 6469-6476.
- (33) Cassou, C. A.; Williams, E. R. *Anal. Chem.* **2014**, *86*, 1640-1647.
- (34) Going, C. C.; Xia, Z.; Williams, E. R. *J. Am. Soc. Mass Spectrom.* **2016**, *27*, 1019-1027.
- (35) Cassou, C. A.; Sterling, H. J.; Susa, A. C.; Williams, E. R. *Anal. Chem.* **2013**, *85*, 138-146.
- (36) Li, Y.; Cole, R. B. *Anal. Chem.* **2003**, *75*, 5739-5746.
- (37) Yuill, E. M.; Sa, N.; Ray, S. J.; Hieftje, G. M.; Baker, L. A. *Anal. Chem.* **2013**, *85*, 8498-8502.
- (38) Ek, P.; Sjodahl, J.; Roeraade, J. *Rapid Commun. Mass Spectrom.* **2006**, *20*, 3176-3182.
- (39) Ek, P.; Schonberg, T.; Sjodahl, J.; Jacksen, J.; Vieider, C.; Emmer, A.; Roeraade, J. *J. Mass Spectrom.* **2009**, *44*, 171-181.
- (40) Mortensen, D. N.; Williams, E. R. *J. Am. Chem. Soc.* **2016**, *138*, 3453-3460.
- (41) Mortensen, D. N.; Williams, E. R. *Anal. Chem., submitted for publication*, **2016**.
- (42) Behrens, S. H.; Grier, D. G. *J. Chem. Phys.* **2001**, *115*, 6716-6721.
- (43) Grimm, R. L.; Beauchamp, J. L. *Anal. Chem.* **2002**, *74*, 6291-6297.
- (44) Jurchen, J. C.; Williams, E. R. *J. Am. Chem. Soc.* **2003**, *125*, 2817-2826.
- (45) Blakney, G. T.; Hendrickson, C. L.; Marshall, A. G. *Int. J. Mass Spectrom.* **2011**, *306*, 246-252.
- (46) Sage, J. T.; Morikis, D.; Champion, P. M. *Biochemistry* **1991**, *30*, 1227-1237.
- (47) Griko, Y. V.; Privalov, P. L.; Venyaminov, S. Y.; Kutyshenko, V. P. *J. Mol. Biol.* **1988**, *202*, 127-138.
- (48) Bergers, J. J.; Vingerhoeds, M. H.; Vanbloois, L.; Herron, J. N.; Janssen, L. H. M.; Fischer, M. J. E.; Crommelin, D. J. A. *Biochemistry* **1993**, *32*, 4641-4649.
- (49) Hemdan, E. S.; Zhao, Y. J.; Sulkowski, E.; Porath, J. *Proc. Natl. Acad. Sci.* **1989**, *86*, 1811-1815.
- (50) Bonincontro, A.; De Francesco, A.; Onori, G. *Colloids Surf. B* **1998**, *12*, 1-5.
- (51) Schmidt, A.; Karas, M.; Dülcks, T. *J. Am. Soc. Mass Spectrom.* **2003**, *14*, 492-500.
- (52) Shastry, R. M. C.; Luck, S. D.; Roder, H. *Biophys. J.* **1998**, *74*, 2714-2721.
- (53) Konno, T. *Protein Sci.* **1998**, *7*, 975-982.
- (54) *CRC Handbook of Chemistry and Physics*, 55th ed.; Weast, R. C., Ed.; CRC Press: Boca Raton, FL, 1974.
- (55) Stein, D.; Kruithof, M.; Dekker, C. *Phys. Rev. Lett.* **2004**, *93*, 035901.
- (56) Gañán-Calvo, A. M.; Dávila, J.; Barrero, A. *J. Aerosol Sci.* **1997**, *28*, 249-275.
- (57) Bushnell, G. W.; Louie, G. V.; Brayer, G. D. *J. Mol. Biol.* **1990**, *214*, 585-595.
- (58) Ainavarapu, S. R. K.; Brujic, J.; Huang, H. H.; Wiita, A. P.; Lu, H.; Li, L.; Walther, K. A.; Carrion-Vazquez, M.; Li, H.; Fernandez, J. M. *Biophys. J.* **2007**, *92*, 225-233.
- (59) Tang, K.; Gomez, A. *J. Colloid Interface Sci.* **1996**, *184*, 500-511.
- (60) Palmer, W. W.; Atchley, D. W.; Loeb, R. F. *J. Gen. Physiol.* **1922**, *4*, 585-589.
- (61) Atchley, D. W.; Nichols, E. G. *J. Biol. Chem.* **1925**, *65*, 729-734.
- (62) Kuwata, K.; Hoshino, M.; Forge, V.; Era, S.; Batt, C. A.; Goto, Y. *Protein Sci.* **1999**, *8*, 2541-2545.

- (63) Kuroda, Y.; Yukinaga, H.; Kitano, M.; Noguchi, T.; Nemati, M.; Shibukawa, A.; Nakagawa, T.; Matsuzaki, K. *J. Pharm. Biomed. Anal.* **2005**, *37*, 423-428.
- (64) Liu, Q.; Shi, J.; Sun, J.; Wang, T.; Zeng, L.; Jiang, G. *Angew. Chem. Int. Ed.* **2011**, *50*, 5913-5917.

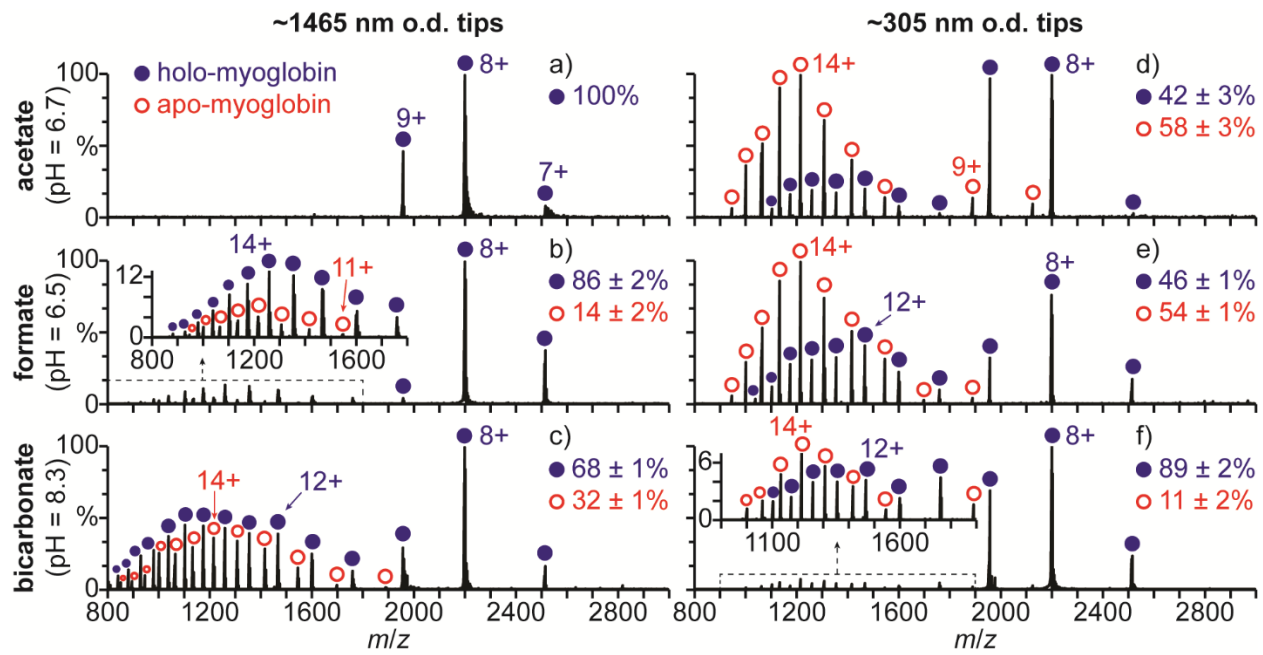


**Figure 6.1.** Mass spectra of hMb ( $pI = 7.4$ ) under electrothermal supercharging conditions (1050 V spray potential) in aqueous solutions containing 100 mM (a,d) ammonium acetate ( $pH = 6.7$ ), (b,e) ammonium formate ( $pH = 6.5$ ), and (c,f) ammonium bicarbonate ( $pH = 8.3$ ) acquired with (a-c)  $\sim 1465$  and (d-f)  $\sim 305$  nm o.d. tips.

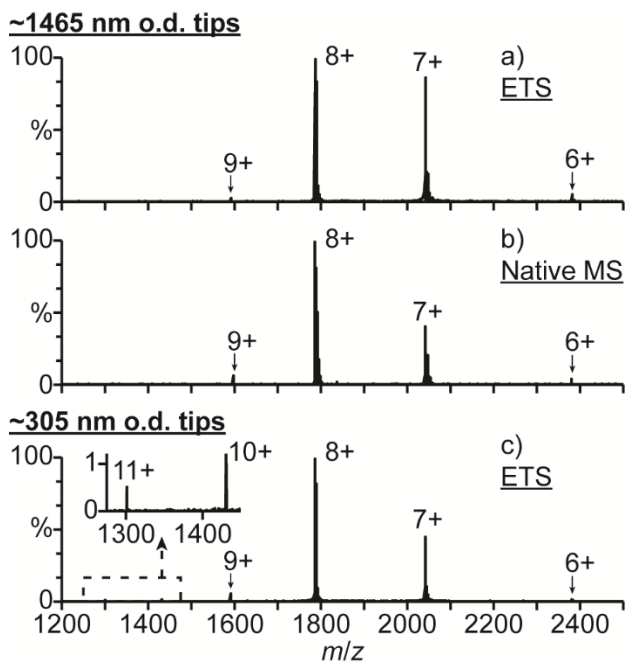


**Figure 6.2.** Mass spectra of lysozyme ( $\text{pI} = 11.3$ ) under (a,c) electrothermal supercharging (1050 V spray potential) and (b) native MS (700 V spray potential) conditions in 100 mM aqueous ammonium acetate ( $\text{pH} = 6.7$ ) acquired with (a,b)  $\sim 1465$  and (c)  $\sim 305$  nm o.d. tips.

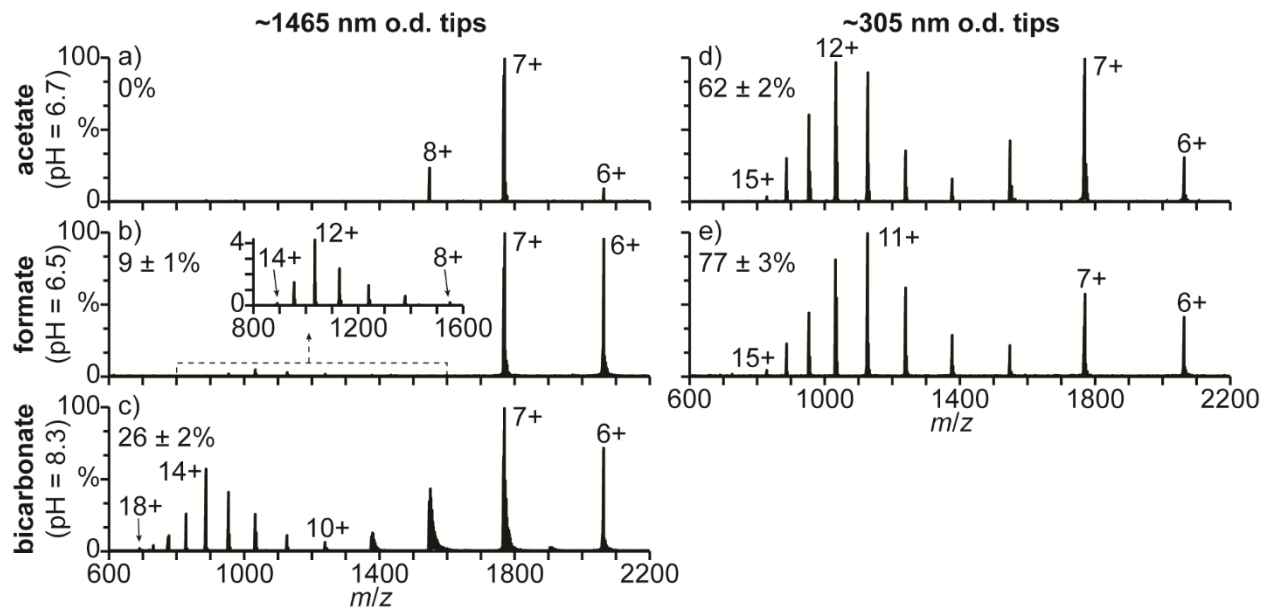


**Figure 6.3.** Mass spectra of cyt *c* (pI = 10.3) under electrothermal supercharging conditions (1050 V spray potential) in aqueous solutions containing 100 mM (a,d) ammonium acetate ( $pH = 6.7$ ), (b,e) ammonium formate ( $pH = 6.5$ ), and (c) ammonium bicarbonate ( $pH = 8.3$ ) acquired with (a-c)  $\sim 1465$  and (d,e)  $\sim 305$  nm o.d. tips. Percentages are the relative abundances of the unfolded fractions ( $\geq 10+$  charge states) of cyt *c*.

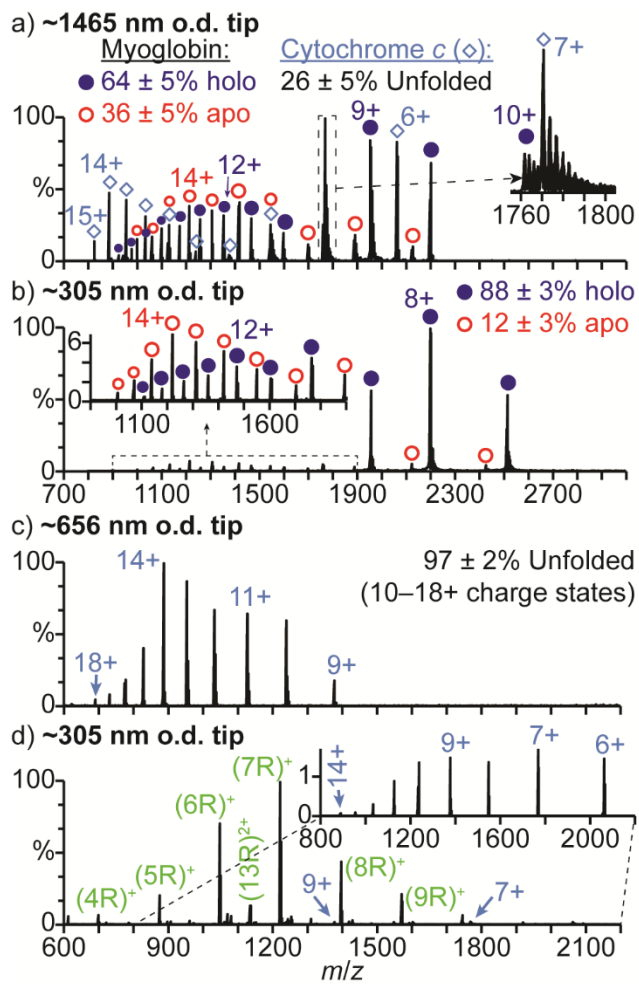


**Figure 6.4.** Mass spectra of cyt c in 100 mM aqueous ammonium bicarbonate solutions (pH = 8.3) acquired with (a) ~1465, (b,d) ~305, and (c) ~656 nm o.d. tips under electrothermal supercharging conditions (1050 V spray potential). The solution used to obtain (a) and (b) contains 10  $\mu$ M hMb, and the solution used to obtain (d) contains 10 mM arginine. The inset in (d) shows only the distribution of ions corresponding to cyt c for clarity.

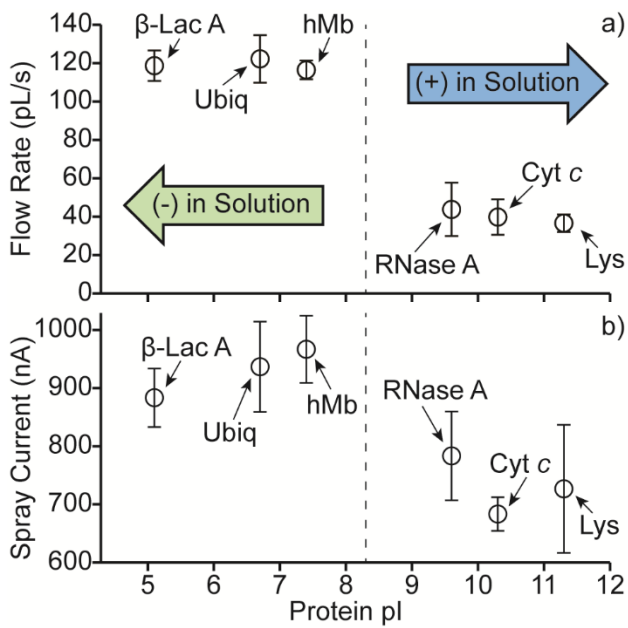


**Figure 6.5.** (a) Flow rates and (b) spray currents of 100 mM aqueous ammonium bicarbonate solutions, each containing a single protein, as a function of the protein pI values. Proteins used include  $\beta$ -lactoglobulin A ( $\beta$ -Lac A, pI = 5.1),<sup>63</sup> ubiquitin (Ubiq, pI = 6.7),<sup>49</sup> holomyoglobin (hMb, pI = 7.4),<sup>48</sup> ribonuclease A (RNase A, pI = 9.6),<sup>64</sup> cytochrome *c* (Cyt *c*, pI = 10.3),<sup>49</sup> and lysozyme (Lys, pI = 11.3).<sup>49</sup>

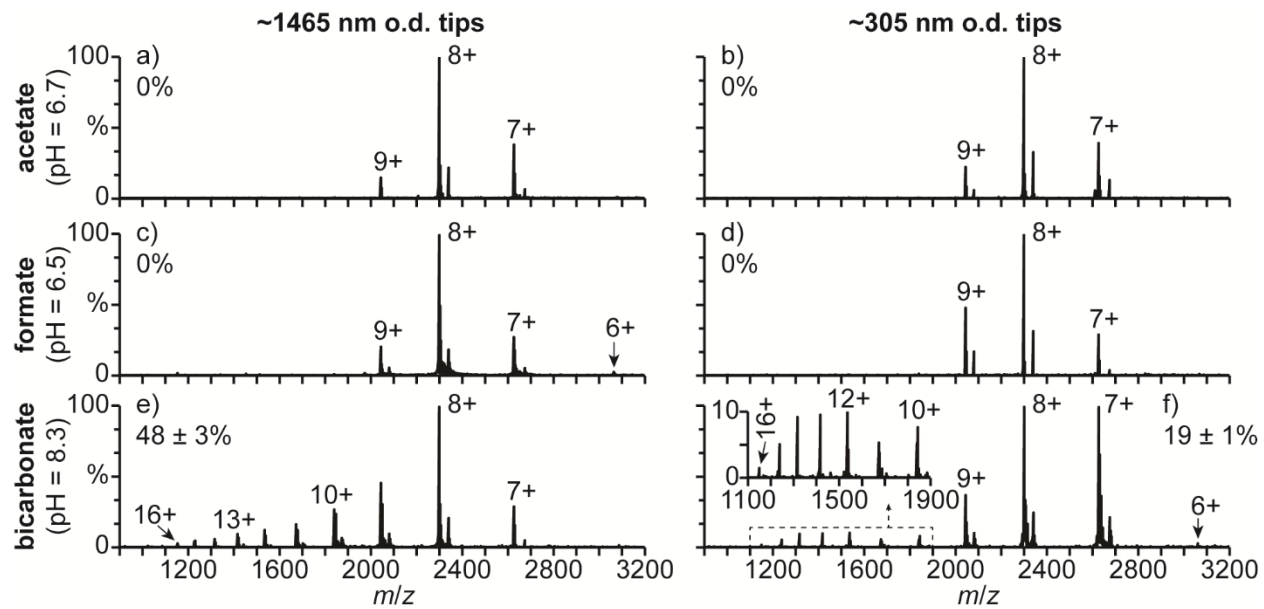


**Figure 6.6.** Mass spectra of  $\beta$ -lac A (pI = 5.1) under electrothermal supercharging conditions (1050 V spray potential) in aqueous solutions containing 100 mM (a,b) ammonium acetate ( $\text{pH} = 6.7$ ), (c,d) ammonium formate ( $\text{pH} = 6.5$ ), and (e,f) ammonium bicarbonate ( $\text{pH} = 8.3$ ) acquired with (a,c,e)  $\sim 1465$  and (b,d,f)  $\sim 305$  nm o.d. tips. Percentages are the relative abundances of the unfolded fractions ( $\geq 10^+$  charge states) of  $\beta$ -lac A.

# Chapter 7

## Microsecond and Nanosecond Polyproline II Helix Formation in Aqueous Nanodrops Measured by Mass Spectrometry

This Chapter is reproduced with permission from  
Mortensen, D.M.; Williams, E.R.

“Microsecond and Nanosecond Polyproline II Helix Formation  
in Aqueous Nanodrops Measured by Mass Spectrometry”

*Submitted to Chemical Communications 2016*  
© 2016 Royal Society of Chemistry

### 7.1 Introduction

Secondary structures in proteins and peptides, such as  $\alpha$ -helices and  $\beta$ -sheets, can form within tens of microseconds or less.<sup>1,2</sup> Explicit-solvent, all-atom simulations now enable folding trajectories of  $\alpha$ -helix and  $\beta$ -structures in biopolymers containing up to 100 amino acids to be computed.<sup>2,3</sup> However, the formation kinetics of other common secondary protein structures, such as that of the polyproline II (PPII) helix, have not been investigated as thoroughly. The PPII helix is an extended left-handed helix with three residues per turn, 3-fold rotational symmetry, and a per residue length of 3.1 Å.<sup>4,5</sup> PPII helices are the primary component of the triple-helix structure of collagen<sup>6</sup> and are commonly found in both natively folded<sup>7–10</sup> and natively unfolded (or disordered)<sup>8,11,12</sup> proteins and peptides. PPII helix structures can occur in polypeptides containing few or no proline residues<sup>13,14</sup> and have been implicated in numerous functional roles,<sup>4,5</sup> including protein-protein interactions,<sup>9</sup> ligand and non-covalent cofactor binding,<sup>15–17</sup> and even in the formation of the amyloid plaques associated with diseases involving protein misfolding, such as Parkinson’s.<sup>5,18,19</sup>

The transitions for several individual peptides between a polyproline I (PPI) helix structure in a mostly organic solution to a PPII helix structure in a mostly aqueous solution have been investigated and occur within minutes to hours, depending on the reaction temperature and on the amino-acid sequence.<sup>20–22</sup> Formation kinetics of PPII helices in more native-like buffered aqueous solutions, however, have not been measured. Recently, double-barrel nano-electrospray ionization (nanoESI) emitters, also known as theta-glass emitters, have been used to rapidly mix solutions during nanoESI to investigate numerous room-temperature reactions,<sup>23–27</sup> including monitoring protein folding reactions that occur in microseconds.<sup>26,27</sup> A 2.2  $\mu$ s folding time constant for the formation of a  $\beta$ -hairpin in a 14 residue peptide was determined, which is the fastest folding event that has been directly measured with a rapid mixing technique.<sup>27</sup> Reaction times of between 1 and 22  $\mu$ s have been achieved with these devices by varying the solution flow rate, which depends on the backing pressure and on the nanoESI-emitter tip size.<sup>27</sup> Here, rapid mixing with theta-glass emitters is used to investigate the rates of formation for PPII helices in two short (16 and 21 residue) peptides. These peptides are prepared in acidified aqueous solutions in which they are highly unfolded and mixed with buffered aqueous solutions during nanoESI to increase the solution pH and induce the formation of the PPII helices. These

structural transitions are measured using mass spectrometry, and information about the equilibrium structures of the peptides is obtained with circular dichroism (CD).

## 7.2 Experimental

Mass spectra are acquired using a 9.4 T Fourier-transform ion cyclotron resonance mass spectrometer that is described elsewhere.<sup>28</sup> Rapid mixing and ion formation are performed using theta glass capillaries (Warner Instruments, LLC; Hamden, CT) pulled into tips with outer diameters of between  $1465 \pm 134$  and  $244 \pm 61$  nm using a model p-87 Flaming/Brown micropipette puller (Sutter Instruments Co., Novato, CA). Grounded platinum wires are brought into contact with the solutions in the emitters, and a backing pressure of either 5 or 10 psi is applied to the back end of the capillary, depending on the desired reaction time.<sup>27</sup> NanoESI is initiated by applying about a -700 V potential to the heated capillary of the ESI interface. Average charges are computed as abundance weighted sums of the charge states, and uncertainties are standard deviations from triplicate measurements. CD spectra are acquired using a model 410 circular dichroism spectrometer (Aviv Biomedical Inc., Lakewood, NJ).

Solutions of [Asp<sup>76</sup>]-parathyroid hormone fragment 64–84 (amino-acid sequence: EKSLG EADKA DVDVL TKAKS Q) and neurogranin fragment 28–43 (amino-acid sequence: AAKIQ ASFRG HMARK K) are prepared with 10  $\mu$ M analyte concentrations. The initial pH of droplets formed during the rapid mixing experiments is estimated to be  $4.7 \pm 0.3$ . This value is determined using the initial concentrations of acetic acid ( $pK_a = 4.8$ ) and ammonia ( $pK_b = 4.8$ , both at 25 °C)<sup>29</sup> in the droplets. Initial concentrations in the nanodrops are determined from the initial concentrations of the solutions in each barrel and the relative flow rates of these solutions during nanoESI. Relative flow rates are determined using Leu- and Met-enkephalin as internal standards as described previously.<sup>25</sup>

## 7.3 Results and Discussion

CD spectra of parathyroid hormone fragment 64-84 (PTH<sub>64-84</sub>) in both a 100 mM aqueous acetic acid solution (pH = 2.9) and the acetic acid solution mixed with a 100 mM aqueous ammonium acetate solution at a 1:1 ratio (equilibrium, pH = 4.7) are shown in Figure 7.1 as dashed red and solid blue lines, respectively. There are negative peaks at  $\leq 200$  and 223 nm in both spectra. These peaks are at similar wavelengths as those in the CD spectrum of the seven residue peptide XAO in a buffered aqueous solution at pH = 7.0, which has negative peaks at 198 and 227 nm.<sup>13</sup> XAO has significant PPII helix structure ( $\geq 50\%$ ), as well as some  $\beta$ -structures, including turns.<sup>13,14</sup> The similarities between the CD spectrum reported here for PTH<sub>64-84</sub> and that reported previously for XAO suggest that PTH<sub>64-84</sub> is composed primarily of PPII helix structures and likely contains some  $\beta$ -structures. These results are consistent with dark field electron microscopy results reported for intact parathyroid hormone in 80 mM aqueous ammonium acetate nanodrops (pH = 7.4),<sup>30</sup> which indicate that residues 69–82 of parathyroid hormone adopt a helical structure and residues 65–68 adopt a turn structure. The intensities of the peaks at  $\leq 200$  and 223 nm in Figure 7.1 are ~2.8 and ~2.6 times greater, respectively, in the CD spectrum of the mixed solution at equilibrium than in that of the acetic acid solution. This result indicates that the structures corresponding to the peaks at  $\leq 200$  and 223 nm are disrupted to a significant extent in the acetic acid solution.

NanoESI of PTH<sub>64-84</sub> in the acetic acid solution (pH = 2.9) results in the formation of the 3+ and 4+ charge states with an average charge of  $3.70 \pm 0.02$  (Figure 7.2a). NanoESI of the acetic acid solution mixed with the ammonium acetate solution at a 1:1 ratio prior to nanoESI (equilibrium, pH = 4.7) results in the 2+ and 3+ charge states with an average charge of  $2.80 \pm 0.01$  (Figure 7.2b). The extent of charging for protein and peptide ions in nanoESI depends on many factors, but solution-phase conformation is one of the most important. Folded conformers charge less than unfolded conformers.<sup>31,32</sup> Therefore, the lower average charge obtained with the mixed solution at equilibrium (2.80) than with the acetic acid solution (3.70) is consistent with PTH<sub>64-84</sub> adopting a more folded structure in the mixed solution than in the acetic acid solution. The 2+ and 3+ charge states comprise ~3.3 times more of the population with the mixed solution at equilibrium (100%, Figure 7.2b) than with the acetic acid solution ( $30 \pm 2\%$ , Figure 7.2a). This result is consistent with the ~2.8 and ~2.6 times greater intensities of the peaks at  $\leq 200$  and 223 nm, respectively, in the CD spectrum of the mixed solution at equilibrium than in the CD spectrum of the acetic acid solution (Figure 7.1). These results suggest that the 2+ and 3+ charge states correspond to PPII helix rich structures, whereas the 4+ charge state corresponds to more highly unfolded structures.

The acidified PTH<sub>64-84</sub> solution was mixed with the aqueous ammonium acetate solution using theta-glass emitters with flow rates of ~48, ~120, and ~383 pL/s (Figure 7.2c-e, respectively). These flow rates were obtained using various tip sizes and backing pressures<sup>27</sup> and correspond to reaction times of  $1.0 \pm 0.0$ ,  $3.0 \pm 0.1$ , and  $5.3 \pm 0.2 \mu s$ , respectively.<sup>27</sup> These reaction times were obtained from the extent of folding that occurred during nanoESI for Trp-cage, a 20 residue mini-protein with a known folding time constant of  $4.1 \mu s$ . The average charge of PTH<sub>64-84</sub> decreases with increasing reaction time from  $3.37 \pm 0.03$  at  $1.0 \mu s$  to  $2.78 \pm 0.04$  at  $5.3 \mu s$ . At  $5.3 \mu s$  (Figure 7.2e), the average charge of PTH<sub>64-84</sub> ( $2.78 \pm 0.04$ ) is the same within error as that obtained for the mixed solution at equilibrium ( $2.80 \pm 0.01$ , Figure 7.2b). At shorter reaction times (Figure 7.2c and 7.2d), the average charge is higher than that obtained at equilibrium. These results indicate that the folding of PTH<sub>64-84</sub> reaches equilibrium within  $5.3 \mu s$  but not within  $\leq 3.0 \mu s$ .

The folding time constant for the formation of the PPII helix conformation in PTH<sub>64-84</sub> can be obtained from the extent of protein folding that occurs by modelling this reaction as a two state folding reaction.<sup>33</sup> Average charges can be used to determine the extent of folding and to obtain protein folding time constants<sup>27</sup> using the equation:

$$t = \tau \ln \left( \frac{q_e - q_o}{q_e - q_t} \right) \quad (1)$$

where t is the reaction time,  $\tau$  is the protein folding time constant, and  $q_e$ ,  $q_o$ , and  $q_t$  are the average charges at equilibrium and at times 0 and t, respectively. The folding time constant for the formation of the PPII helix structure in PTH<sub>64-84</sub> is obtained from the rapid mixing data in which equilibrium is not reached (Figure 7.2c and 7.2d) using eq 1. Folding time constants of  $1.6 \pm 0.2$  and  $1.4 \pm 0.3 \mu s$  are obtained at reaction times of  $1.0$  and  $3.0 \mu s$ , respectively (Figure 7.2c and 7.2d). These values are the same within error, and the average value is  $1.5 \pm 0.3 \mu s$ . These results show that PTH<sub>64-84</sub> folds from a highly unfolded structure to a mostly PPII helix structure within a few microseconds.

To confirm that PPII helices can form within this time frame, experiments were also performed with a second peptide with a PPII helix conformation. CD spectra of neurogranin

fragment 28–43 ( $\text{Ng}_{28-43}$ ) in a 100 mM aqueous acetic acid solution ( $\text{pH} = 2.9$ ) and in the acetic acid solution mixed with a 100 mM aqueous ammonium acetate solution at a 1:1 ratio (equilibrium,  $\text{pH} = 4.7$ ) are shown in Figure 7.3 as dashed red and solid blue lines, respectively. There is only a small negative peak centered at  $\leq 200$  nm for the acetic acid solution. However, there are negative peaks at 202 and 233 nm and a positive peak at 219 nm for the premixed solution at equilibrium. A negative peak at 202 nm and a positive peak at 219 nm also occur in the CD spectrum of native polyproline, which adopts a PPII helix structure.<sup>34</sup> The similarities between the CD spectrum of native polyproline and that of  $\text{Ng}_{28-43}$  in the mixed solution at equilibrium indicates that  $\text{Ng}_{28-43}$  adopts a PPII helix conformation in the mixed solution. The weak negative peak centered at 233 nm may correspond to a small portion of  $\text{Ng}_{28-43}$  adopting an  $\alpha$ -helix conformation. Two broad negative peaks centered at  $\sim 208$  and  $\sim 222$  nm are typically observed in the CD spectra of  $\alpha$ -helices.<sup>35</sup> The negative peak normally observed at 208 nm may be unresolved from the strong negative peak at 202 nm. Overlap with the positive peak at 219 nm corresponding to  $\alpha$ -helix regions of  $\text{Ng}_{28-43}$  may result in reduced signal intensity at 222 nm and thus an apparent shift to the higher 233 nm wavelength. The absence of peaks at 202, 219, and 233 nm in the CD spectrum of the acetic acid solution indicates that the majority of the PPII helix structure is disrupted in this solution.

Mass spectra of  $\text{Ng}_{28-43}$  in the acetic acid solution ( $\text{pH} = 2.9$ ) and the acetic acid solution mixed with the ammonium acetate solution at a 1:1 ratio prior to nanoESI (equilibrium,  $\text{pH} = 4.7$ ) are shown in Figure 7.4a and 7.4b, respectively. With the acetic acid solution (Figure 7.4a), the 3+ and 4+ charge states are formed and the 4+ is the most abundant (average charge =  $3.95 \pm 0.02$ ).  $\text{Ng}_{28-43}$  is a 16 residue peptide, so 25% of the residues are charged in the 4+ charge state. To obtain similar extents of charging for ubiquitin and cytochrome *c* ions (27.6% and 23.1% of residues charged, respectively), the proteins must be significantly unfolded and the ions adopt near-linear conformations.<sup>36</sup> This result suggests that the 4+ charge state of  $\text{Ng}_{28-43}$  corresponds to highly unfolded conformations in solution. In the mass spectrum of the mixed solution at equilibrium (Figure 7.4b), the 2–4+ charge states are formed and the 3+ is the most abundant (average charge =  $3.04 \pm 0.04$ ). The average charge obtained from this solution is significantly less than that obtained with the acetic acid solution ( $3.95 \pm 0.02$ ). This result is consistent with  $\text{Ng}_{28-43}$  adopting a more folded structure in the mixed solution at equilibrium than in the acetic acid solution, consistent with the results obtained for these respective solutions using CD.

The acidified  $\text{Ng}_{28-43}$  solution was mixed with the ammonium acetate solution using the theta-glass emitters with a flow rate ( $\sim 48$  pL/s) that results in a reaction time of 1.0  $\mu\text{s}$  (Figure 7.4c). The 2–4+ charge states are formed with an average charge of  $3.02 \pm 0.04$ . This average charge is the same to within error as that obtained for a 1:1 mixture of these solutions at equilibrium ( $3.04 \pm 0.04$ , Figure 7.4b). This result indicates that the formation of the PPII helix structure in  $\text{Ng}_{28-43}$  reaches equilibrium within 1.0  $\mu\text{s}$ . An upper limit to the folding time constant of  $\text{Ng}_{28-43}$  can be obtained with these results. An average charge of 3.10 ( $2\sigma$  above that obtained in the rapid mixing experiments) corresponds to a folding time constant of  $\sim 400$  ns. To obtain the lower average charge of 3.02 obtained in the rapid mixing experiments would require an even shorter folding time constant. Therefore, the formation of the PPII helix in  $\text{Ng}_{28-43}$  occurs with a time constant of  $< 400$  ns. An approximate “speed limit” of  $n/100$   $\mu\text{s}$ , where  $n$  is the number of residues, has been reported for the folding of single-domain proteins and peptides.<sup>1</sup>  $\text{Ng}_{28-43}$  is a 16 residue peptide and thus has an approximate speed limit for folding of the entire peptide of 160 ns. The  $< 400$  ns folding time constant obtained for the formation of the PPII helix in  $\text{Ng}_{28-43}$  indicates that the PPII helix in this peptide must form at a rate very close to the speed limit for

the formation of  $\alpha$ -helix and  $\beta$ -structures in similarly sized peptides. In contrast, the 1.5  $\mu$ s folding time constant for the formation of the PPII helix structure in PTH<sub>64-84</sub> is about an order of magnitude greater than the approximate speed limit (210 ns for a 21 residue peptide). The significant difference in folding time constants obtained for these two peptides shows that the formation time of PPII helices from highly unfolded structures depends on the amino-acid sequence, consistent with results reported for the transition from PPI to PPII helices.<sup>20-22</sup>

#### 7.4 Conclusions

Results from this study demonstrate that the formation of PPII helix structures can occur within a few microseconds or less in buffered aqueous solutions and that the formation of these structures can be monitored with mass spectrometry using rapid mixing from theta-glass emitters. To the best of our knowledge, the time constants measured here for the formation of PPII helix structures in buffered aqueous solutions are the first of their kind. These measurements should serve as useful benchmarks for comparisons with computational simulations. The formation time constants of other structures that fold on a similar time scale should be readily measurable using this technique.

The authors thank Charlotte Nixon and Professor Susan Marqusee for use of the circular dichroism spectrometer and the National Institutes of Health for funding (R01GM097357).

## 7.5 References

- (1) Kubelka, J.; Hofrichter, J.; Eaton, W. A. *Curr. Opin. Struct. Biol.* **2004**, 14, 76-88.
- (2) Lindorff-Larsen, K.; Piana, S.; Dror, R. O.; Shaw, D. E. *Science* **2011**, 334, 517-520.
- (3) Lane, T. J.; Shukla, D.; Beauchamp, K. A.; Pande, V. S. *Curr. Opin. Struct. Biol.* **2013**, 23, 58-65.
- (4) Schweitzer-Stenner, R. *Mol. BioSyst.* **2012**, 8, 122-133.
- (5) Adzhubei, A. A.; Sternberg, M. J. E.; Makarov, A. A. *J. Mol. Biol.* **2013**, 425, 2100-2132.
- (6) Shoulders, M. D.; Raines, R. T. *Annu. Rev. Biochem.* **2009**, 78, 929-958.
- (7) Adzhubei, A. A.; Sternberg, M. J. E. *J. Mol. Biol.* **1993**, 229, 472-493.
- (8) Bochicchio, B.; Tamburro, A. M. *Chirality* **2002**, 14, 782-792.
- (9) Cubellis, M. V.; Caillez, F.; Blundell, T. L.; Lovell, S. C. *Proteins Struct. Funct. Bioinf.* **2005**, 58, 880-892.
- (10) Berisio, R.; Loguercio, S.; De Simone, A.; Zagari, A.; Vitagliano, L. *Protein Peptide Lett.* **2006**, 13, 847-854.
- (11) Shi, Z. S.; Woody, R. W.; Kallenbach, N. R. *Adv. Protein Chem.* **2002**, 62, 163-240.
- (12) Zhu, F.; Kapitan, J.; Tranter, G. E.; Pudney, P. D. A.; Isaacs, N. W.; Hecht, L.; Barron, L. D. *Proteins Struct. Funct. Bioinf.* **2008**, 70, 823-833.
- (13) Shi, Z. S.; Olson, C. A.; Rose, G. D.; Baldwin, R. L.; Kallenbach, N. R. *Proc. Natl. Acad. Sci.* **2002**, 99, 9190-9195.
- (14) Schweitzer-Stenner, R.; Measey, T. J. *Proc. Natl. Acad. Sci.* **2007**, 104, 6649-6654.
- (15) Detlefsen, D. J.; Thanabal, V.; Pecoraro, V. L.; Wagner, G. *Biochemistry* **1991**, 30, 9040-9046.
- (16) Elangovan, S.; Margolis, H. C.; Oppenheim, F. G.; Beniash, E. *Langmuir* **2007**, 23, 11200-11205.
- (17) Pascal, C.; Pate, F.; Cheynier, V.; Delsuc, M. *Biopolymers* **2009**, 91, 745-756.
- (18) Blanch, E. W.; Morozova-Roche, L. A.; Cochran, D. A. E.; Doig, A. J.; Hecht, L.; Barron, L. D. *J. Mol. Biol.* **2000**, 301, 553-563.
- (19) Syme, C. D.; Blanch, E. W.; Holt, C.; Jakes, R.; Goedert, M.; Hecht, L.; Barron, L. D. *Eur. J. Biochem.* **2002**, 269, 148-156.
- (20) Shi, L.; Holliday, A. E.; Khanal, N.; Russell, D. H.; Clemmer, D. E. *J. Am. Chem. Soc.* **2015**, 137, 8680-8683.
- (21) Lin, Y.; Chu, L.; Horng, J. *J. Phys. Chem. B* **2015**, 119, 15796-15806.
- (22) Shi, L.; Holliday, A. E.; Glover, M. S.; Ewing, M. A.; Russell, D. H.; Clemmer, D. E. *J. Am. Soc. Mass Spectrom.* **2016**, 27, 22-30.
- (23) Mark, L. P.; Gill, M. C.; Mahut, M.; Derrick, P. J. *Eur. J. Mass Spectrom.* **2012**, 18, 439-446.
- (24) Fisher, C. M.; Kharlamova, A.; McLuckey, S. A. *Anal. Chem.* **2014**, 86, 4581-4588.
- (25) Mortensen, D. N.; Williams, E. R. *Anal. Chem.* **2014**, 86, 9315-9321.
- (26) Mortensen, D. N.; Williams, E. R. *Anal. Chem.* **2015**, 87, 1281-1287.
- (27) Mortensen, D. N.; Williams, E. R. *J. Am. Chem. Soc.* **2016**, 138, 3453-3460.
- (28) Jurchen, J. C.; Williams, E. R. *J. Am. Chem. Soc.* **2003**, 125, 2817-2826.

- (29) *CRC Handbook of Chemistry and Physics*, 55th ed.; Weast, R. C., Ed.; CRC Press: Boca Raton, FL, **1974**.
- (30) Fiskin, A. M.; Cohn, D. V.; Peterson, G. S. *J. Biol. Chem.* **1977**, 252, 8261-8268.
- (31) Kaltashov, I.; Eyles, S. *Mass Spectrom. Rev.* **2002**, 21, 37-71.
- (32) Liu, J.; Konermann, L. *J. Am. Soc. Mass Spectrom.* **2009**, 20, 819-828.
- (33) Gilmanshin, R.; Callender, R.; Dyer, R. *Nat. Struct. Biol.* **1998**, 5, 363-365.
- (34) Lopes, J. L. S.; Miles, A. J.; Whitmore, L.; Wallace, B. A. *Protein Sci.* **2014**, 23, 1765-1772.
- (35) Greenfield, N. J.; Fasman, G. D. *Biochemistry* **1969**, 8, 4108-4116.
- (36) Going, C. C.; Williams, E. R. *Anal. Chem.* **2015**, 87, 3973-3980.

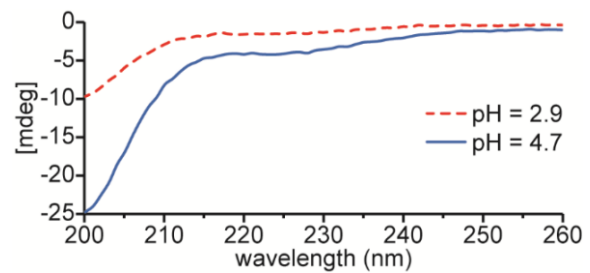


**Figure 7.1.** Circular dichroism spectra of PTH<sub>64-84</sub> in a 100 mM aqueous acetic acid solution (pH = 2.9, dashed red line) and the acetic acid solution mixed with a 100 mM aqueous ammonium acetate solution at a 1:1 ratio (equilibrium, pH = 4.7, solid blue line).

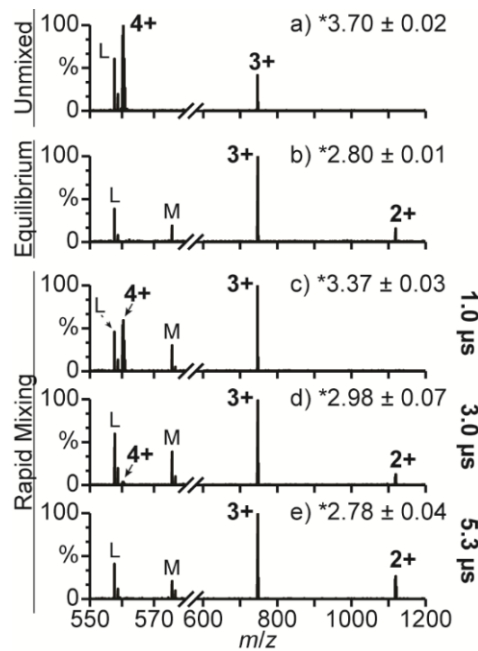


**Figure 7.2.** Mass spectra of (a) PTH<sub>64-84</sub> in a 100 mM aqueous acetic acid solution (pH = 2.9), (b) the acetic acid solution mixed with a 100 mM aqueous ammonium acetate solution at a 1:1 ratio prior to nanoESI (equilibrium, pH = 4.7), and (c) the acetic acid solution mixed with the ammonium acetate solution using the theta-glass emitters with flow rates that result in reaction times of (c) 1.0, (d) 3.0, and (e) 5.3  $\mu$ s. (\*) denotes average charge state. (L) and (M) denote Leu- and Met-enkephalin, respectively, which are used as internal standards to measure the relative flow rates of the solutions in the individual barrels of the theta-glass emitters.

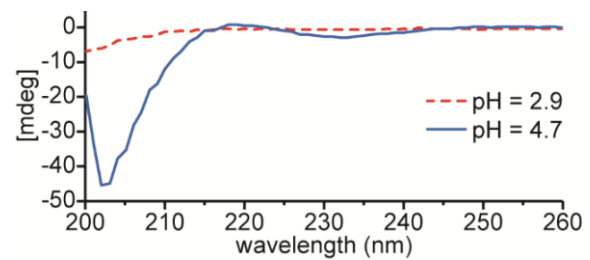


**Figure 7.3.** Circular dichroism spectra of Ng<sub>28-43</sub> in a 100 mM aqueous acetic acid solution (pH = 2.9, dashed red line) and the acetic acid solution mixed with a 100 mM aqueous ammonium acetate solution at a 1:1 ratio (equilibrium, pH = 4.7, solid blue line).

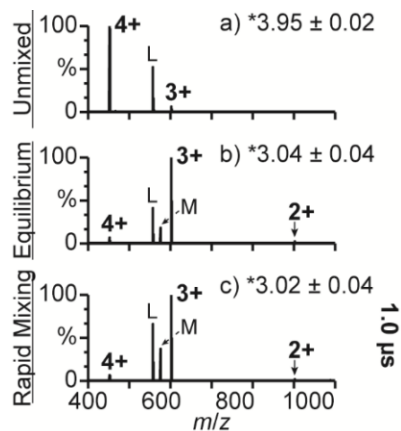


**Figure 7.4.** Mass spectra of (a) Ng<sub>28-43</sub> in a 100 mM aqueous acetic acid solution (pH = 2.9), (b) the acetic acid solution mixed with a 100 mM aqueous ammonium acetate solution at a 1:1 ratio prior to nanoESI (equilibrium, pH = 4.7), and (c) the acetic acid solution mixed with the ammonium acetate solution using the theta-glass emitters with a flow rate that results in a reaction time of 1.0  $\mu$ s. (\*) denotes average charge state. (L) and (M) denote Leu- and Met-enkephalin, respectively, which are used as internal standards to measure the relative solution flow rates.

# Chapter 8

## Collisional Cross Sections with T-Wave Ion Mobility Spectrometry without Experimental Calibration

This Chapter is reproduced with permission from

Mortensen, D.M.; Susa, A.C.; Williams, E.R.

“Collisional Cross Sections with T-Wave Ion

Mobility Spectrometry without Experimental Calibration”

*Submitted to International Journal of Mass Spectrometry 2016*

© 2016 American Chemical Society

### 8.1 Introduction

Ion mobility spectrometry (IMS) separates gaseous ions on the bases of their collisional cross sections, which depend on shape, mass, charge state, temperature, and ion-neutral interactions.<sup>1</sup> IMS has been used in many applications, including the separation of atomic ions,<sup>2,3</sup> small clusters,<sup>3-5</sup> and tryptic digests,<sup>6-8</sup> as well as for studying the gas-phase conformations of biopolymers,<sup>9-11</sup> biopolymer complexes,<sup>12-14</sup> and viruses.<sup>15</sup> IMS can be done using static drift tube,<sup>16-18</sup> field-asymmetric,<sup>18-21</sup> aspiration,<sup>22,23</sup> and travelling-wave<sup>24,25</sup> IMS devices. In travelling-wave IMS (TWIMS), a potential wave is generated by applying a DC potential to a set of adjacent ring electrodes, and this wave is moved through the device with time.<sup>26</sup> Some ions traverse the device at the velocity of the wave, and others are overtaken by the wave, resulting in ion separation.<sup>26,27</sup> The shape of the wave and the distance between consecutive waves can differ between TWIMS devices depending on instrument design and parameters.<sup>25</sup>

In static drift tube (DT)IMS, ion cross section can be directly determined from the measured ion drift times.<sup>28,29</sup> Determining ion cross sections with TWIMS is typically done by calibrating the drift times to collisional cross sections measured using DTIMS.<sup>30-33</sup> Cross sections obtained for ions generated from denaturing solutions using TWIMS chemical calibration techniques are generally very similar to those obtained using DTIMS (average difference  $\pm 1\sigma = 1 \pm 2\%$ ),<sup>31,34-36</sup> although differences in cross sections as high as 9% have been reported.<sup>36</sup> Obtaining accurate collisional cross sections for ions generated from buffered aqueous solutions in which the proteins have native conformations and activities using TWIMS is often more challenging.<sup>35,37</sup> This is because the collisional cross sections of protein ions formed from buffered aqueous solutions increase in TWIMS cells as the velocity of the traveling wave increases as a result of ion heating and subsequent unfolding.<sup>38,39</sup> Methods for obtaining collisional cross sections of ions formed from buffered aqueous solutions have been presented and rely on selecting calibrant ions which unfold during TWIMS at similar rates as the ions of interest.<sup>35,37</sup>

A method for directly measuring the mobility of ions using TWIMS was reported.<sup>40</sup> SIMION modeling was used to derive an equation that relates the ion mobility and the wave velocity to the minimum wave height required to cause an ion to traverse the TWIMS device at the velocity of the wave. The minimum wave height is determined by incrementally increasing the wave height until the ion traverses the device at the wave velocity. Cross sections obtained using this method are the same within 5% as those obtained with DTIMS.<sup>40</sup> However, there are

currently no methods that enable cross sections to be determined from single TWIMS drift time measurements.<sup>12,27,33,41</sup>

Here, a method for relating TWIMS drift times with collisional cross sections using computational simulations is presented. This method is developed using SIMION modelling of the TWIMS potential wave and equations that describe the velocity of ions in gases under the influence of electric fields. Cross sections obtained using this method using low wave velocities that do not result in protein unfolding are very similar to those obtained with DTIMS (average difference = 0.3%) for ions formed from both denaturing and buffered aqueous solutions. At high wave velocities, the collisional cross sections obtained using the computational method presented here are significantly larger (as much as 64% larger) than those obtained with DTIMS, especially for ions formed from buffered aqueous solutions. These higher cross sections are likely a result of protein unfolding during TWIMS as a result of ion heating.<sup>38,39</sup> Results from this study show that ion collisional cross sections can be determined from single TWIMS drift time measurements but that gentle instrument settings should be used to reduce any uncertainties due to protein unfolding during the measurement.

## 8.2 Experimental

Experiments are performed using a Synapt G2 high definition mass spectrometer (Waters Corp., Milford, MA). Ions are formed by nanoESI using borosilicate capillaries pulled into tips with a model P-87 Flaming/Brown micropipette puller (Sutter Instruments Co., Novato, CA). A platinum wire is brought into contact with the solution loaded into the capillary, and nanoESI is initiated by applying a ~800 V potential to the platinum wire relative to the entrance of the mass spectrometer. Flow rates in the helium and TWIMS cells are kept constant at 180 and 90 mL/min, respectively. The pressure in the TWIMS cell was 3.2 mbar in all experiments. TWIMS separation begins after a period of time, known as the mobility trapping release time, has passed at the beginning of each drift experiment. To correct for this time delay, the measured drift times are adjusted by subtracting the 200  $\mu$ s mobility trapping release time. With some wave conditions, low mobility ions do not traverse the TWIMS cell within the time frame of a single drift experiment. When this occurs, the measured drift times are adjusted by adding the 36.268 ms length of a single drift experiment less the 200  $\mu$ s mobility trapping release time. 200 drift bins are used for all experiments, resulting in a bin width of ~181  $\mu$ s. SIMION version 8.0<sup>42</sup> is used to model the electric field along the axis of the TWIMS device.

Bovine serum albumin, ubiquitin, equine cytochrome *c*, myoglobin, concanavalin A from canavalia ensiformis, bradykinin, angiotensin II, and DL-polyalanine are obtained from Sigma-Aldrich (St. Louis, MO), and acetonitrile, glacial acetic acid, and methanol are from Fisher Scientific (Fair Lawn, NJ). Solutions are prepared in 18.2 M $\Omega$  water from a Milli-Q water purification system (Millipore, Billerica, MA). Polyalanine solutions are prepared with 0.1 mg/ml analyte concentrations, and all other solutions are prepared with 10  $\mu$ M analyte concentrations. Serum albumin and concanavalin A ions are formed from 200 mM aqueous ammonium acetate solutions in which they have native-like conformations and activities. Denatured polyalanine ions are formed from a 49/49/2 water, acetonitrile, acetic acid solution, and all other denatured protein and peptide ions are formed from 49/49/2 water, methanol, acetic acid solutions. DTIMS cross sections for polyalanine are from reference 37, and all other DTIMS cross sections are from reference 36.

### 8.3 Calculations

**8.3.1 Modelling the TWIMS Electric Potential.** The ion drift velocity,  $v$ , is the velocity of an ion in a gas that is induced by an electric field<sup>28,29</sup> and is defined in eq. 1:

$$v = KE \quad (1)$$

where  $E$  is the electric field strength and  $K$  is the ion mobility. The ion mobility is described by the Mason–Schamp equation<sup>1</sup>:

$$K = \frac{3ze}{16N} \left( \frac{2\pi}{\mu k_b T} \right)^{1/2} \frac{1}{\Omega} \quad (2)$$

where  $z$  is the ion charge state,  $e$  is the elementary charge,  $N$  is the background gas number density,  $\mu$  is the reduced mass between the ion and the background gas,  $k_b$  is Boltzmann's constant,  $T$  is the background gas temperature, and  $\Omega$  is the ion cross section. In order to determine the ion drift velocity using eq. 1, the electric field strength must be known. The geometry of the electric field varies between TWIMS devices depending on instrument design.<sup>25</sup> In a second generation TWIMS device, such as that used in these experiments, the electric field is generated by applying a DC potential with an amplitude referred to as the “wave height” to two consecutive plate pairs, followed by two plate pairs held at instrument ground, and this pattern is repeated throughout the device.<sup>25</sup> The electric field is varied incrementally with time by stepping the DC potential forward by single plate pairs. The electric potential and electric field strength along the axis of a second generation TWIMS device at a given point in time obtained with SIMION using a 40 V wave height are shown as blue lines in Figure 8.1a and 8.1b, respectively. The effective wave height obtained with SIMION is equal to ~89.6% of the applied wave height potential (Figure 8.1a), consistent with the ~90% value reported previously.<sup>25</sup> The electric potential along the axis of the device (Figure 8.1a) appears to be mostly sinusoidal, whereas the electric field strength (Figure 8.1b) resulting from this electric potential appears to have both sinusoidal and triangular wave characteristics.

The electric field strength obtained with SIMION (blue line, Figure 8.1b) is modeled as a sine wave (eq. 3):

$$E = A \sin(\theta x) \quad (3)$$

where  $A$  is the wave amplitude,  $\theta$  is the wave frequency, and  $x$  is the ion position along the axis of the TWIMS device. For convenience,  $x = 0$  is defined as the position at which the maximum electric potential occurs (see Figure 8.1a). The values of  $A$  and  $\theta$  are listed in Table 1. The electric field strength obtained with eq. 3 for a 40 V wave height is shown as a black dashed line in Figure 8.1b. The difference between the calculated electric field strength and that obtained from eq. 3 is shown as a black dashed line in Figure 8.1c. There are significant differences ( $\leq 11.4\%$ ) between the electric field strength obtained with SIMION and that obtained with eq. 3 (Figure 8.1c), indicating that the electric field strength is only crudely modeled by a single sine wave.

A linear combination of three sine waves can more accurately model the electric field strength (eq. 4):

$$E = A_1 \sin(\theta x) + A_2 \sin(30x) + A_3 \sin(50x) \quad (4)$$

where  $A_1$ ,  $A_2$ , and  $A_3$  are the amplitudes of the different waves, respectively (Table 1). The electric field strength along the axis of the TWIMS device obtained with eq. 4 for a 40 V wave height is shown as black exes in Figure 8.1b, and the difference between this electric field and that obtained with SIMION is shown as a solid black line in Figure 8.1c. The difference between these electric field strengths is less than 0.1% at all positions (Figure 8.1c), indicating that the electric field strength along the axis of the TWIMS device is described more accurately by eq. 4 than by eq. 3.

**8.3.2. Calculating Ion Drift Times.** Because the electric field strength is not homogenous throughout the TWIMS device, the ion drift velocity changes with the ion position and, thus, with time as the ion travels through the device. Therefore, a time dependent function is required to describe the motion of ions through the device. Velocity is defined as the change in position over time. Therefore, eq. 1 can be rewritten as:

$$\frac{dx}{dt} = KE \quad (5)$$

where  $t$  is time. Different equations describing the motion of ions through the TWIMS device are derived by combining eq. 5 with eqs. 3 and 4, respectively. Combining eq. 5 with eq. 3 and rearranging results in eq. 6:

$$KAdt = \frac{dx}{\sin(\theta x)} \quad (6)$$

This equation is integrated over a period of time equal to the duration of a single wave step. This duration of time is known as the “dwell” time ( $t_{\text{dwell}}$ ) and is equal to the 254 mm length of the TWIMS device divided by the wave velocity. Integrating eq. 5 over the dwell time and rearranging results in eq. 7:

$$x_t = \frac{2}{\theta} \tan^{-1} \left[ \tan \left( \frac{\theta x_o}{2} \right) \exp(KAt_{\text{dwell}}) \right] \quad (7)$$

where  $x_o$  and  $x_t$  are the ion positions at  $t = 0$  and  $t_{\text{dwell}}$ , respectively. This equation can be used to determine the distance an ion travels through the device during a single wave step ( $x_t - x_o$ ) as a function of the initial ion position and dwell time.

Combining eq. 5 with eq. 4 and rearranging results in eq. 8:

$$Kdt = \frac{dx}{A_1 \sin(\theta x) + A_2 \sin(30x) + A_3 \sin(50x)} \quad (8)$$

The right side of eq. 8 cannot readily be integrated explicitly over time. Therefore, eq. 8 is integrated numerically from  $t = 0$  to  $t_{\text{dwell}}$  using MatLab. An implicit approximation in both eqs. 7 and 8 is that the velocity of an ion changes instantaneously with the change in electric field strength. Therefore, when an ion reaches a position where the electric field strength is zero (i.e.,  $x = -6.05, 0$ , and  $+6.05$  mm, Figure 8.1b), the ion stops moving.

The total distance an ion travels when multiple waves pass through the device is obtained by summing the distance the ion travels during each wave step. The initial ion position in the first computational wave step is chosen arbitrarily, and the final ion position in this wave step is computed from this initial ion position and the instrument dwell time. The potential wave is then stepped forward, resulting in a change in the electric field strength experienced by the ion. The distance the ion travels during this new wave step is then computed as a function of the initial ion position in this wave step and the instrument dwell time. The potential wave is stepped forward and the distance the ion travels during each step is computed over multiple wave steps until the motion of the ion through the device is well characterized.

In order to simulate the motion of an ion as it traverses the TWIMS cell under different conditions, wave parameters are used that result in the same ion traversing the cell at the wave velocity and being overtaken by the travelling waves. In order to simulate an ion traversing the TWIMS cell at the wave velocity a 100 m/s wave velocity and a 40 V wave height are used. For convenience, the ion cross section times the square root of the reduced mass per unit charge ( $\Omega \mu^{1/2} z^{-1}$ ) is defined here as the adjusted cross section. Ion mobility is inversely proportional to the adjusted cross section (eq. 2). A representative plot of the total distance travelled by an ion with an adjusted cross section of  $17.0 \text{ nm}^2 \text{ Da}^{1/2}$  as a function of the number of times the wave is stepped through the device is shown in Figure 8.2a. This adjusted cross section corresponds to the 14+ charge state of bovine serum albumin, which traverses the TWIMS device at the wave velocity with the parameters used to obtain Figure 8.2a but is overtaken by the waves with higher wave velocities. The results in Figure 8.2a are obtained with eq. 7 (black dashed line) and numerical integration of eq. 8 (blue line) using a 1.0 mm initial ion position in the first step. The results obtained with both eqs. 7 and 8 indicate that the ion traverses the 254 mm length of the device after the wave is stepped forward 84 times, which is the same as the number of plate pairs in the device, consistent with an ion traversing the device at the wave velocity.

In order to simulate this same ion under conditions where it is overtaken by the travelling waves, a 2000 m/s wave velocity and a 20 V wave height are used (Figure 8.2b). The results in Figure 8.2b are obtained with eqs. 7 (black dashed line) and 8 (blue line) using a 1.0 mm initial ion position in the first step. When the ion is on the front of the wave, it moves forward through the device towards the detector, but when it is overtaken by a wave, it moves backwards through the device away from the detector (Figure 8.2b). Thus, the position of the ion oscillates as waves are stepped through the device. The results in Figure 8.2b obtained with both eqs. 7 and 8 indicate that under the conditions used here, the ion is overtaken by the wave once every four wave steps but on average moves forward through the device towards the detector, consistent with the motion of a low mobility ion moving through the device.

The average ion drift velocity during a wave step ( $v_{\text{ave}}$ ) is obtained by dividing the average distance the ion travels per wave step ( $d_{\text{ave}}$ ) by the dwell time:

$$v_{\text{ave}} = \frac{d_{\text{ave}}}{t_{\text{dwell}}} \quad (9)$$

The distance the ion travels varies between wave steps, especially when the ion is overtaken by a wave. Therefore, the effect that the number of steps used has on the average distance the ion travels per wave step and, thus, on  $v_{ave}$  is investigated using conditions that result in the ion being overtaken by the travelling waves ( $17.0 \text{ nm}^2 \text{ Da}^{1/2}$  adjusted cross section, 20 V wave height, 2000 m/s wave velocity, Figure 8.3a). Under these conditions, the average ion drift velocity varies significantly for the first several steps (from 51 m/s after step 1 to -27 m/s after step 3) but damps out quickly. With ~3,650 or more steps the variability in the average drift velocity is less than 1%, indicating that the uncertainty in the average drift velocity is negligible after ~3,650 wave steps. For ions with smaller adjusted cross sections, the waves pass by the ion less frequently, which reduces the uncertainty in the average ion drift velocity.

The drift time of an ion through the entire TWIMS device ( $t_{drift}$ ) is determined from the average ion drift velocity per wave step using eq. 10:

$$t_{drift} = \frac{L_{TWIMS}}{v_{ave}} \quad (10)$$

where  $L_{TWIMS}$  is the length of the TWIMS device (254 mm). Drift times obtained with eq. 10 using values for  $v_{ave}$  obtained with eq. 7 and numerical integration of eq. 8 are shown in Figure 8.3b as blue circles and red diamonds, respectively. These drift times are obtained using 10,000 wave steps, a  $17.0 \text{ nm}^2 \text{ Da}^{1/2}$  adjusted cross section, a 20 V wave height, and wave velocities of between 100 and 2000 m/s. The variability in the average distance travelled per wave step is less than 0.4% with 10,000 or more wave steps. Surprisingly, the drift times obtained with eqs. 7 and 8 are the same to within <1.5% at each wave velocity despite the  $\leq 11.4\%$  difference between the electric field strengths obtained with the equations used to derive eqs. 7 and 8 (eqs. 3 and 4, respectively). Similar drift times may be obtained with eqs. 7 and 8 because the average difference between the electric field strengths obtained with eqs. 3 and 4 over a full wavelength (between  $x = -6.05$  and  $+6.05$  mm) is approximately zero (Figure 8.1c). Therefore, any errors that may occur in calculating the distance an ion travels in the individual steps is greatly reduced by using multiple steps. Calculating a single drift time using eq. 7 takes less than 1 s, whereas the same calculation using numerical integration of eq. 8 can take greater than 1 min, depending on instrument conditions. Therefore, it may be advantageous to use eq. 7 when simulating a large number of ions.

## 8.4 Results and Discussion

**8.4.1 Accuracy of the Computed Drift Times.** The drift times of 70 different reference ions are calculated with eq. 10 for wave velocities of between 100 and 2000 m/s and wave heights of 20 and 40 V. These calculated drift times are obtained using average distances traveled per wave step obtained with eq. 7 using 10,000 wave steps, a 1.0 mm initial ion position in the first wave step, and adjusted cross sections calculated using DTIMS cross sectional values. The reference ions range in mass from 231 Da to 103 kDa, in charge from 1+ to 24+, and in collisional cross section measured with DTIMS from 1.51 to  $60.9 \text{ nm}^2$ , and correspond to adjusted cross sections of between  $7.5$  and  $17.0 \text{ nm}^2 \text{ Da}^{1/2}$ . The data obtained with 20 and 40 V wave heights are shown as a function of the adjusted cross sections calculated using DTIMS cross sectional values in Figure 8.4a and 8.4b, respectively. Also shown in these respective

figures are the drift times measured for the reference ions using 20 and 40 V wave heights and various wave velocities. Open and filled shapes correspond to ions formed from denaturing and buffered aqueous solutions, respectively.

The difference between the drift times that are measured in TWIMS and the calculated drift times obtained using the same experimental parameters and the DTIMS cross sectional values is small for ions formed from denaturing solutions (average difference  $\pm 1\sigma = 0 \pm 6\%$ ) for wave velocities of  $\leq 1500$  m/s and both wave heights. These results indicate that TWIMS drift times for a wide variety of protein and peptide ions formed from denaturing solutions can be accurately predicted using the computational method presented here for low wave velocities. In contrast, the measured drift times acquired with a 2000 m/s wave velocity are significantly larger than the calculated drift times at this same wave velocity ( $12 \pm 6\%$  and  $20 \pm 6\%$  larger in Figure 8.4a and 8.4b, respectively). The difference between the measured and calculated drift times for ions generated from buffered aqueous solutions is also low for low wave velocities ( $1 \pm 8\%$  difference for wave velocities of  $\leq 500$  m/s), but the measured drift times are  $32 \pm 6\%$  and  $56 \pm 6\%$  larger than the calculated drift times for wave velocities of 1000 and 1500 m/s, respectively. The width of the ion mobility peaks increases as the wave velocity increases, and with the 2000 m/s wave velocity, the width of the peaks corresponding to the ions formed from buffered aqueous solutions are too broad for measured drift times to be obtained.

**8.4.2 Obtaining Collisional Cross Sections with the Computational Method.** In order to obtain absolute collisional cross sections from TWIMS drift times without experimental calibration, the computed drift times as a function of the adjusted cross sections are fit with second-order polynomials ( $R^2 = 1.00$ ). Although DTIMS cross sectional values were used to calculate the computed drift times used to obtain these polynomial fits, nearly identical fits can be obtained using purely hypothetical adjusted cross sections (Appendix E, Figure E.1), and the relationship between adjusted cross section and TWIMS drift time described by these polynomial fits is entirely independent of any DTIMS cross sectional values. Second-order polynomials are used to obtain these fits because second-order polynomials have been reported to result in the lowest absolute errors for TWIMS chemical calibration curves, compared to that obtained with linear, third-order polynomial, and natural-log fits<sup>36</sup>. Cross sections were obtained from these polynomial fits and the measured drift times of the reference ions. Cross sections are not determined for ions that traverse the TWIMS cell at the wave velocity because no separation occurs for these ions and therefore only an upper limit to the mobility of the ions is obtained. The cross sections obtained for the reference ions using the computational method with 20 and 40 V wave heights and the various wave velocities are plotted in Figure 8.5a and 8.5b, respectively, as a function of the DTIMS cross sections.

The TWIMS computational calibration cross sections obtained for the ions formed from denaturing solutions are extremely similar to those obtained with DTIMS (average difference  $\pm 1\sigma = 0 \pm 3\%$ ) for wave velocities of  $\leq 1500$  m/s. This uncertainty is similar to the uncertainty resulting from the standard experimental calibration approach<sup>36</sup> for obtaining collisional cross sections with TWIMS ( $1 \pm 2\%$ ).<sup>31,34-36</sup> These results indicate that the cross sections for ions formed from denaturing solutions obtained using TWIMS computational calibration with low wave velocities are approximately as accurate as those obtained using TWIMS chemical calibration.

Significantly larger cross sections are obtained for the ions formed from denaturing solutions with TWIMS computational calibration with a 2000 m/s wave velocity than are

obtained with DTIMS ( $7 \pm 4\%$  and  $12 \pm 4\%$  larger in Figure 8.5a and 8.5b, respectively). The higher than expected cross sections are likely due to unfolding of the proteins and peptides during TWIMS as a result of ion heating.<sup>38,39</sup> The extent of unfolding is on average greater for the 40 V wave height ( $12 \pm 4\%$ ) than for the 20 V wave height ( $7 \pm 4\%$ ). This is likely because the electric field strength within the TWIMS cell increases with increasing wave height, resulting in higher drift velocities and, thus, higher energy collisions between the ions and the buffer gas. The difference between the cross sections obtained here with the computational method and those obtained with DTIMS is greater for low charge state ions than for high charge state ions of the same species. For example, the cross section of the 9+ ubiquitin ion obtained with a 2000 m/s wave velocity and a 20 V wave height is about 20% larger than the  $20.9 \text{ nm}^2$  DTIMS cross section for this ion, whereas the cross section of the 13+ ubiquitin ion is only 8% larger than the  $26.0 \text{ nm}^2$  DTIMS cross section for this ion. More unfolding likely occurs for the lower charge states because the lower charge state ions are initially more compact than the high charge state ions<sup>43,44</sup> and can thus unfold to a greater extent during TWIMS.

The extent of unfolding that occurs for polyalanine ions in these experiments depends on the number of amino-acid residues in the peptides. The difference between the collisional cross sections for polyalanine ions obtained here using the computational method with a 2000 m/s wave velocity and 20 and 40 V wave heights compared with those obtained using DTIMS is shown as a function of peptide length in Figure 8.6a and 8.6b, respectively. Circles, squares, and triangles correspond to singly, doubly, and triply charged ions, respectively. The relative extent of unfolding that occurs increases with increase peptide length for each charge state. For example, with the doubly charged ions and a 40 V wave height (blue squares, Figure 8.6b), the difference in cross sections increases from 7% for the 11-residue peptide to 18% for the 26-residue peptide. More unfolding is likely obtained with the longer peptides because these peptides have more structural flexibility than the shorter peptides. More unfolding also occurs for lower charge states than for higher charge states for peptide ions with the same number of residues, and on average, more unfolding occurs with the 40 V wave height ( $10 \pm 4\%$ , Figure 8.6b) than with the 20 V wave height ( $5 \pm 3\%$ , Figure 8.6a), consistent with the results obtained for the protein ions.

The collisional cross sections obtained here with low wave velocities ( $\leq 500 \text{ m/s}$ ) for ions formed from buffered aqueous solutions are also very similar to those obtained with DTIMS ( $1 \pm 5\%$ , Figure 8.5, upper panels), but with 1000 and 1500 m/s wave velocities, the cross sections obtained here are  $19 \pm 6\%$  and  $54 \pm 10\%$  larger, respectively, than those obtained with DTIMS. The relative extent of unfolding that occurs at the high wave velocities is greater for the ions formed from the buffered aqueous solutions than for the ions formed from the denaturing solutions. This is likely because the ions formed from the denaturing solutions are already partially unfolded upon gaseous ion formation, whereas the ions formed from the buffered aqueous solutions are initially more compact. These results are consistent with previous results indicating that collisional cross sections obtain with experimental calibration of TWIMS increase with increasing wave velocity for ions formed from both denaturing and buffered aqueous solutions but that this effect is more prominent for ions formed from buffered aqueous solutions.<sup>38</sup> In summation, the results in Figure 8.5 indicate that computational calibration of TWIMS can be used to obtain absolute collisional cross sections of protein and peptide ions formed from both denaturing and buffered aqueous solutions that are similar to those obtained with DTIMS, but that gentle instrument settings should be used to minimize any unfolding that might occur.

## 8.5 Conclusions

A method for calibrating TWIMS drift times with collisional cross sections using computational simulations is presented. The accuracy of this method is investigated by comparing the collisional cross sections of 70 different reference ions obtained using this method with those obtained using DTIMS. The cross sections obtained here with low wave velocities are very similar to those obtained with DTIMS (average difference = 0.3%) both for ions formed from denaturing solutions and those formed from buffered aqueous solutions. These results demonstrate that collisional cross sections can be obtained from single TWIMS drift time measurements without prior experimental calibration. The method presented here does not take into account intermolecular potentials between the ions and the buffer gas, nor does it include corrections for surface topology.<sup>45</sup> However, the uncertainty in the collisional cross sections obtained using this method is about the same as that in the collisional cross sections obtained using TWIMS experimental calibration techniques. Therefore, this technique eliminates the need for experimental calibration, thereby expediting the process of obtaining collisional cross sections with TWIMS.

The collisional cross sections obtained here with high wave velocities are larger than those obtained with DTIMS, especially for ions formed from buffered aqueous solutions. Larger than expected cross sections are likely obtained with the high wave velocities as a result of protein unfolding that can occur during TWIMS as a result of ion heating. These results indicate that low wave velocities should be used for obtaining collisional cross sections with TWIMS in order to minimize any uncertainties that may result from protein unfolding occurring. Uncertainty in TWIMS computational calibration cross sections may also arise from uncertainties in the pressure within the TWIMS cell. It may be possible to determine the pressure in a TWIMS drift cell by measuring the drift time of an ion that is not likely to unfold during TWIMS and by varying the pressure used to calculate the drift time of this same ion until a value similar to the measured drift time is obtained.

## 8.6 References

- (1) *Transport properties of ions in gases*, ed.; Mason, E. A. and McDaniel, E. W., Ed.; Wiley: New York, NY, **1988**.
- (2) Cohen, M. J.; Karasek, F. W. *J. Chromatogr. Sci.* **1970**, *8*, 330-337.
- (3) Bowers, M. T.; Kemper, P. R.; Vonhelden, G.; Vankoppen, P. A. M. *Science* **1993**, *260*, 1446-1451.
- (4) St Louis, R. H.; Hill, H. H. J.; Eiceman, G. A. *Crit. Rev. Anal. Chem.* **1990**, *21*, 321-356.
- (5) Jarrold, M. F. *J. Phys. Chem.* **1995**, *99*, 11-21.
- (6) Kaur-Atwal, G.; Weston, D. J.; Green, P. S.; Crosland, S.; Bonner, P. L. R.; Creaser, C. *S. Rapid Commun. Mass Spectrom.* **2007**, *21*, 1131-1138.
- (7) Djidja, M. C.; Francese, S.; Loadman, P. M.; Sutton, C. W.; Scriven, P.; Claude, E.; Snel, M. F.; Franck, J.; Salzet, M.; Clench, M. R. *Proteomics* **2009**, *9*, 2750-2763.
- (8) Stauber, J.; MacAleese, L.; Franck, J.; Claude, E.; Snel, M.; Kaletas, B. K.; Wiel, I. M. V. D.; Wisztorski, M.; Fournier, I.; Heeren, R. M. A. *J. Am. Soc. Mass Spectrom.* **2010**, *21*, 338-347.
- (9) Shelimov, K. B.; Clemmer, D. E.; Hudgins, R. R.; Jarrold, M. F. *J. Am. Chem. Soc.* **1997**, *119*, 2240-2248.
- (10) Badman, E. R.; Hoaglund-Hyzer, C. S.; Clemmer, D. E. *Anal. Chem.* **2001**, *73*, 6000-6007.
- (11) Myung, S.; Badman, E. R.; Lee, Y. J.; Clemmer, D. E. *J. Phys. Chem. A* **2002**, *106*, 9976-9982.
- (12) Ruotolo, B. T.; Giles, K.; Campuzano, I.; Sandercock, A. M.; Bateman, R. H.; Robinson, C. V. *Science* **2005**, *310*, 1658-1661.
- (13) Loo, J. A.; Berhane, B.; Kaddis, C. S.; Wooding, K. M.; Xie, Y. M.; Kaufman, S. L.; Chernushevich, I. V. *J. Am. Soc. Mass Spectrom.* **2005**, *16*, 998-1008.
- (14) Utrecht, C.; Versluis, C.; Watts, N. R.; Wingfield, P. T.; Steven, A. C.; Heck, A. J. R. *Angew. Chem. Int. Ed.* **2008**, *47*, 6247-6251.
- (15) Thomas, J. J.; Bothner, B.; Traina, J.; Benner, W. H.; Siuzdak, G. *Spectrosc. Int. J.* **2004**, *18*, 31-36.
- (16) McDaniel, E. W.; Barnes, W. S.; Martin, D. W. *Rev. Sci. Instrum.* **1962**, *33*, 2-6.
- (17) Hoaglund, C. S.; Valentine, S. J.; Sporleder, C. R.; Reilly, J. P.; Clemmer, D. E. *Anal. Chem.* **1998**, *70*, 2236-2242.
- (18) Tang, K. Q.; Li, F. M.; Shvartsburg, A. A.; Strittmatter, E. F.; Smith, R. D. *Anal. Chem.* **2005**, *77*, 6381-6388.
- (19) Purves, R. W.; Guevremont, R. *Anal. Chem.* **1999**, *71*, 2346-2357.
- (20) Robinson, E. W.; Williams, E. R. *J. Am. Soc. Mass Spectrom.* **2005**, *16*, 1427-1437.
- (21) Shvartsburg, A. A.; Li, F. M.; Tang, K. Q.; Smith, R. D. *Anal. Chem.* **2006**, *78*, 3706-3714.
- (22) Räsänen, R.; Nousiainen, M.; Peräkorpi, K.; Sillanpää, M.; Polari, L.; Anttalainen, O.; Utriainen, M. *Analyt. Chim. Acta* **2008**, *623*, 59-65.
- (23) Arnanthigo, Y.; Anttalainen, O.; Safaei, Z.; Sillanpää, M. *Int. J. Ion Mobility Spectrom.* **2016**, *19*, 15-30.
- (24) Giles, K.; Williams, J. P.; Pringle, S. D.; Wildgoose, J. L.; Slade, S. E.; Thalassinos, K.; Bateman, R. H.; Bowers, M. T.; Scrivens, J. H. *Int. J. Mass Spectrom.* **2007**, *261*, 1-12.

- (25) Giles, K.; Williams, J. P.; Campuzano, I. *Rapid Commun. Mass Spectrom.* **2011**, *25*, 1559-1566.
- (26) Giles, K.; Pringle, S. D.; Worthington, K. R.; Little, D.; Wildgoose, J. L.; Bateman, R. H. *Rapid Commun. Mass Spectrom.* **2004**, *18*, 2401-2414.
- (27) Shvartsburg, A. A.; Smith, R. D. *Anal. Chem.* **2008**, *80*, 9689-9699.
- (28) Kanu, A. B.; Dwivedi, P.; Tam, M.; Matz, L.; Hill, H. H., Jr. *J. Mass Spectrom.* **2008**, *43*, 1-22.
- (29) Bohrer, B. C.; Merenbloom, S. I.; Koeniger, S. L.; Hilderbrand, A. E.; Clemmer, D. E. *Ann. Rev. Anal. Chem.* **2008**, *1*, 293-327.
- (30) Ruotolo, B. T.; Benesch, J. L. P.; Sandercock, A. M.; Hyung, S.; Robinson, C. V. *Nat. Protoc.* **2008**, *3*, 1139-1152.
- (31) Thalassinos, K.; Grabenauer, M.; Slade, S. E.; Hilton, G. R.; Bowers, M. T.; Scrivens, J. H. *Anal. Chem.* **2009**, *81*, 248-254.
- (32) Smith, D. P.; Knapman, T. W.; Campuzano, I.; Malham, R. W.; Berryman, J. T.; Radford, S. E.; Ashcroft, A. E. *Eur. J. Mass Spectrom.* **2009**, *15*, 113-130.
- (33) Lanucara, F.; Holman, S. W.; Gray, C. J.; Eyers, C. E. *Nat. Chem.* **2014**, *6*, 281-294.
- (34) Ridenour, W. B.; Kliman, M.; McLean, J. A.; Caprioli, R. M. *Anal. Chem.* **2010**, *82*, 1881-1889.
- (35) Salbo, R.; Bush, M. F.; Naver, H.; Campuzano, I.; Robinson, C. V.; Pettersson, I.; Jorgensen, T. J. D.; Haselmann, K. F. *Rapid Commun. Mass Spectrom.* **2012**, *26*, 1181-1193.
- (36) Bush, M. F.; Campuzano, I. D. G.; Robinson, C. V. *Anal. Chem.* **2012**, *84*, 7124-7130.
- (37) Bush, M. F.; Hall, Z.; Giles, K.; Hoyes, J.; Robinson, C. V.; Ruotolo, B. T. *Anal. Chem.* **2010**, *82*, 9557-9565.
- (38) Michaelevski, I.; Eisenstein, M.; Sharon, M. *Anal. Chem.* **2010**, *82*, 9484-9491.
- (39) Morsa, D.; Gabelica, V.; De Pauw, E. *J. Am. Soc. Mass Spectrom.* **2014**, *25*, 1384-1393.
- (40) Giles, K.; Wildgoose, J. L.; Langridge, D. J.; Campuzano, I. *Int. J. Mass Spectrom.* **2010**, *298*, 10-16.
- (41) Ruotolo, B. T.; Hyung, S.; Robinson, P. M.; Giles, K.; Bateman, R. H.; Robinson, C. V. *Angew. Chem. Int. Ed.* **2007**, *46*, 8001-8004.
- (42) Manura, D.; Dahl, D. A. Scientific Instrument Services, Inc.: Ringoes, NJ, **2006**.
- (43) Sterling, H. J.; Williams, E. R. *J. Am. Soc. Mass Spectrom.* **2009**, *20*, 1933-1943.
- (44) Liu, J.; Konermann, L. *J. Am. Soc. Mass Spectrom.* **2009**, *20*, 819-828.
- (45) Wyttenbach, T.; Bleiholder, C.; Anderson, S. E.; Bowers, M. T. *Mol. Phys.* **2015**, *113*, 2344-2349.

**Table 8.1.** Parameters for eqs. 3 and 4. “WH” denotes the wave height.

$\theta$	$519.5 \text{ m}^{-1}$
A	$\text{WH} \times 213.5 \text{ m}^{-1}$
$A_1$	$\text{WH} \times 213.7 \text{ m}^{-1}$
$A_2$	$\text{WH} \times -25.1 \text{ m}^{-1}$
$A_3$	$\text{WH} \times 2.0 \text{ m}^{-1}$

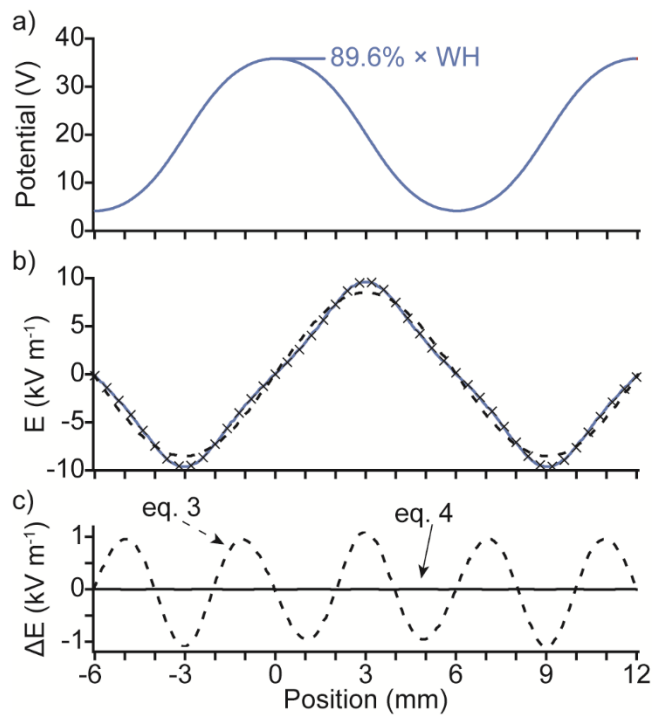


**Figure 8.1.** (a) The electric potential and (b) the electric field strength along the axis of the TWIMS device obtained with a 40 V wave height using SIMION (blue lines), eq. 3 (black dashed line), and eq. 4 (black exes). (c) The difference between the electric field strength along the axis of the TWIMS device obtained with SIMION compared to that obtained with eqs. 3 (dashed line) and 4 (solid line). “WH” denotes wave height.

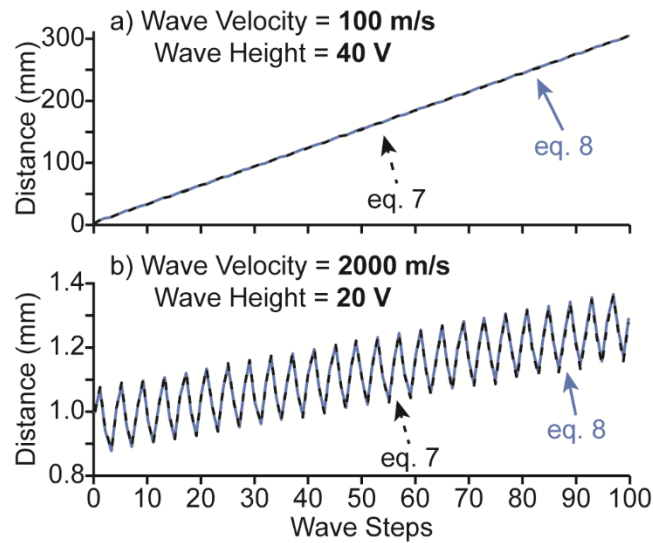


**Figure 8.2.** The total distance travelled by an ion with a  $17.0 \text{ nm}^2 \text{ Da}^{1/2}$  adjusted cross section as a function of the number of waves that have passed through the TWIMS device. These results are obtained using eq. 7 (black dashed lines) and numerical integration of eq. 8 (blue lines) and instrumental settings that result in the ion (a) traversing the TWIMS cell at the wave velocity and (b) being overtaken by the travelling waves.

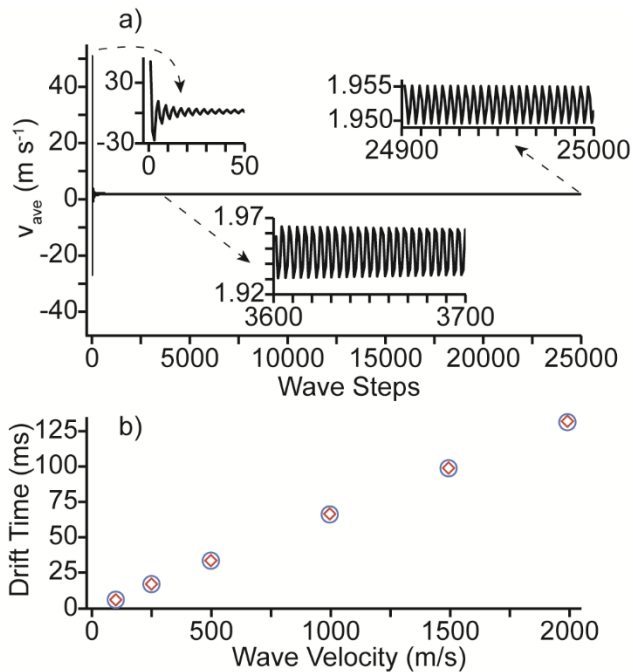


**Figure 8.3.** (a) The average ion drift velocity as a function of the number of wave steps that have passed through the TWIMS device obtained with a  $17.0 \text{ nm}^2 \text{ Da}^{1/2}$  adjusted cross section, a 20 V wave height, and a 2000 m/s wave velocity. (b) Calculated drift times obtained using average ion drift velocities obtained with eq. 7 (blue circles) and numerical integration of eq. 8 (red diamonds) with a  $17.0 \text{ nm}^2 \text{ Da}^{1/2}$  adjusted cross section, a 20 V wave height, and wave velocities of between 100 and 2000 m/s.

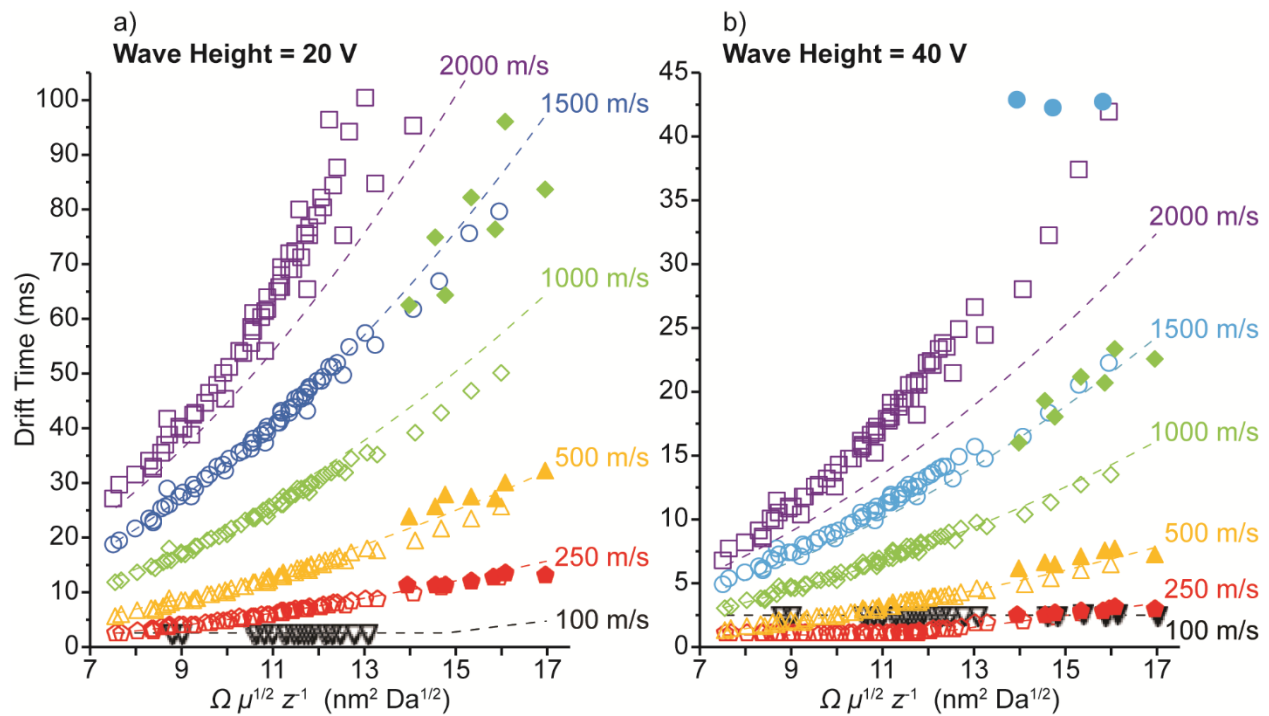


**Figure 8.4.** Measured (shapes) and calculated (dashed lines) drift times as a function of the adjusted cross sections determined using DTIMS cross sectional values. These results are obtained with (a) 20 and (b) 40 V wave heights and 100 (black inverted triangles), 250 (red pentagons), 500 (yellow triangles), 1000 (green diamonds), 1500 (blue circles), and 2000 (purple squares) m/s wave velocities. Open and filled shapes correspond to ions formed from denaturing and buffered aqueous solutions, respectively.

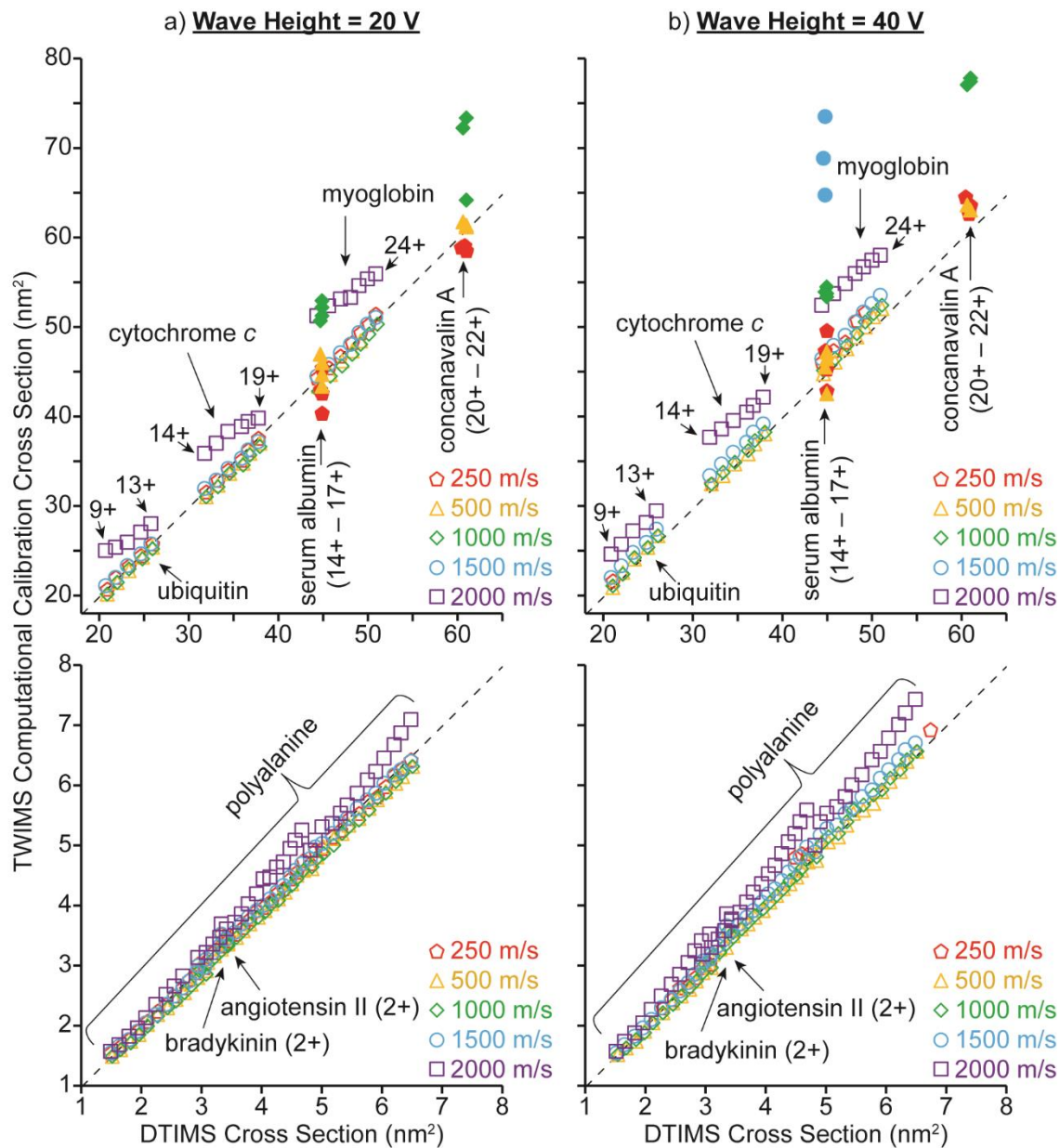


**Figure 8.5.** TWIMS computational calibration cross sections obtained with (a) 20 and (b) 40 V wave heights and 250 (red pentagons), 500 (yellow triangles), 1000 (green diamonds), 1500 (blue circles), and 2000 (purple squares) m/s wave velocities as a function of the corresponding DTIMS cross sections. Opened and closed shapes correspond to ions formed from denaturing and buffered aqueous solutions, respectively. Black dashed lines are a one-to-one correspondence between the axes.

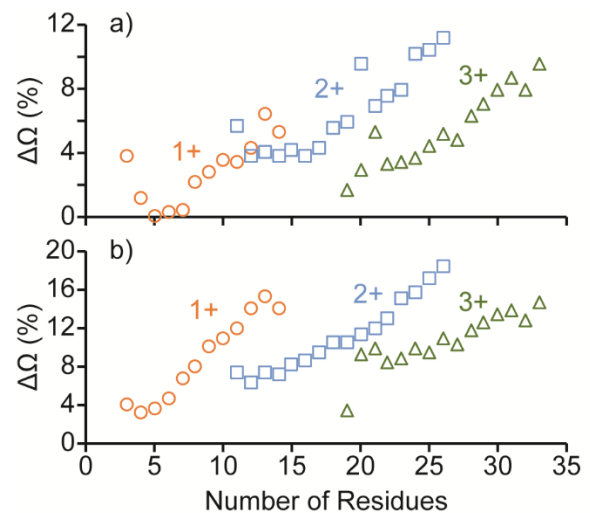


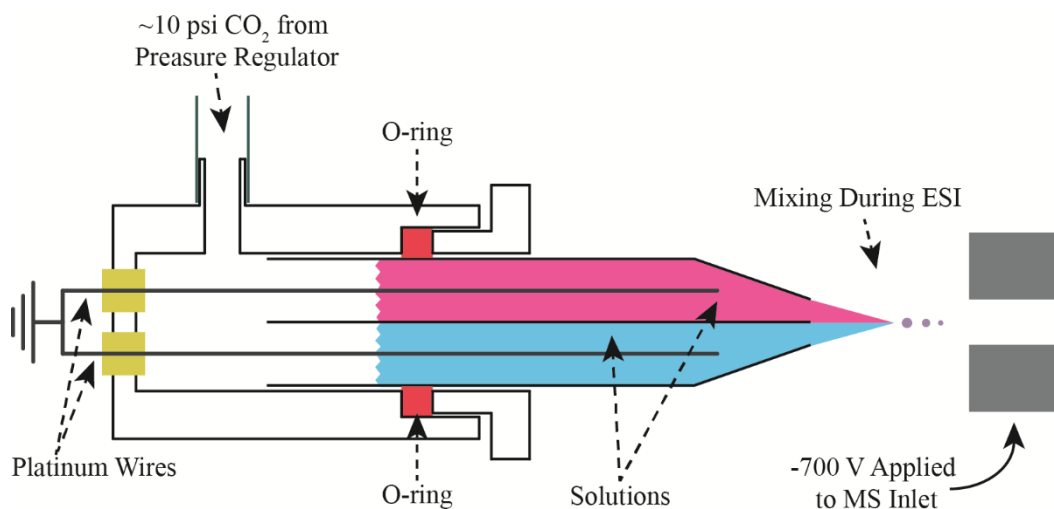
**Figure 8.6.** Difference between the collisional cross sections of polyalanine ions obtained with the computational method with (a) 20 and (b) 40 V wave height and a 2000 m/s wave velocity and those obtained with DTIMS as a function of the length of the peptides. Circles, squares, and triangles correspond to 1+, 2+, and 3+ charge state ions, respectively.

## Appendix A

### Schematic Diagram of the Experimental Setup and Relative Ionization Efficiency Measurements of Oxidized and Reduced DCIP

This appendix is reproduced with permission from  
Mortensen, D.M.; Williams, E.R.

"Theta-Glass Capillaries in Electrospray Ionization:  
Rapid Mixing and Short Droplet Lifetimes"  
*Analytical Chemistry* **2014**, *86*, 9315–9321  
© 2014 American Chemical Society



**Scheme A.1.** A schematic diagram of the experimental setup showing the grounded platinum wires in contact with the solutions in each barrel of the theta-glass emitter. Electrospray was initiated by applying a potential of  $\sim 700$  V to the inlet of the mass spectrometer, and a backing pressure of  $\sim 10$  psi ( $\text{CO}_2$ ) was applied to the solutions during electrospray using a pressure regulator.

**A.2 The relative ionization efficiency of oxidized DCIP to reduced DCIP.** The relative ionization efficiency of the oxidized form of 2,6-dichloroindophenol (oDCIP) with respect to its reduced form (rDCIP) was measured by preparing a solution containing oDCIP and 18-crown-6 (18C6) and a solution containing rDCIP and 18C6, all at 10  $\mu$ M concentrations and at pH = 3. The most abundant ion in the ESI mass spectra of both solutions is  $[18\text{C}6 + \text{K}]^+$ , which was used as an internal standard. The relative abundances of  $[\text{oDCIP} + \text{H}]^+$  and  $[\text{rDCIP} + \text{H}]^+$  were  $24.4 \pm 4.0$  and  $25.5 \pm 2.0$ , respectively (representative mass spectra of the solutions containing oDCIP and rDCIP are shown in Figure S-1 a and b, respectively). The relative ionization efficiency of oDCIP to rDCIP was determined from these results and is  $1.0 \pm 0.2$ .

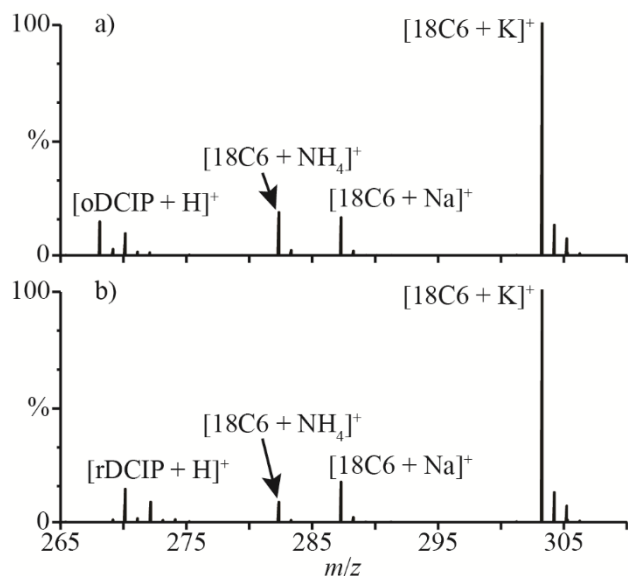


**Figure A.1.** Representative mass spectra of aqueous solutions containing (a) oDCIP and 18C6 (pH = 3) and (b) rDCIP and 18C6, all at 10  $\mu$ M concentrations and at pH = 3.

## Appendix B

### Electron Micrographs of the Tips of the Emitters, Mixing Efficiency Measurements, and TWIMS Drift Profiles

This appendix is reproduced with permission from  
Mortensen, D.M.; Williams, E.R.  
“Ultrafast (1  $\mu$ s) Mixing and Fast Protein Folding in  
Nanodrops Monitored by Mass Spectrometry”  
Journal of the American Chemical Society **2016**, *138*, 3453–3460  
© 2016 American Chemical Society

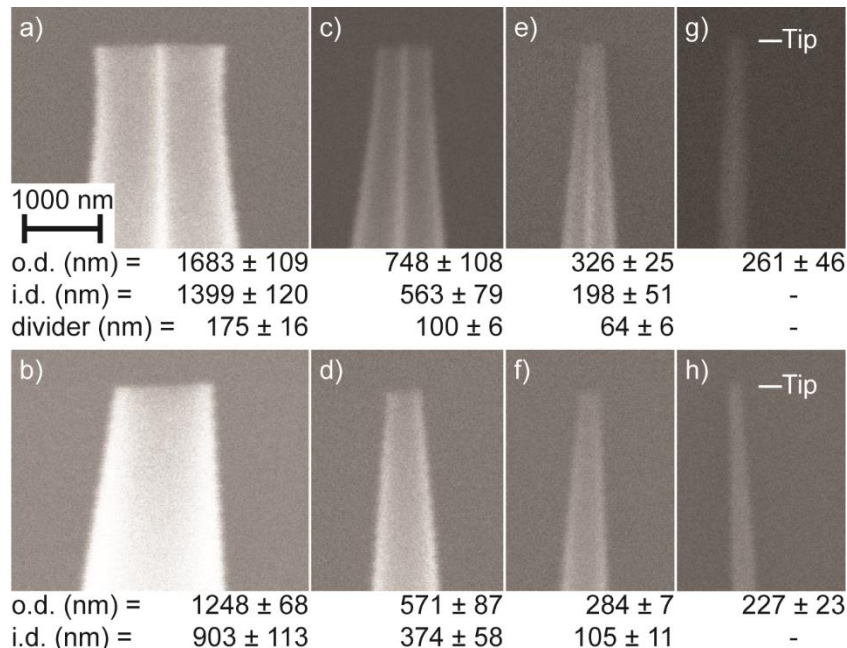


**Figure B.1.** Electron micrographs of the tips of the theta-glass emitters with average o.d.s of (a,b)  $1465 \pm 134$ , (c,d)  $659 \pm 135$ , (e,f)  $305 \pm 32$ , and (g,h)  $244 \pm 61$  nm. The inner divider is perpendicular to and parallel to the sample stand in the upper and lower panels, respectively. White lines were added to (g) and (h) to indicate where the tips end. For the ~244 nm o.d. tips, the i.d. and divider width are not resolved.

**B.2 Mixing Efficiencies.** To determine if complete mixing occurs between solutions loaded into the different barrels of the theta-glass emitters, a rapid equilibration complexation reaction is performed. If incomplete mixing occurs between the solutions loaded into either barrel of the theta-glass emitters, only a portion of the reagents in either solution will interact and the product to reagent ratio in the resulting mass spectra will be less than in that of a premixed solution that is in equilibrium. 18-crown-6 (18C6) and K<sup>+</sup> form the complex [18C6 + K]<sup>+</sup> with a forward rate constant of  $2.45 \times 10^9$  mol s<sup>-1</sup> (average of values measured by others).<sup>1</sup> Protonated 18C6 is not observed in the mass spectra, so the product to reagent ratio cannot be directly observed. Therefore, NaCl is added to the 18C6 solution to form the complex [18C6 + Na]<sup>+</sup>.

Aqueous solutions containing (A) 50 μM 18C6 and 50 μM NaCl and (B) 5 μM KCl are mixed both at a 1:1 ratio prior to nanoESI (equilibrium) and using the theta-glass emitters with flow rates between 48 and 2878 pL/s (rapid mixing). These flow rates are obtained using various tip sizes and backing pressures. A mass spectrum of these solutions mixed prior to nanoESI, acquired at 913 pL/s, is shown in Figure S2a. [18C6 + Na]<sup>+</sup> and [18C6 + K]<sup>+</sup> are both present at a ratio of 1 to  $1.6 \pm 0.1$ , respectively. The ratio, [18C6 + K]<sup>+</sup>/[18C6 + Na]<sup>+</sup>, for both the equilibrium and rapid mixing experiment are shown in Figure S2b as a function of flow rate. These data were corrected for the relative abundance of [18C6 + K]<sup>+</sup> in the mass spectra of solution A at each flow rate. The ratios of these complexes are the same to within error between the equilibrium and rapid mixing experiments at each flow rate. This result indicates that this reaction reaches equilibrium during nanoESI and that complete mixing occurs between the solutions. The ratio of the complexes in these experiments has a relatively constant value of ~1.3 at each flow rate obtained using the ~1465 nm o.d. tips, a slightly higher value of ~1.6 when the ~659 nm o.d. tips are used, and significantly higher values of ~2.1 and ~1.9 when the ~305 and ~244 nm o.d. tips are used, respectively. The diminished tip diameter of the smaller tips results in an increased tip surface area relative to the solution volume in these experiments, and this could result in more K<sup>+</sup> being released from the glass, resulting in an increased ratio of [18C6 + K]<sup>+</sup> to [18C6 + Na]<sup>+</sup> in the resulting mass spectra. The change in tip geometry may also result in an increased ionization efficiency of [18C6 + K]<sup>+</sup> relative to [18C6 + Na]<sup>+</sup> for the smaller tip sizes, resulting in the increased relative abundance of [18C6 + K]<sup>+</sup> in the resulting mass spectra.

## Reference

- (1) Izatt, R. M.; Bradshaw, J. S.; Nielsen, S. A.; Lamb, J. D.; Christensen, J. J.; Sen, D. *Chem. Rev.* **1985**, 85, 271-339.

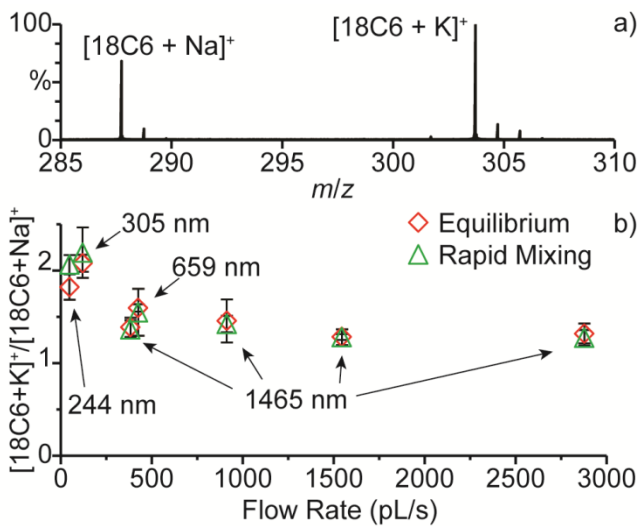


**Figure B.2.** (a) Mass spectrum of a solution containing  $\text{Na}^+$ ,  $^{18}\text{C}_6$ , and  $\text{K}^+$  at a ratio of 10:10:1. (b) The ratio,  $[18\text{C}_6 + \text{K}]^+ / [18\text{C}_6 + \text{Na}]^+$ , in the mass spectra obtained from the equilibrium (diamonds) and rapid mixing (triangles) experiments as a function of the solution flow rate. The average o.d. of the tips used in these experiments are indicated.

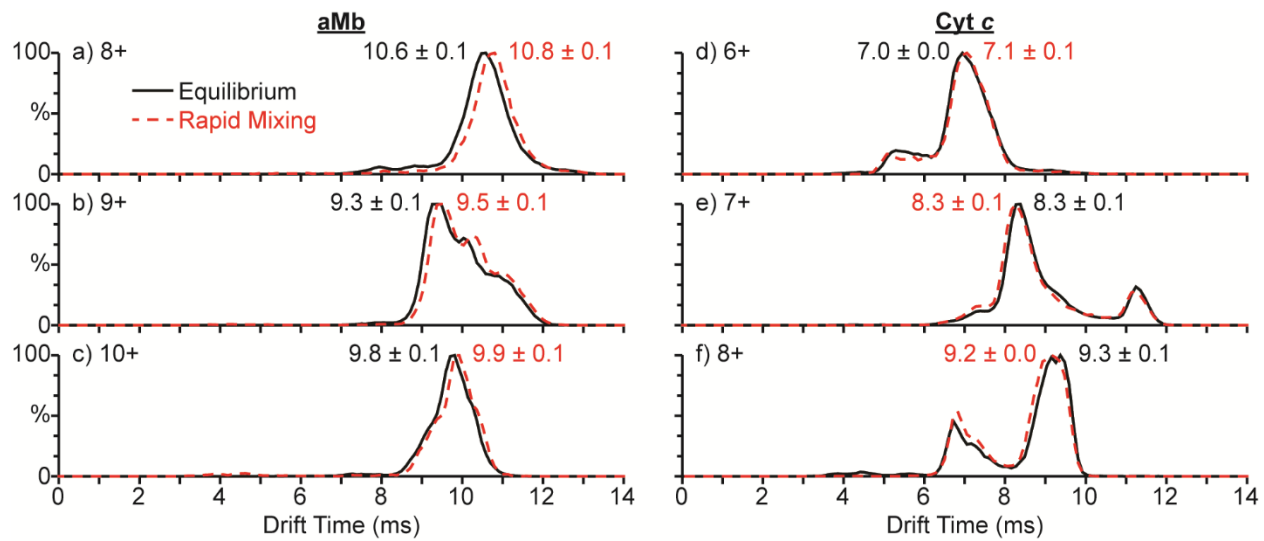


**Figure B.3.** TWIMS drift profiles of the (a) 8+, (b) 9+, and (c) 10+ charge states resulting from mixing an acidified aqueous aMb solution ( $\text{pH} = 2.9$ ) with a 100 mM aqueous ammonium acetate solution at a 1:1 ratio prior to nanoESI (equilibrium;  $\text{pH} = 4.7$ ) (black lines) and using a theta-glass emitter (dashed red lines). TWIMS drift profiles of the (d) 6+, (e) 7+, and (f) 8+ ions resulting from mixing an acidified aqueous cyt c solution ( $\text{pH} = 2.8$ ) with a 100 mM aqueous ammonium acetate solution at a 1:1 ratio prior to nanoESI (equilibrium;  $\text{pH} = 4.4$ ) (black lines) and using a theta-glass emitter (dashed red lines).

## Appendix C

### Mass spectra of hMb in 10, 100 and 500 mM aqueous ammonium acetate and ammonium bicarbonate solutions obtained with ~1465 and ~305 nm o.d. tips

This Chapter is reproduced with permission from  
Mortensen, D.M.; Williams, E.R.  
“Surface-Induced Protein Unfolding in  
Submicron Electrospray Emitters”  
*Submitted to Analytical Chemistry 2016*  
© 2016 Royal Society of Chemistry

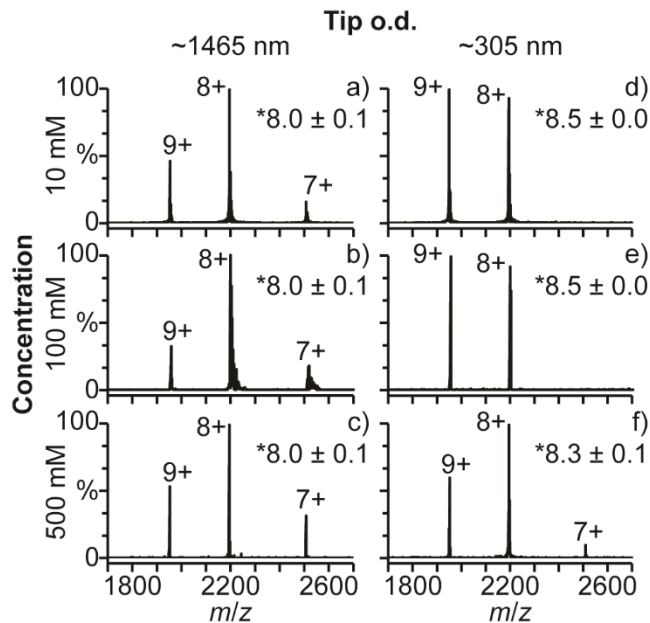


**Figure C.1.** Mass spectra of hMb ( $pI = 7.4$ ) in aqueous solutions containing (a,d) 10, (b,e) 100, and (c,f) 500 mM ammonium acetate ( $pH = 6.7$ ) acquired with (a-c)  $\sim 1465$  and (d-f)  $\sim 305$  nm o.d. tips. (\*) denotes average charge state.

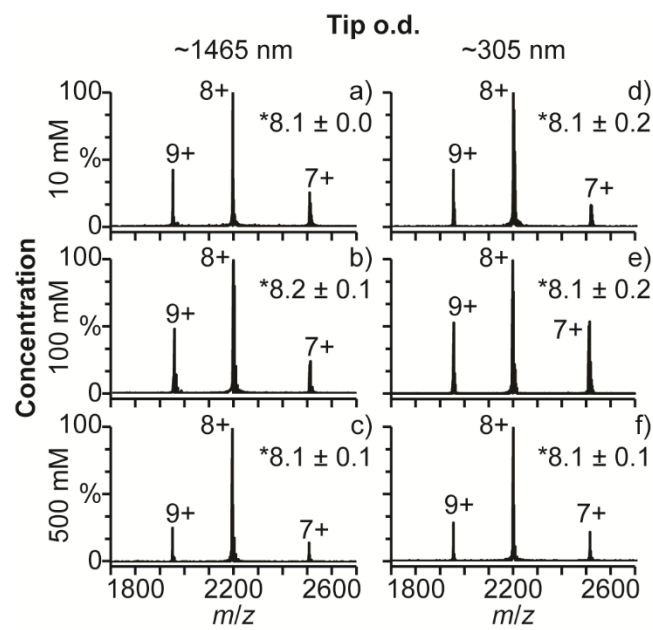


**Figure C.2.** Mass spectra of hMb ( $pI = 7.4$ ) in aqueous solutions containing (a,d) 10, (b,e) 100, and (c,f) 500 mM ammonium bicarbonate ( $pH = 8.3$ ) acquired with (a-c)  $\sim 1465$  and (d-f)  $\sim 305$  nm o.d. tips. (\*) denotes average charge state.

## Appendix D

### Electron micrographs of the tips of the emitters and mass spectra of hMb, cyt c, and $\beta$ -lac A in 100 mM aqueous ammonium acetate, formate, and bicarbonate solutions acquired under native MS conditions

This Chapter is reproduced with permission from  
Mortensen, D.M.; Williams, E.R.  
“Electrothermal Supercharging of Proteins in Native  
MS: Effects of Protein Isoelectric Point, Buffer,  
and nanoESI-Emitter Tip Size”  
*Analyst* **2016**, DOI: 10.1039/c6an01380e  
© 2016 Royal Society of Chemistry

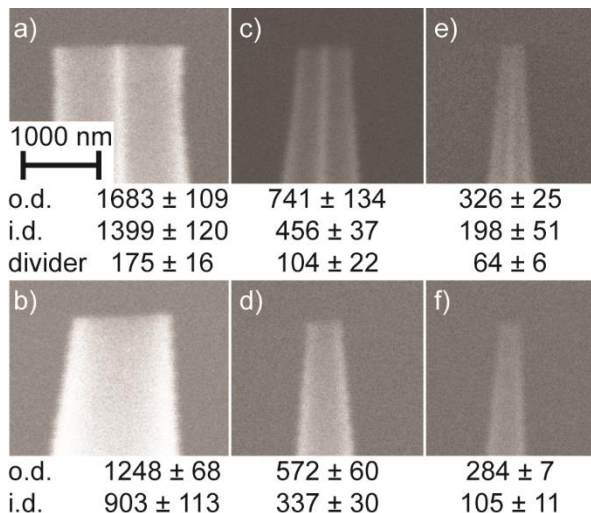


**Figure D.1.** Electron micrographs of the tips of the theta-glass emitters with average outer diameters of (a,b)  $1465 \pm 134$ , (c,d)  $656 \pm 131$ , and (e,f)  $305 \pm 32$  nm with the inner divider perpendicular to and parallel to the sample stand in the upper and lower panels, respectively.

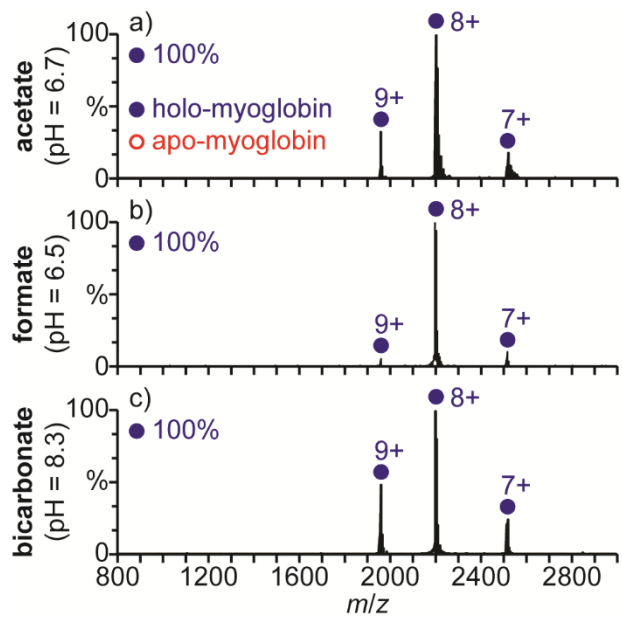


**Figure D.2.** Mass spectra of hMb ( $\text{pI} = 7.4$ ) under native MS conditions (700 V spray potential) in aqueous solutions containing 100 mM (a) ammonium acetate ( $\text{pH} = 6.7$ ), (b) ammonium formate ( $\text{pH} = 6.5$ ), and (c) ammonium bicarbonate ( $\text{pH} = 8.3$ ) acquired with  $\sim 1465$  nm o.d. tips.

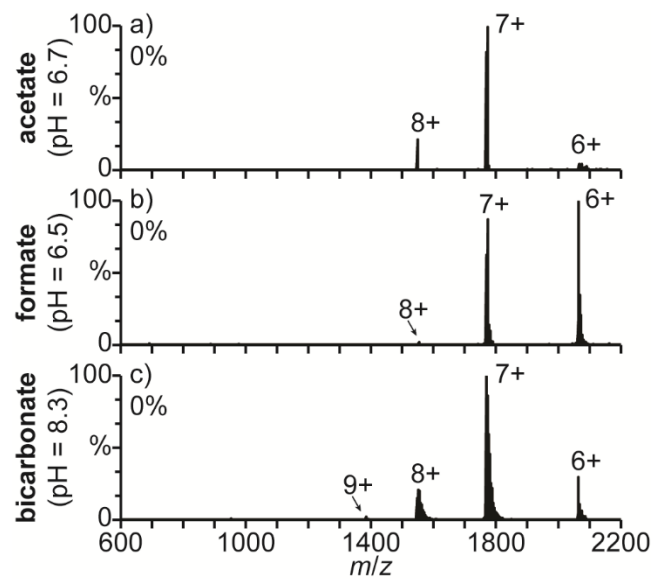


**Figure D.3.** Mass spectra of cyt *c* ( $pI = 10.3$ ) under native MS conditions (700 V spray potential) in aqueous solutions containing 100 mM (a) ammonium acetate ( $pH = 6.7$ ), (b) ammonium formate ( $pH = 6.5$ ), and (c) ammonium bicarbonate ( $pH = 8.3$ ) acquired with ~1465 nm o.d. tips. Percentages are the relative abundances of the unfolded fractions ( $\geq 10+$  charge states) of cyt *c*.

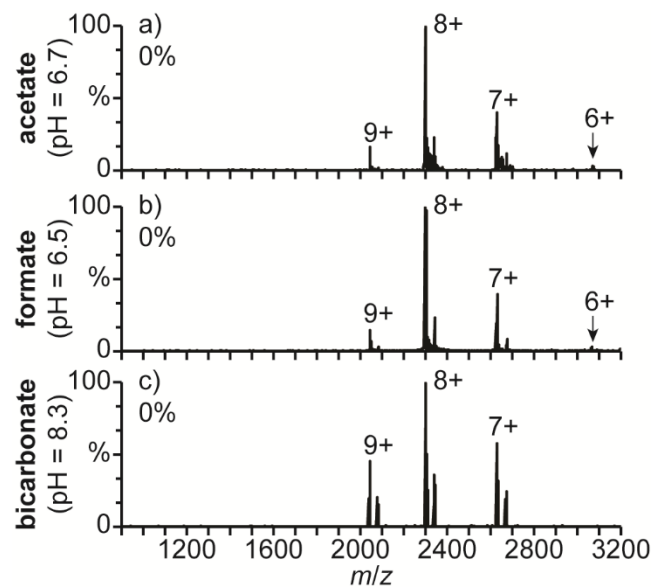


**Figure D.4.** Mass spectra of β-lac A ( $\text{pI} = 5.1$ ) under native MS conditions (700 V spray potential) in aqueous solutions containing 100 mM (a) ammonium acetate ( $\text{pH} = 6.7$ ), (b) ammonium formate ( $\text{pH} = 6.5$ ), and (c) ammonium bicarbonate ( $\text{pH} = 8.3$ ) acquired with ~1465 nm o.d. tips. Percentages are the relative abundances of the unfolded fractions ( $\geq 10^+$  charge states) of β-lac A.

## Appendix E

### A second-order polynomial relating TWIMS drift times with adjusted cross sections obtained using DTIMS cross sectional values is compared with that obtained using purely hypothetical adjusted cross sectional values.

This Chapter is reproduced with permission from  
Mortensen, D.M.; Susa, A.C.; Williams, E.R.  
“Collisional Cross Sections with T-Wave Ion  
Mobility Spectrometry without Experimental Calibration”  
*Submitted to International Journal of Mass Spectrometry* **2016**  
© 2016 American Chemical Society

**E.1 Polynomial Fits Obtained with Different Adjusted Cross Sections.** The drift times of the reference ions calculated using DTIMS cross sectional values, a 20 V wave height, and a 1000 m/s wave velocity are shown as a function of adjusted cross section in Figure S-1a. These reference ions have adjusted cross sections of between 7.5 and 17.0 nm<sup>2</sup> Da<sup>1/2</sup>. The drift times of purely hypothetical ions with adjusted cross sections ranging by half-integer values from 7.5 to 17.0 nm<sup>2</sup> Da<sup>1/2</sup> are also calculated using the same wave parameters (Figure S-1b). The data in Figure S-1a and S-1b are fit with second-order polynomials (shown as black lines). The drift times predicted by these two polynomial fits are the same to within less than 0.1% for all of the adjusted cross sections within the range of adjusted cross sections used (Figure S-1c). The difference between the two polynomial fits is greatest for adjusted cross sections below ~12 nm<sup>2</sup> Da<sup>1/2</sup> because most of the reference ions (70%) have adjusted cross sectional values that are below 12 nm<sup>2</sup> Da<sup>1/2</sup>. In contrast, the adjusted cross sections of the hypothetical ions are evenly distributed across the range of values used. Thus, the polynomial fit obtained with the reference ions is slightly biased towards lower adjusted cross sectional values, whereas the polynomial fit obtained with the hypothetical ions is not biased towards either high or low values. The results in Figure S-1 indicate that nominally identical polynomial fits can be obtained using adjusted cross sections obtained with DTIMS cross sectional values and using purely hypothetical adjusted cross sections as long as the same range of adjusted cross sections is used.

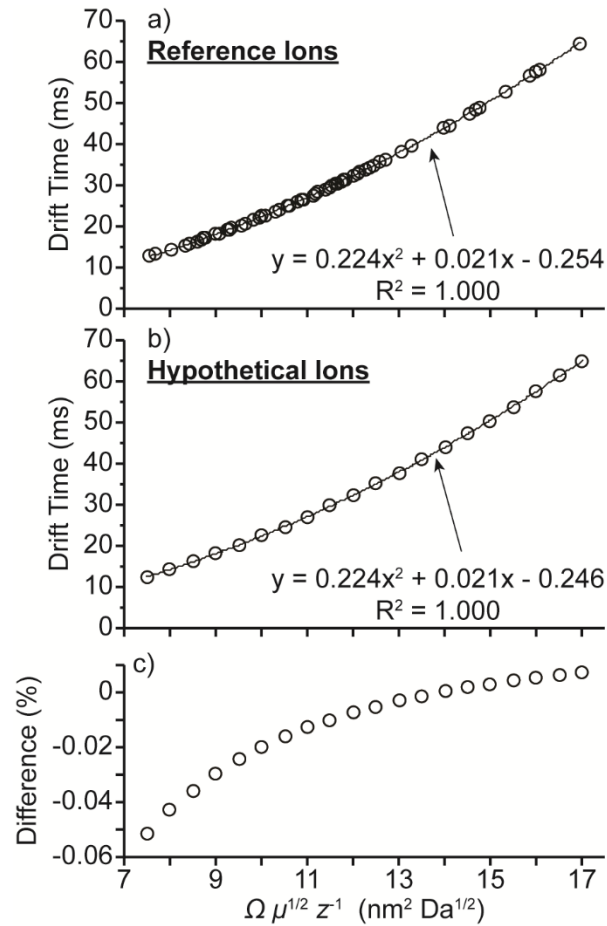


**Figure E.1.** Calculated drift times as a function of adjusted cross section obtained (a) for the reference ions using DTIMS cross sectional values and (b) for purely hypothetical ions. These results are obtained with a 20 V wave height and a 1000 m/s wave velocity. Black lines are second-order polynomial fits to the data. (c) The difference between the polynomial fit obtained for the reference ions and that obtained for the hypothetical ions as a function of adjusted cross section.